

T₂ Decay Curve Acquisition and Analysis in MRI
Noise Considerations, Short T₂, and B₁ Field Encoding

by

Craig K. Jones

M.Sc., The University of Western Ontario, 1997

B.Sc., Simon Fraser University, 1992

A THESIS SUBMITTED IN PARTIAL FULFILMENT OF
THE REQUIREMENTS FOR THE DEGREE OF

DOCTOR OF PHILOSOPHY

in

The Faculty of Graduate Studies

(Department of Physics and Astronomy)

We accept this thesis as conforming
to the required standard

THE UNIVERSITY OF BRITISH COLUMBIA

July 31, 2003

© Craig K. Jones, 2003

In presenting this thesis in partial fulfilment of the requirements for an advanced degree at the University of British Columbia, I agree that the Library shall make it freely available for reference and study. I further agree that permission for extensive copying of this thesis for scholarly purposes may be granted by the head of my department or by his or her representatives. It is understood that copying or publication of this thesis for financial gain shall not be allowed without my written permission.

Department of Physics and Astronomy

The University Of British Columbia
Vancouver, Canada

Date July 31, 2003

Abstract

The myelin sheath is a lipid bilayer wrapped around axons in the human brain. The myelin allows faster conduction and uses less energy than along non-myelinated axons. Diseases, such as multiple sclerosis, break down the myelin sheath resulting in cognitive and physical disability. Water trapped between the myelin bilayers has a $T_2 \approx 15$ ms compared to intra/extra-cellular water with a $T_2 \approx 80$ ms and cerebrospinal fluid which has a $T_2 \approx 2000$ ms. A multi-echo MRI pulse sequence is used to acquire a T_2 decay curve which is fit using a non-negative least-squares (NNLS) curve fitting algorithm to calculate the signal as a function of the T_2 (T_2 distribution). The myelin water fraction (MWF) is calculated as the signal with a $T_2 < 50$ ms divided by the total signal in the T_2 distribution. Quantification of the MWF *in vivo*, is slow, prone to errors due to artifacts in the T_2 decay curve, and requires many data acquisition averages to attain the necessary high signal-to-noise ratio. Each of these areas were addressed in this thesis. First, I compared the accuracy and precision of MWF estimates from a set of simulated and *in vivo* multi-echo data with and without noise reduction filters applied. The MWF estimated from anisotropically filtered multi-echo data had the smallest variability, over homogeneous regions, compared to MWF estimates from other filtered data. Second, I created a new technique to optimize coefficients that when linearly combined with multi-echo data, result in fast, accurate estimates of the MWF. Simulations and *in vivo* estimates of the MWF were as accurate as those from the NNLS algorithm and 20,000 times faster. Finally, the standard multi-echo sequence was optimized to remove artifacts due to inaccurate refocusing pulses. I created a novel T_2 curve fitting algorithm, based on NNLS, to accurately estimate the T_2 distribution and refocusing pulse flip angle from a T_2 decay curve. Simulations and data acquired on phantoms showed the new technique was as accurate as the NNLS algorithm in quantifying the T_2 distribution parameters. *In vivo* myelin water maps were as good as those estimated from the optimized multi-echo pulse sequence.

Table of Contents

Abstract	ii
Table of Contents	iii
List of Tables	vii
List of Figures	ix
List of Algorithms	xi
Acknowledgements	xii
Glossary	xiv
1 Introduction	1
1.1 Magnetic Resonance Imaging	1
1.2 T_2 and T_1 Relaxation	2
1.2.1 Spectral Density	2
1.2.2 Bloch Equations	3
1.3 Central Nervous System	4
1.4 Tissue Relaxation	6
1.5 T_2 Decay Curve	7
1.5.1 Mono-Exponential T_2 Relaxation	7
1.5.2 Multi-Exponential T_2 Relaxation	8
1.6 T_2 Decay Curve Acquisition	9
1.6.1 K-Space	9
1.6.2 Optimized Multi-Echo Pulse Sequence	10
1.6.3 Standard Multi-Echo Pulse Sequence	11
1.6.4 Noise in Decay Curve	14
1.6.5 Artifacts Influencing the T_2 Decay Curve	16
1.7 T_2 Decay Curve Analysis	18
1.7.1 Decay Curve Inversion (Decay Curve to T_2 Distribution)	18
1.7.2 T_2 Decay Curve Requirements	24
1.8 Phantoms	25
1.9 Overview of Thesis	26

2	Myelin Water Fraction Noise Reduction	27
2.1	Introduction	27
2.2	SNR Effect on Myelin Water Fraction	28
2.3	Description of Spatial Filters	29
2.3.1	Anisotropic Diffusion Filter	30
2.3.2	Susan Filter	31
2.3.3	Median Filter	31
2.3.4	Wavelet Filter	32
2.4	Spatial Filters on Simulated Data	32
2.4.1	Methods	32
2.4.2	Results	36
2.4.3	Conclusions	40
2.5	Spatial Filters Applied to <i>In Vivo</i> Data	40
2.5.1	Data Acquisition and Analysis	40
2.5.2	Results	41
2.5.3	Conclusions	44
2.6	Spatial Filtering vs Averaging	44
2.6.1	Methods	44
2.6.2	Results	46
2.6.3	Discussion	50
2.6.4	Conclusions	53
2.7	Conclusions	53
3	Myelin Water Fraction from Linear Combination	55
3.1	Introduction	55
3.1.1	Linear Combination for T_2 Selectivity	56
3.1.2	Properties of a Linear Combination	57
3.1.3	Overview	57
3.2	Calculation of Coefficients	58
3.2.1	Coefficients for Short T_2	59
3.2.2	Coefficients for All T_2	60
3.2.3	Description of the Algorithm	61
3.2.4	Results	62
3.2.5	Discussion	63
3.3	Linear Combination Simulations	64
3.3.1	Model	64
3.3.2	Results and Discussion	64
3.3.3	Conclusions	65
3.4	Selectivity of Mono-Exponential Phantoms	66
3.4.1	Methods	66
3.4.2	Results and Discussion	66
3.4.3	Conclusions	68
3.5	<i>In Vivo</i> Myelin Water Fraction: NNLS vs. T_2 Filter	68
3.5.1	Methods	69
3.5.2	Scan Results	69
3.5.3	Conclusions	72

3.6	Calculation of Coefficients by Matrix Inversion	72
3.6.1	Calculation of Coefficients	72
3.6.2	Results and Discussion	74
3.6.3	Conclusions	76
3.7	Calculation of Coefficients by Backus-Gilbert	76
3.7.1	Calculation of Coefficients	76
3.7.2	Results and Discussion	77
3.7.3	Conclusions	80
3.8	Optimal Echo Times	80
3.8.1	Filter Measures	80
3.8.2	Equally Spaced Echoes	82
3.8.3	Non-Equidistant	85
3.8.4	Discussion	88
3.8.5	Four Echo Non-equidistant Sampling	90
3.9	Conclusions	92
4	Non-180 Refocusing Pulses	94
4.1	Introduction	94
4.1.1	Motivation	94
4.1.2	Previous Work	95
4.1.3	Implementation of Algorithm	98
4.1.4	Overview of Work	102
4.2	Mono-Exponential T_2 Decay Curve Fit	102
4.2.1	Mono-Exponential Fit Algorithm	102
4.2.2	Monoexponential Fit – Noise Simulation	103
4.2.3	Phantom Verification	105
4.3	Multi-Exponential T_2 Decay Curve Fit	111
4.3.1	Multi-Exponential Fit Algorithm	111
4.3.2	Bi-Exponential Parameters From Incorrect α	115
4.3.3	NNLS $^\alpha$ Multi-Exponential Simulations	116
4.3.4	Phantoms	117
4.3.5	<i>In Vivo</i> Multi-Exponential Fits	120
4.4	Multi-Slice, Multi-Echo	126
4.4.1	Introduction	126
4.4.2	Methods	127
4.4.3	Results and Discussion	127
4.4.4	Conclusions	135
4.5	Non 90° Excitation Pulse	136
4.5.1	Decay Curve Calculation	136
4.5.2	Simulation Methods	136
4.5.3	Simulation 1: Inaccurate Excitation and Accurate Refocusing, Assume both Accurate	137
4.5.4	Simulation 2: Inaccurate Excitation and Inaccurate Refocusing, Assume Accurate Excitation	138
4.5.5	Simulation 3: Inaccurate Excitation and Inaccurate Refocusing	139
4.5.6	Discussion	140

Table of Contents

4.5.7	Conclusions	141
4.6	Non-Constant Train of Flip Angles	141
4.6.1	Simulations	143
4.6.2	Scanning	144
4.6.3	Conclusion	149
4.7	Conclusions	149
5	Conclusions	150
5.1	Filtering	150
5.2	Linear Combination	150
5.3	B_1/T_2	152
5.4	Preferred T_2 Quantification Protocol	153
	Bibliography	154
	A Related Publications	162

List of Tables

1.1	T_1 and T_2 of mono-exponential nickel/agarose phantoms	25
2.1	The mean global error in myelin water fraction over the 10 noisy data sets for each filter	37
2.2	The mean error in myelin water fraction over the 10 noisy data sets for each filter for the area of 15% myelin water	37
2.3	The mean error in myelin water fraction over the 10 noisy data sets for each filter for the area of 30% myelin water	38
2.4	<i>In vivo</i> myelin water fraction as a function of filter.	41
2.5	The number of times each filter had the smallest myelin water fraction	42
2.6	Number of holes per ROI as a function of iterations of the anisotropic diffusion filter.	48
3.1	The coefficients for the short T_2 and all T_2 linear combination method	62
3.2	Mean and standard deviation of the signal in the short T_2 phantom image	67
3.3	Coefficients for the short, medium and long T_2 selection based on matrix inversion.	74
3.4	Coefficients calculated by the Backus-Gilbert method	77
3.5	Coefficients for short and all T_2 filter based on four unevenly spaced echoes.	90
4.1	Mono-exponential noise simulation as a function of α	104
4.2	Mono-exponential noise simulation as a function of α and SNR scaled by a function of the refocusing pulse	104
4.3	Parameters of phantom derived from mono-exponential fit	106
4.4	Bi-exponential noise simulation to assess accuracy and precision of parameter estimation from non-180° refocusing pulse train	116
4.5	Noise simulation to estimate variability of multi-exponential decay curve parameters.	117
4.6	T_2 time calculated from the MESE _o sequence and the MESE _c (with the flip angle calculated).	119
4.7	Refocusing pulse flip angle calculated from multi-echo decay curve.	119
4.8	Estimated T_1 from curve fits of five points (TR = 100, 300, 800, 2000, 3000 ms) from a pulse saturation experiment.	119
4.9	Percent myelin water estimated from scans with $\alpha_{\text{nom}} = 150^\circ$ and $\alpha_{\text{nom}} = 180^\circ$	121
4.10	Refocusing pulse flip angle calculated over the regions from the scans with $\alpha_{\text{nom}} = 150^\circ$ and $\alpha_{\text{nom}} = 180^\circ$	123
4.11	Geometric mean T_2 of the medium component from select regions throughout the image.	124
4.12	Decay curve parameters estimated from <i>in vivo</i> scan as a function of pulse sequence.	133
4.13	The excitation pulse was varied from 90° to 50° and the parameters were calculated assuming only the refocusing pulse was incorrect	138

4.14	The excitation and refocusing pulses were varied with $\alpha_e = 90^\circ, 85^\circ, \dots, 50^\circ$ and $\alpha_r = 2\alpha_e$	139
4.15	The excitation and refocusing pulses were varied with $\alpha_e = 90^\circ, 85^\circ, \dots, 50^\circ$ and $\alpha_r = 2\alpha_e$	140
4.16	Simulation to assess decay curve parameter estimation from non-constant refocusing pulse train (16 echoes).	144
4.17	The T_2 and refocusing pulse flip angle (for the first echo) calculated from each train of refocusing pulses	147
4.18	The resulting χ^2 misfit given the scaling of the RF pulses was 1.0, 1.0, 1.0, s_{90} from $\mathbf{s}^{(4)}$	148

List of Figures

1.1	Myelinated axon	5
1.2	Electron-micrograph of a myelinated cell	6
1.3	Simulated mono-exponential decay curves	8
1.4	Standard MRI image and corresponding k-space.	10
1.5	Optimized single-slice, multi-echo pulse sequence (MESE _o)	11
1.6	Conventional multiple echo 2D spin-echo pulse sequence (MESE _c)	12
1.7	Conventional multiple echo 3D spin-echo pulse sequence (MESE _c)	13
1.8	Rice distribution as a function of the mean	14
1.9	Decay and T ₂ distribution of a bi-exponential white matter model	19
1.10	Least squares and regularized T ₂ distributions of a white matter model	21
2.1	Histograms of myelin water fraction from simulated decay curves.	29
2.2	Simulated myelin water fraction image annotated with six regions.	33
2.3	Simulated myelin water fraction image (truth) from which the 32-echo data set was constructed.	35
2.4	Myelin water maps calculated from spatially filtered, simulated multi-echo data.	39
2.5	Myelin water maps calculated from spatially filtered MRI data.	43
2.6	Myelin water maps from unfiltered and filtered (anisotropic diffusion filter) multi-echo data.	49
2.7	Histograms of unfiltered and filtered myelin water fractions.	51
3.1	Constraints on the short T ₂ filter.	60
3.2	Constraints on the “all” T ₂ filter.	61
3.3	T ₂ filters for short T ₂ components and all T ₂ components	63
3.4	Myelin water fraction noise simulation to compare linear combination and NNLS.	65
3.5	Linear combination short T ₂ selectivity of phantoms.	67
3.6	Mean signal from phantoms in selected image versus T ₂ filter.	68
3.7	<i>In vivo</i> myelin water maps calculated by linear combination and NNLS.	70
3.8	Myelin water fractions calculated per region from the linear combination method and NNLS	71
3.9	Bland-Altman plots for white matter regions and gray matter regions.	71
3.10	T ₂ filters based on coefficients calculated by matrix inversion.	73
3.11	Brain images T ₂ filtered from coefficients calculated by matrix inversion.	75
3.12	Coefficients calculated by Backus-Gilbert method	78
3.13	T ₂ filters based on coefficients calculated by Backus-Gilbert method	79
3.14	The measures of the effectiveness of a short T ₂ filter	81
3.15	The coefficients as a function of the number of echoes and TE.	83
3.16	Width of T ₂ filter for equally spaced echo times.	84

3.17	The coefficients as a function of the number of echoes and TE.	86
3.18	Width of T_2 filter for unequally spaced echo times.	87
3.19	The T_2 filter, $\exp(-TE/T_2)$ as a function of TE.	89
3.20	The short T_2 filter as a function of a consecutive subset of echoes based on the thirty-two coefficients	89
3.21	Short T_2 filter calculated from four echoes compared to filter calculated from 32 echoes.	91
3.22	Myelin water map calculated by linear combination from four echoes and from 32 echoes.	92
4.1	Phase coherence diagram	96
4.2	Decay curves, collected with $\alpha_p = 180^\circ$, fit to obtain T_2 and α	107
4.3	Decay curves, collected with $\alpha_p = 150^\circ$, fit to obtain T_2 and α	108
4.4	Decay curves, collected with $\alpha_p = 110^\circ$, fit to obtain T_2 and α	109
4.5	Decay curves, collected with $\alpha_p = 90^\circ$, fit to obtain T_2 and α	110
4.6	The χ^2 misfit plotted as a function of refocusing pulse flip angle	112
4.7	The rank and inverse of the condition number of A^α based on a 32 echo decay	114
4.8	The rank and inverse of the condition number of A^α based on a 200 echo decay	115
4.9	The myelin water maps calculated from the pulse sequence with a refocusing pulse flip angle prescribed as 180° and 150°	121
4.10	Refocusing pulse flip angle maps calculated with a refocusing pulse flip angle prescribed as 180° and 150°	122
4.11	The arithmetic mean T_2 maps calculated from the pulse sequence with a refocusing pulse flip angle prescribed as 180° and 150°	123
4.12	The χ^2 maps calculated from the pulse sequence with a refocusing pulse flip angle prescribed as 180° and 150°	125
4.13	The myelin water maps calculated from the pulse sequence with a refocusing pulse flip angle prescribed as 180° and 150°	126
4.14	The TE = 10 ms image from the four average, 32 echo MESE _o sequence and six slices of the six slice slab MESE _c acquisition	129
4.15	Myelin water maps calculated from a 6-slice slab MESE _c	130
4.16	Difference between the myelin water map calculated from the MESE _o sequence and the myelin water map calculated from the MESE _c sequence.	131
4.17	<i>In vivo</i> decay curve from MESE _c and MESE _o from the genu of the corpus callosum (WM).	134
4.18	Maps of the refocusing pulse flip angle calculated from a 6-slice slab MESE _c	135
4.19	Spin-echo sequence with three 180° followed by 13 90°	142
4.20	Spin-echo sequence with an exponential decay of the refocusing pulse amplitudes.	143
4.21	Decay curve fit of decay curves collected with non-constant refocusing pulse train, phantom with $T_2 = 85$ ms	145
4.22	Decay curve fit of decay curves collected with non-constant refocusing pulse train, phantom with $T_2 = 23$ ms	146
4.23	Measured and fitted data from non-constant train of refocusing pulses.	148

List of Algorithms

1.1	Small norm NNLS regularization.	23
4.1	Signal calculation from a train of refocusing pulses	100
4.2	T_1 relaxation	101
4.3	T_2 relaxation	101
4.4	Phase evolution of magnetization	101

Acknowledgements

When I first moved to Vancouver in 1997, I began working for Dr. Don Paty, Dr. David Li, and Andrew Riddehough at the MS/MRI Research Group. After a little over a year, it became clear that to pursue further research I would have to do a PhD. My first conversations with Dr. Paty and Dr. Li, were overwhelmingly supportive. Dr. Paty's comment was, "I was wondering when you would come and talk to me about this." With a lot of work from Andrew, an arrangement was worked out such that I worked in the MS/MRI Research group very part-time while I did my PhD. The financial, academic and other support (Ken Bigelow and Vilmos Soti, in particular), during the past four years, has allowed me to complete this PhD. Without the MS/MRI Research Group, this thesis would not exist. Thanks!

Anne, my wife, was the one who pushed me, in the beginning, to do a PhD. I will never forget the evening we sat at Starbucks, talking over the direction of my career. It became more evident the only way to pursue what I wanted was to do a PhD and the only thing holding me back was the desire to support my family. Anne challenged me on that desire and made it clear that we would make it through just fine. In hindsight, she was correct. We have been able to live our lives, for the most part as if I had a (real paying) job, and, in fact, have probably had a better lifestyle.

The first year of my PhD was spent with my supervisor, San. I was doing courses and trying to find a project that to which I could take hold. Then, after some discussion with Alex, and some choices by other grad students, some interesting possibilities came along that led to the work in this thesis. It is interesting to see that the direction of the thesis, in the first year, is very different than the content of the work herein. I would like to thank Alex for the support, interesting projects and allowing me to take on the project. I would like to thank San for the many discussions we had on the different topics. The meetings with San were always extremely interesting, his enthusiasm for research and science always rubbed off on me. His knowledge of

physics and MRI as well as his natural ability to describe complex ideas, using analogies, greatly enhanced my understanding. On more than one occasion my patient wife was waiting for me as I got lost in conversation with San (“talking to San again?”) Other people with influence in the thesis were my committee members: Dr. Anna Celler, Dr. Carl Michal, and Dr. Ken Poskitt. Each of them brought knowledge from their respective areas, which enhanced the quality of the science in this work. My committee meetings were very positive times and put the work in perspective.

There are many friends who have been a great influence and who have enabled such an interesting time for Anne and me in Vancouver. For myself, in particular, Ken Nixon, who I met with Wednesday mornings for several years. The one question Ken always asked me, “Do you have a chapter done?”. He is a great friend and someone who helped put the work in perspective.

Finally, the one person who has had a significant impact in my life is Dr. Ken Whittal. Ken has been a great friend, and more importantly, a mentor for me. He was very patient, with my many questions, and always ready and available. The word mentor is defined as “...[a] wise and trusted counselor and teacher...” and Ken was...

Glossary

Abbreviation	Meaning
BG	Backus-Gilbert
CSF	Cerebrospinal Fluid
FOV	Field of View (cm)
FWHM	Full-Width-at-Half-Max
GM	Gray Matter
ME	Multi-echo
MESE	Multi-echo Spin-Echo Pulse Sequence
MRI	Magnetic Resonance Imaging
MS	Multiple Sclerosis
MT	Magnetization Transfer
MWF	Myelin Water Fraction
NNLS	Non-Negative Least Squares
RF	Radiofrequency
ROI	Region-of-Interest
RMS	Root-Mean-Square
SAR	Specific Absorption Rate
SI	Signal Intensity
SNR	Signal to Noise Ratio
τ	Echo spacing (ms)
TE	Echo Time (ms)
T ₁	Spin-Lattice Relaxation Time (ms)
TR	Repetition Time (ms)
T ₂	Spin-Spin Relaxation Time (ms)

WM White Matter

Chapter 1

Introduction

In magnetic resonance imaging, information about the local water environment is quantified by T_1 and T_2 proton relaxation times and the density of the protons, ρ . The measurement process and analysis is complex, but enables different information to be obtained from the local water environment. The thesis will describe new techniques for better quantification and analysis of T_2 , as well as the encoding of extra information using “artifacts” that arise from data collection.

The introduction has an overview of magnetic resonance imaging (Section 1.1) and the physics of relaxation (Section 1.2). Then, the central nervous system is described (Section 1.3) and the motivation to use quantitative T_2 to assess tissue and pathology (Section 1.4). The T_2 decay curve is discussed (Section 1.5) and then the data collection (Section 1.6) and data analysis (Section 1.7). A set of phantoms was created to validate the acquisition and curve fitting of the decay curves (Section 1.8).

1.1 Magnetic Resonance Imaging

Magnetic resonance imaging (MRI) uses a strong main magnetic field, B_0 , to align the protons in the human body parallel and anti-parallel to the main field. A set of smaller magnetic field gradients, along X, Y, and Z, are used to spatially encode the protons and a radiofrequency (RF) coil is used to excite the sample and to receive RF signal from the protons. The spatially encoded RF signal is reconstructed into an image. The signal intensity of each voxel in the image is a function of the number of protons in the voxel (ρ), the spin-spin relaxation time (T_2) and the spin-lattice relaxation time (T_1).

1.2 T₂ and T₁ Relaxation

The T₂ relaxation time calculated from a multi-echo decay curve acquired using the MRI scanner is related to the local water environment, the acquisition method, and the main magnetic field (B₀). The local water environment affects the interaction of the water molecules (protons). The effect of the interaction is modeled as a spectral density function and is used to define the T₁ and T₂ relaxation times. The relaxation times relate, classically, to the magnetization through a set of phenomenological equations derived by Bloch [1]. The local water environment in human tissue, on the scale of an MRI voxel, typically contains several distinct water compartments. Each of the water compartments may have a different T₂, therefore, a modified set of magnetization equations must be analyzed to calculate the T₂ of each compartment.

1.2.1 Spectral Density

The T₁ and T₂ relaxation times are related to the Larmor frequency of the proton, ω₀, and the correlation time, τ_c, of the spins through the spectral density function [2]:

$$J^{(n)}(\omega) = \frac{k^{(n)}}{r_{ij}^6} \frac{\tau_c}{1 + \omega^2 \tau_c^2} \quad (1.1)$$

where r_{ij} is the distance between spins, k(0) = 24/15, k(1) = 4/15, and k(2) = 16/15. The correlation time is a characteristic time scale of molecular motion. The relaxation rates, inverse of the relaxation times, are then defined as [2]:

$$1/T_1 = k \left[J^{(1)}(\omega_0) + J^{(2)}(2\omega_0) \right] \quad (1.2)$$

$$1/T_2 = k \left[\frac{1}{4} J^{(0)}(0) + \frac{5}{2} J^{(1)}(\omega_0) + \frac{1}{4} J^{(2)}(2\omega_0) \right] \quad (1.3)$$

where J⁽ⁿ⁾(ω) is defined in Equation 1.1 and k = (μ₀/4π)² γ⁴ ħ² 3/2 I(I+1) [2].

1.2.2 Bloch Equations

The magnetization, as a function of time, was defined in a set of phenomenological equations by Felix Bloch [1]:

$$\frac{d}{dt}\mathbf{M}(t) = \gamma[\mathbf{M}(t) \times \mathbf{B}] - \frac{M_x(t)}{T_2}\hat{x} - \frac{M_y(t)}{T_2}\hat{y} + \frac{M_0 - M_z(t)}{T_1}\hat{z} \quad (1.4)$$

where $\mathbf{M}(t)$ is the magnetization vector; \mathbf{B} is the applied magnetic field; T_2 is the spin-spin relaxation time; T_1 is the spin-lattice relaxation time; $\gamma = 42.577$ MHz/T is the gyromagnetic ratio of a proton; M_0 is the magnetization vector at thermal equilibrium; and \hat{x} , \hat{y} , and \hat{z} are unit vectors along X , Y , and Z . Equation 1.4 can be written as a function of the magnetization in each orthogonal direction:

$$\frac{d}{dt}M_x(t) = \gamma M_y B_0 - \frac{M_x}{T_2} \quad (1.5)$$

$$\frac{d}{dt}M_y(t) = \gamma M_x B_0 - \frac{M_y}{T_2} \quad (1.6)$$

$$\frac{d}{dt}M_z(t) = -\frac{M_z - M_0}{T_1}. \quad (1.7)$$

The solution to the coupled differential equations in Equations 1.5,1.6,1.7 is:

$$M_x(t) = [M_x(0) \cos(\omega_0 t) + M_y(0) \sin(\omega_0 t)] \exp(-t/T_2). \quad (1.8)$$

$$M_y(t) = [-M_x(0) \sin(\omega_0 t) + M_y(0) \cos(\omega_0 t)] \exp(-t/T_2) \quad (1.9)$$

$$M_z(t) = M_0 + [M_z(0) - M_0] \exp(-t/T_1). \quad (1.10)$$

where $\omega_0 = \gamma B_0$ and M_0 is the equilibrium magnetization. By defining the transverse magnetization, $M_{xy}(t)$, as $M_{xy}(t) = M_x(t) + iM_y(t)$, special solutions to Equations 1.5, 1.6, 1.7, where the initial magnetization is aligned in the transverse plane (e.g., after a 90° excitation pulse) is given by:

$$M_{xy}(t) = M_0 e^{-t/T_2} e^{i\omega_0 t} \quad (1.11)$$

$$M_z(t) = M_0 \left(1 - e^{-t/T_1}\right). \quad (1.12)$$

where $M_{xy}(0) = 1$ and $M_z(0) = 0$. The frequency of precession ω_0 is typically demodulated out of the transverse magnetization to obtain:

$$M_{xy}(t) = M_0 e^{-t/T_2} \quad (1.13)$$

$$M_z(t) = M_0 \left(1 - e^{-t/T_1}\right). \quad (1.14)$$

The measured signal intensity, $y(t_i)$ is a function of the magnitude of the transverse magnetization $y(t) \propto K |M_{xy}(t)| = K \left| M_0 e^{-t/T_2} \right|$. The measured signal from the RF coil is digitized and filtered to obtain the signal intensity. The primary interest, for this thesis, is T_2 relaxation, therefore, the acquisition and analysis of T_2 decay curves will be discussed further.

1.3 Central Nervous System

Myelin [3, 4] is a fatty sheath, composed of a bi-layer of lipids, which surround axons in the human brain. The biochemical composition is approximately 70% lipid and 30% protein (myelin basic protein, proteolipid proteins) [5]. In the central nervous system (brain, cerebellum, and spinal cord) the myelin sheath are processes from oligodendroglial cells, and in the peripheral nervous system, from Schwann cells. Each oligodendrocyte can myelinate as many as 50 different axons [6]. Each oligodendrocyte process wraps around the axon multiple times. The sheath is interrupted, along the axon, by the Nodes of Ranvier, approximately 1 mm apart [6], and, therefore, the electrical conduction jumps from one Node of Ranvier to the next at approximately 100 m/s. This jumping (saltatory conduction) results in faster conductivity, relative to an unmyelinated axon, and requires less energy. To maintain the conduction velocity of a myelinated axon 20 microns in diameter, an unmyelinated axon would have to be several millimeters in diameter [3]. The thickness of the each myelin bilayer is approximately $0.1 \mu\text{m}$ [7] and each radial line in the myelin sheath is approximately 300 - 400 Å apart [7].

There are many diseases (e.g., multiple sclerosis, adrenoleukodystrophy [9, 10], and attention deficit-hyperactivity disorder [11]) which affect the myelin, and therefore, the water trapped between the myelin bilayers. To assess the disease progression or drug effect, it is important to analyze the progression of demyelination *in vivo*. MRI is well suited for this and therefore, will continue to be an important factor in assessment, research and treatment of disease.

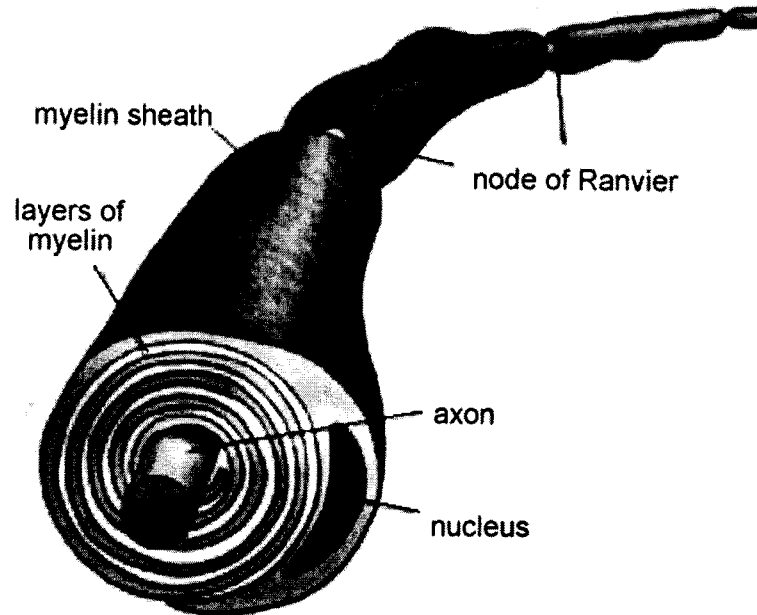


Figure 1.1: Myelinated axon [8] showing the multiple layers of the myelin sheath around the nerve and the nodes of Ranvier.

The integrity of the myelin bilayer can be measured by measuring the relaxation time, T_2 , which is a function of the local water environment. The T_2 decay curve acquisition, from a standard MRI pulse sequence, results in signal which decays as an exponential function of T_2 . Simple systems decay as a function of a single T_2 (mono-exponential decay), as there is a single water compartment. Complex tissues (e.g., brain and muscle) do not have a single water compartment at the resolution of MRI (≈ 1 mm in-plane resolution) and therefore, the signal decays as a sum of single T_2 exponentials (multi-exponential decay).

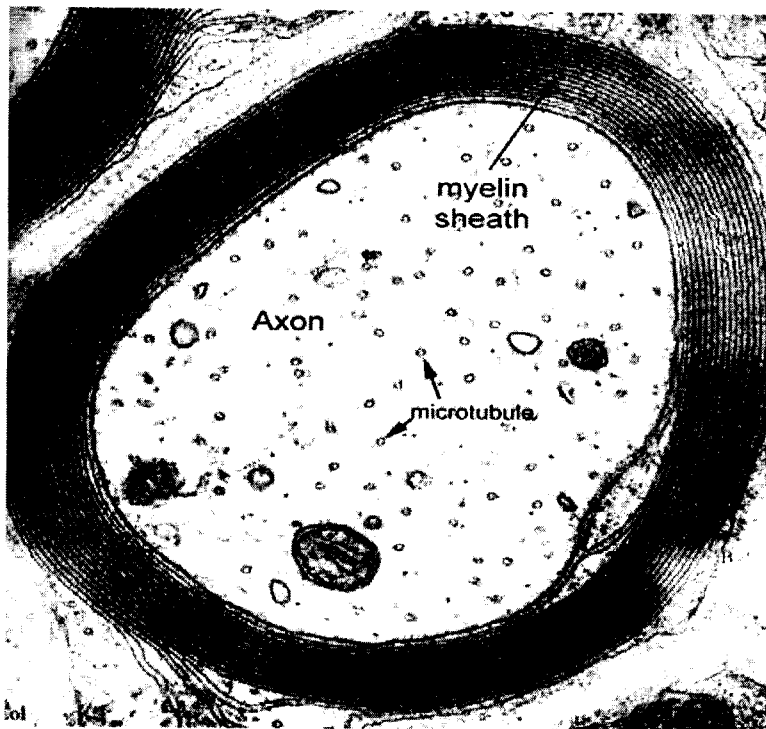


Figure 1.2: Electron-micrograph of a myelinated cell

1.4 Tissue Relaxation

In 1978, Vasilescu *et al.* [12] published quantitative results of multi-exponential T_2 decay curve analysis of frog sciatic nerve. They found three distinct T_2 water compartments based on a “peeling-off” mathematical procedure applied to multi-echo data. A slowly relaxing compartment, $T_2 \approx 300 - 500$ ms, attributed to water in the intra-cellular space. An intermediate relaxing component, $T_2 \approx 80$ ms ascribed to axoplasmic water. And a fast relaxing component, $T_2 \approx 20$ ms, ascribed to water closely associated with proteins and phospholipids. This paper was the first one to describe multi-exponential behavior in myelinated nerve.

A little later, in 1986, Kroeker *et al.* [13] suggested the problem of analyzing biological relaxation times to allow the data determine the appropriate model. They appropriately assumed the data can be described by an integral of weighted exponentials and used the CONTIN curve fitting program (written by Provencher) to solve integral equations for multi-exponential data.

It wasn't until 1991, when Menon *et al.* [14] analyzed myelinated nerves from cat brains, the short T_2 peak ($T_2 \approx 15$ ms) was attributed to water trapped between the myelin bilayers. Menon fit T_2 decay curves, using NNLS, acquired from myelinated cat brain nerves and found

four distinct components: component near $T_2 = 1$ ms attributed to phospholipid protons in the tissue, component near $T_2 = 12.7$ ms attributed to water in the myelin layers, component near $T_2 = 89$ ms attributed to intra and extra-cellular water, and a component not attributed to anything at $T_2 \approx 340$ ms. The short component, $T_2 = 12.7$ ms, contributed 6.8% to the total water in the T_2 distribution. Menon also noted the myelin bound water would be in slow exchange with the intra- and extra-cellular water due to myelin lipid bilayers acting as a diffusion barrier.

The first *in vivo* corroboration of a short T_2 component was by MacKay *et al.* [15, 16]. *In vivo* T_2 relaxation measurements [17, 18, 19] distinguish three water compartments in the brain: water trapped between the myelin bilayers ($10 \leq T_2 \leq 50$ ms), intra/extra axonal water ($T_2 \approx 80$ ms) and water associated with cerebrospinal fluid (CSF) ($T_2 \geq 2000$ ms). The fraction of the water trapped between the myelin bilayers, relative to the total, was approximately 1:6 based on x-ray diffraction measurements [7] among other techniques [17].

Since these first few studies, there have been many other studies to further describe and assess the short T_2 component. Beaulieu *et al.* [20] compared T_2 distributions from myelinated and non-myelinated nerves from the garfish and found the short T_2 component only in the myelinated axon. More recently, many studies have compared the short T_2 component to other MRI phenomenon such as magnetization transfer imaging [21, 22, 23] and diffusion imaging [24]. Each water compartment is “visible” to MRI [17, 18, 19, 25], therefore, MRI is a unique tool to probe the water environments and assess normal and pathological tissue *in vivo*.

1.5 T_2 Decay Curve

1.5.1 Mono-Exponential T_2 Relaxation

The T_2 decay curve is the signal intensity measured from the radiofrequency coils as a function of time t , for this thesis the signal intensity will be denoted $y(t)$. The signal intensity, $y(t)$, is defined as the magnitude of the transverse magnetization $y(t) = |M_{xy}(t)|$ as defined in Equation 1.13. A vector of signal intensities will be denoted \mathbf{y} and a vector of echo times denoted \mathbf{t} . For standard multi-echo pulse sequences, t is the time of the spin echo and is typically measured in milliseconds.

Figure 1.9 shows three simulated decay curves of $T_2 = 20$ ms (circles), $T_2 = 80$ ms (crosses), and $T_2 = 2000$ ms (diamonds). For each curve, $\mathbf{y} = \rho \exp(-\mathbf{t}/T_2)$, the proton density $\rho = 1000$ and the time of the echoes was $\mathbf{t} = 10, 20, \dots, 320$ ms.

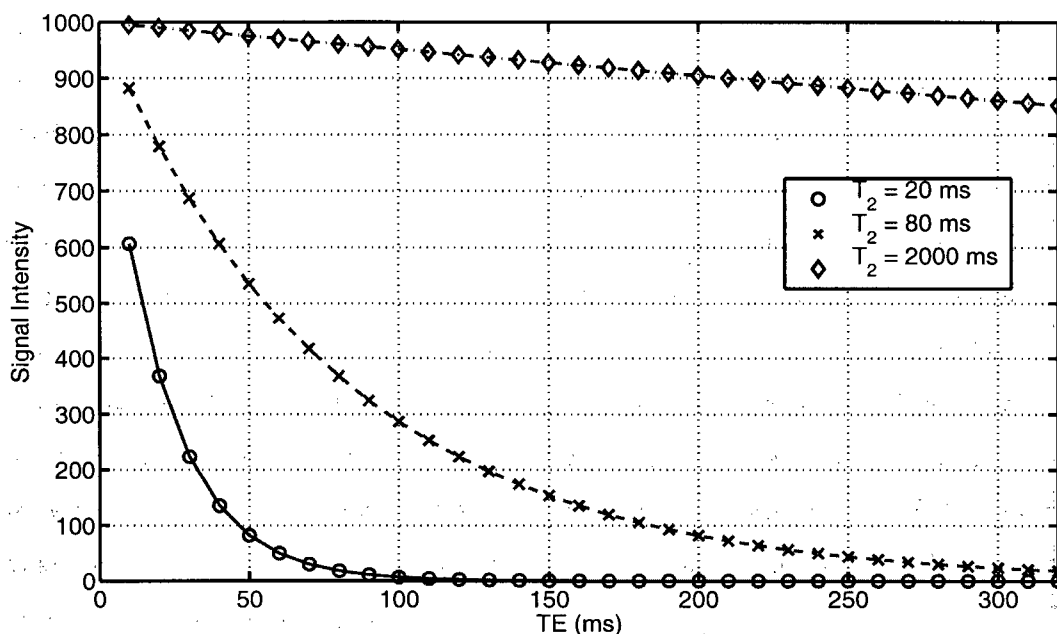


Figure 1.3: Simulated decay curve with signal intensity $S(t) = \rho \exp(-t/T_2)$ with $\rho = 1000$, $t = 10, 20, \dots, 320$ ms and $T_2 = 20$ ms (circles), $T_2 = 80$ ms (crosses), and $T_2 = 2000$ ms (diamonds). TR was considered infinite.

1.5.2 Multi-Exponential T_2 Relaxation

Many tissues in the human body have more than one water compartment visible to MRI (Section 1.4). Multiple water compartments within one imaging element give rise to a multi-exponential relaxation process given by the equation:

$$y(t_i) = \int_{T_{min}}^{T_{max}} s(T) \exp(-t_i/T) dT \quad (1.15)$$

where $y(t_i)$ is the signal intensity at echo time t_i , $s(T)$ is the amplitude of the component at $T_2 = T$. Equation 1.15 is a Fredholm equation of the first kind. A Fredholm equation [26] is defined as:

$$g(x) = h(x)f(x) + \int_a^b K(x, y)f(y)dy \quad (a \leq x \leq b) \quad (1.16)$$

and is of the first kind if $h(x) = 0$. Fredholm equations can be solved [26] by linear and non-linear fitting methods. Non-linear methods require a starting model and have inherent difficulties at converging to the global minimum [27]. Linear inversion techniques [28] assume a large number of T and solve for the amplitudes $s(T)$, most of which are 0.

To solve integral equations on the computer, Equation 1.15 is discretized:

$$s(T) = \sum_{j=1}^M s_j \delta(T - T_j) \quad (1.17)$$

where M is the number of T₂ components and $\delta(x)$ is the Dirac delta function defined as:

$$\delta(x) = \begin{cases} \infty, & \text{if } x = 0 \\ 0, & \text{otherwise.} \end{cases} \quad (1.18)$$

Substituting Equation 1.17 into Equation 1.15 gives:

$$y(t_i) = \sum_{j=1}^M s_j \exp(-t_i/T_j) \quad i = 1 \dots N. \quad (1.19)$$

Equation 1.19 is a matrix equation which can be solved by linear inversion techniques (discussed further in Section 1.7).

1.6 T₂ Decay Curve Acquisition

Decay curve data, \mathbf{y} , is acquired with a multi-echo, spin-echo pulse sequence. Two types of spin-echo pulse sequences were used in this work: an optimized, single slice spin-echo and a conventional spin-echo, slice selective pulse sequence. A standard MRI pulse sequence is described by gradients along three orthogonal axes G_x , G_y , and G_z ; the RF pulse train; and the acquired data. The acquisition of the data and the relationship to the image is discussed (Section 1.6.1). Each pulse sequence will be discussed (Sections 1.6.2 and 1.6.3), as well as noise considerations (Section 1.6.4) and artifacts (Section 1.6.5).

1.6.1 K-Space

Standard MRI images are created by calculating the magnitude of the data encoded in the Fourier transform space – called k-space [29]. Mathematically, the relationship between the data in image space, $M(x, y)$, and the data in k-space, $S(k_x, k_y)$, is related by:

$$S(k_x, k_y) = \int_x \int_y M(x, y) \exp(i x k_x) \exp(i y k_y) dy dx \quad (1.20)$$

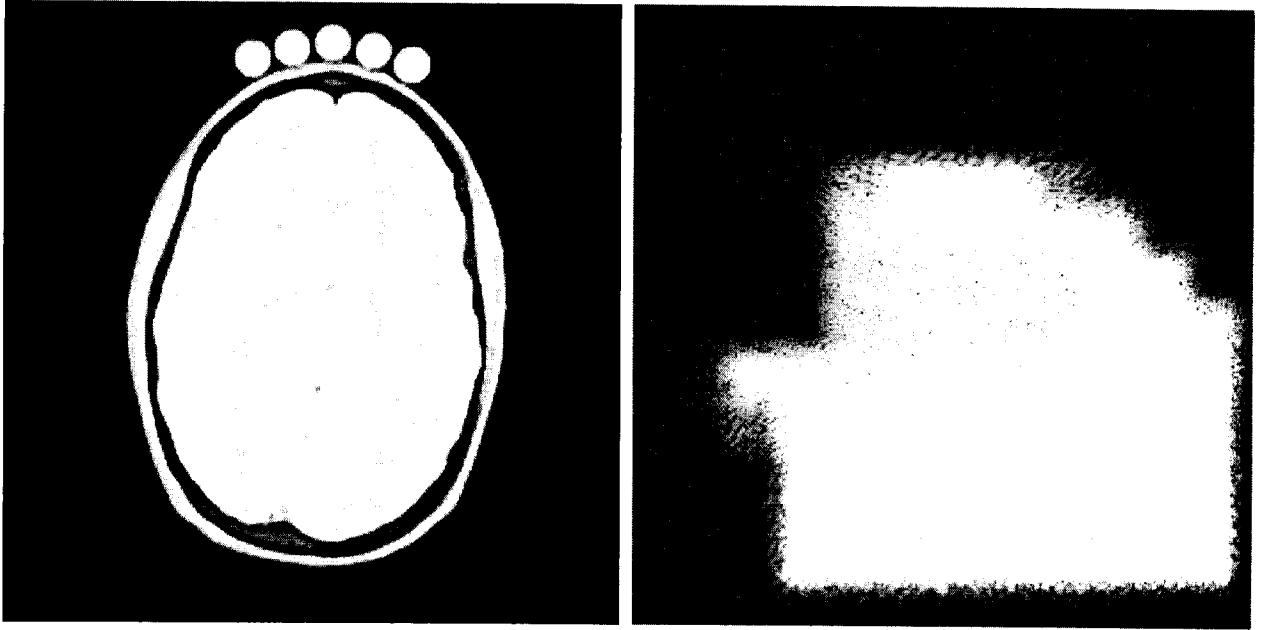


Figure 1.4: Standard MRI image of a brain (left) and the magnitude of the corresponding k-space image (right).

where $S(k_x, k_y)$ is the signal at k_x, k_y and $M(x, y)$ is the image space signal at x, y . The variables k_x and k_y describe the “distance” moved in k-space and are defined as:

$$k_x = \gamma \int_0^t G_x(t') dt' \quad (1.21)$$

$$k_y = \gamma \int_0^t G_y(t') dt' \quad (1.22)$$

where γ is the gyromagnetic ratio, $G_x(t')$ and $G_y(t')$ are the gradient shapes, t is the duration of the gradient. Each point in the MRI image is a weighted sum over *all* points in k-space. The k-space formalism allows the description of all possible pulse sequence data acquisition schemes (e.g., Cartesian, spiral, concentric circles). The theory is easily extended for 3 dimensions.

1.6.2 Optimized Multi-Echo Pulse Sequence

An optimized, multiple echo spin-echo pulse sequence (Figure 1.5) was used to acquire multi-echo images from which multiple component T₂ measurements were calculated. The implementation of the pulse sequence used for this thesis had a train of 32 composite refocusing pulses (90_x-180_y-

90_x) where the duration of the 90° hard pulse was $300 \mu s$ and the duration of the 180° hard pulse was $600 \mu s$. Composite pulses were necessary to reduce the effect of inhomogeneous B_1 [30]. The excitation pulse is a sinc pulse of duration 3.2 ms. Alternating, descending gradient crushers along Z [31] further reduce the effect of stimulated echoes and signal from out of slice. Decay curve artifacts are discussed in Section 1.6.5. This pulse sequence will be annotated as $MESE_o$ in this thesis.

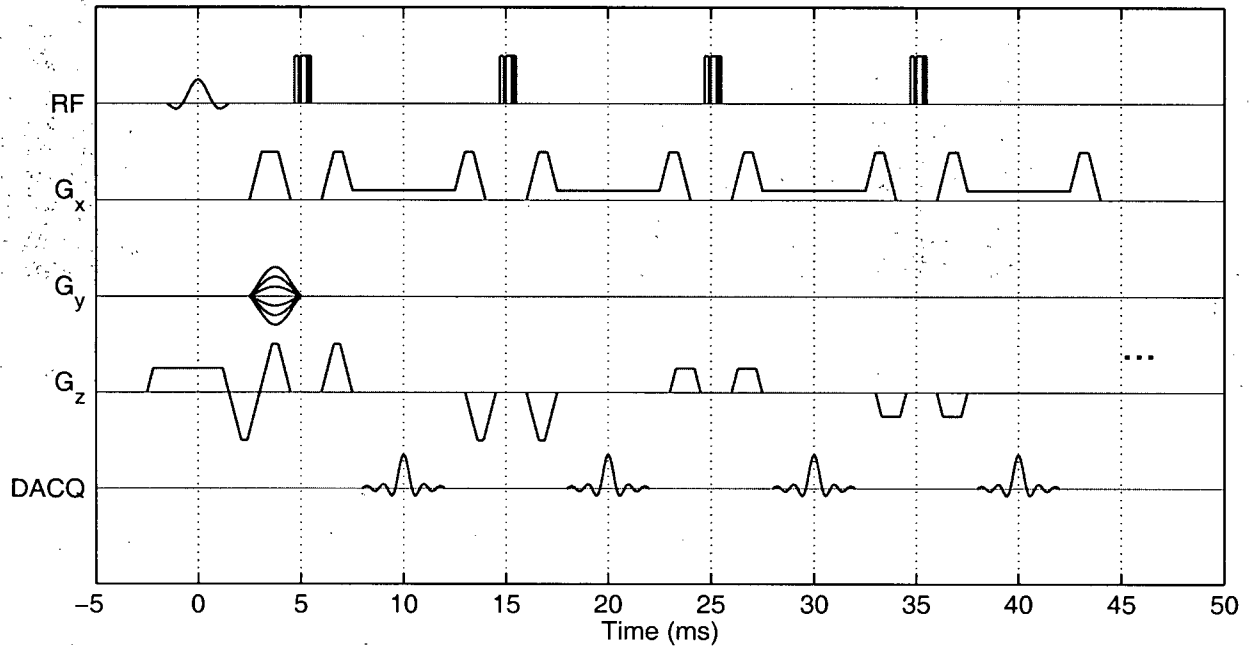


Figure 1.5: Optimized single-slice, multi-echo pulse sequence ($MESE_o$). The excitation pulse is a slice-selective, sinc pulse and the refocusing pulses are composite pulses $90_x^\circ-180_y^\circ-90_x^\circ$. Large alternating-descending gradient crushers on G_z were used to remove signal from stimulated echoes and signal out-of-slice.

1.6.3 Standard Multi-Echo Pulse Sequence

The standard multi-echo pulse sequence (Figure 1.6) consists of a selective excitation pulse followed by a train of selective refocusing pulses. This pulse sequence was used in both 2D and 3D mode. In 2D mode, both the excitation and refocusing pulses were slice selective. In 3D mode, shown in Figure 1.7, the excitation pulse was slab selective the refocusing pulses were slice selective, and phase encodes along G_y and G_z were used to encode the data acquisition in the 3D k-space. A slab selective pulse selectively excites spins within a thickness of Ns where N is the

number of slices and s is the thickness of each slice. In the 3D implementation used in this thesis, the phase encodes along G_z were added to the constant gradient crushers along G_z . The large, constant gradient crushers along G_z were applied to reduce signal from out-of-slice spins, but did not reduce the stimulated echo artifact. This pulse sequence will be denoted by $MESE_c$ in this thesis.

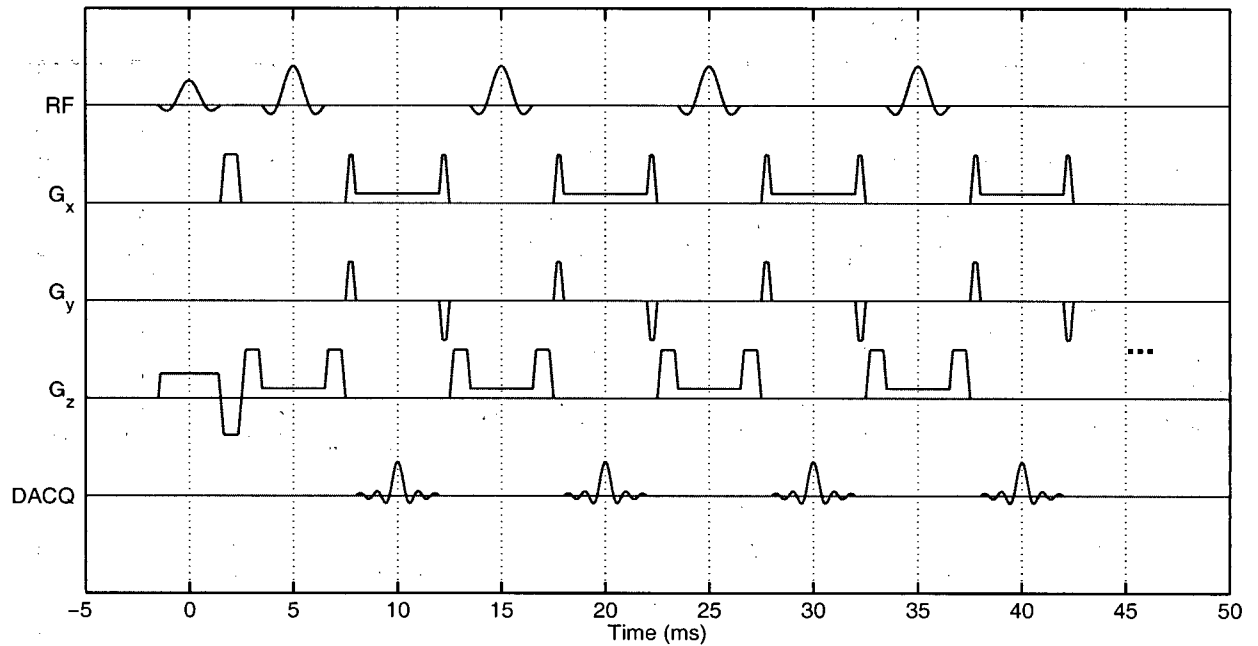


Figure 1.6: Conventional multiple echo 2D spin-echo pulse sequence ($MESE_c$). The excitation pulse and refocusing pulses are slice selective.

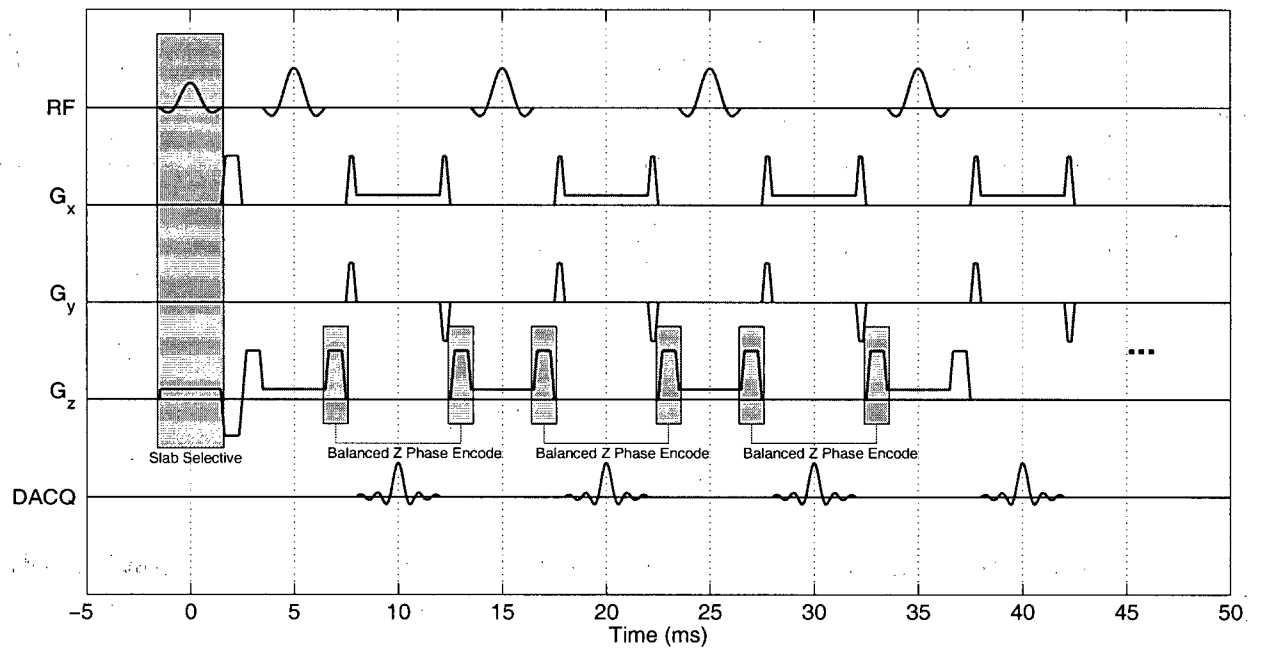


Figure 1.7: Conventional multiple echo 3D spin-echo pulse sequence (MESE_c). The excitation pulse is slab selective (gray bar centered around 0 ms) and signal is phase encoded along G_y and G_z . The slice phase encodings are added to the large crushers in a way analogous to the phase encoding already on G_y .

1.6.4 Noise in Decay Curve

Standard imaging techniques acquire complex k-space data, then an image is calculated as the magnitude of the Fourier transform of the k-space data. The noise in the magnitude images [32] has a Rician distribution, based on the assumption that the noise on the real and imaginary channels is Gaussian. The probability density function for a Rice distribution is defined [33] as:

$$P_{\text{Rice}}(x) = \frac{x}{\sigma^2} \exp\left(-\frac{\mu^2 + x^2}{2\sigma^2}\right) I_0\left(\frac{\mu x}{\sigma^2}\right) \quad (1.23)$$

where σ is the “standard deviation” of the function, μ is the mean, x is the parameter, and $I_0(x)$ is a modified Bessel function of the first kind. The two interesting implications of the Rice distribution is what happens as a function of μ/σ .

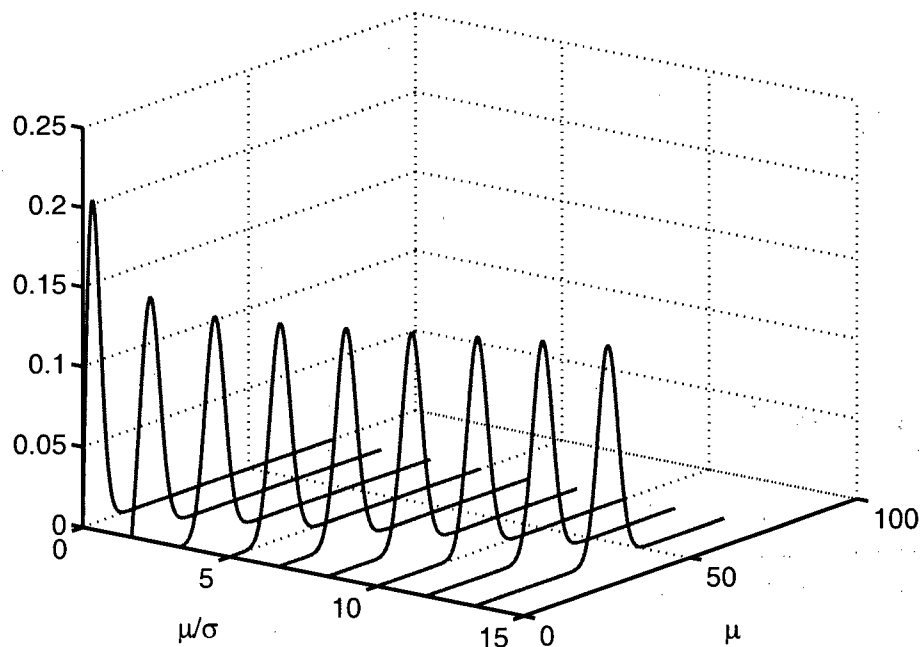


Figure 1.8: Rice distribution as a function of μ/σ . When μ/σ is zero, for example in the black area of an MRI image, then the noise is Rayleigh distributed. When μ/σ is large, for example in the object of an MRI image, then the noise approximates a Gaussian distribution.

As $\mu/\sigma \rightarrow 0$, the Rician distribution becomes a Rayleigh distribution. The Bessel function

$I_0(\mu) = 1$ when $\mu = 0$ and $\exp\left(-\frac{\mu^2+x^2}{2\sigma^2}\right) = \exp\left(-\frac{x^2}{2\sigma^2}\right)$ when $\mu = 0$. Therefore,

$$P_{\text{Rice}}(x) = \frac{x}{\sigma^2} \exp\left(-\frac{x^2}{2\sigma^2}\right) \quad (1.24)$$

$$= P_{\text{Rayleigh}}(x) \quad (1.25)$$

As $\mu/\sigma \rightarrow \infty$, the Rician distribution becomes similar to a Gaussian distribution. The asymptotic expansion [34] of the Bessel function $I_0(x)$ when x is large is:

$$I_0(x) \sim \frac{e^x}{\sqrt{2\pi x}} \left[1 + \frac{1}{8x} + \frac{1 \cdot 9}{2!(8x)^2} + \frac{1 \cdot 9 \cdot 25}{3!(8x)^3} + \dots \right] \quad (1.26)$$

then for sufficiently large x , $I_0(x) \cong \frac{e^x}{\sqrt{2\pi x}}$. Therefore, considering $P_{\text{Rice}}(x)$ around $x = \mu$:

$$P(x) = \frac{x}{\sigma^2} \exp\left(-\frac{\mu^2+x^2}{2\sigma^2}\right) I_0\left(\frac{\mu x}{\sigma^2}\right) \quad (1.27)$$

$$\simeq \frac{x}{\sigma^2} \exp\left(-\frac{x^2+\mu^2}{2\sigma^2}\right) \frac{\sigma}{\sqrt{2\pi\mu x}} \exp\left(\frac{\mu x}{\sigma^2}\right) \quad (1.28)$$

$$= \sqrt{\frac{x}{2\pi\sigma^2\mu}} \exp\left[-\frac{(x-\mu)^2}{2\sigma^2}\right] \quad (1.29)$$

$$(1.30)$$

then, because $x \approx \mu$ the scaling factor in front of the exponential can be simplified leaving:

$$P(x) = \frac{1}{\sqrt{2\pi\sigma^2}} \exp\left[-\frac{(x-\mu)^2}{2\sigma^2}\right] \quad (1.31)$$

$$= P_{\text{Gaussian}}(x) \quad (1.32)$$

which is the probability function for Gaussian distribution.

All simulations, in the following chapters, used Rician noise. The Rician noise was created as $y_e(t_i) = \sqrt{[y(t_i) + e_1]^2 + e_2^2}$, where y is the true signal, and e_1 and e_2 are random numbers from a Gaussian distribution with zero mean and standard deviation σ . The standard deviation, σ , for the Gaussian distribution was defined as $y(t_1)/\text{SNR}$.

1.6.5 Artifacts Influencing the T_2 Decay Curve

Artifacts in the T_2 decay curve are non-random changes to the decay curve during data acquisition. The artifacts could result from mis-tuned hardware or limitations of the underlying assumptions. Four effects that arise during acquisition of the T_2 decay curve are: 1) signal from out-of-slice, 2) magnetization transfer, 3) stimulated echoes, and 4) T_2 dependence on the echo spacing τ .

Out-of-Slice

The signal measured from a voxel includes signal from protons outside the desired slice. This is because the slice profile of an RF pulse is non-rectangular. The goal of shaped RF pulses is to create a slice profile that is close to rectangular, but there is always some ripple within the slice (pass band) and outside the slice (stop band). The goal of hard RF pulses is the opposite, the desire is to flip all protons across a sample. Therefore, whether shaped RF pulses or hard RF pulses, there is a need to suppress signal from outside the desired slice profile.

The standard method to suppress signal from outside the desired slice profile is to include a large pair of gradients on G_z around each refocusing pulse [31, 35]. These gradients add a large phase to the spins outside the slice, so that the signals do not get refocused during data acquisition.

Magnetization Transfer Effects

The pulse sequence must be carefully designed so as to not introduce artifacts during acquisition which may affect the quantification of the myelin water fraction. The standard MRI acquisition for quantification of the myelin water is a single slice pulse sequence described in Section 1.6.2. A multi-slice acquisition would be a desirable feature, but would need to be implemented carefully. For slice-selective imaging, a magnetic field gradient is applied along G_z which spatially encodes the spins with a frequency. It was shown previously [36] that an off-resonance RF pulse (magnetization transfer [MT] pulse) will reduce the signal from water trapped between the myelin bilayers due to direct saturation. Therefore, the acquisition of multi-echo, multi-slice data may reduce the signal from the myelin water as an RF pulse on-resonance for a given slice will be an off-resonance pulse for other slices in the volume. There are three possible ways around this: 1) acquire single slice images only, 2) acquire data in which a slab is excited and multiple slices are

phase encoded within the slab, or 3) it may be possible to acquire multiple slices if the slices are distributed in time and space so the magnetization transfer effect is minimized.

Stimulated Echoes

Stimulated echoes are overlaid on top of the primary echo and are due to imperfectly refocused magnetization. Stimulated echoes are a major artifact in T_2 decay curves [31]. In the presence of an RF pulse [37], dephasing magnetization will be rotated such that a portion will continue dephasing, a portion will begin to rephase and a portion will be stored along the longitudinal axis. The magnetization along the longitudinal axis does not accrue phase, therefore, when the magnetization along the longitudinal axis is rotated back into the transverse plane, it will not have the same phase as the magnetization that was in the transverse plane. The lack of phase coherence results in magnetization refocusing at a different echo time. The stimulated echo artifact is described further in Chapter 4

T_2 Dependence on Inter-Echo Spacing

The standard method to measure T_2 *in vivo* is to use a multi-echo spin-echo pulse sequence where the constant echo spacing is τ ($TE = 2\tau$). The T_2 estimated from a multi-echo spin-echo pulse sequence was shown [38] to be dependent on τ due to iron, in the form of ferritin, in the brain (e.g., basal ganglia). Iron in the brain has strong magnetic properties leading to microscopic magnetic field inhomogeneities. Jensen *et al.* modeled the relaxation rate R_2 ($R_2 = 1/T_2$) as $R_2 = R_{2a} + \Delta R_2$. The relaxation rate R_{2a} was defined independent of microscopic field inhomogeneities, and ΔR_2 was derived to be a function which was approximated as being proportional to $x^{3/2}$ where $x = 4D\tau/R^2$, D is the diffusion time, and $R = 3.5 \mu\text{m}$ was the radius of the iron which were modeled as spheres [38]. As ΔR_2 is a function of τ , the measured R_2 would also be a function of τ . R_2 is several orders of magnitude smaller than the measurement error for the typical τ of 5 ms. Therefore, comparing T_2 from different techniques, requires knowledge of τ and the underlying tissue composition.

1.7 T₂ Decay Curve Analysis

Decay curve data acquired by either technique described in Section 1.6 must be fit to determine the underlying T₂.

1.7.1 Decay Curve Inversion (Decay Curve to T₂ Distribution)

Decay curves acquired from voxels which contain multiple water compartments are composed of a linear combination of decay curves each corresponding to one water compartment. Figure 1.9 (top) shows three decay curves: the short T₂ decay curve of $y_{\text{short}}(t) = 200 \exp(-t/20)$; the medium T₂ decay curve of $y_{\text{medium}}(t) = 800 \exp(-t/80)$, and the total bi-exponential decay curve $y_{\text{biexp}}(t) = 200 \exp(-t/20) + 800 \exp(-t/80)$. Echo times at $t = 10, 20, \dots, 320$ ms.

The goal of any data inversion technique is to calculate the single or multiple T₂ times and amplitudes, \mathbf{s} , for a given decay curve \mathbf{y} . The bottom plot of Figure 1.9 shows the amplitudes, s_j , and T₂ times of the T₂ decay curves in the top plot of Figure 1.9. In this example, $s_1 = 200$ at $T_{2,1} = 20$ ms and $s_2 = 800$ at $T_{2,2} = 80$ ms. The plot of \mathbf{s} versus T₂ is called the T₂ distribution. Each data inversion technique may assume positions for the spikes in the T₂ distribution, upper and lower bound for the positions, or non-negativity of the amplitudes. Most inversion techniques minimize a misfit based on the measured data.

1.7.1.1 Misfit Measures

The misfit is a scalar measure of the difference between the predicted data \mathbf{y} and the measured data $\hat{\mathbf{y}}$. Two common definitions for the misfit between the predicted and measured data are L_1 , which measures $\|\mathbf{y} - \hat{\mathbf{y}}\|_1 = \sum_{i=1}^N |y_i - \hat{y}_i|$, and L_2 which measures $\|\mathbf{y} - \hat{\mathbf{y}}\|_2 = \sum_{i=1}^N |y_i - \hat{y}_i|^2$.

Another misfit measure, χ^2 , accounts for the difference between the predicted and measured data, as well as the noise in the measurement, is defined as:

$$\chi^2 = \sum_{i=1}^N \frac{(y_i - \hat{y}_i)^2}{\sigma_i^2} \quad (1.33)$$

where N is the number of data points, y_i is a measured datum, \hat{y}_i is a reconstructed datum, and σ_i is the standard deviation of the i^{th} datum. The χ^2 misfit is a logical misfit to minimize in curve fitting algorithms, as it accounts for noise in the measurements.

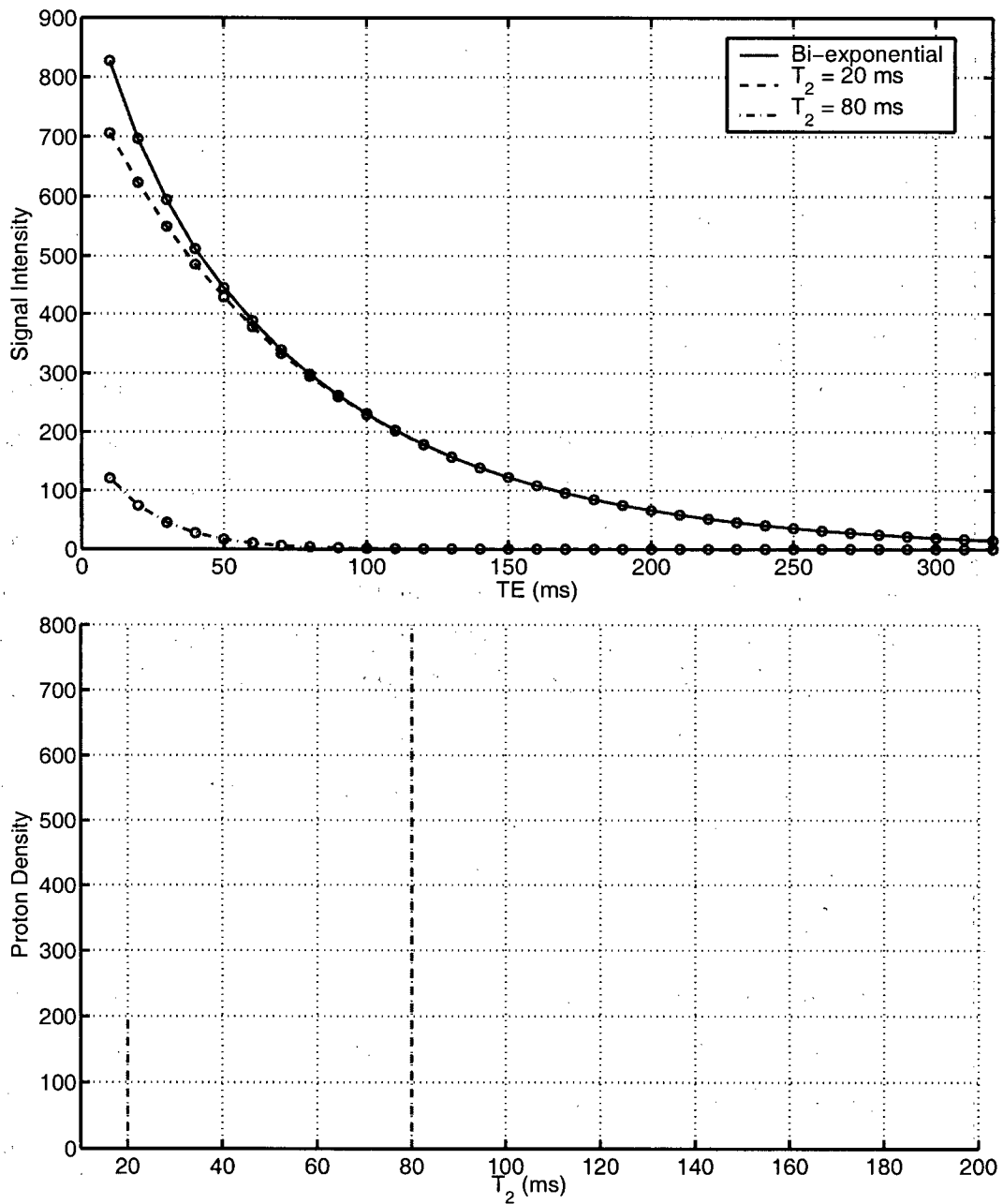


Figure 1.9: Decay curves (top) and T_2 distribution (bottom) of a bi-exponential white matter model. The short T_2 peak at 20 ms in the T_2 distribution (bottom) corresponds to the fast decaying exponential ($\exp(-t/20)$, dashed-dotted line in the top plot). The medium T_2 peak at 80 ms in the T_2 distribution (bottom) corresponds to the slower decaying exponential ($\exp(-t/80)$, dash line in the top plot). The two peaks in the T_2 distribution (bottom) correspond to the sum of the two decaying exponentials and is the solid line in the top plot ($200 \exp(-t/20) + 800 \exp(-t/80)$). The echo times are $t = 10, 20, \dots, 320$ ms.

The expected value $E(\chi^2) = N$ and the standard deviation $\sigma_{\chi^2} = \sqrt{2N}$. Solutions with $\chi^2 \ll N$ reproduce the noise and solutions with $\chi^2 \gg N$ misrepresent the measurement. Intuitively, if the only difference between the predicted and measured data is noise, then Equation 1.33 is $\sum_{i=1}^N \sigma_i^2 / \sigma_i^2 = \sum_{i=1}^N 1 = N$.

1.7.1.2 Non-Negative Least Squares

The primary curve fit algorithm used in this thesis was a non-negative least squares algorithm. The T₂ distribution is calculated from a decay curve by applying the non-negative least squares (NNLS) algorithm [39] to the decay curve [40]. The objective function NNLS minimizes is:

$$\min_{\mathbf{s}} \|\mathbf{A}\mathbf{s} - \mathbf{y}\| \quad (1.34)$$

where $A_{ij} = \exp(-t_i/T_{2,j})$, y_i is the datum at t_i , and \mathbf{s} is the set of amplitudes over T₂. Therefore, $\mathbf{A}\mathbf{s}$ is the predicted data and \mathbf{y} is the measured data. To incorporate the standard deviation, σ_i , at the data point y_i , each datum y_i is divided by σ_i as is the corresponding row A_i . When NNLS is used to solve this modified system, it minimizes the χ^2 misfit in Equation 1.33.

NNLS is guaranteed to minimize Equation 1.34 [39], or the χ^2 , if the standard deviation is divided through both sides $\mathbf{A}\mathbf{s} = \mathbf{y}$. It is interesting to note that each column of A is a mono-exponential decay curve with $T_2 = T_{2,j}$ at echo times \mathbf{t} . Therefore, NNLS minimizes the misfit of a linear combination of mono-exponential decay curves to create multi-exponential decay curve with the minimum χ^2 misfit.

Regularization

The standard NNLS technique can be modified to apply different types of smoothing to the T₂ distribution. This is accomplished by including a second term in the objective function (Equation 1.34). The modified objective function to minimize is:

$$\min_{\mathbf{s}} \|\mathbf{A}\mathbf{s} - \mathbf{y}\|_2 + \mu \|\mathbf{H}\mathbf{s} - \mathbf{f}\|_2 \quad (1.35)$$

where μ controls the contribution of the second term. If $\mu = 0$, then the minimization yields the least squares NNLS solution.

The matrix H and vector \mathbf{f} could take on many forms depending on the type of regularization desired. To minimize the changes in the distribution, H would be defined as:

$$H = \begin{bmatrix} 1 & -1 & 0 & \cdots & 0 \\ 0 & 1 & -1 & \cdots & 0 \\ 0 & 0 & \vdots & 1 & -1 \end{bmatrix} \quad (1.36)$$

and $\mathbf{f} = 0$. Or the matrix could be designed to minimize the amplitudes as in:

$$H = \begin{bmatrix} 1 & 0 & 0 & \cdots & 0 \\ 0 & 1 & 0 & \cdots & 0 \\ 0 & 0 & \vdots & 1 & 0 \\ 0 & 0 & \cdots & 0 & 1 \end{bmatrix} \quad (1.37)$$

and $\mathbf{f} = 0$.

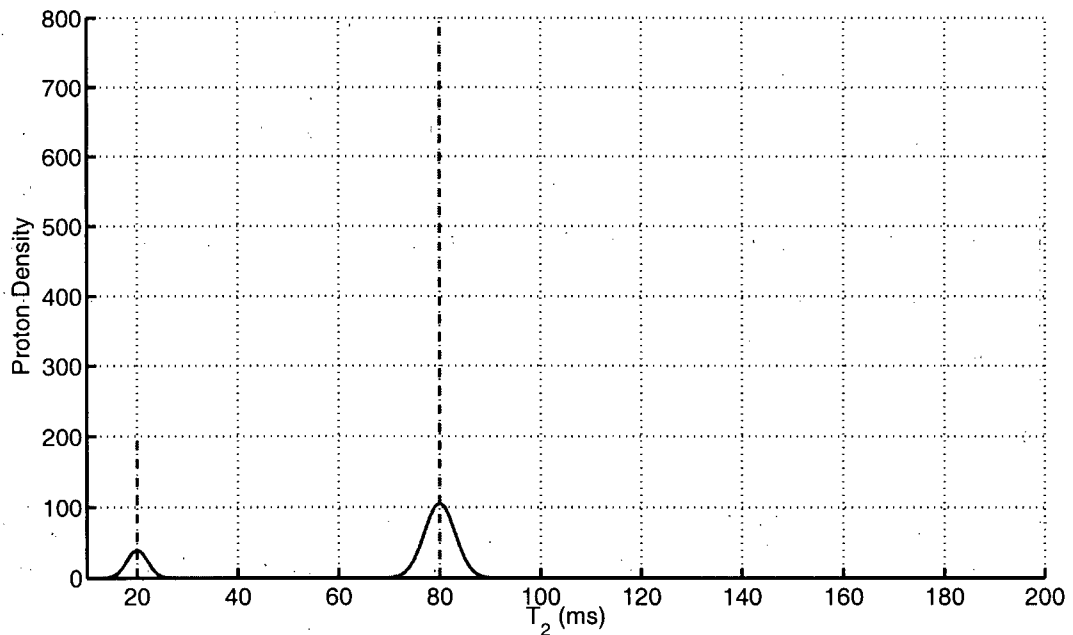


Figure 1.10: T_2 distribution of a two compartment model. The spike distribution (dashed-dot lines) represents the least squares solution to a bi-exponential distribution. The continuous distribution represents a regularized solution to the bi-exponential distribution. The area of the spike at 20 ms is the same as the area of the distribution centered at 20 ms (same for 80 ms spike and distribution).

Implementation

The baseline effect due to the non-zero mean of the Rician distribution at low signal (Section 1.6.4) must be accounted for within the NNLS curve fitting [41]. To account for the baseline offset during the curve fitting, an extra column of ones is added to the A matrix and a variable B is included as one more row in the s vector, then:

$$\begin{bmatrix} a_{11} & a_{12} & \cdots & a_{1N} & 1 \\ a_{21} & a_{22} & \cdots & a_{2N} & 1 \\ a_{31} & a_{32} & \cdots & a_{3N} & 1 \\ & & \vdots & & \vdots \\ a_{M1} & a_{M2} & \cdots & a_{MN} & 1 \end{bmatrix} \begin{bmatrix} s_1 \\ s_2 \\ \vdots \\ s_N \\ B \end{bmatrix} = \begin{bmatrix} y_1 \\ y_2 \\ \vdots \\ y_M \end{bmatrix}. \quad (1.38)$$

The set of T₂ was defined to be 120 logarithmically spaced T₂ = 10.00, 10.52, 11.06, . . . , 4000.0 ms. Therefore N , in Equation 1.38 was 120 and M was the number of data collected from the pulse sequence (discussed in Section 1.6).

A regularized NNLS solution was used and consisted of finding the minimum χ^2 solution, χ_{min}^2 , then regularizing the T₂ distribution until a solution was found with $1.02 \chi_{min}^2 \leq \chi^2 \leq 1.025 \chi_{min}^2$. The regularization matrix $H = \mu I$, as shown in Equation 1.37, was used for the work in this thesis. The algorithm to determine the regularized χ^2 is described in Algorithm 1.1.

1.7.1.2.1 T₂ Distribution Bins

The T₂ distribution calculated using NNLS from a tissue sample is expected to have broad distributions due to the underlying heterogeneity of the tissue [42] and the regularization method [42, 43]. To quantify the T₂ relaxation time or amplitude, the T₂ distribution is typically binned. A bin is defined with a start T₂ and end T₂.

There are several measures defined for a bin. The most important measure, in particular for the short T₂, is the fraction of signal in the bin relative to the total signal:

$$fr = \frac{\sum_{T=T_{start}}^{T=T_{end}} s(T)}{\sum_{T=0}^{T_{max}} s(T)}. \quad (1.39)$$

Algorithm 1.1 Small norm NNLS regularization.

Regularized NNLS

- 1: Define $f_{low} = 1.02$ $\{\chi_{low}^2 = f_{low}\chi_{min}^2\}$
- 2: Define $f_{high} = 1.025$ $\{\chi_{high}^2 = f_{high}\chi_{min}^2\}$
 { Calculate the least squares solution }
- 3: Solve $\mathbf{s} = \text{nnls}(A, \mathbf{y})$
- 4: Calculate χ_{min}^2 from $A, \mathbf{y}, \mathbf{s}$
- 5: Define a vector, μ , logarithmically spaced between 10^{-5} and 10^{-1}
 { Find μ_i such that χ_i^2 is between χ_{low}^2 and χ_{high}^2 }
- 6: **while** $\chi^2 < \chi_{low}^2$ OR $\chi^2 > \chi_{high}^2$ **do**
- 7: **for all** μ_i in μ **do**
- 8: Solve $\mathbf{s} = \text{nnls}(A, \mathbf{y}, \mu_i)$
- 9: Calculate χ_i^2 from $A, \mathbf{y}, \mathbf{s}$
- 10: **end for**
- 11: Do linear fit of χ^2 vs μ
- 12: From linear fit, calculate μ at midpoint between χ_{low}^2 and χ_{high}^2
- 13: Solve $\mathbf{s} = \text{nnls}(A, \mathbf{y}, \mu_i)$
- 14: Calculate χ_i^2 from $A, \mathbf{y}, \mathbf{s}$
- 15: **if** $\chi_i^2 < \chi_{low}^2$ **then**
- 16: Set μ to be linear spaced between μ_i and $\mu(1)$
- 17: **else if** $\chi_i^2 > \chi_{high}^2$ **then**
- 18: Set μ to be linear spaced between $\mu(\text{end})$ and μ_i
- 19: **else**
- 20: Do Nothing
- 21: **end if**
- 22: **end while**

The arithmetic mean T₂ of a bin is defined as:

$$\bar{T} = \frac{\sum_{T=T_{start}}^{T=T_{end}} s(T) T}{\sum_{T=T_{start}}^{T=T_{end}} s(T)} \quad (1.40)$$

and the energy for the bin is $\sum_{T=T_{start}}^{T=T_{end}} s(T)^2$.

For this thesis, two compartments were defined. The short T₂ compartment (related to water trapped between the myelin bilayers, see Section 1.4) was defined as a bin with $10 \leq T_2 \leq 50$ ms. The medium T₂ bin was defined as $50 \leq T_2 \leq 120$ ms and is related to the inter and intra-cellular water.

1.7.2 T₂ Decay Curve Requirements

1.7.2.1 SNR Requirements

It has been shown [44] that a signal-to-noise ratio (SNR) of 700 is required to separate T₂ components of one order of magnitude apart in a T₂ distribution. The standard method to attain high SNR, in the MESE₀ sequence, is to acquire four averages for each line acquired in k-space [18]. The SNR is proportional to \sqrt{N} where N is the number of averages – therefore, an image acquired from four averages has twice the SNR of an image acquired from one average. The total scan time for a sequence with four averages, 128 phase encode lines and TR = 3s is approximately 26 minutes. This is a long time for a volunteer or patient to attempt to remain motionless in the scanner for one sequence. Therefore, other methods of attaining the required SNR must be assessed.

1.7.2.2 T₂ Decay Curve Sampling

The T₂ decay curve must be sampled sufficiently to accurately estimate the T₂ components and amplitudes. Whittall *et al.* [45] analyzed 95 *in vivo* white matter decay curves and concluded that 91 of them (96%) were multi-exponential based on an F-test of the misfit. Eighty-nine of the 114 gray matter decay curves (78%) and 15 of the 30 multiple sclerosis lesion decay curves (50%) were mono-exponential. A white matter model was created and mono-exponential fits of simulated four echo data (TE = 30, 60, 90, 120 ms) missed the short T₂ component, underestimated the T₂, and overestimated the proton density. Multi-exponential fits of the same simulated data sampled at

32 echoes ($TE = 10, 20, \dots, 320$ ms) accurately reproduced the two T_2 components. Whittall *et al.* compared mono-exponential T_2 solutions from simulated decay curves sampled with different sets of echo times. They found the T_2 and proton density calculated from two different sampling schemes to be statistically different even though the underlying T_2 and proton density were the same. Therefore, *in vivo* white matter has a multi-exponential decay and few echoes (four or less) are insufficient to calculate a robust set of T_2 and amplitudes.

1.8 Phantoms

Decay curve acquisition and analysis were validated using a set of mono-exponential phantoms. The set of six mono-exponential phantoms were created with T_1 and T_2 times (see Table 1.1) similar to the brain [46]. Nickel-chloride ($NiCl_2$) was chosen, as the paramagnetic ion Ni is an effective T_1 modulator and is relatively independent of temperature and field strength [46, 47] and remains stable over long periods of time. The nickel/agarose was mixed [48] and put into glass tubes that were vacuum sealed.

The T_1 were measured from a saturation recovery experiment with $TR = 100, 300, 800, 2000, 3000$ ms. Other parameters were $TE = 11.0$ ms, $FOV = 16$ cm, 2 averages. For each phantom, the mean signal intensity over the phantom was fit to the equation $y(TR_i) = \rho[1 - \exp(-TR_i/T_1)]$.

The T_2 measurements were done with a 48 echo MESE_o pulse sequence with $TE = 10, 20, \dots, 480$ ms. Other parameters were $TR = 3000$ ms, 2 averages, and $FOV = 16$ cm.

Phantom	T_2 (ms)	T_1 (ms)	mM $NiCl_2$	% Agarose
1	237	712	2	0.2
2	91	712	2	1
3	98	1858	0.5	1
4	24	333	5	4
5	84	342	5	1
6	26	690	2	4

Table 1.1: T_1 and T_2 of mono-exponential nickel/agarose phantoms.

1.9 Overview of Thesis

Noise and artifacts which result from decay curve acquisition can confound the analysis and interpretation of T_2 decay curves. The thesis focused on three aspects of the noise and artifacts as they relate to T_2 decay curve analysis.

First, the curve fitting algorithms used to fit T_2 decay curves are strongly affected by the SNR of the acquired data. I analyzed noise reduction filters applied to the multi-echo data, to determine if post-processing was as good or better than multiple acquisitions (averaging). I compared the myelin water fractions and myelin water maps calculated from simulated and *in vivo* multi-echo data. For the simulated and *in vivo* data, I applied six noise reduction filters and compared the variability in the myelin water fraction.

Second, the standard method to calculate the myelin water fraction from a T_2 decay curve is to use a curve fitting algorithm. The standard algorithm is slow and problematic for low SNR multi-echo data. The short T_2 is of particular interest as it relates to the myelin water fraction. I developed a method to linearly combine the multi-echo data, which acts as a filter in the T_2 space. The myelin water fraction calculated from the linear combination method was compared to the myelin water fraction calculated from the standard curve fit technique.

Third, it was previously shown that stimulated echoes encoded over the primary echoes will lead to inaccurate T_2 estimation. Chapter 4 discusses a method to estimate the T_2 and refocusing pulse flip angle from a decay curve that has stimulated echoes. The accuracy and precision of the estimation of T_2 and refocusing pulse flip angle were assessed using noise simulations. The phantoms were scanned with the $MESE_o$ sequence to validate the theory. Myelin water fractions and maps estimated from the $MESE_c$ decay curves were compared to those estimated from the $MESE_o$ decay curves. Several extensions are discussed.

Chapter 2

Myelin Water Fraction Noise Reduction

2.1 Introduction

Myelin is a fatty sheath that surrounds neurons and allows for faster propagation of electrical impulses using less energy than that required by non-myelinated neurons. Over 1,000,000 people in the US are affected by diseases that either breakdown the myelin (e.g., multiple sclerosis [MS]) or impair its initial growth (e.g., adrenoleukodystrophy); therefore, it is important to have an *in vivo* technique able to measure myelin. Magnetic resonance imaging inherently measures properties of water molecules associated with tissues in the brain and body. There is evidence [17, 19, 25] of three water compartments in the brain: water trapped between the myelin bilayers ($10 \leq T_2 \leq 50$ ms), intra/extra axonal water ($T_2 \approx 80$ ms) and water associated with cerebrospinal fluid (CSF) ($T_2 \geq 2000$ ms). The multiple water compartments in normal white matter result in a multi-exponential MR signal decay as a function of echo time (TE) and the shortest T_2 component may be capable of providing *in vivo* information about myelin.

Previous work [49] showed that voxel-by-voxel decay curves from a spin-echo pulse sequence optimized to collect images at multiple echo times was able to sample the white matter decay curve. The relative proportion of water, as a function of T_2 (T_2 distribution), was calculated voxel-by-voxel from the T_2 decay curves by a regularized non-negative least-squares (NNLS [28]) algorithm. A high signal-to-noise ratio (SNR) is required to distinguish components in the T_2 distribution [44] and therefore, image processing techniques may be beneficial to reduce the variability due to random noise.

The anisotropic diffusion filter was created by Perona [50] and introduced to MRI by Gerig [51]. It is a locally adaptive smoothing filter that incorporates the local image intensity gradient

strength into the smoothing based on an input parameter, κ , which is a measure of the strength of an edge in the image. Therefore, the algorithm smooths local areas of homogeneity without blurring edges. Modifications to the method were presented by Gerig [51] to filter 3D MRI volumes and MRI volumes that contain multiple channels (e.g., multi-echo data). In MRI, the anisotropic diffusion filter has been applied to work in quantification of MS lesion volumes [52], intra-cranial boundary detection and RF correction [53], vessel visualization [54] and detection of brain contour [55].

My hypothesis is that myelin water fractions (MWFs) calculated from spatially filtered spin-echo data should yield better qualitative and quantitative results than MWFs calculated from unfiltered MRI data. A set of spatial noise reduction filters, with the property that edges are preserved, are described in Section 2.3. The filters were evaluated on a simulated image to determine the filter that reduces the noise the most (Section 2.4). I collected three sets of scans with 1, 2 and 4 averages on five normal volunteers. The myelin water fractions were calculated from filtered and unfiltered multi-echo data and the results are shown in Section 2.5. The myelin water fraction variability was compared from MRI data with different numbers of averages and with and without filtering and is shown in Section 2.6.

2.2 SNR Effect on Myelin Water Fraction

The signal-to-noise ratio affects the variability and robustness of the myelin water fraction (Section 1.7.2:1). The effect of SNR on myelin water fraction will be shown by a noise simulation study.

The variability of the myelin water fractions, as a function of SNR, was calculated from simulated decay curves. A 32-echo decay curve was created with $TE = 10, 20, \dots, 320$ ms, a short water compartment with $\rho^s = 200$ and $T_2^s = 20$ ms, and a medium water compartment with $T_2^m = 80$ ms and $\rho^m = 800$. One thousand realizations of noise were added in quadrature for each of $SNR = 50, 100, 200, \text{ and } 400$. The myelin water fraction, for each noisy decay curve, was calculated with NNLS. Histograms of the myelin water fraction were calculated as a function of SNR.

The mean and standard deviation of the calculated myelin water fractions were plotted as a histogram (Figure 2.1). The mean and standard deviation of each of the histograms was: 0.1997

± 0.1290 (SNR 50), 0.2126 ± 0.0828 (SNR 100), 0.2144 ± 0.0490 (SNR 200), and 0.2078 ± 0.0293 (SNR 400). The spread in the histogram was very large for SNR < 100 and the shape of the histogram was non-Gaussian. When the SNR was greater than 100, the estimated myelin water fractions were closer to the true value of 0.2 and the histogram was closer to a Gaussian.

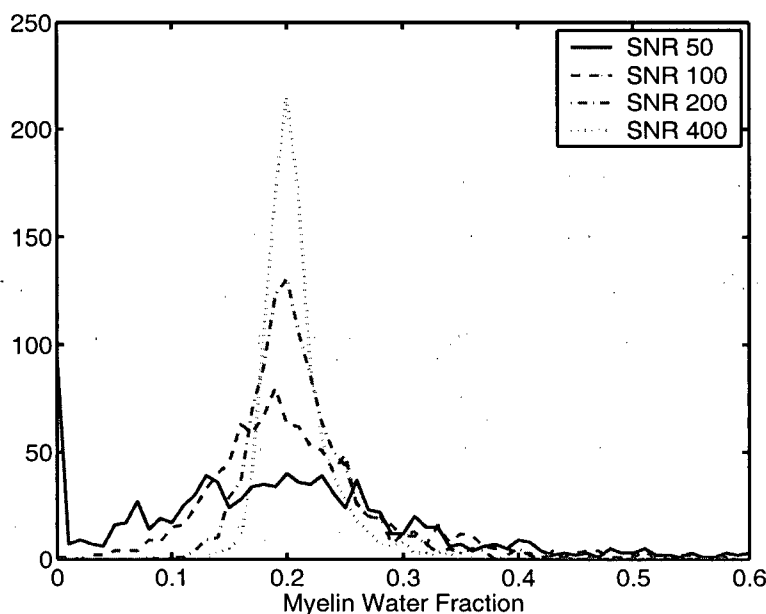


Figure 2.1: Histograms of the myelin water fraction from simulated decay curves with SNR of 50, 100, 200, and 400. The true myelin water fraction was 0.2.

Therefore, the signal-to-noise ratio must be high enough to obtain accurate and precise myelin water fraction measurements. There are two methods to obtain high SNR images: averaging during data acquisition and noise reduction image processing. Data acquisition averaging is a standard technique in MRI to obtain higher SNR images, but the cost is a longer scan time. The scan time of the MESE₀ pulse sequence with four averages is 26 minutes and is considered long relative to standard clinical imaging (average scan time of 5 minutes). Therefore, it would be beneficial if post-processing of the MRI data could replace the data acquisition averaging. The rest of the chapter describes results from simulated and *in vivo* work to assess this possibility.

2.3 Description of Spatial Filters

The post-processing of MRI data using spatial filters decreases the effective noise in the image without the need of a longer scan time. There are a large variety of spatial filters that decrease

the noise (noise reduction filters) each with a different set of properties and assumptions. One class of filters has the property that the edges within an image are retained, or enhanced, as opposed to blurred. This property would be desirable in a noise reduction filter as small objects and edges would remain visible in the post-processed image. There are several spatial filters with this property: anisotropic diffusion filter, SUSAN filter, median filter and wavelet filter. Each of these filters is described in more detail below.

2.3.1 Anisotropic Diffusion Filter

The anisotropic diffusion filter was created by Perona [50] and introduced to MRI by Gerig [51]. It is a non-linear, locally adaptive smoothing filter that incorporates local gradient strength into the smoothing based on an input parameter, κ , which is a measure of the strength of an edge in the image. Therefore, the algorithm smooths local areas of homogeneity without blurring edges.

The anisotropic diffusion filter was applied as follows. For each pixel, the signal difference was calculated in each of the four directions (E, W, N, S):

$$\begin{aligned} D_E &= I_e(x+1, y) - I_e(x, y) \\ D_W &= I_e(x, y) - I_e(x-1, y) \\ D_N &= I_e(x, y+1) - I_e(x, y) \\ D_S &= I_e(x, y) - I_e(x, y-1) \end{aligned} \quad (2.1)$$

where $I_e(x, y)$ was the signal intensity at spatial location (x, y) in the e^{th} echo image. Then the signal intensity at (x, y) was updated:

$$I'(x, y) = I(x, y) + \Delta (c_E D_E - c_W D_W + c_N D_N - c_S D_S) \quad (2.2)$$

where the integration constant Δ was defined as 1/5 for 2D data and 1/7 for 3D data [51] and c_d (where d is one of the four directions, E, W, N or S) was defined as:

$$c_d(x, y) = \exp \left\{ - \left[\frac{\sqrt{D_{d_1}^2 + D_{d_2}^2 + \dots + D_{d_N}^2}}{\kappa} \right]^2 \right\} \quad (2.3)$$

where N was the number of echoes.

The channel diffusion filter [51] was used for all filtering and the kernel defined as:

$$c(\vec{x}) = \exp \left\{ - \left[\frac{\sqrt{\nabla I_1(\vec{x})^2 + \nabla I_2(\vec{x})^2 + \dots + \nabla I_M(\vec{x})^2}}{\kappa} \right]^2 \right\} \quad (2.4)$$

where I_1, \dots, I_M are the M echo images and \vec{x} is the vector of spatial co-ordinates and ∇ was the gradient operator [51]. For this work two spatial dimensions (2D) were used and the data was filtered across echoes using Equation 2.4.

2.3.2 Susan Filter

The Susan filter [56] (Smallest Univalve Segment Assimilating Nucleus) is a non-linear spatial filter similar to the anisotropic diffusion filter. The Susan filter preserves image structure by smoothing neighbors which form part of the same region as the central pixel. The primary difference between the Susan filter and the anisotropic diffusion filter is that the Susan filter uses the Univalve Segment Assimilating Nucleus (USAN) weighting to determine similarity of signal intensities. One other important difference is the center pixel is not included in the summation over the neighborhood. This difference allows for a reduction of impulse noise – spikes in signal intensity. The primary equation governing the smoothing is:

$$J(x, y) = \frac{\sum_{(i,j) \neq (0,0)} I(x+i, y+j) \exp \left\{ -\frac{r^2}{2\sigma^2} - \frac{[I(x+i,y+j)-I(x,y)]^2}{t^2} \right\}}{\sum_{(i,j) \neq (0,0)} \exp \left\{ -\frac{r^2}{2\sigma^2} - \frac{[I(x+i,y+j)-I(x,y)]^2}{t^2} \right\}} \quad (2.5)$$

where $r = \sqrt{i^2 + j^2}$, σ controls the scale of the smoothing, t is the brightness threshold.

2.3.3 Median Filter

The median filter is a non-linear filter based on finding the median of a set of neighbouring pixels. It is implemented as a convolution across the image and replaces each voxel by the median of the 4-connected neighboring voxels and the central voxel. The median of these voxels is calculated by sorting the voxel signal intensities in numerical order and replacing the voxel under consideration by the middle value of the sorted list. For all the work in this thesis, the median filter was applied in two dimensions to each of the 32 echo images in turn.

2.3.4 Wavelet Filter

The wavelet packet filter [57, 58, 59] is a non-linear filter based on the wavelet decomposition. Each image was transformed, using the 12-point coiflet wavelet [60] into a complete tree of $\log_2(N)$ levels where $N = 256$. The best basis set was found by a minimum entropy criterion to find the most compact basis set which represented the original signal. The best basis set was then thresholded to divide the structure from the noise in the decomposed signal.

All wavelet packet filtering was kindly processed by Dr. John Wood at the University of Southern California.

2.4 Spatial Filters on Simulated Data

I created a simulated set of images with different areas of myelin water fraction. Noise was added to the set of images and each filter was applied, in turn, to the noisy images, and the estimated myelin water fraction was compared to truth. Simulated images enable the assessment of each of the filters and not in the presence of other scanner problems. As well, processing of simulated images allows results to be compared back to truth.

2.4.1 Methods

A simulated 32-echo MRI data set was created which modeled important aspects of white matter in an MRI image: areas of constant myelin water fraction, areas with a low gradient in myelin water fraction, and edges from myelin water fraction to no myelin water fraction. The myelin water fraction was calculated from the filtered and unfiltered data and was compared to truth.

2.4.1.1 Simulated Image

A simulated myelin water fraction image was created, with different types of edges and gradients. The image was 256 rows by 256 columns, where r is the row number and ranges from 1 at the top of the image to 256 at the bottom of the image, c is the column number and ranges from 1 at the left side of the image to 256 at the right side of the image. The pixels in the image are the true myelin water fraction, f , which ranges from $0 \leq f \leq 1$. Six regions, shown in Figure 2.2, were used to define the image:

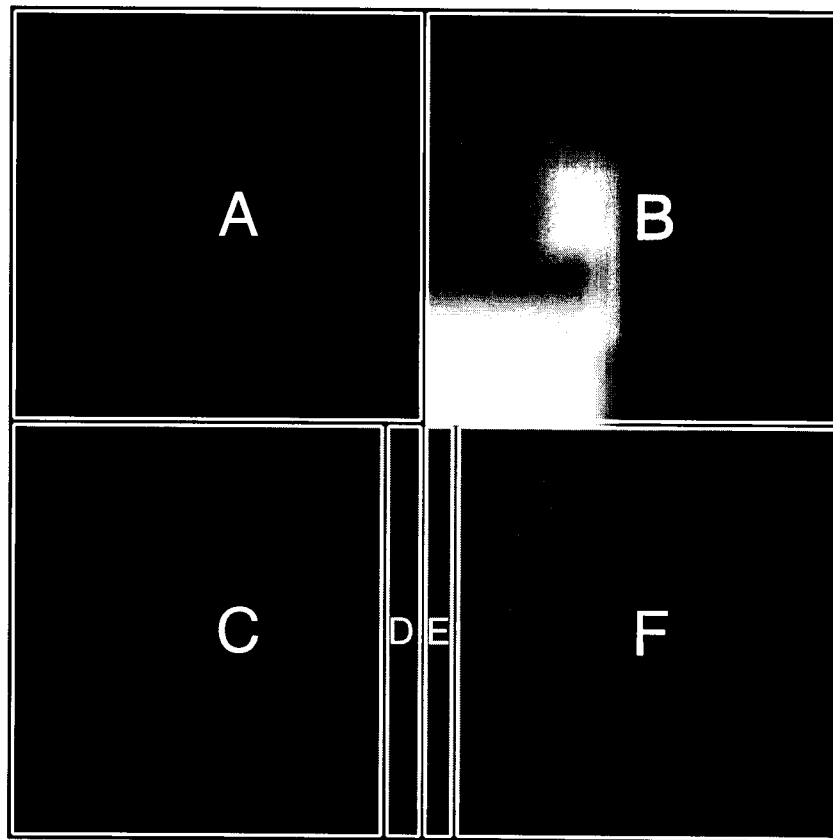


Figure 2.2: Simulated myelin water fraction image annotated with six regions.

- Region A: Large region of zero myelin water fraction, $f(r, c) = 0$ for $1 \leq r \leq 128$ and $1 \leq c \leq 128$.
- Region B: Each row was defined:

$$f(r, c) = \begin{cases} h(r) & 129 \leq c \leq 139 \\ h(r)(149 - c)/(149 - 140) & 140 \leq c \leq 149 \\ 0 & 150 \leq c \leq 256 \end{cases} \quad (2.6)$$

and $h(r) = (r - 1)/117$ for $11 \leq r \leq 128$. For rows $1 \leq r \leq 10$, $h(r)$ was set to 0.

- Region C: Each row, $129 \leq r \leq 246$, was defined as:

$$f(r, c) = \begin{cases} 0 & 1 \leq c \leq s(r) \\ 0.15[c - s(r)]/[117 - s(r)] & s(r) \leq c \leq 118 \end{cases} \quad (2.7)$$

where $s(r) = r - 129 + 1$.

- Region D: Constant region of $f(r, c) = 0.15$ for $129 \leq r \leq 256$ and $119 \leq c \leq 128$.
- Region E: Constant region of $f(r, c) = 0.30$ for $129 \leq r \leq 256$ and $129 \leq c \leq 139$.
- Region F: Each row, $129 \leq r \leq 246$, was defined as:

$$f(r, c) = \begin{cases} 0.30[s(r) - c]/[s(r) - 139] & 139 \leq c \leq s(r) \\ 0 & s(r) \leq c \leq 256 \end{cases} \quad (2.8)$$

where $s(r) = (246 - r)/117 * (256 - 140) + 140$.

The regions and boundaries between the regions were defined to simulate regions and boundaries between tissues in the brain. The upper two quadrants have a sharp edge between 0 myelin water fraction and a positive myelin water fraction to simulate the boundary between white matter and ventricles. The myelin water fraction gradients in Regions C and F simulated regions of changing myelin water fraction in the brain due to changes in tissue. The resulting simulated myelin water fraction image is shown in Figure 2.3.

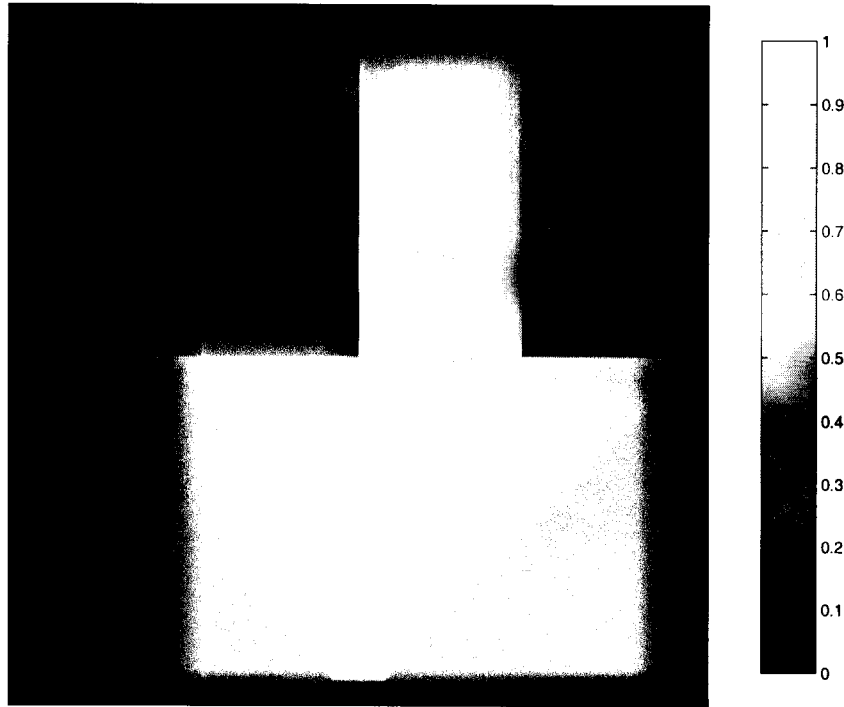


Figure 2.3: Simulated myelin water fraction image (truth) from which the 32-echo data set was constructed.

A 32-echo dataset was created based on the simulated image. Each echo was defined as:

$$y(r, c, t) = f(r, c) \exp(-t/20) + [1 - f(r, c)] \exp(-t/80) \quad (2.9)$$

where f was the fraction at location row r and column c defined in Figure 2.3 and $t = 10, 20, \dots, 320$ ms.

The 32-echo dataset, created from the simulated image, had 10 realizations of SNR =100:1 quadrature noise (Section 1.6.4) added to it.

2.4.1.2 Filtering

The filters tested in these simulations were: anisotropic diffusion filter of 1 iteration (`aniso1`), anisotropic diffusion filter of 3 iterations (`aniso3`), anisotropic diffusion filter of 5 iterations (`aniso5`), median filter (`median`), susan filter (`susan`), a median filter of the myelin water map calculated from the unfiltered data (`postmedian`) and a wavelet packet filter with thresholds of 46 (`wavelet46`), 48 (`wavelet48`), 50 (`wavelet50`), and 52 (`wavelet52`). Each filter was applied

to each of the 10 noisy 32-echo dataset.

2.4.1.3 NNLS

The small norm, non-negative least squares algorithm (Section 1.7.1.2) was applied point-by-point to each filtered dataset.

2.4.1.4 Analysis

Two measures were used to assess the myelin water fraction calculated from the filtered data. First, a global error was calculated between the true myelin water fraction and the reconstructed. Second, an error was calculated for the region of 0.15 and 0.30 myelin water fraction.

The myelin water fraction calculated from the noisy unfiltered and filtered images was compared to the true myelin water fraction. The measure was defined as:

$$\text{RMS} = \sqrt{\frac{\sum_{r,c} (f(r,c) - \widehat{f(r,c)})^2}{N}} * 100 \quad (2.10)$$

where $f(r,c)$ is the true myelin water fraction at row r and column c , $\widehat{f(r,c)}$ is the measured myelin water fraction, and N is the number of pixels summed over. The global error was defined such that it did not come within 5 pixels of the border, so the boundary does not create a bias in the error measure. For each of the local measures, r,c was defined to range over the constant myelin water fractions.

The mean and standard deviation of the errors were calculated over the ten realizations of noise. The mean and standard deviation were calculated for each filter and compared.

2.4.2 Results

Global Myelin Water Fraction

The mean and standard deviation of the error is shown in Table 2.1. The filter that produced the lowest global myelin water fraction error was the anisotropic diffusion filter (5 iterations) followed closely by the susan filter. There was very little difference between the estimated myelin water fraction and the true myelin water fraction in the areas of the simulated image where the true myelin water fraction was 0. In the areas of the true myelin water fraction where the myelin

Filter	Global Error Measure
none	1.964 (0.005)
aniso1	1.208 (0.009)
aniso3	0.758 (0.012)
aniso5	0.637 (0.011)
median	1.175 (0.014)
susan	0.741 (0.013)
postmedian	1.340 (0.010)
wavelet46	0.723 (0.016)
wavelet48	2.504 (5.809)
wavelet50	0.818 (0.084)
wavelet52	1.048 (0.008)

Table 2.1: The mean global error in myelin water fraction over the 10 noisy data sets for each filter. The standard deviation is shown in brackets.

water fraction was greater than 0, the difference between the true fraction and the estimated fraction was relatively constant, that is, no bias with increasing true myelin water fraction. The wavelet48 filter was the only filter to increase the global RMS error and this is likely due to the threshold chosen.

Error in 15% Myelin Water Fraction

For this section, the error was calculated within the section in the lower half of the image toward the mid-line that was constant at 15% myelin water. The results are shown in Table 2.2.

Filter	Error Measure
none	2.623 (0.081)
aniso1	1.773 (0.081)
aniso3	1.038 (0.061)
aniso5	0.813 (0.056)
median	1.584 (0.075)
susan	0.928 (0.054)
postmedian	1.719 (0.086)
wavelet46	1.021 (0.052)
wavelet48	2.340 (4.329)
wavelet50	1.208 (0.162)
wavelet52	1.570 (0.077)

Table 2.2: The mean error in myelin water fraction over the 10 noisy data sets for each filter for the area of 15% myelin water. The standard deviation is shown in brackets.

The filter that produced the lowest global myelin water fraction error was the anisotropic diffusion filter (5 iterations) followed closely by the susan filter. The median filters did not perform well.

Error in 30% Myelin Water Fraction

The error was calculated within the section in the lower half of the image toward the mid-line that was constant at 30% myelin water. The results are shown in Table 2.3.

Filter	Error Measure
none	2.891 (0.065)
aniso1	1.927 (0.079)
aniso3	1.247 (0.113)
aniso5	0.957 (0.123)
median	1.733 (0.087)
susan	1.124 (0.091)
postmedian	1.326 (0.082)
wavelet46	1.270 (0.079)
wavelet48	4.030 (8.903)
wavelet50	1.499 (0.147)
wavelet52	1.819 (0.080)

Table 2.3: The mean error in myelin water fraction over the 10 noisy data sets for each filter for the area of 30% myelin water. The standard deviation is shown in brackets.

The filter that produced the lowest global myelin water fraction error was the anisotropic diffusion filter (5 iterations) followed closely by the susan filter. The median filters did not perform well.

Myelin Water Maps

The simulated myelin water maps were calculated from each of the filtered data sets. One example set of data is shown in Figure 2.4.

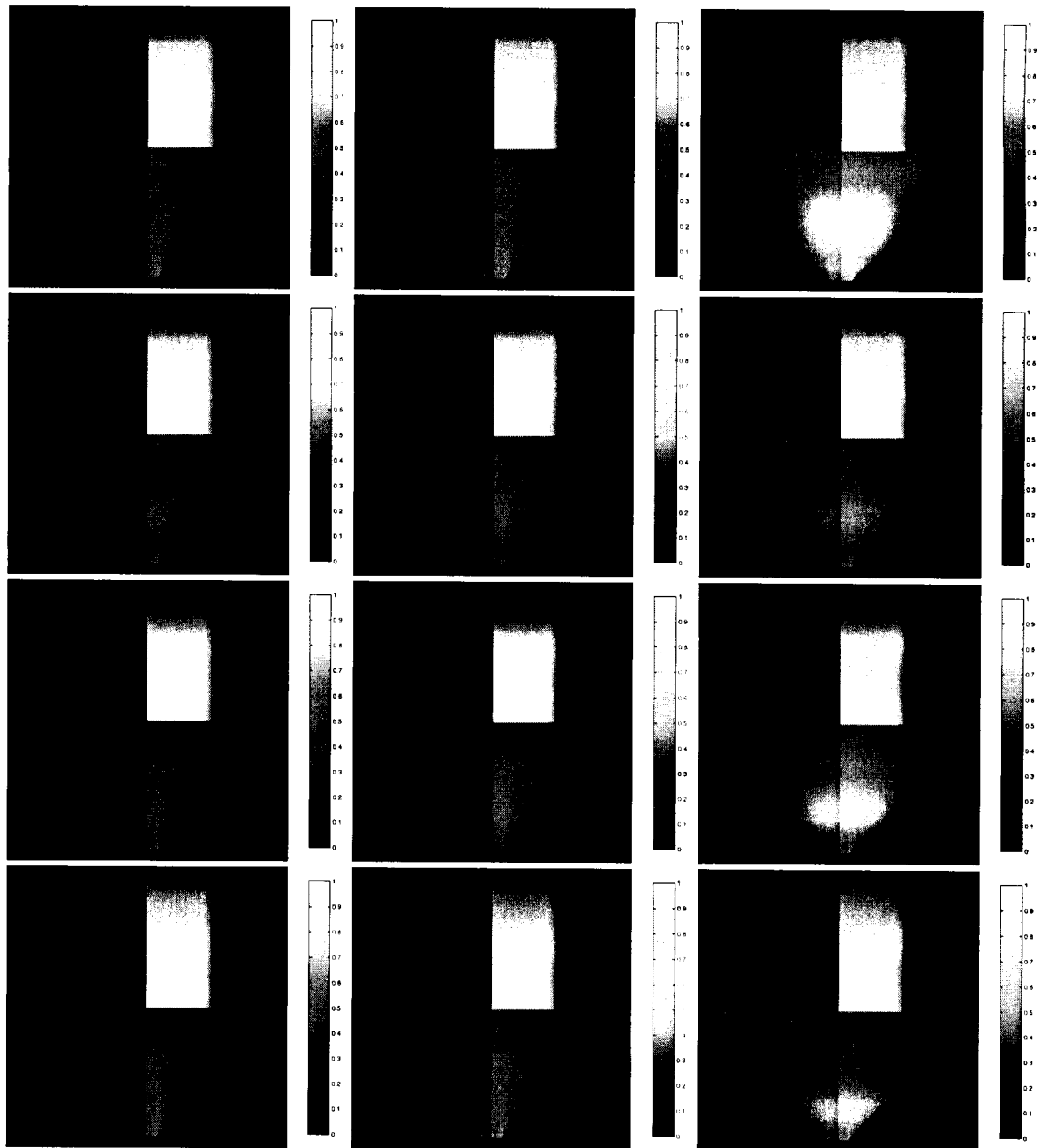


Figure 2.4: Myelin water maps of the true fraction (top left), unfiltered (top middle), susan (top right), aniso1 (second row, left), aniso3 (second row, middle), aniso5 (second row, right), median (third row, left), postmedian (third row, middle), wavelet46 (third row, right), wavelet48 (fourth row, left), wavelet50 (fourth row, middle), wavelet52 (fourth row, right).

2.4.3 Conclusions

The simulations provided an excellent environment to assess the filters as a function of noise and compare the estimated myelin water fraction back to the true myelin water fraction. Each of the filters reduced the RMS error except for the `wavelet48` filter. The anisotropic diffusion filter of five iterations was the filter that produced the smallest error measures.

2.5 Spatial Filters Applied to *In Vivo* Data

In vivo MRI images of the brain are more complex, than simulated images, as they contain flow artifacts, truncation artifacts, and head motion. A study similar to the simulation study was done based on a set of MRI scans of five volunteers. The myelin water fraction was calculated from a set of regions for each volunteer and compared as a function of the filters.

2.5.1 Data Acquisition and Analysis

An optimized multi-echo (ME), spin-echo pulse sequence (descending, alternating crushers [31] and composite 180° pulses) was used to collect 32 echoes at $TE = 10, 20, \dots, 320$ ms from a single axial slice through the genu and splenium of the corpus callosum. Five normal volunteers had three sets of ME scans: 1) a scan of 4-averages (28 minutes), 2) a scan of 2 averages (13 minutes) and 3) a scan of one average (6 minutes 30 seconds). An N -average image is acquired by collecting each line of k -space N times (see Section 1.6.1). The volunteers remained in the magnet in the same position for all three scans. Other MRI parameters were $FOV = 24$ cm, $TR = 3,000$ ms, slice thickness = 5 mm, 256×128 frequency/phase encoding, and pixel size of 0.94×0.94 mm. All data was collected on a 1.5T GE Signa Horizon system with EchoSpeed gradients (General Electric Medical Systems, Milwaukee WI).

Regions were drawn on the $TE = 80$ ms image in white matter, gray matter and CSF areas. The myelin water fraction was calculated voxel-by-voxel over each slice and the mean and standard deviation of the myelin water fractions were calculated for each region.

Each 32 echo data set was filtered with: No filter (`none`), Anisotropic diffusion filter 1 iteration (`aniso1`), Anisotropic diffusion filter 3 iteration (`aniso3`), anisotropic diffusion filter 5 iterations (`aniso5`), Susan filter (`susan`), median filter(3x3) (`medfilt`), Median filter applied to MWM from

unfiltered data (3x3) (`postmed`), Wavelet filter (20) (`wavelet20`), Wavelet filter (25) (`wavelet25`), and Wavelet filter (30) (`wavelet30`).

2.5.2 Results

The mean and standard deviation of the myelin water fraction were calculated over each region and compared to the mean and standard deviation from the unfiltered data. The mean change in myelin water fraction over all regions, filters and volunteers was -0.3121 with a standard deviation of 0.6793. Therefore, there was very little bias introduced in the mean myelin water fraction as a result of filtering the multi-echo data.

Filter	fWM	genu	postWM	postIC	splen
none	9.6 (4.8)	15.7 (4.1)	12.1 (4.1)	12.1 (5.7)	15.0 (5.2)
aniso1	8.9 (3.6)	15.5 (3.6)	11.7 (3.3)	12.2 (6.2)	14.9 (4.8)
aniso3	8.1 (2.2)	15.3 (3.5)	12.0 (2.6)	12.9 (6.8)	14.7 (4.0)
aniso5	7.8 (2.0)	15.2 (3.0)	11.7 (2.4)	13.0 (6.8)	14.4 (3.4)
susan	8.5 (3.9)	15.5 (3.6)	12.3 (3.1)	12.1 (6.0)	15.1 (5.0)
medfilt	8.7 (3.0)	15.2 (3.9)	12.2 (3.7)	12.9 (6.6)	16.0 (3.8)
postmed	8.8 (2.2)	15.8 (2.9)	12.2 (2.6)	11.5 (4.6)	15.2 (3.0)
wavelet20	8.5 (3.4)	15.1 (4.3)	12.0 (3.4)	12.4 (5.0)	14.8 (5.8)
wavelet25	8.6 (3.4)	15.3 (4.2)	12.0 (3.2)	12.6 (5.7)	15.0 (5.5)
wavelet30	8.8 (3.6)	15.4 (4.2)	12.2 (3.6)	12.3 (5.8)	15.1 (5.1)

Table 2.4: Mean myelin water percent for four anatomical regions (standard deviation shown in brackets) from one example volunteer. The regions were: caudate nucleus (`caud`), frontal white matter (`fWM`), posterior internal capsules (`postIC`), and the splenium of the corpus callosum (`splen`).

One measure for assessing the filter is to count the number of times each filter resulted in the myelin water fraction with the smallest standard deviation. This measure was done for all regions and for white matter regions only and the results are shown in Table 2.5. Over all the regions, the myelin water fraction, calculated from the anisotropic diffusion filter (5 iterations), had the smallest standard deviation.

Filter	All Regions	WM Regions
none	9	0
aniso1	0	0
aniso3	1	0
aniso5	50	35
susan	0	0
medfilt	4	1
postmed	33	17
wavelet20	5	1
wavelet25	0	0
wavelet30	0	0

Table 2.5: The number of times each filter had the smallest myelin water fraction standard deviation over all the regions (middle column) and over the white matter (WM) regions (last column).

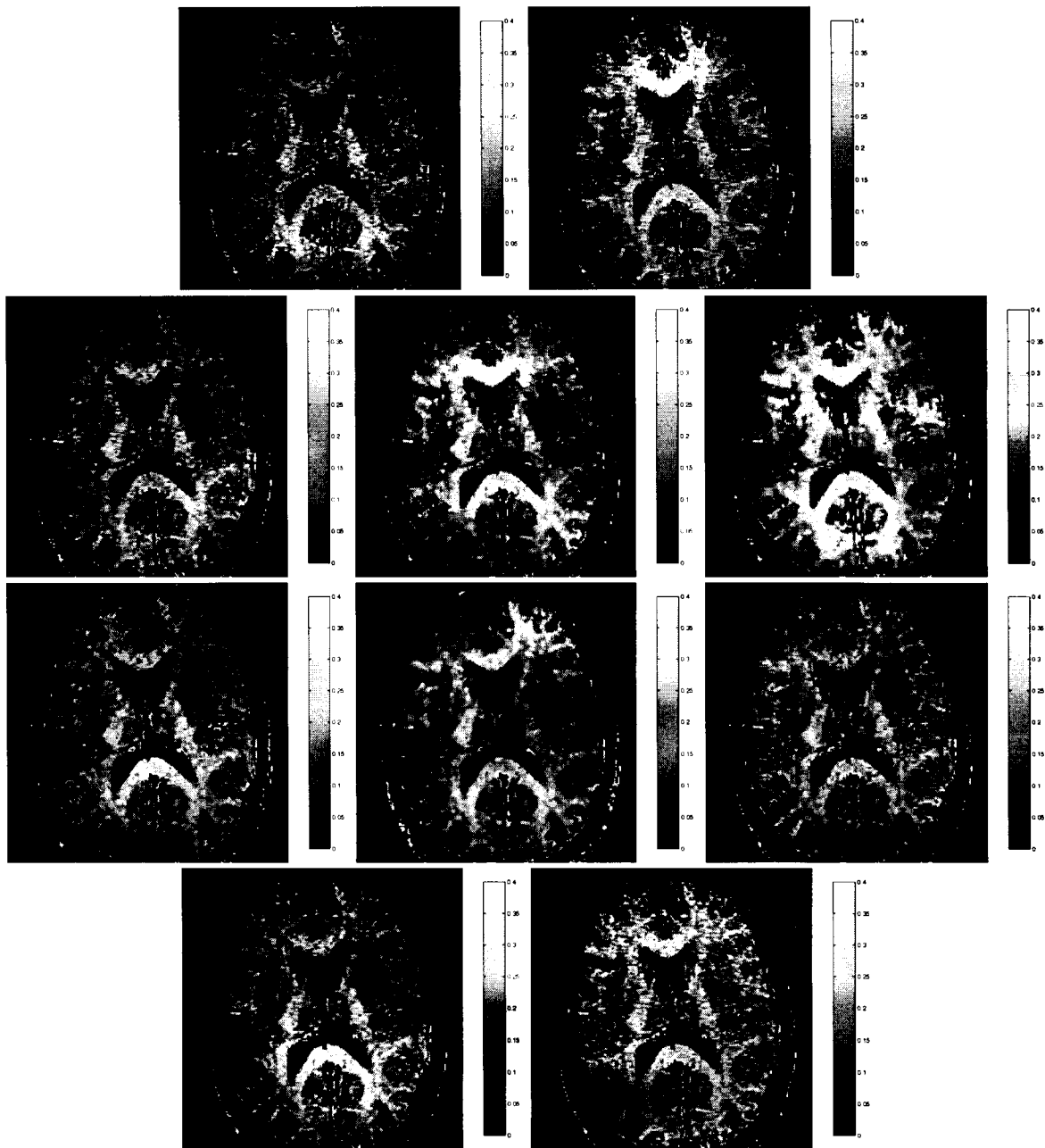


Figure 2.5: Myelin water maps of the unfiltered (top left), *susan* (top right), *aniso1* (second row, left), *aniso3* (second row, middle), *aniso5* (second row, right), *median* (third row, left), *postmedian* (third row, middle), *wavelet20* (third row, right), *wavelet25* (fourth row, left), *wavelet30* (fourth row, right).

2.5.3 Conclusions

The anisotropic diffusion filter applied five times is the best filter to use to minimize the standard deviation in the myelin water fraction. The resulting myelin water map is smoother and less blurred than the original myelin water map that is median filtered.

The data that is input into the NNLS routine should be as good as possible and therefore the data should be filtered with the anisotropic filter rather than applying the median filter afterward.

2.6 Spatial Filtering vs Averaging

Myelin water signal, in the brain, was calculated from an optimized multi-echo spin-echo MRI scan by fitting the decay curves using a non-negative least squares algorithm. The anisotropic diffusion filter is an adaptive smoothing filter that reduces the variability in homogeneous regions without blurring edges. This filter was applied to the multi-echo data to decrease the local variability and therefore increase the local signal-to-noise ratio. Forty regions, from five volunteers, were analyzed by three methods of computing the myelin water fraction. A consistent decrease in the myelin water fraction variability with no bias in the mean was found for the 40 regions. The myelin water fraction of white matter was more contiguous and had fewer “holes” than maps from unfiltered echoes.

2.6.1 Methods

The *in vivo* data acquisition is described in Section 2.5.1.

2.6.1.1 Data Filtering

The three multi-echo (ME) scans from each volunteer were filtered with 0, 1, 3 and 5 iterations of the anisotropic diffusion filter with parameter $\kappa = 3\sigma$ where σ was the standard deviation in the noise on the TE = 10 ms image (measured in the air outside the head) divided by $\sqrt{2 - \pi/2}$ (for normalization of the Rician distributed noise [61] at zero signal).

The channel diffusion filter [51] (Section 2.3) was used for all filtering.

2.6.1.2 Data Analysis

Eight regions-of-interest (ROIs) (number pixels average/minimum/maximum was 123/104/168) were drawn in white matter on the 4-average, TE = 80 ms scan of each of the five volunteers: frontal white matter (left and right), internal capsules (left and right), posterior white matter (left and right), genu of the corpus callosum and the splenium of the corpus callosum. The average SNR over all ROIs was 199:1.

The T_2 distribution was calculated by the regularized NNLS algorithm [40]. The MWF was defined as:

$$\text{MWF} = \frac{\sum_{T_2=0}^{50} s(T_2)}{\sum_{T_2=0}^{2000} s(T_2)} \quad (2.11)$$

where $s(T_2)$ was the amplitude of the T_2 distribution calculated by NNLS and the maximum T_2 was 2000 ms.

Two sets of analysis were performed: 1) MWFs calculated per ROI and 2) MWFs calculated voxel-by-voxel (myelin water maps). For the first analysis, three myelin water measures were calculated for each ROI:

1. Average the decay curves in the ROI and apply the NNLS algorithm to the averaged decay curve then calculate the MWF (**average-invert**).
2. Apply the NNLS algorithm to each decay curve in the ROI, calculate the MWF from each result then average the MWFs (**invert-average**).
3. Apply the bootstrap algorithm as defined below (**bootstrap**).

The standard MWF measure was defined to be the **average-invert**, ROI analysis applied to the 4-average, unfiltered scan for each volunteer because simulations showed least bias and lowest standard deviation versus other approaches.

The second analysis was on myelin water maps which were composed of myelin water fractions calculated from T_2 distributions calculated voxel-by-voxel by the NNLS algorithm (no averaging of neighboring decay curves).

The number of "holes" in an ROI of the myelin water map was defined as the number of voxels in a white matter ROI with a MWF less than 0.03.

All data was processed using in-house software and Matlab (The Mathworks, Natick, Mass.)

2.6.1.3 Bootstrap Theory

The bootstrap algorithm [62] is a means of estimating confidence intervals and other statistical measures on a set of data. Consider an ROI containing N decay curves. The bootstrap method essentially simulates having many ROIs each containing N decay curves. The standard deviation of the mean MWFs from all the realizations is the standard error of the mean. The bootstrap algorithm is applied as follows: A single bootstrap resampling randomly selects N (same N as defined above) decay curves with replacement from the ROI. Some voxels may be represented more than once and some may be missing. The mean decay curve is formed from this sample and the MWF found. The bootstrap resampling is repeated 1,000 times and the mean and standard deviation of the corresponding MWFs found. This mean is very close to the simple mean from the N decay curves in the ROI. The standard deviation is an estimate of the standard error of the MWF mean.

2.6.2 Results

2.6.2.1 Effect of Filtering Spin-Echo Images

To confirm the anisotropic diffusion filter did not introduce a bias in the signal intensity (SI) of the ME data, I compared the mean and variance of the intensities of the anisotropically filtered ME data in the 40 ROIs to the original unfiltered ME data. The maximum SI change in the ME data on the TE = 10 ms image over all ROIs and averages was 0.24%. The mean SI changes, over all ROIs, as a function of the smoothing iterations, were not statistically significant ($p > 0.19$). The average change in standard deviation of the signal intensities was -1.4% (1 iteration), -4.0% (3 iterations) and -6.0% (5 iterations) over all ROIs and averages relative to the unfiltered spin-echo data. The standard deviation decreased for every ROI but was significant (ratio of variances using the F test) in only 10 ROIs in the 1-average data, 3 ROIs for the 2-average data and 0 ROIs for the 4-average data (all with 5 iterations).

2.6.2.2 Bootstrap Validation of Mean Myelin Water Fraction

The bootstrap algorithm was used to estimate the myelin water fraction variability over an ROI. To confirm the mean myelin water fractions were the same as calculated by the bootstrap method a two-tailed t-test was used to compare the MWF from the bootstrap method, f_b , to the "gold

standard" average-invert, f_{ai} . The statistic $D = \frac{f_b - f_{ai}}{f_{ai}} \times 100$ was calculated for each set of iterations of the filter for each of the averages, and was compared to zero. In every ROI the MWFs calculated from the bootstrap method were found to be statistically the same as those calculated by the average-invert method (minimum $p=0.11$). For the rest of the work the mean MWF within an ROI was calculated using the bootstrap method unless otherwise stated.

2.6.2.3 Myelin Water Fraction

2.6.2.3.1 Four Average Data

The standard MWF measure (MWF calculated from the 4-average, unfiltered ME data) was compared to the MWF calculated from the 4-average, filtered ME data to determine if the MWF measurement had less variability after the application of the filter to the 4-average ME data. The average relative change in mean MWF for the ROIs, calculated with the bootstrap method from the 4-average data, was 1.6% for 1 iteration, 3.6% for 3 iterations and 4.8% for 5 iterations. The mean MWF decreased in 20 of the 40 ROIs for each of 1, 3 and 5 iterations relative to the unfiltered. The number of ROIs with a significant change in the mean MWF as a function of iterations was 6 (1 iteration), 26 (3 iterations) and 28 (5 iterations) based on a t-test of the difference in mean MWF. The mean of the magnitude of the relative decrease in the standard deviation of the MWF over the ROIs was 13% (1 iteration), 32% (3 iterations) and 44% (5 iterations) and the number of ROIs that had a significant decrease in the variance was 21 (1 iteration), 36 (3 iterations) and 40 (5 iterations).

2.6.2.3.2 Two Average Data

The 2-average ME data can be collected in half the scan time of the ME data required for the standard (4-averages); therefore, if the MWFs calculated from the 2-average, filtered ME data are as robust as those calculated from the standard, then the 2-average, filtered ME data could be used for future work (which would be a significant savings in scan time). The mean relative difference between the MWF calculated from the 2-average (with and without filtering) multi-echo data and the standard MWF over the 40 ROIs was 26%. Only one 2-average, 5 iteration ROI had a mean MWF statistically the same as the standard.

The myelin water map was created by applying NNLS voxel-by-voxel to calculate the myelin

water fraction therefore it was important to compare *invert-average* to the standard *average-invert*. The relative difference in mean MWF between the *invert-average* method (based on the 4-average MWF data) and the standard MWF was 29% (unfiltered), 26% (1 iteration), 20% (3 iterations) and 17% (5 iterations). Only 1/4 of the 40 ROIs calculated by the *invert-average* method were statistically the same as the standard MWF (based on a two tailed t-test). The *invert-average* myelin water fractions were greater than those calculated using the bootstrap method in 72% of the 40 ROIs.

2.6.2.3.3 Qualitative Myelin Water Maps

Figure 2.6 shows the myelin water maps of anisotropically filtered spin-echo MRI scans. The myelin water maps calculated from the 4-average multi-echo data with 5 iterations of the filter were more contiguous in white matter. The average number of holes calculated in each of the ROIs decreased as a function of the number of iterations and as a function of averages (Table 2.6). There was an average of only 2.5 holes in the ROIs in the myelin water maps calculated from the 4-average data filtered with 5 iterations. Similar results were found if the definition of a hole was a voxel with a MWF less than 0.02, 0.04 or 0.05.

Averages	Unfiltered	1 Iteration	3 Iterations	5 Iterations
1	20 (8)	19 (9)	17 (9)	14 (9)
2	15 (9)	14 (9)	13 (9)	12 (10)
4	8 (6)	6 (5)	4 (3)	3 (3)

Table 2.6: Number of holes per ROI as a function of iterations of the anisotropic diffusion filter (standard deviations shown in brackets).

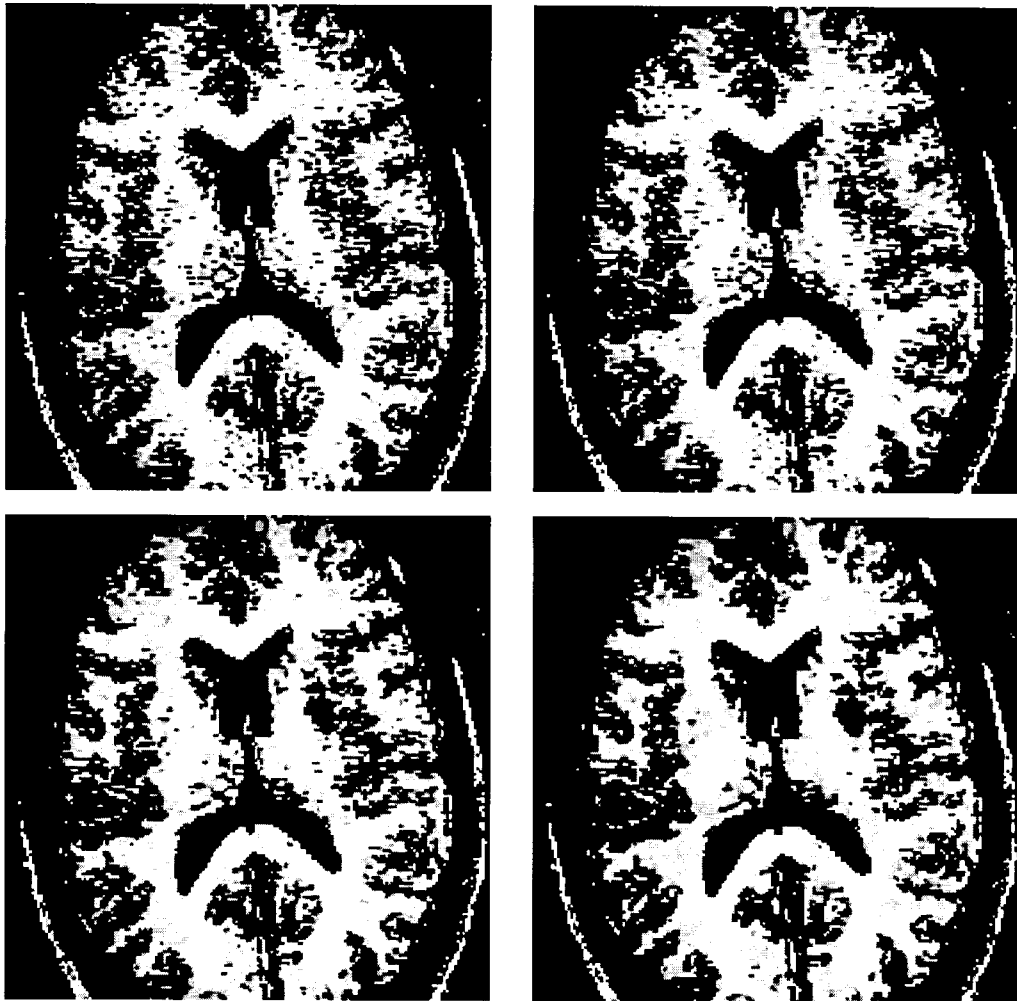


Figure 2.6: Myelin water maps calculated from unfiltered (top left), 1 iteration (top right), 3 iterations (bottom left) and 5 iterations (bottom right) of the anisotropic diffusion filter applied to the 4-average, spin-echo data. Note the fewer “holes” in the white matter and more continuity through the maps as the number of iterations is increased.

2.6.3 Discussion

The anisotropic diffusion filter was applied to the original multi-echo data although it could have been applied to the myelin water maps instead. The curve fitting algorithm to compute the myelin water fractions from the decay curves is a non-linear algorithm and, as all curve fitting algorithms, requires a high SNR. Therefore, it was important to apply the curve fitting to data that was the best I could provide which required the application of the anisotropic diffusion filter before the curve fitting.

I confirmed no bias in the ME SI was introduced by the anisotropic diffusion filter (a bias could result in artificial changes in the amplitudes or T_2 times of the peaks in the calculated T_2 distribution) and the standard deviation decreased for each ROI as more iterations of the filter were applied. The number of significant decreases in the standard deviation was more in the 1-averaged ME data as a result of the lower signal-to-noise ratio.

As κ was defined to be 3σ , the number of iterations of the filter was the only free parameter. I applied seven and nine iterations of the filter but found both the filtered ME data and myelin water maps were “over filtered” as local areas of smoothly changing intensity became iso-intense. Five iterations of the filter offered a reasonable trade-off between a decrease in local standard deviation without “over filtering”. Therefore, the decrease in the standard deviation, without introducing a bias in the SIs should lead to better qualitative MWF results.

The MWF calculated from the 4-average, filtered ME data was expected to be more homogeneous than the MWF calculated from the 4-average ME data (standard) because the local variability in the SI of the ME data decreased as more iterations of the filter were applied. As expected, there was only a small change ($< 5\%$) in the mean MWF for all the ROIs. There was no discernible bias in the MWF with filtering because half the ROI's MWF decreased and half increased. The anisotropic filtering of the ME data was shown to improve the MWF ROI measurement compared to the standard.

I expected that the mean MWF calculated from the 2-average, multi-echo data with 5 iterations of the anisotropic diffusion filter would be as accurate as the standard mean MWF calculated from the 4-average, unfiltered spin-echo data. The results did not corroborate this. To understand this, I analyzed MWF histograms in each ROI (for example, see Figure 2.7). The MWF in the 4-average, unfiltered ROI data had a distinct peak (top right plot in Figure 2.7) corresponding

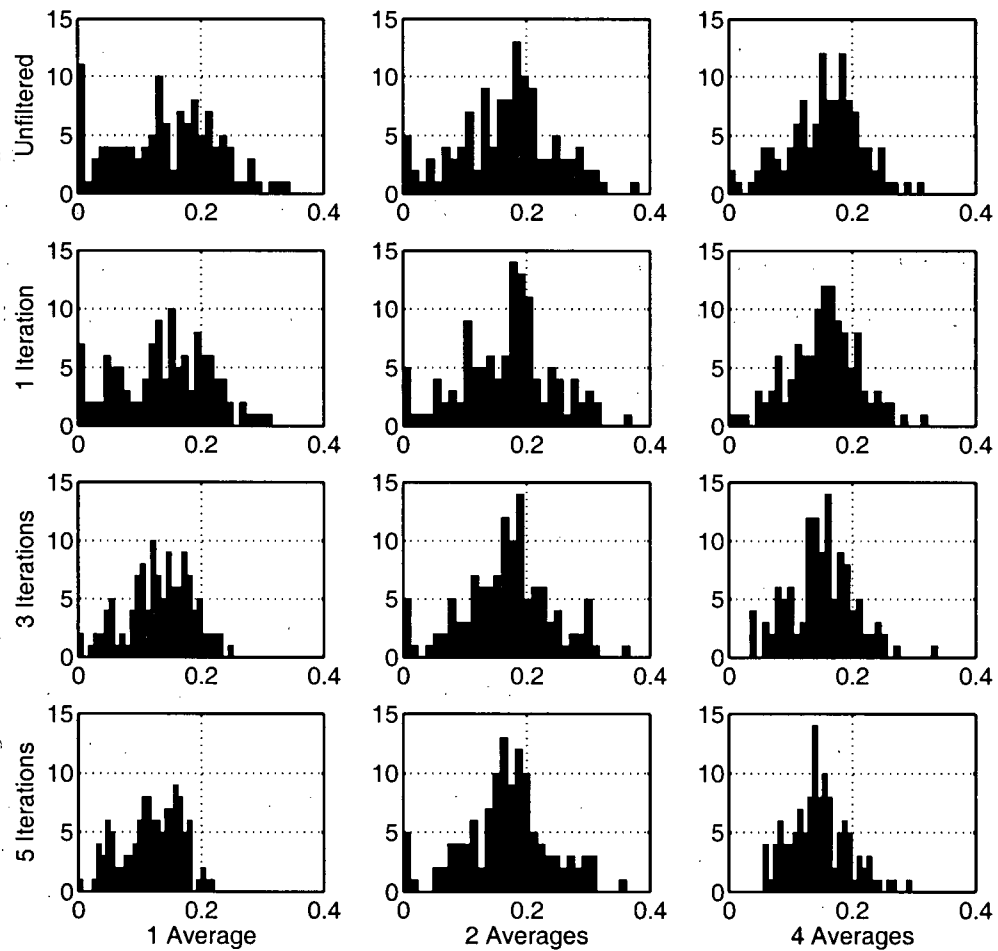


Figure 2.7: Histograms of myelin water fraction calculated from the 1-average (first column), 2-average (second column) and 4-average (third column) spin-echo data with 0 iterations (first row), 1 iteration (second row), 3 iterations (third row) and 5 iterations (fourth row) of the anisotropic diffusion filter.

to a true MWF that did not vary spatially in the ROI. The MWF histogram of an ROI from the 2-average unfiltered data (top, center) had a broader peak than the histogram of the 4-average unfiltered. The 1-average, unfiltered myelin water fraction histogram had a peak with a mean value higher than the 4-average and, as well, a wider distribution. There are two possible reasons for the broad peak in the histogram, the first due to noise in the original multi-echo data and second due to a variability in the underlying myelin water content in the white matter across the ROI. To verify that the wider distribution was due to noise, I created a white matter model with 10% of the signal at 20 ms and 90% of the signal at 80 ms and then added 1,000 realizations each of SNR = 50, 100 and 200 noise. The NNLS algorithm was applied to each model with noise and the mean, standard deviation and skew were calculated for the area under the curve between 0 ms and 50 ms normalized by the total area in the distribution. Based on these simulations, I found similar broad peaks in the 1- and 2-average histograms were due to the noise. In the MRI data the filtering did sharpen the peak in the 1-average ROI but did not shift it lower. I believe that this was a result of using the non-linear curve fitting technique on low SNR data.

The *invert-average* method has been used to create the myelin water maps and therefore is important to validate compared to the standard. Even though there was a large relative difference in the mean MWF (16% for 5 iterations for the 4-average data) between the *invert-average* and *bootstrap* methods, the relative difference decreased from over 29% for the unfiltered *invert-average* to 16%. The MWF calculated from the *invert-average* method tended to be closer to the standard as more iterations of the anisotropic filter were applied to the original ME data. Therefore, the myelin water maps calculated from filtered ME data do tend to be representative of the local MWF. The myelin water fractions were greater in 72% of the 40 ROIs as calculated by the *invert-average* method compared to the *bootstrap* method (on the 4-average data). This apparent increase in the myelin water fraction was due to the non-linear NNLS algorithm applied to lower SNR data in the *invert-average* method.

The anisotropic diffusion filter applied to the 4-average, ME data resulted in myelin water maps that had better continuity in all white matter regions. The number of holes within an ROI in the myelin water map decreased in most cases but there were several cases when a hole increased in size. If several voxels clustered together in the original MRI data had a decreased SI then several iterations of the anisotropic filter could decrease the SI of other adjacent voxels and may result in a filtered image that have more local voxels with a lower SI. The NNLS algorithm

would then calculate the myelin water fraction as being decreased in the local area.

2.6.4 Conclusions

The hypothesis was that the anisotropic diffusion filter applied to spin-echo data would result in more precise quantitative myelin water fractions and better quality myelin water maps. Myelin water fractions calculated from the 1-average and 2-average data, with and without application of the filter, had large biases. There was no bias introduced by the filter but there was a large decrease in the standard deviation for the 4-average images. Therefore, the anisotropic diffusion filter was excellent for 4-average data and reduced the standard deviation by 40% which, effectively, was similar to collecting an 8-average scan.

2.7 Conclusions

Reliable estimation of the myelin water fraction is dependent on the underlying SNR of the multi-echo data. The current method to acquire sufficient SNR is to collect multiple averages of the multi-echo data, but this results in a long scan time. A second approach to have higher SNR data is to apply a noise reduction filter to the multi-echo data. The advantage is the filter can be applied after acquiring the data.

There are many types of noise reduction filters, but I chose four, each of which designed to retain the edges in the original data. I compared the four filters on simulated and *in vivo* multi-echo data. For the *in vivo* data, I acquired 1-average, 2-average and 4-average *in vivo*, multi-echo data sets on six volunteers. For the simulated and *in vivo* data, I compared the variability of the MWF in regions.

For the simulated data, five iterations of the anisotropic diffusion filter (`aniso5`) had the greatest reduction in the regional variability. The `susan` and `postmedian` filters were similar to the five iteration anisotropic diffusion filter.

The application of the filters to multi-echo, *in vivo* data showed similar results. The anisotropic diffusion filter of five iterations resulted in the smallest variability over different regions of the brain. Again, the `susan` and `postmedian` filters had a similar result to `aniso5`.

The MWF estimated from multi-echo data of different number of averages and with the application of no filter, `aniso1`, `aniso3`, and `aniso5` filter were then compared. The expectation

was the MWF estimated from filtered, 2-average data would have a similar accuracy and variability to the unfiltered, 4-average data - but this was not the case. The lack of similarity was likely due to a requirement of a lower bound of the SNR to obtain similar results to the 4-average data. The minimum lower bound on the SNR is likely a result of the non-negativity constraint of the NNLS algorithm. The noise reduction filter was good for reducing the variability of the MWF over assumed homogeneous regions.

Chapter 3

Myelin Water Fraction from Linear Combination

3.1 Introduction

Many tissues in the human body consist of several water compartments (or components) within the same voxel. White matter, for example, has two compartments, a short compartment with $T_2 \approx 20$ ms and medium compartment with $T_2 \approx 80$ ms [18]. The ratio of the areas of the short to medium compartments is approximately 1:6. The short T_2 component was shown [18] to be associated with myelin water and is important to quantify for such diseases as multiple sclerosis and adrenoleukodystrophy.

The standard method to calculate the short T_2 fraction, *in vivo*, is to collect a decay curve with 32 [18] or more echoes and to fit the curve with a non-negative least squares (NNLS) curve fitting algorithm (Section 1.7.1.2). The 32-echo pulse sequence, defined by MacKay [18], consisted of composite refocusing pulses and alternating descending crushers [31] to reduce the effect of stimulated echoes. A regularized NNLS algorithm minimized the total signal of the T_2 distribution, such that $1.02\chi_{min}^2 \leq \chi^2 \leq 1.025\chi_{min}^2$ where χ_{min}^2 was the minimum misfit of the unregularized solution.

An alternative method to calculate the short T_2 area is to calculate a linear combination of the multi-echo data. The linear combination of the multi-echo data is a filter defined as:

$$A(T_2) = \sum_{i=1}^N c_i \exp\left(-\frac{t_i}{T_2}\right) \quad (3.1)$$

where $A(T_2)$ is the filter of interest, \mathbf{c} is a vector of coefficients. The image corresponding to the

filter is defined as:

$$I_L(\mathbf{x}) = \sum_{i=1}^N c_i I_i(\mathbf{x}) \quad (3.2)$$

where $I_i(\mathbf{x}) = \sum_{j=1}^M \rho_j(\mathbf{x}) \exp(-t/T_{2,j}(\mathbf{x}))$. The goal, then, is to define coefficients, \mathbf{c} , such that $A(T_2)$ includes T_2 between 10 and 50 ms and excludes all other T_2 . The method to calculate the coefficients \mathbf{c} is the novel work in this chapter.

3.1.1 Linear Combination for T_2 Selectivity

Two groups investigated the calculation of a good set of coefficients \mathbf{c} . Both groups used a linear algorithm to calculate the coefficients.

3.1.1.1 Calculation of Coefficients by Matrix Inversion

In 1982 Macovski [63] first described the “projection image” in the context of medical imaging. The projection image was based on a linear combination of images collected from an imaging modality. The technique was used to calculate coefficients to linearly combine images so the resulting projection image enhanced a desired material and eliminated interfering materials. The method was described more fully [64] as a matrix inversion problem $I = FL$ where I was the set of image data at a voxel $I_i(\mathbf{x})$, F was a matrix of exponential kernels $[e^{-t_i/T_{2,j}(\mathbf{x})}]$ and L the amplitudes of the T_2 distribution. This method is described further in Section 3.6.1.

3.1.1.2 Calculation of Coefficients by Backus-Gilbert Method

In 1991 Whittall [65] used the Backus-Gilbert technique [66, 67] to calculate the coefficients. To solve for the coefficients using the Backus-Gilbert method, a misfit equation is defined as a function of a target filter and a linear combination of decaying exponentials. The partial derivative, with respect to the coefficients, of the misfit equation is taken and set to zero. The coefficients, that minimize the misfit, are calculated by solving the derivative of the misfit equation set to zero. The Backus-Gilbert method is described further in Section 3.7.1.

Both methods, above, used linear methods to **calculate** the coefficients. However, use of a non-linear method to calculate the coefficients, enables more constraints to be placed on the shape of the filter, $A(T_2)$, and therefore allows a better selection.

3.1.2 Properties of a Linear Combination

A linear system must obey two conditions, homogeneity and additivity [68].

- Homogeneity: If the amplitude of the input into the system is scaled by a factor A then the output from the system is scaled by a factor A .

$$f(\mathbf{x}) \rightarrow g(\mathbf{x}) \quad (3.3)$$

$$Af(\mathbf{x}) \rightarrow Ag(\mathbf{x}) \quad (3.4)$$

- Additivity: If two functions are input in to the system then the output response will be a sum of the two individual input responses.

$$f_1(\mathbf{x}) + f_2(\mathbf{x}) \rightarrow g_1(\mathbf{x}) + g_2(\mathbf{x}) \quad (3.5)$$

A system that satisfies *both* conditions can be considered a linear system. The two rules when taken together are referred to as the principle of superposition. A system is shift invariant if the responses to an identical stimulus presented shifted in time and space are the same except for the corresponding shift in time and space. The conditions are important as they define the relationship between the noise in the original images, I_i , and the noise in the output image, L .

Noise propagates linearly:

$$\sigma_L^2 = \sum_{i=1}^N c_i^2 \sigma_i^2 \quad (3.6)$$

where σ_i is the noise related to image I_i and c_i is the coefficient defined above.

3.1.3 Overview

I designed a non-linear algorithm to calculate coefficients which define an optimal filter for the short T_2 component. The nonlinear algorithm allows a larger variety of constraints on the filter that were not possible using previous methods. As my primary focus for the work was to calculate the fraction of water with $T_2 \leq 50$ ms relative to the total water, I calculated two sets of coefficients, one set that selects short T_2 , \mathbf{c}^s , and a second set that selects all T_2 , \mathbf{c}^a . To verify the linear combination was selecting the appropriate T_2 components, a set of nickel/agarose phantoms of known T_1/T_2 times were scanned using a multi-echo sequence and images of the short

T_2 were calculated. To validate the myelin water fraction, I simulated noisy multi-exponential decay curves and compared the myelin water fraction calculated by the new technique to that calculated by the standard NNLS algorithm. Five volunteers were scanned with the multi-echo sequence and the short T_2 fraction (in white matter and gray matter regions) calculated by the linear combination method was compared to the standard NNLS method.

3.2 Calculation of Coefficients

The goal for each desired filter is to calculate a set of coefficients such that the filter defined by the coefficients is unity in the range of T_2 of interest and zero elsewhere. Coefficients for both filters, $A^s(T_2)$ and $A^a(T_2)$, were calculated in a similar manner, but each with slightly different sets of constraints applied to the desired filters. The algorithm described below was used to calculate the two sets of coefficients: one set, \mathbf{c}^s , that selects for $10 \leq T_2 \leq 50$ ms and the second set, \mathbf{c}^a , that selects $T_2 > 10$ ms.

The selection filter for the short T_2 coefficients was defined as $A^s(T_2) = \sum_{i=1}^N c_i^s \exp(-t_i/T_2)$ (and similarly for the total T_2). The desired filter $A^s(T_2)$ is a boxcar:

$$A^s(T_2) = \begin{cases} 1 & T_2^{\text{lower}} \leq T_2 \leq T_2^{\text{upper}} \\ 0 & \text{elsewhere} \end{cases} \quad (3.7)$$

and for $A^a(T_2)$:

$$A^a(T_2) = \begin{cases} 1 & T_2 \geq 10 \text{ ms} \\ 0 & T_2 < 10 \text{ ms} \end{cases} \quad (3.8)$$

though neither definition is able to be constructed from a finite set of exponential decays. Similarly, the desired filter for $A^a(T_2)$ is 1 for $T_2 > 10$ ms (a step function). Therefore, the goal was to create a filter, $A^s(T_2)$, as broad as possible and near 0 for $T_2 > 80$ ms (to suppress the signal from the large peak at $T_2 \approx 80$ ms).

Let a T_2 weighted image I_i be defined as:

$$I_i(\mathbf{x}) = k\rho(\mathbf{x}) \sum_{j=1}^M s_j \exp[-t_i/T_{2,j}(\mathbf{x})] + \sigma_i(\mathbf{x}) \quad (3.9)$$

where $\rho(\mathbf{x})$ is the proton density, k represents RF inhomogeneity and other factors, s_j is the frac-

tional contribution of component $T_{2,j}$ and $\sigma_i(\mathbf{x})$ is the noise. A voxel-by-voxel linear combination of N T_2 weighted images was defined as:

$$I_L(\mathbf{x}) = \sum_{i=1}^N c_i I_i(\mathbf{x}) \quad (3.10)$$

where c_i are the weights. The noise variance in I_L is $\sigma_{I_L}^2 = \sum_{i=1}^N c_i^2 \sigma_i^2$.

An effective criterion for calculating the coefficients was to maximize the SNR at a specified $T_{2,0}$:

$$\text{SNR}_{I_L} = \frac{k\rho(\mathbf{x}) \sum_{i=1}^N c_i \exp(-t_i/T_{2,0})}{\sqrt{\sum_{i=1}^N c_i^2 \sigma_i^2}} \quad (3.11)$$

The inverse of Equation 3.11 was used as the objective function to minimize for the calculation of each set of coefficients.

3.2.1 Coefficients for Short T_2

Coefficients, \mathbf{c}^s , for short T_2 selection were calculated by minimizing the inverse of the SNR (Equation 3.11) based on a set of assumptions and constraints.

If we assume the noise variance, σ_i^2 in Equation 3.11, is constant for each image, then k , $\rho(\mathbf{x})$ and σ_i can be incorporated into a constant SNR_0 and Equation 3.11 becomes:

$$\text{SNR}_s = \frac{\text{SNR}_0 \sum_{i=1}^N c_i^s \exp(-t_i/T_{2,0})}{\sqrt{\sum_{i=1}^N (c_i^s)^2}} \quad (3.12)$$

$T_{2,0}$ was defined to be 25 ms (as opposed to 20 ms) to force a broader filter in the short T_2 range of interest.

Four constraints were necessary in the minimization procedure for calculating \mathbf{c}^s :

1. $A^s(T_2) \geq 0$ for $10 \leq T_2 \leq 70$ ms

Force the filter $A^s(T_2)$ to be positive in the range of interest for the short T_2 . Previous to adding this constraint, the algorithm tended to find a minimum where $A^s(T_2)$ fluctuated positive and negative in the range $10 \leq T_2 \leq 70$ ms.

2. $A^s(T_2) \leq \delta$ for $T_2 \geq 80$ ms where $\delta = \max[A_s(T_2)]/100$

This is the key constraint to suppress signal from T_2 outside of the range of interest. Intu-

itively, the magnitude of the filter response for $T_2 > 80$ ms, relative to the filter response for $T_2 = 15$ ms, must be much less than a factor of six, as the area of the medium T_2 component in white matter is approximately six times larger than the area of the short T_2 component. The factor of 100 was chosen to provide greater suppression of the medium T_2 component.

$$3. \sum c^s = 0$$

The filter $A^s(T_2)$ must go to 0 at long T_2 .

$$4. \int A^s dT_2 = 1 \pm 0.01$$

The area under the filter must be near 1 so there is no increase or decrease in I_L^s from the filter.

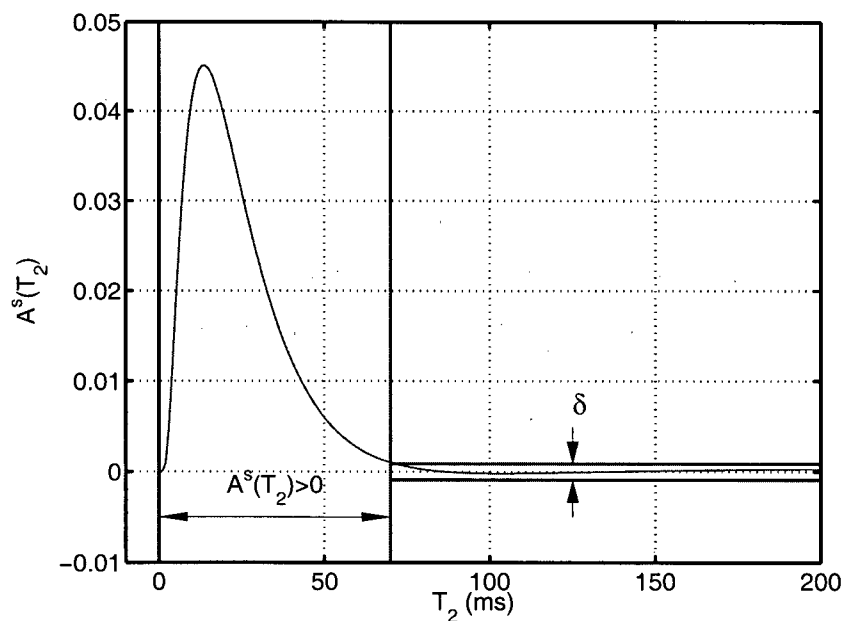


Figure 3.1: Constraints on the short T_2 filter.

The physical interpretation of the constraints are shown in Figure 3.1.

3.2.2 Coefficients for All T_2

Similarly, coefficients to select for $T_2 > 10$ ms, c^a , were calculated by minimizing the inverse of the SNR in Equation 3.11 based on a set of assumptions and constraints.

The function to maximize was:

$$\text{SNR}_a = \frac{\text{SNR}_0 \sum_{i=1}^N c_i^a \exp(-t_i/T_{2,0})}{\sqrt{\sum_{i=1}^N (c_i^a)^2}} \quad (3.13)$$

where $T_{2,0} = 25$ ms.

Two constraints were included in the minimization procedure for calculating c_a :

1. $A^a(T_2) \geq 0$ for $T_2 \geq 10$ ms

Force the filter $A^a(T_2)$ to be positive for T_2 greater than 10 ms.

2. $|A^a(T_2) - M| \leq \delta$ for $T_2 \geq 10$ ms where $M = \max[A^a(T_2)]$, $\delta = M/40$

This will constrain the fluctuations in the filter response to be less than 1/40 for $T_2 > 10$ ms.

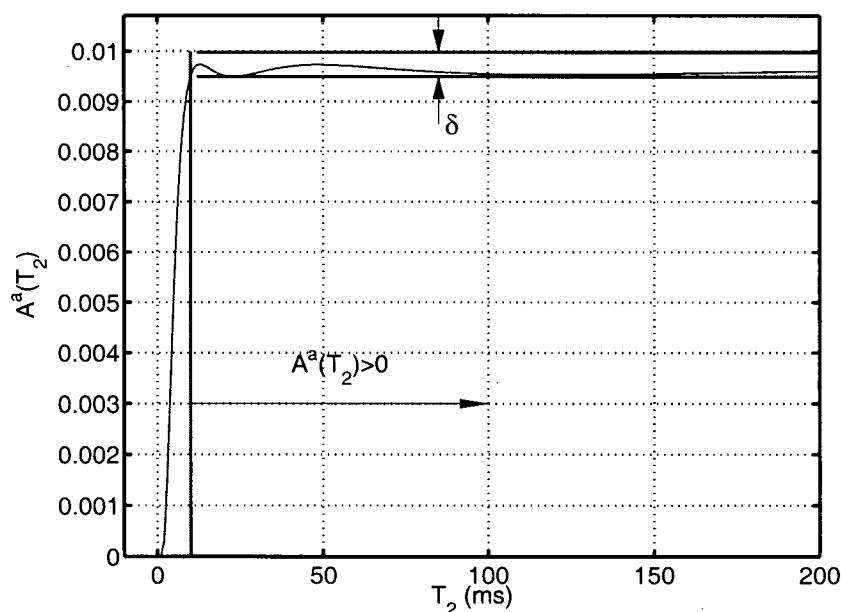


Figure 3.2: Constraints on the “all” T_2 filter.

The physical interpretation of the constraints are shown in Figure 3.2.

3.2.3 Description of the Algorithm

The minimization algorithm used to calculate the coefficients was `fmincon`, a standard Levenburg-Marquardt routine in Matlab (Natick, MA). The short T_2 fraction was the signal calculated as

the linear combination of the short T_2 coefficients with the images divided by the signal calculated from linear combination of the total T_2 coefficients with the images.

The constraints, incorporated into the minimization algorithm, required a T_2 filter be created, at each iteration, based on the current set of coefficients. The requirements placed on the T_2 filter, for both the short and all filters, required a large number of constraints, one for each point in the filter. The δ in the above constraints were set to values consistent with what is known about the relative amplitudes of the peaks in the T_2 distribution. Small δ were tried but the minimization algorithm was not able to find a feasible solution.

3.2.4 Results

The coefficients, \mathbf{c}^s and \mathbf{c}^a calculated based on the minimization procedure above, are shown in Table 3.1. The corresponding filters, $A^s(T_2)$ and $A^a(T_2)$, are shown in Figure 3.3.

t (ms)	\mathbf{c}^s	\mathbf{c}^a	t (ms)	\mathbf{c}^s	\mathbf{c}^a
10	3.0820	4.8727	170	0.0576	-0.4878
20	-0.5698	-5.9451	180	-0.1574	-0.4606
30	-1.8381	-1.3997	190	-0.3481	1.1084
40	-1.9002	1.9780	200	-0.5033	1.4641
50	-1.4213	2.5442	210	-0.6275	-0.0698
60	-0.7650	1.2543	220	-0.6940	-0.1675
70	-0.1330	0.6837	230	-0.7184	-0.1988
80	0.3858	-0.4731	240	-0.6962	0.3600
90	0.7583	-1.3316	250	-0.6253	-0.1289
100	0.9756	-1.4437	260	-0.5100	0.4137
110	1.0576	-0.7389	270	-0.3503	0.3065
120	1.0266	-0.9576	280	-0.1441	0.1169
130	0.9113	-0.0542	290	0.1020	-0.0424
140	0.7384	0.1944	300	0.3769	-0.4811
150	0.5188	0.6518	310	0.6918	-0.7215
160	0.2860	0.2573	320	1.0333	-0.1254

Table 3.1: The coefficients for the linear combination method. Coefficients \mathbf{c}^s were for the short T_2 filter and \mathbf{c}^a were for selecting all T_2 .

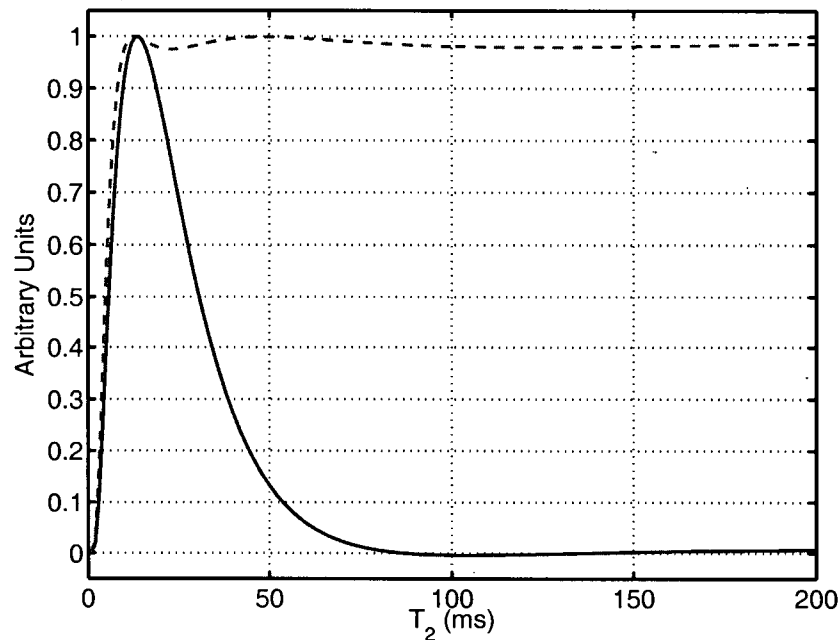


Figure 3.3: T_2 filters for short T_2 components ($A^s(T_2)$, solid) and all T_2 components ($A^a(T_2)$, dashed). The maximum of each curve was normalized to 1 for sake of comparison.

3.2.5 Discussion

Objective Function

The goal of most imaging is to acquire an image with a signal-to-noise ratio as high as possible, to allow accurate interpretation. This goal was used in the calculation of the coefficients to maximize the signal-to-noise ratio of the myelin water selection. Therefore, the objective function, to maximize, was defined as the signal in the resultant linear combination image (numerator of Equation 3.12) divided by the noise amplification (denominator of Equation 3.12). The goal of the algorithm was to maximize the signal of the myelin water, $T_2 \approx 15$ ms, relative to the noise. The variable $T_{2,0}$ was defined slightly longer than that of myelin water to increase the width of the filter $A^s(T_2)$. Larger values of $T_{2,0}$ were tried, but resulted in poor filters $A^s(T_2)$ or large coefficients and therefore increased noise amplification.

Model Independence

The power of the linear combination technique, in addition to greatly reduced processing time, is that the solution does not depend on a particular construction technique. This is in contrast

to NNLS which must construct a solution based on a model. Therefore, the linear combination method does not assume the number of exponentials in the underlying data.

3.3 Linear Combination Simulations

A simulation was created to confirm the mean and standard deviation of the MWF calculated by linear combination were similar to the mean and standard deviation of the MWF calculated by NNLS.

3.3.1 Model

A white matter model was created based on the equation:

$$I_i = \rho [f^s \exp(-t_i/T_2^s) + f^m \exp(-t_i/T_2^m)] \quad (3.14)$$

where $\rho = 1000$ was the proton density, $T_2^s = 20$ ms for the short component, $f^m = 1 - f^s$ and $T_2^m = 80$ ms were the fraction and T_2 of the medium component. Seven values for f^s were used ($f^s = 0, 0.01, 0.02, 0.05, 0.10, 0.20, 0.30$), to test the linear combination method over a range of typical myelin water fractions. One thousand realizations of Gaussian noise (SNR = 100) were added in quadrature to the model, and the estimated short fraction \tilde{f}^s was calculated by both the linear combination and the NNLS algorithms. Other parameters included $N = 32$ echoes, $t = 10, 20, \dots, 320$ ms and TR was considered infinite.

The estimated short amplitude from both techniques was compared to the true (known) short amplitude by calculating $\tilde{f}^s - f^s$. The estimated short fraction \tilde{f}^s was compared to the true fraction f^s by both a t-test (assumes the data comes from a normally distributed population) and a Wilcoxon signed rank test (no underlying assumption of distribution). A Lilliefors modification of the Kolmogorov-Smirnov test was used to determine whether the resulting \tilde{f}^s were normally distributed.

3.3.2 Results and Discussion

The mean short T_2 fractions calculated by both methods agreed with the true short fraction (Figure 3.4), but the only solution \tilde{f}^s statistically equal to the truth was for the NNLS solution

with the true $f^s = 0.20$. The mean short T_2 fraction was within 0.02 of the true fraction. The short T_2 fractions calculated by the linear combination method were normally distributed for each of the true fractions, but only when $f^s \geq 0.10$ were the NNLS results normally distributed.

On average the linear combination method calculated approximately 10,000 solutions per second and the regularized NNLS method calculated one solution every two seconds.

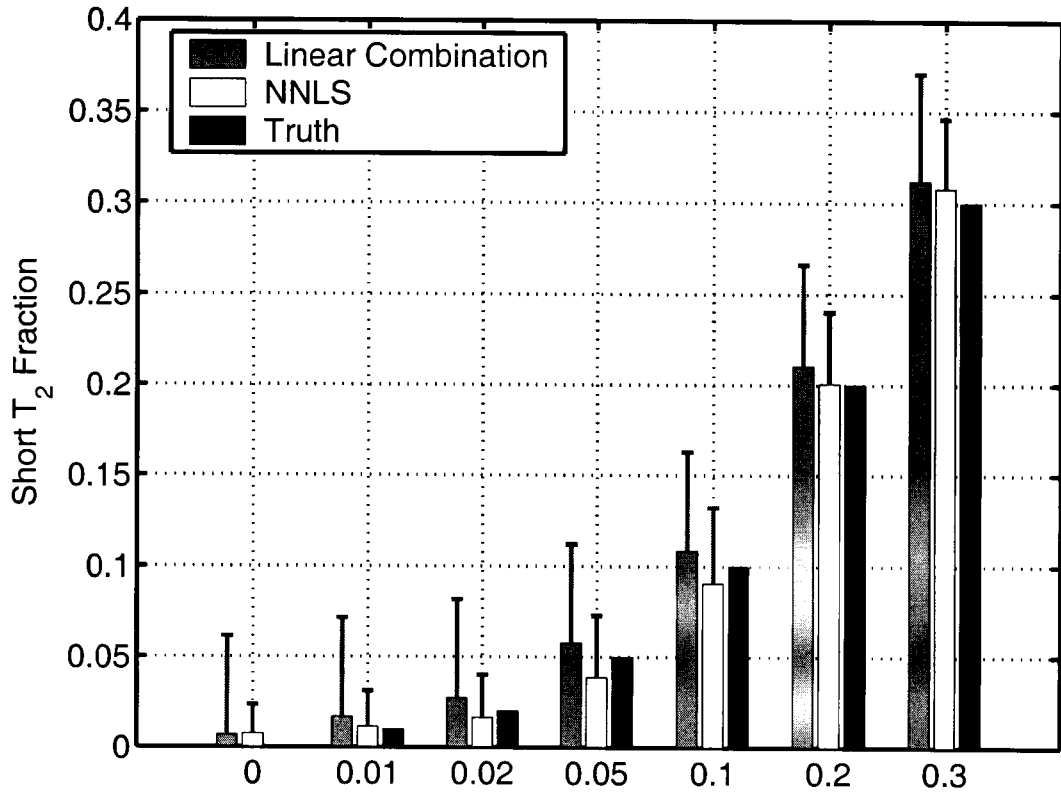


Figure 3.4: Mean short fraction over 1,000 realizations of quadrature noise (standard deviation bars) calculated by the linear combination method (left bar), NNLS (middle bar) and the true short fraction (right bar).

3.3.3 Conclusions

The simulations were used to determine the accuracy and precision of the myelin water fraction calculated from the linear combination method to that calculated by the NNLS method. The NNLS method is the current standard method to estimate the myelin water fraction, therefore, if the linear combination method is as accurate, it would be a useful technique for fast myelin water fraction estimation. The mean myelin water fraction from the linear combination had a

small positive bias of at most 0.012 compared to the truth. The small positive bias, near zero myelin water fraction, could be attributed to the Rician distributed noise. The linear combination method calculated approximately 10,000 solutions per second, compared to one solution every two seconds for the NNLS method. The linear combination method was shown to be a very fast and accurate method for estimating the myelin water fraction from a multi-echo decay curve.

3.4 Selectivity of Mono-Exponential Phantoms

The selectivity of the short T_2 coefficients, in Table 3.1, was analyzed. The short T_2 image was calculated as the linear combination of the multi-echo data to show the selectivity of the short T_2 phantoms and the suppression of the longer T_2 phantoms.

3.4.1 Methods

The phantoms (Section 1.8) were scanned using the 32 echo MESE_o pulse sequence (Section 1.6.2). The images were combined linearly using the short T_2 filter weights defined in Table 3.1.

3.4.2 Results and Discussion

Excellent suppression of the longer T_2 phantoms was found as shown in Figure 3.5. The T_2 of the nine phantoms surrounding the water bottle were (clock-wise starting from bottom left) $T_2 = 264, 101, 25, 23, 97, 363, 157, 77, 23$ ms.

The short T_2 map was analyzed quantitatively by calculating the mean and standard deviation in each of the nine nickel/agarose phantoms, the water bottle and the air (Table 3.2). The mean signal of the short T_2 phantoms in the short T_2 map was at least fifteen times higher than the mean signal of the longer T_2 phantoms. The standard deviation measured from the selected regions was comparable to the standard deviation of the suppressed regions. There was a small increase in the magnitude of the signal from phantoms with T_2 of approximately 100 ms compared to the phantoms with T_2 greater than 200 ms. This was not unexpected as the T_2 filter is close to zero near 100 ms, but not zero. Overall the quantitative selectivity of the short T_2 phantoms was excellent.

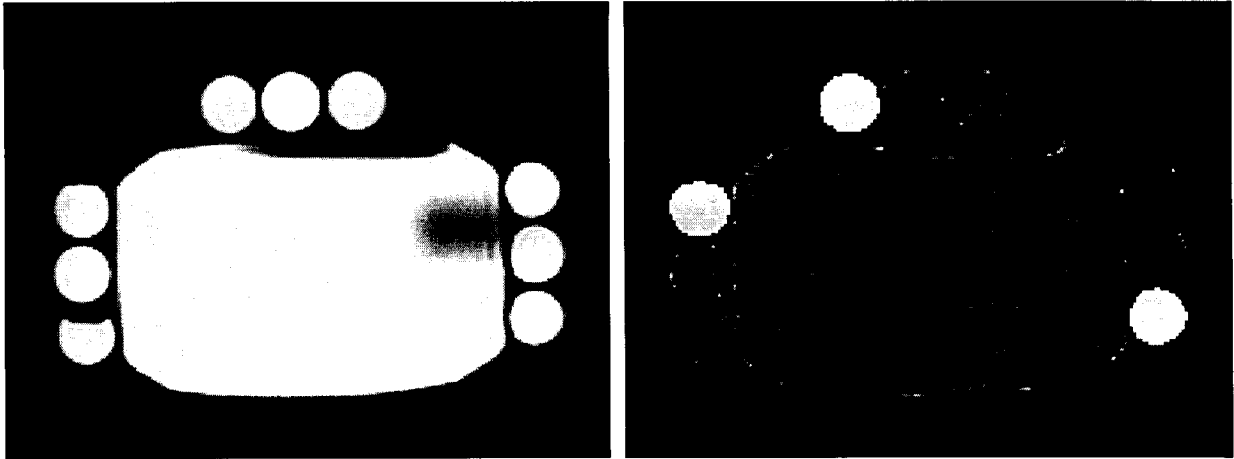


Figure 3.5: MRI image (TE =10 ms, left) of nine nickel/agarose phantoms (and the large water bottle) and the short T_2 image (right) based on the linear combination of the original 32 spin-echo images.

Region	Mean Signal	T_2 (ms)
1	-0.3 (17.1)	264
2	-12.3 (34.6)	101
3	470.9 (30.8)	25
4	433.5 (19.4)	23
5	-9.9 (15.1)	97
6	-2.7 (15.0)	363
7	-28.9 (22.6)	157
8	-29.1 (20.0)	77
9	547.1 (28.8)	23
Outside 1	0.7 (10.4)	-
Outside 2	-1.4 (10.5)	-
Outside 3	0.8 (10.5)	-
Water 1	6.8 (15.9)	2000
Water 2	4.3 (16.6)	2000
Water 3	8.0 (13.6)	2000

Table 3.2: The mean and standard deviation of the signal in the short T_2 image (right image of Figure 3.5). Regions one through nine are the phantoms around the outside and are numbered clock-wise starting in the bottom left hand corner. The three regions labeled “Outside” are regions drawn in the noise area. The three regions labeled “Water” were drawn in the large water phantom.

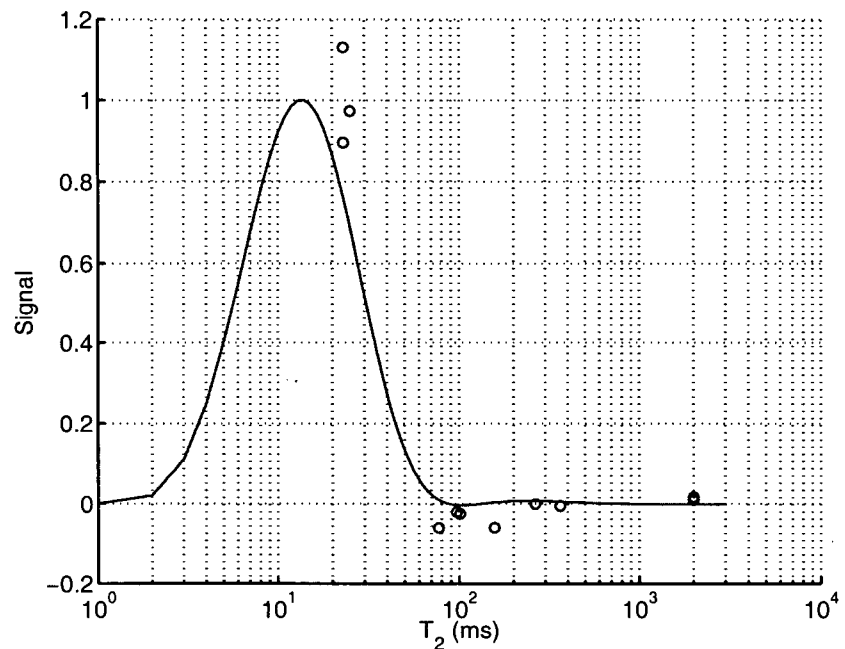


Figure 3.6: The mean signal from each phantom plotted against the T_2 of the phantom overlaid on the short T_2 filter.

3.4.3 Conclusions

The selectivity of the short T_2 phantoms, from the linear combination method was excellent as was the suppression of the long T_2 phantoms. For mono-exponential phantoms, the filter behaved as well as expected.

3.5 *In Vivo* Myelin Water Fraction: NNLS vs. T_2 Filter

The selectivity and suppression of mono-exponential phantoms was excellent. In this section, the linear combination method is applied to a multi- T_2 component system. The short T_2 fraction calculated by the T_2 filter method was compared to those calculated by NNLS (Section 1.7.1.2). Normal volunteers were scanned using the optimized multi-echo pulse sequence (Section 1.6.2) and the myelin water maps were calculated with each method and compared.

3.5.1 Methods

Five normal volunteers were scanned with the 32 echo MESE_o pulse sequence (Section 1.6.2). The axial slice was selected to intersect the corpus callosum. Each of the five scans were processed by the linear combination method and NNLS method. Six regions (each left and right) were selected (on the TE = 80 ms image for each scan): cortical gray matter, frontal white matter, genu of the corpus callosum, internal capsules, putamen and posterior white matter. The mean and standard deviation of the calculated short T₂ fractions from each technique were compared with a Wilcoxon signed rank test. A Bland and Altman [69, 70] plot, used to compare two measurement techniques, was used to compare the myelin water fraction calculated by the linear combination method to that from NNLS. Given a pair of data, d_i^1 calculated by measurement technique 1, and d_i^2 calculated by measurement technique 2, Bland and Altman plotted the difference of the points $d_i^1 - d_i^2$, versus the mean of the points $(d_i^1 + d_i^2)/2$ for all i .

3.5.2 Scan Results

Myelin water maps were calculated by each technique and are shown in Figure 3.7. There was very good similarity between the two maps. Note the short T₂ phantoms selected on each side of the head. The internal capsules, within the mid portion of the brain, were previously shown to have a higher myelin water fraction than most other regions of the brain. This region, in the map from the linear combination method, shows an isointensity to white matter regions close by. This is likely due to an increased T₂ in the short compartment. An increase in the short T₂ compartment will lead to a decreased myelin water fraction because of the shape of the filter.

The mean and standard deviation of the myelin water fraction, for each region, calculated by the two techniques is shown in Figure 3.8.

A Bland-Altman plot was calculated for the white matter and gray matter regions (Figure 3.9). White matter had 87.5% of the differences within 1.96σ and a small bias toward small fractions calculated by NNLS. Gray matter had 90% of the differences within 1.96σ and a slight bias toward larger fractions calculated by NNLS. For each of the plots there was no significant correlation between difference and mean.

The standard deviation was lower for the linear combination method in 85% of the white matter regions (over volunteers and regions). For gray matter, the standard deviation was lower

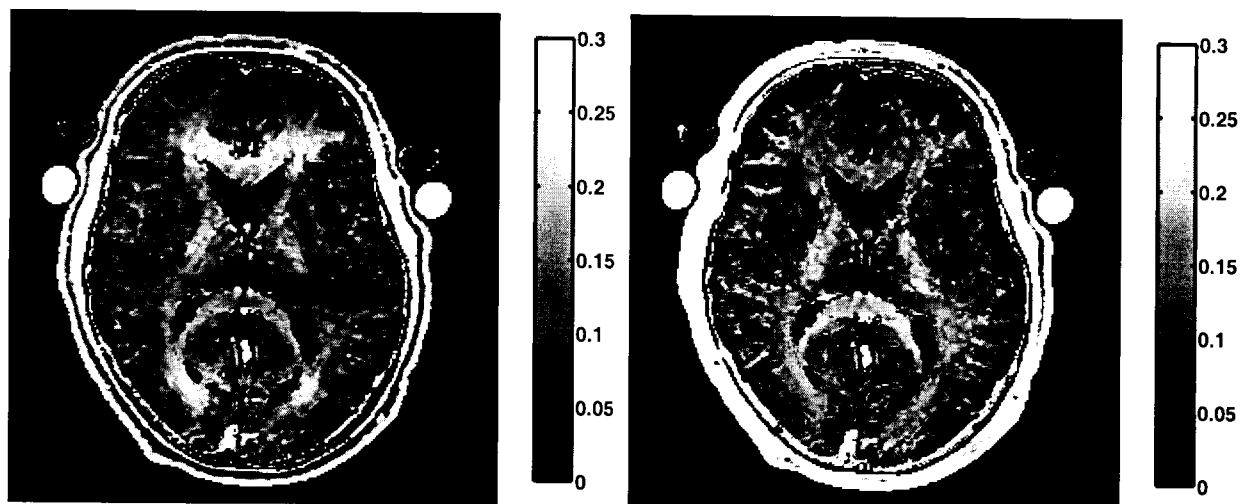


Figure 3.7: Myelin water maps calculated by the linear combination method (left) and from the non-negative least squares solution (right). Data collected from a 32 echo ($TE = 10$ ms), single slice optimized pulse sequence. Bright circles were the same short T_2 nickel/agarose phantoms as shown in Figure 3.5

in 17.5% of the regions for the linear combination method.

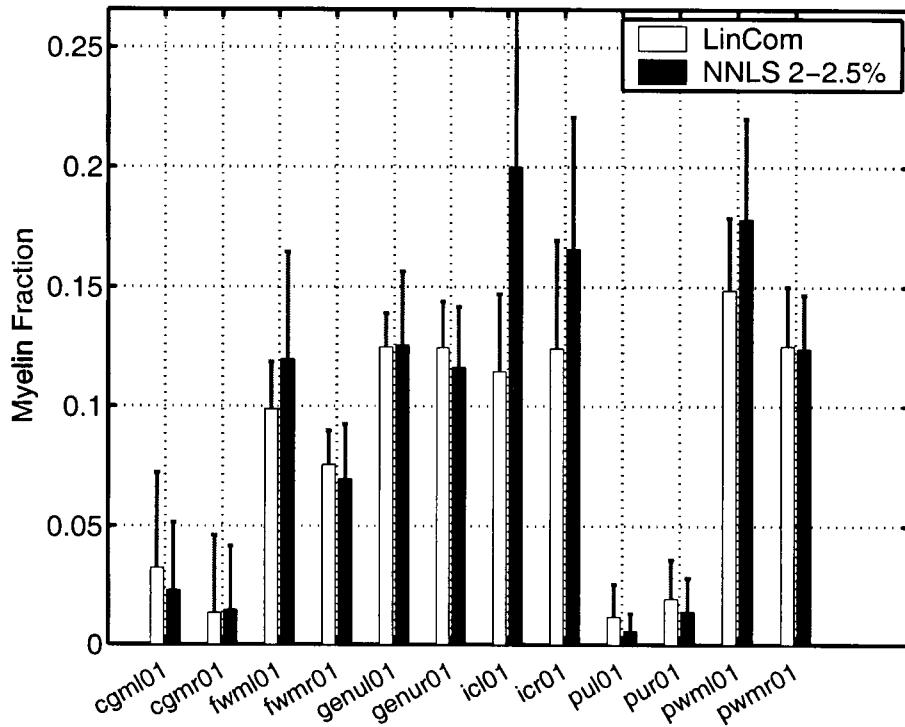


Figure 3.8: Myelin water fractions calculated per region from the linear combination method (light bars) and NNLS (dark bars). (Standard deviation shown as whiskers.) Regions were drawn on the left (l) and right (r) sides of: cortical gray matter (cgm), frontal white matter (fwm), genu of the corpus callosum (genu), internal capsules (ic), putamen (pu), and posterior white matter (pwm).

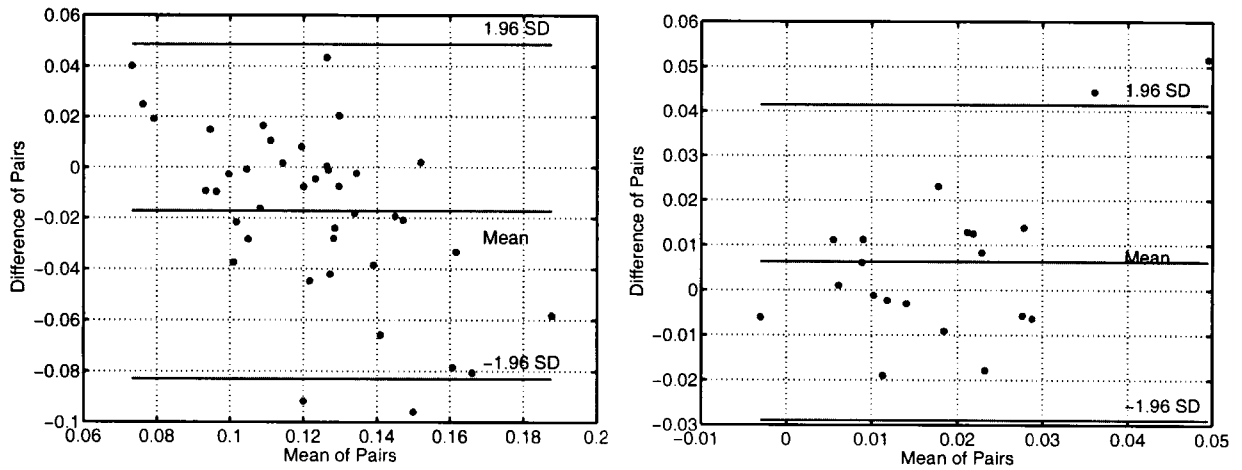


Figure 3.9: Bland-Altman plots for white matter regions (left) and gray matter regions (right). Most data lay within one standard deviation and little bias as a function of the size of the myelin water fractions.

3.5.3 Conclusions

Myelin water fractions calculated from linear combinations of T_2 decay data is extremely fast and does not rely on assumptions about any underlying models (compared to traditional methods). Myelin water maps were very similar and showed the myelin water fraction even into the white matter folds of the cortex.

3.6 Calculation of Coefficients by Matrix Inversion

In 1982, Macovski [63] defined a method to calculate coefficients for T_2 selection using a matrix inversion technique. Matrix inversion does not allow constraints on the coefficients nor on the filter. Therefore, the expectation is the filter will be very broad compared to the filters defined in Section 3.2.

In this section, I calculated coefficients to select for short T_2 (\mathbf{c}^s , $10 \leq T_2 \leq 50$ ms), medium T_2 (\mathbf{c}^m , $70 \leq T_2 \leq 120$ ms), and long T_2 (\mathbf{c}^l , $T_2 > 2000$ ms). Each set of coefficients was applied to *in vivo* data and the results were discussed and compared to my technique.

3.6.1 Calculation of Coefficients

A matrix inversion problem was defined, $I = FL$, where I was the vector of image data, F was the matrix of exponential kernels $[\exp(-t_i/T_{2,j})]$, and L was the amplitudes which correspond to the T_2 . The coefficients were the rows of F^{-1} where $F_{ij} = [\exp(-t_i/T_{2,j})]$ for $t = 10, 20, \dots, 320$ ms and $T_2 = 20, 80, 3000$ ms.

The coefficients calculated are shown in Table 3.3. The coefficients for the short T_2 , \mathbf{c}^s , follow a similar trend of positive in the early echoes, then negative, and then positive.

The T_2 filters, $f(T_2)$, shown in Figure 3.3, were constructed by calculating the filter $f^t(T_2) = (F^{-1})_t \exp(-t/T_2)$. The short T_2 filter, top left filter of Figure 3.10, should be compared with the short T_2 filter in Figure 3.3 (solid line).

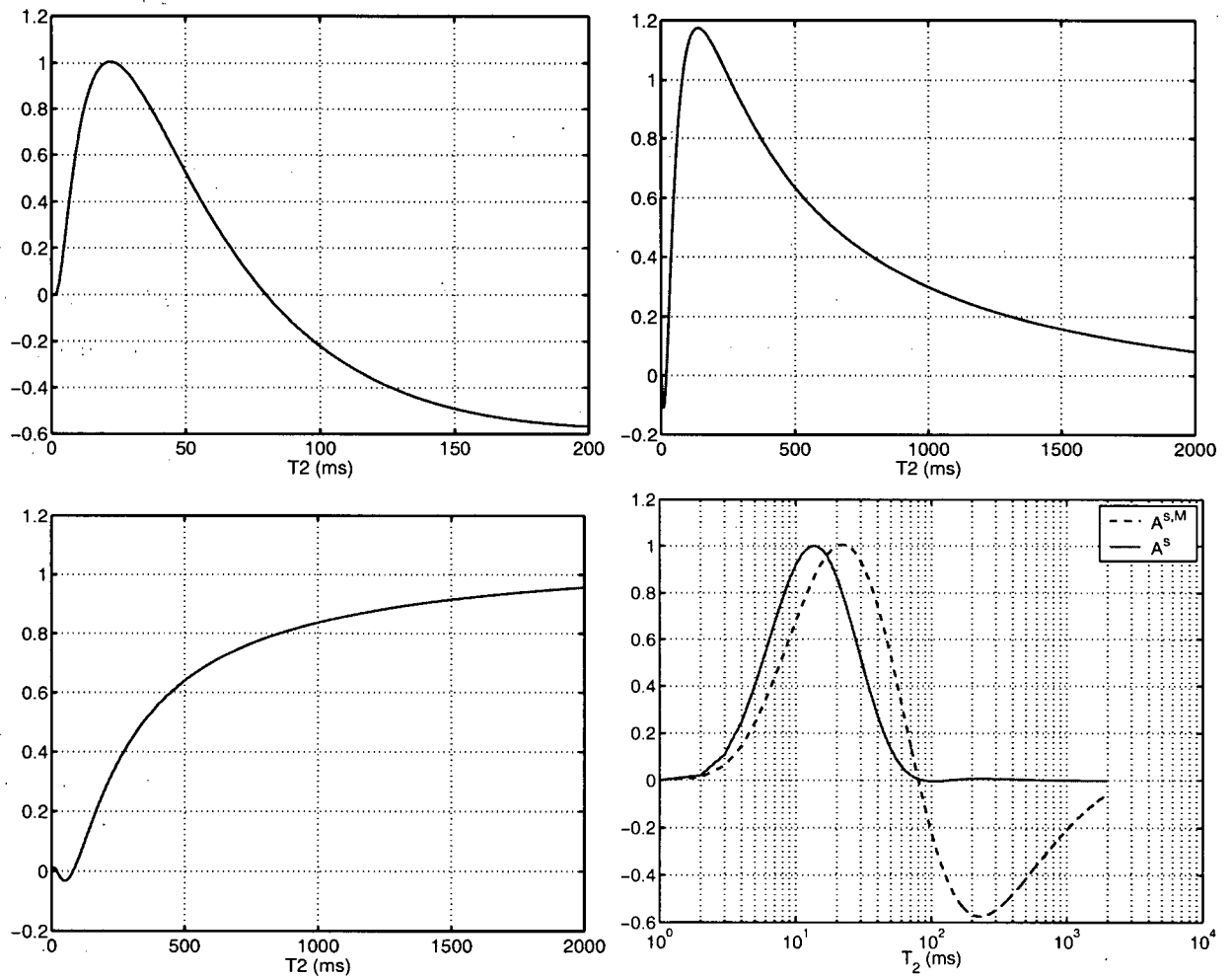


Figure 3.10: The filters calculated from the matrix inversion technique to calculate coefficients. Short T_2 filter (top left), medium T_2 filter (top right) and the long T_2 filter (bottom left). The short T_2 filter calculated by the inversion method ($A^{s,M}(T_2)$, dashed line) compared to the short T_2 filter ($A^s(T_2)$, solid line) calculated by the non-linear method (bottom right, plotted on a log scale to visualize the whole filter).

t (ms)	c^s	c^m	c^l	t (ms)	c^s	c^m	c^l
10	1.72393	-0.40229	0.04356	170	0.01337	-0.07379	0.05064
20	0.49791	0.08544	-0.01328	180	0.05159	-0.09854	0.05469
30	-0.16482	0.32873	-0.03897	190	0.08533	-0.12034	0.05823
40	-0.49547	0.42999	-0.04681	200	0.11505	-0.13950	0.06134
50	-0.63314	0.45058	-0.04474	210	0.14120	-0.15632	0.06404
60	-0.66120	0.42708	-0.03749	220	0.16418	-0.17107	0.06640
70	-0.62934	0.38113	-0.02781	230	0.18434	-0.18398	0.06845
80	-0.56695	0.32531	-0.01728	240	0.20202	-0.19527	0.07022
90	-0.49114	0.26685	-0.00681	250	0.21749	-0.20513	0.07176
100	-0.41172	0.20972	0.00314	260	0.23102	-0.21372	0.07308
110	-0.33408	0.15599	0.01233	270	0.24283	-0.22120	0.07421
120	-0.26105	0.10661	0.02068	280	0.25313	-0.22768	0.07518
130	-0.19391	0.06188	0.02819	290	0.26209	-0.23330	0.07601
140	-0.13308	0.02176	0.03487	300	0.26987	-0.23815	0.07670
150	-0.07849	-0.01400	0.04080	310	0.27660	-0.24233	0.07728
160	-0.02982	-0.04573	0.04603	320	0.28242	-0.24591	0.07776

Table 3.3: The coefficients for the short, medium and long T_2 selection based on the matrix inversion method of calculation.

3.6.2 Results and Discussion

The short T_2 filter (Figure 3.10, top left) is a very broad peak centered on $T_2 = 22$ ms and crosses 0 at $T_2 = 80$ ms. The primary problem with the short T_2 filter is that it extends below 0. The filter which extends below 0 will decrease I_L (the myelin water contribution) if the voxel has contributions from $T_2 > 80$ ms. If the system has only mono-exponential contributions for all voxels, then this is not a problem, but if multiple T_2 compartments are possible per voxel, then this could lead to a mis-interpretation of water compartments $10 \leq T_2 \leq 80$ ms, as the myelin water will appear lower even though the short T_2 was not lower. The short T_2 filter, calculated from this method, is compared to the short T_2 filter, $A^s(T_2)$ calculated in Section 3.2.4 and is shown in Figure 3.10, bottom right. The filters are plotted on a log-scale to visualize the whole range of the filter. The selectivity of the short T_2 filter is very effective if objects in the image are all mono-exponential. In this case, objects with a short T_2 near 20 ms will be selected and objects with a $T_2 > 80$ ms will be negative.

The medium T_2 filter (Figure 3.10, top right), and long T_2 filter (Figure 3.10, bottom), both have a very broad selection.

T_2 Selected Images

The coefficients calculated in Section 3.6.1, were applied to a multi-echo MRI dataset. The short T_2 (top left), medium T_2 (top right), and long T_2 filtered images (bottom left) are shown in Figure 3.11. The image at the bottom right of Figure 3.11 is the myelin water fraction calculated as the ratio of the short T_2 image to the sum of the short T_2 , medium T_2 , and long T_2 images. The myelin water map has very sharp edges but has a darker signal in the posterior white matter.

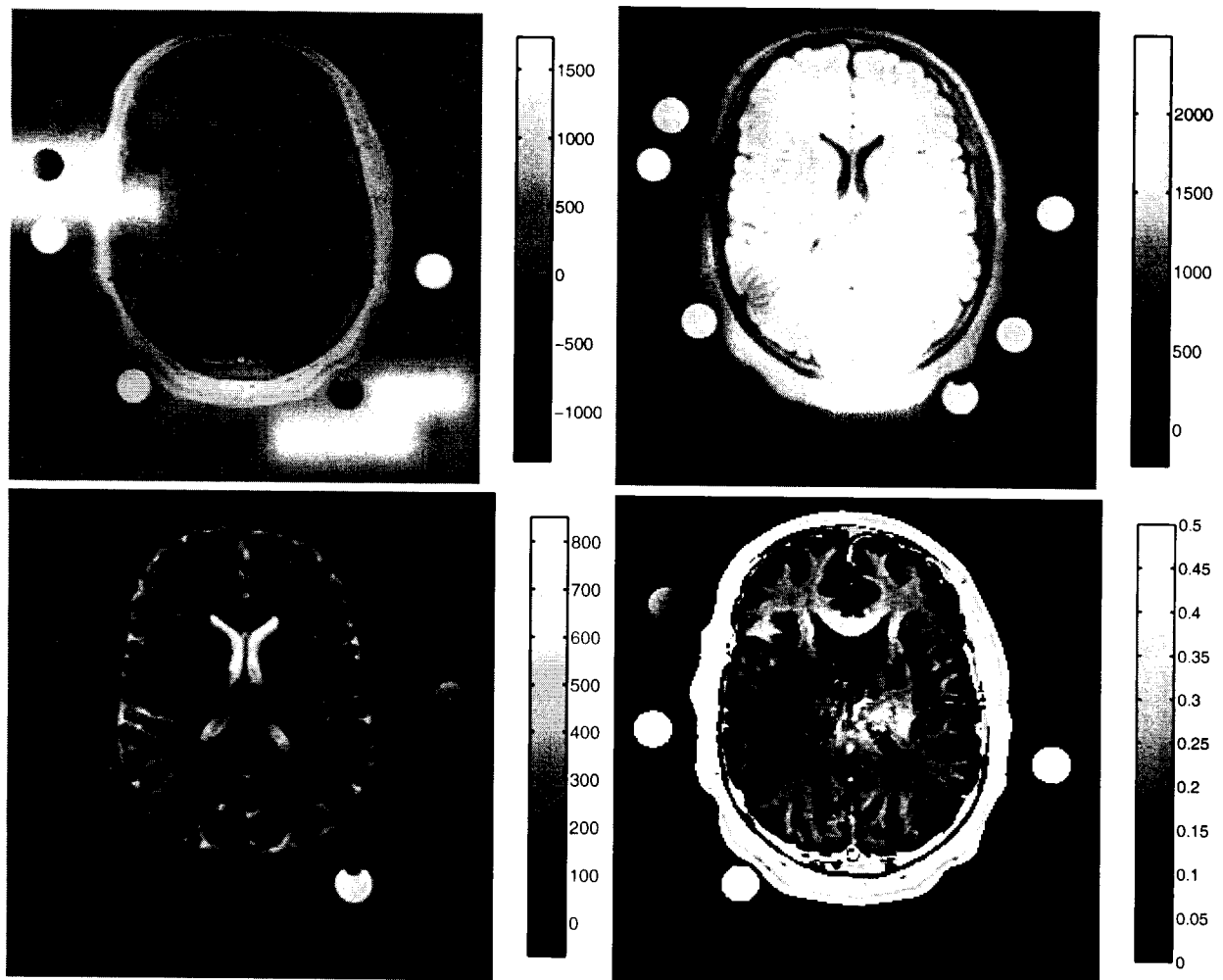


Figure 3.11: Filtered images of the short T_2 (top left), medium T_2 (top right), long T_2 (bottom left) and the myelin water fraction (ratio of the short T_2 to the sum of the three, bottom right).

3.6.3 Conclusions

The method of calculating the coefficients by matrix inversion is extremely fast, but lacks the ability to apply constraints on the coefficients or filter. The filter would be appropriate for use to select T_2 when the underlying data are mono-exponential, but would not be appropriate when the underlying data are multi-exponential as is the case for *in vivo* brain.

3.7 Calculation of Coefficients by Backus-Gilbert

The Backus-Gilbert method is a linear algorithm to calculate the coefficients, \mathbf{c} , which minimize a misfit. The misfit function incorporates a desired filter and the filter defined by \mathbf{c} . The Backus-Gilbert method is described further and three sets of coefficients are calculated and the corresponding filters are compared to the filter $A^s(T_2)$ as defined in Section 3.2.4.

3.7.1 Calculation of Coefficients

The standard misfit function, to minimize, includes two terms: the first term is an error term between the constructed filter (“averaging function”) and a target filter and the second term is a noise amplification term. The two terms are linearly combined with a trade-off parameter, θ , which can be adjusted to arbitrarily weight one term more than another. The coefficients, \mathbf{c} , were calculated to minimize:

$$\phi = \cos(\theta) \int_0^\infty [A(T_2, T_{2,0}) - \Pi(T_2, T_{2,min}, T_{2,max})]^2 dT_2 + \sin(\theta) \sum_{i=1}^N c_i^2 \sigma_i^2 \quad (3.15)$$

where θ is the trade-off parameter, $A(T_2, T_{2,0}) = \sum_{i=1}^N c_i \exp(-TE/T_{2,0})$, and $\Pi(T_2, T_{2,min}, T_{2,max})$ is the boxcar function defined as:

$$\Pi(T_2, T_{2,min}, T_{2,max}) = \begin{cases} 1 & \text{if } T_{2,min} \leq T_2 \leq T_{2,max} \\ 0 & \text{otherwise} \end{cases} \quad (3.16)$$

The coefficients which minimize Equation 3.15 are found by calculating the partial derivative of ϕ with respect to each coefficient c_i , and setting the derivative to zero:

$$\frac{\partial}{\partial c_i} \phi = 0 \quad i = 1 \dots N \quad (3.17)$$

The linear set of N equations, defined by Equation 3.17, is then solved for \mathbf{c} .

3.7.2 Results and Discussion

Three sets of coefficients were calculated using the Backus-Gilbert algorithm and are shown in Table 3.4. The first set of coefficients, \mathbf{c}^{bg1} , had a higher trade-off parameter, the second set, \mathbf{c}^{bg2} , had a lower trade-off parameter and third set, \mathbf{c}^{bg3} , was designed to have a similar noise amplification factor as \mathbf{c}^s . The short T_2 filters, corresponding to each set of coefficients, is shown in Figure 3.13, along with the filter created using the algorithm introduced in this paper.

All four filters had a similar selectivity in the T_2 of interest. The differences in the filter were around $T_2 = 500$ ms. The filters, corresponding to the coefficients \mathbf{c}^{bg1} and \mathbf{c}^{bg3} , deviated from 0 much more than the filters defined by the coefficients calculated in this paper. This deviation would introduce signal in I_L from water compartments with $100 \leq T_2 \leq 1000$ ms. The signal from $T_2 > 100$ ms is undesirable as the filter was designed for short T_2 . The filter, corresponding to coefficients, \mathbf{c}^{bg2} , had a similar response to the filter defined by the coefficients calculated in this paper, but the noise amplification ($\sum_{i=1}^N c_i^2$) was 113.4 for, \mathbf{c}^{bg2} and was 29.8 for \mathbf{c}^s .

t (ms)	\mathbf{c}^{bg1}	\mathbf{c}^{bg2}	\mathbf{c}^{bg3}	\mathbf{c}^{c^j}	t (ms)	\mathbf{c}^{bg1}	\mathbf{c}^{bg2}	\mathbf{c}^{bg3}	\mathbf{c}^{c^j}
10	3.3504	6.8123	4.0186	3.0820	170	0.1805	-0.1123	0.1191	0.0576
20	-1.6519	-7.5974	-2.3374	-0.5698	180	0.1162	-0.2007	0.0372	-0.1574
30	-1.6415	-2.2797	-2.0012	-1.8381	190	0.0558	-0.2456	-0.0350	-0.3481
40	-1.1697	-0.1489	-1.2865	-1.9002	200	0.0006	-0.3335	-0.0984	-0.5033
50	-0.7032	0.5016	-0.6791	-1.4213	210	-0.0470	-0.3556	-0.1489	-0.6275
60	-0.3204	0.6398	-0.2204	-0.7650	220	-0.0873	-0.3552	-0.1872	-0.6940
70	-0.0287	0.6525	0.1119	-0.1330	230	-0.1196	-0.3735	-0.2113	-0.7184
80	0.1796	0.6430	0.3350	0.3858	240	-0.1420	-0.3452	-0.2212	-0.6962
90	0.3183	0.5675	0.4668	0.7583	250	-0.1561	-0.2870	-0.2187	-0.6253
100	0.3985	0.5403	0.5312	0.9756	260	-0.1611	-0.2300	-0.2021	-0.5100
110	0.4340	0.4623	0.5414	1.0576	270	-0.1575	-0.1456	-0.1741	-0.3503
120	0.4337	0.3956	0.5123	1.0266	280	-0.1456	-0.0473	-0.1314	-0.1441
130	0.4088	0.2962	0.4564	0.9113	290	-0.1259	0.0793	-0.0800	0.1020
140	0.3642	0.2009	0.3812	0.7384	300	-0.0980	0.2389	-0.0171	0.3769
150	0.3078	0.1028	0.2950	0.5188	310	-0.0634	0.3758	0.0556	0.6918
160	0.2455	-0.0174	0.2066	0.2860	320	-0.0228	0.5630	0.1385	1.0333

Table 3.4: Coefficients calculated by the Backus-Gilbert method with with a different set of trade-off parameters and, therefore, properties. Coefficients calculated by the method defined in this thesis, \mathbf{c}^s , are shown for reference.

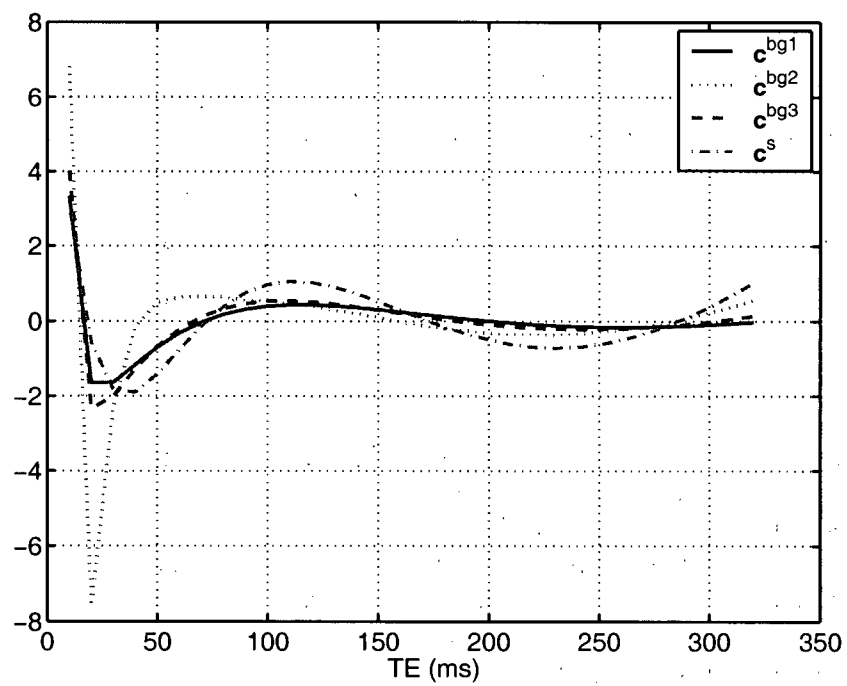


Figure 3.12: Plot of the coefficients calculated from the Backus-Gilbert technique. Coefficients, c^s , calculated in Section 3.2 are shown for reference.

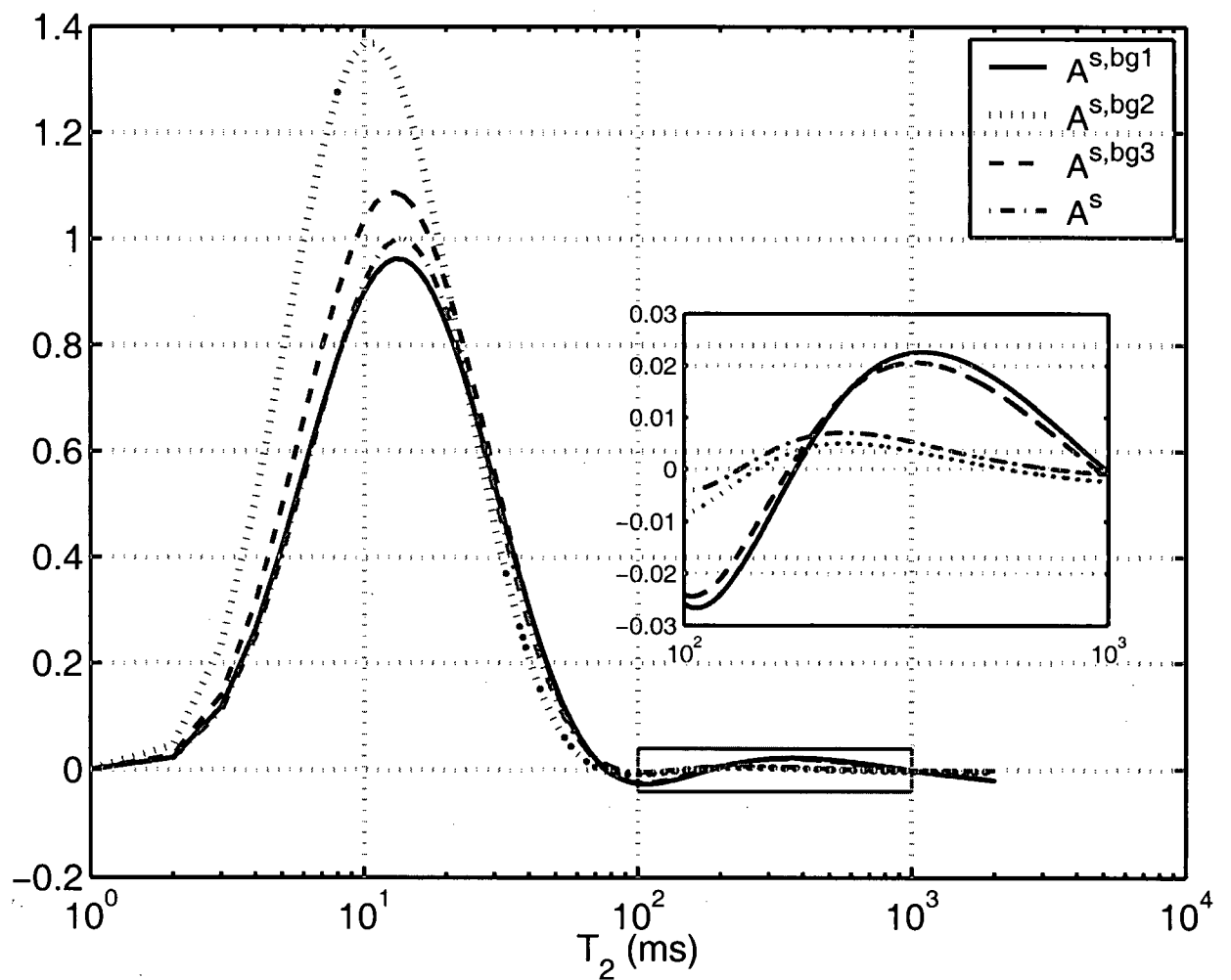


Figure 3.13: The filters calculated from the Backus-Gilbert technique. Filter, $A^s(T_2)$, calculated based on the coefficients c^s , is shown for reference.

3.7.3 Conclusions

Several sets of coefficients were calculated using the Backus-Gilbert method. The coefficients, and corresponding filters, were compared to those calculated by the method in Section 3.2. The filter, $A^s(T_2)$, resulted in a smaller contribution for $T_2 > 100$ ms and a small noise amplification. Better filters can be created when non-linear constraints can be used.

3.8 Optimal Echo Times

Coefficients defined in the previous sections were specific to 32 echoes spaced 10 ms apart as most data, to date, were collected using an optimized, multi-echo sequence with those parameters. Both sets of parameters, number of echoes and the echo spacing, can be varied and a different set of parameters may result in a better filter for the short T_2 .

Two sets of experiments were done to determine the quality of the short T_2 as a function of the number of echoes and the echo spacing. First, coefficients were calculated for equally spaced echoes, and second, coefficients were calculated where the echo spacing was allowed to vary. A set of measures was defined to facilitate the comparison.

3.8.1 Filter Measures

A set of measures, calculated from the T_2 filters, were defined to allow comparison as the number of echoes and echo spacing were allowed to vary. The goal of the measures was to quantify the width of the filter for $10 \leq T_2 \leq 50$ ms and the T_2 at which the filter reaches 1/100 of the filter maximum. The filter is defined as $A(T_2) = \sum_{i=1}^N c_i \exp(-t_i/T_2)$, where N is the number of echoes.

The goal of the filter is to be as wide as possible for $10 \leq T_2 \leq 50$ ms and near zero for $T_2 > 80$ ms. Figure 3.14 shows a short T_2 filter. Therefore, the measure of the goodness of a filter is based on the full width at half the maximum (FWHM), which should be as wide as possible and the T_2 that the curve comes down to 1/100 of the maximum height of the curve (full width at 1/100 max [FW100M]). The FW100M is important as the medium T_2 peak around 80 ms is at least $6\times$ larger than the peak around 20 ms. The FW100M measure is less important as it is determined, in part, by the constraint in the algorithm.

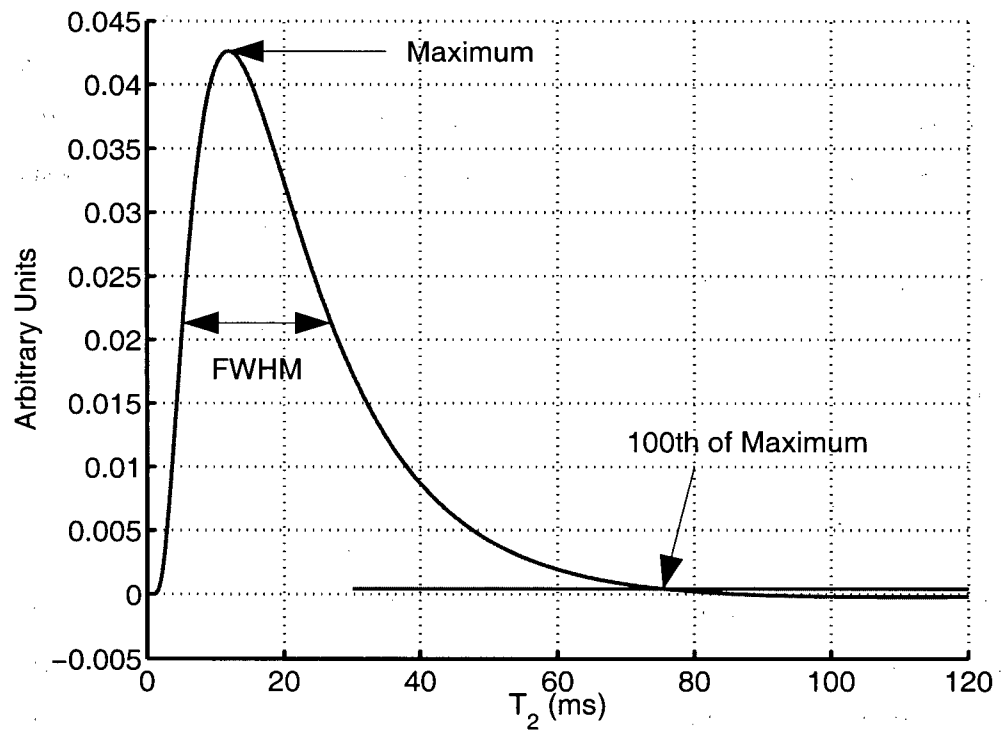


Figure 3.14: The measures of the effectiveness of a short T_2 filter. The full width at half the maximum should be as large as possible and the T_2 where the filter reaches 1/100 of the maximum should be less than $T_2 = 80$ ms and greater than $T_2 = 50$ ms.

3.8.2 Equally Spaced Echoes

The number of echoes is expected to influence the quality of the filter. Therefore, the calculation of the coefficients was re-run for $N = 1$ to $N = 32$ equally spaced echoes. The short T_2 filter is analyzed for each N and compared based on measures defined below.

3.8.2.1 Methods

For the case of equally spaced echoes, the echo spacing, Δt , was allowed to vary along the coefficients. The objective function used was the same as the one defined previously. The inverse of the objective function was defined as:

$$\max_{c, \Delta t} \frac{\sum_{i=1}^N c_i \exp(-t_i/25)}{\sqrt{\sum_{i=1}^N \sigma_i^2 c_i^2}} \quad (3.18)$$

with constraints $-2 \leq c_i \leq 2$ for $i = 1 \dots N$, $10 \leq \Delta t \leq 1000$ ms, and $t = \Delta t, 2\Delta t, \dots, N\Delta t$. The constraints on c_i were defined to constrain the noise amplification $\sum_{i=1}^N \sigma_i^2 c_i^2$.

3.8.2.2 Results and Discussion

The echo spacing was allowed to vary to determine the best set of equally spaced echo times. The constraints on the echo spacing were implemented to be within a realistic range. The lower bound was set to be the minimum allowed by the MESE_o sequence. The maximum echo spacing was defined but not relevant as the minimization procedure used the minimum echo spacing.

The coefficients were calculated given the number of echoes from $N = 1$ to $N = 32$ and are shown in Figure 3.15. Coefficients for one and two echoes did not produce an appropriate short T_2 filter. Coefficients of three or more echoes were very similar. The first coefficient was positive, the following echoes were negative up to the coefficient that corresponded to $TE \approx 80$ ms, and the following coefficients oscillated positive and negative.

The top plot of Figure 3.16 shows the width of the FWHM of $A^s(T_2)$. The width is relatively constant from 4 echoes to 19 echoes. When more than 19 echoes are linearly combined, the width of the filter increases linearly with the number of echoes. Therefore, if having fewer echoes is more important, then one could use 5 echoes with little degradation of the filter.

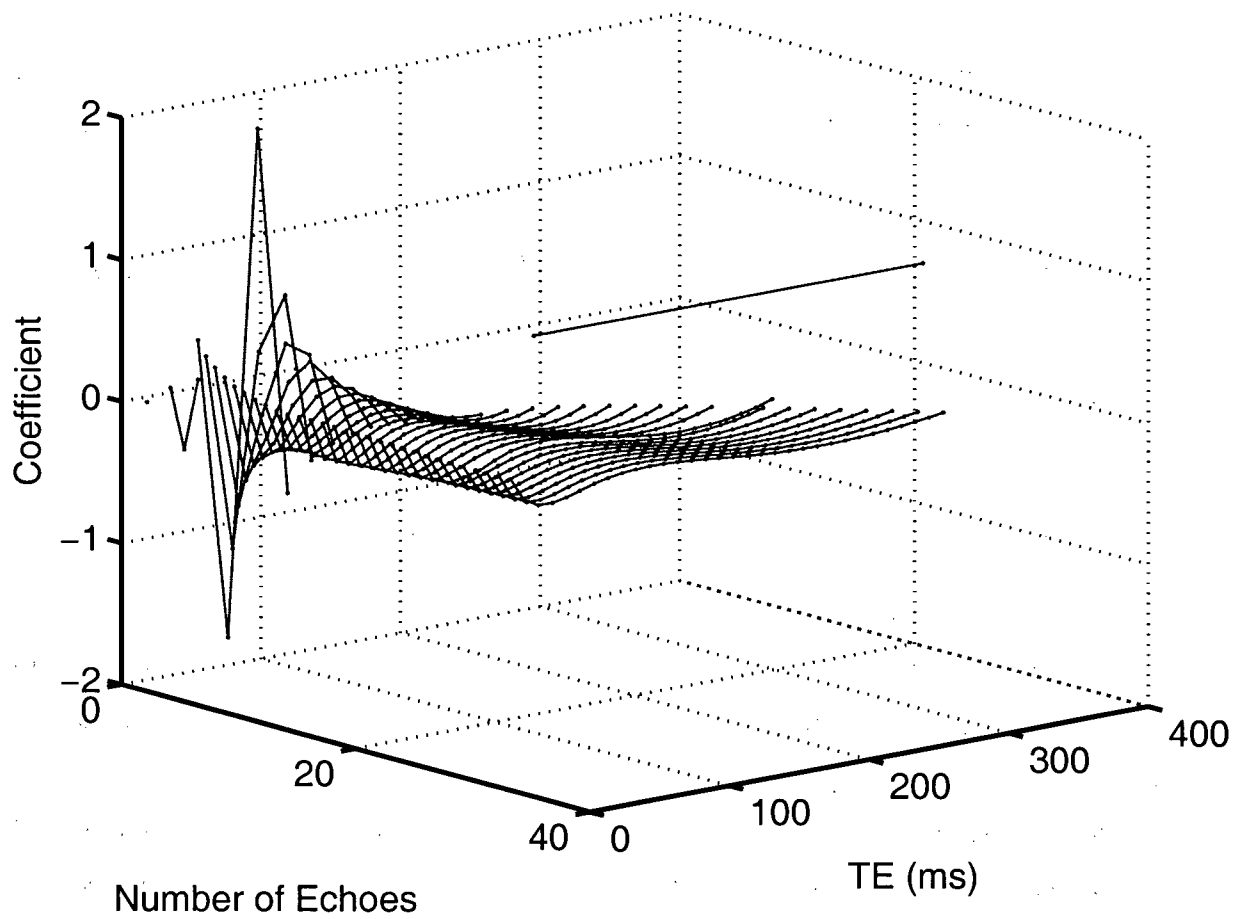


Figure 3.15: The coefficients as a function of the number of echoes and TE. The line segment is the coefficients for two echoes, and appears out of place only because of the perspective of the axes.

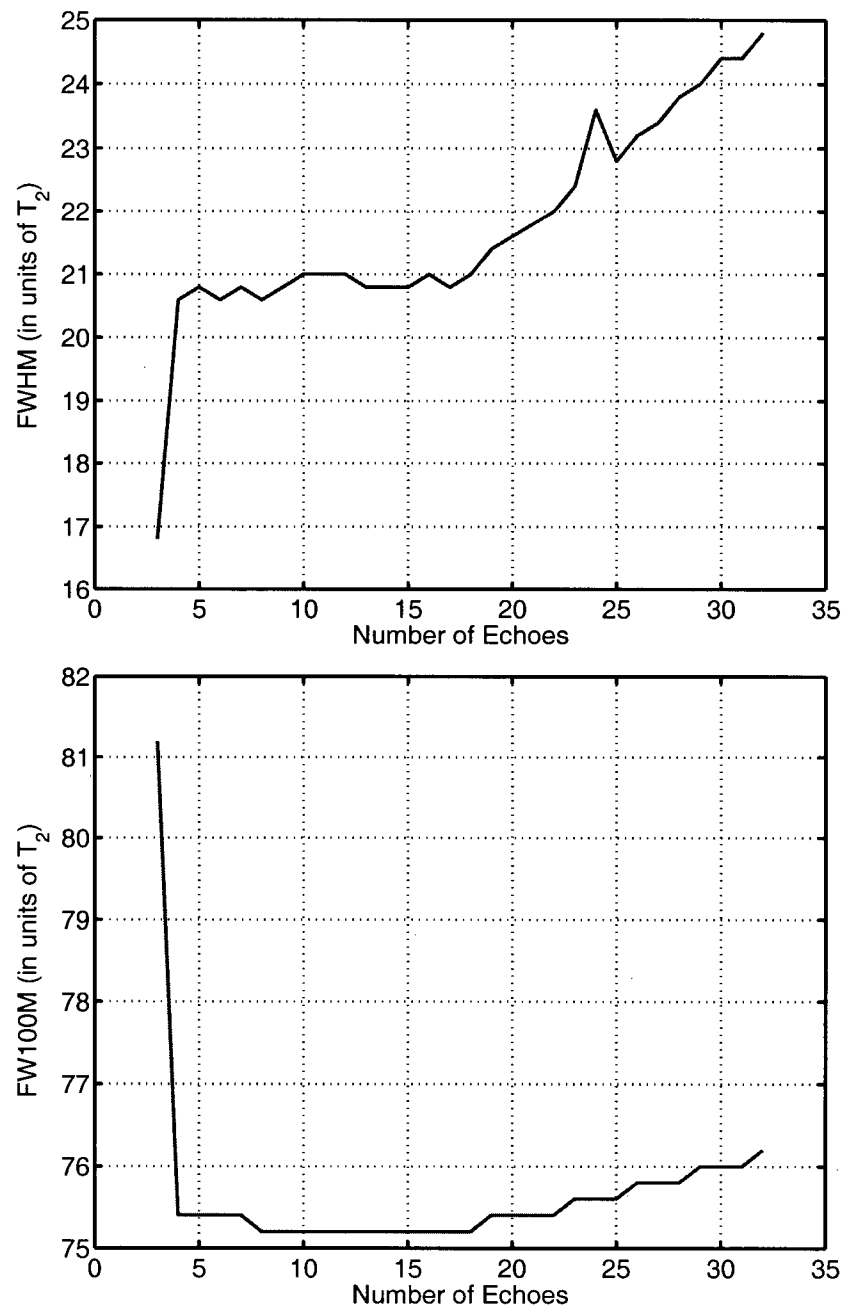


Figure 3.16: The full width at half max (FWHM) of the filter $A^s(T_2)$ as a function of the number of echoes (top) and the full width at 1/100 max (bottom). The wider the FWHM the better.

One interesting thing is that for evenly spaced echoes it is very important to have data included from near 80 ms. Therefore, for fewer echoes, for example $N = 4$, the echo spacing must be increased to have an echo near 80 ms. This means the first echo must be near 20 ms. There is a tradeoff between having an echo at shorter TE, near 10 ms, and having an echo near 80 ms.

3.8.2.3 Conclusions

The objective function was maximized when the echo spacing, Δt , was the minimum allowed $\Delta t = 10$ ms. The measures defined for the short T_2 filter had little change for $5 \leq N \leq 19$ and got progressively better for $N > 19$ echoes. Therefore, if a minimum number of echoes are needed for equidistant sampling, then $N = 5$ should be sufficient, but if more echoes are possible, the filter would be better with more.

3.8.3 Non-Equidistant

Multi-echo data can also be collected with non-equidistant echo spacing. A study, similar to the previous one of equidistant samples, was done with non-equidistant samples.

3.8.3.1 Methods

The objective function was the same as that used in the other sections. The inverse of the objective function was defined as:

$$\max_{t,c} \frac{\sum_{i=1}^N c_i \exp(-t_i/25)}{\sqrt{\sum_{i=1}^N \sigma_i^2 c_i^2}} \quad (3.19)$$

with constraints $-2 \leq c_i \leq 2$ for all i . There was also a constraint on the minimum spacing between consecutive echoes (10 ms) because of hardware constraints. The constraints on c_i were defined to constrain the noise amplification $\sum_{i=1}^N \sigma_i^2 c_i^2$.

3.8.3.2 Results

The echo times were calculated along with the coefficients. The minimum spacing between consecutive echoes could likely be decreased slightly, but was a reasonable number. A constraint on the maximum echo time, t_N , was defined to be 2000 ms as the maximum echo time affects the TR and T_1 weighting.

The non-equidistant coefficients are shown in Figure 3.17. The coefficients and echo times are similar to the coefficients and echo times calculated for equidistant echo sampling. The FWHM was approximately 2 ms wider, and the FW100M was approximately 2 ms less, when the echo sampling was allowed to vary compared to echoes equally spaced.

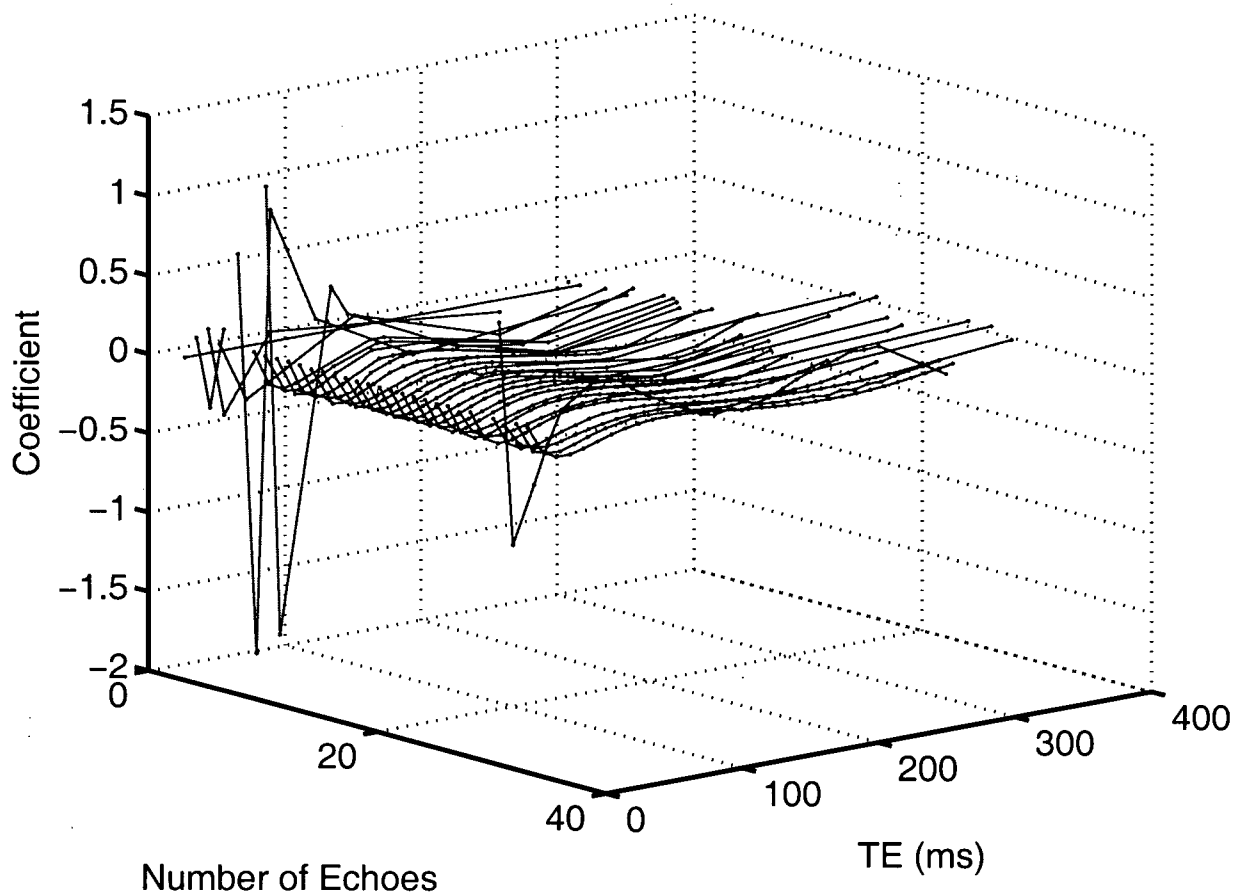


Figure 3.17: The coefficients as a function of the number of echoes and TE.

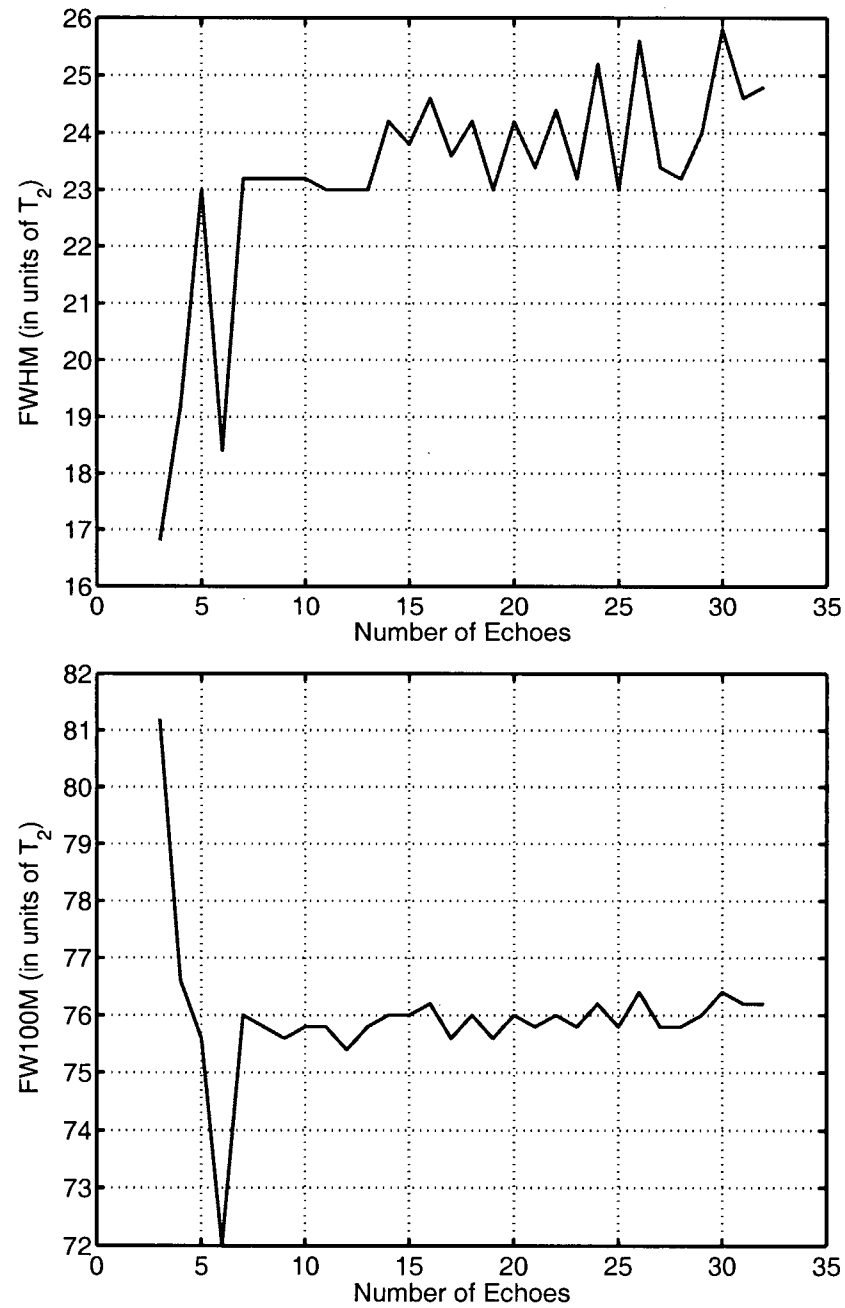


Figure 3.18: The full width at half max (FWHM) of the filter $A^s(T_2)$ as a function of the number of echoes (top) and the full width at 100th max (bottom).

The echo times calculated for four equally spaced echoes required a longer echo spacing, and therefore a later first echo, to have an echo near 80 ms. For unequally spaced echoes, the time of the first echo was 10 ms, as the other three echoes could be spread out in T_2 space.

3.8.3.3 Conclusions

The short T_2 filter was slightly better when the echo spacing was allowed vary compared to a fixed echo spacing. The echo times tended to be similar to the equidistant echo times. Therefore, to create a better short T_2 filter, shorter echo times would be required, which would be difficult on an MRI machine, but would be possible on an NMR spectrometer.

3.8.4 Discussion

The selectivity of the short T_2 filter, $A^s(T_2)$, for $10 \leq T_2 \leq 50$ ms is a function of the echo and corresponding coefficients. Figure 3.19 shows the T_2 information in spin-echo signal acquired at echo times $t = 10, 80, 100, 200,$ and 800 ms. As expected the later the echo time, t , the less information is available for $T_2 \leq t$. Therefore, a sharp rise on the left side of $A^s(T_2)$ requires signal collected at a short echo time. The goal of the coefficients was to select appropriate weightings of the signal, at different echo times, to create a selection in the short T_2 range of interest.

The signal from each echo contributes different information depending on the echo time of the acquisition. The 32 coefficients, c^s , in Table 3.1 vary from positive to negative and back to positive. The first echo, which has a positive coefficient, is the primary echo that provides the sharp increase in the curve (upper solid line). The next six echoes have a negative coefficient and provide the change in slope from positive to negative (dot-dashed curve). The following ten echoes have a positive coefficient and bring the filter positive. Then the next eleven echoes have a negative coefficient. The effect of increasing number of echoes contributed to $A^s(T_2)$ is shown in Figure 3.20. As more signal from more echoes were added to the selection curve, the selection was better at later echo times.

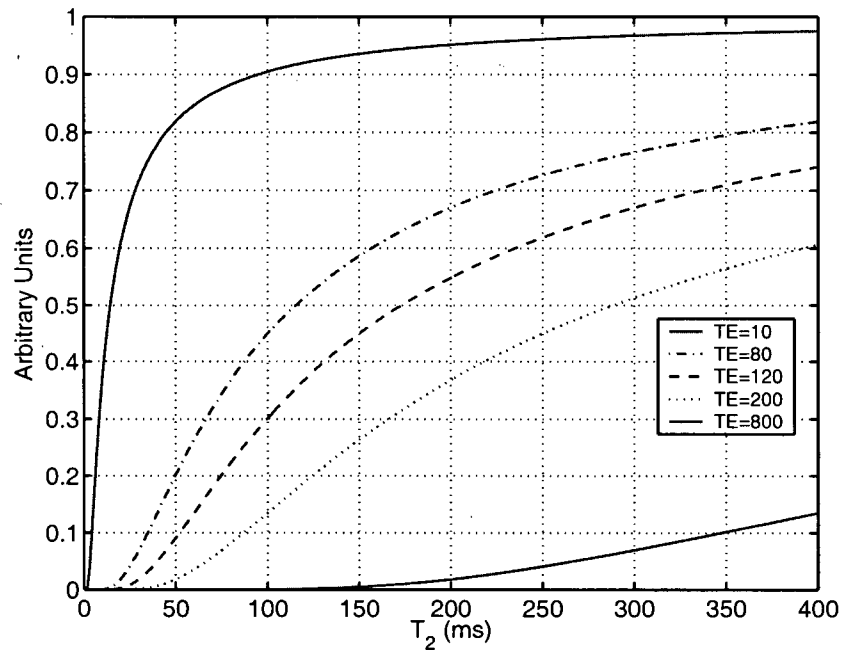


Figure 3.19: The filter, as a function of T_2 , based on echo time $TE = 10$ ms (upper solid line), $TE = 80$ ms (dash-dotted line), $TE = 120$ ms (dashed line), $TE = 200$ ms (dotted line), and $TE = 800$ ms (lower solid line). Each filter is zero at $TE = 0$ ms and goes to one as $T_2 \rightarrow \infty$.

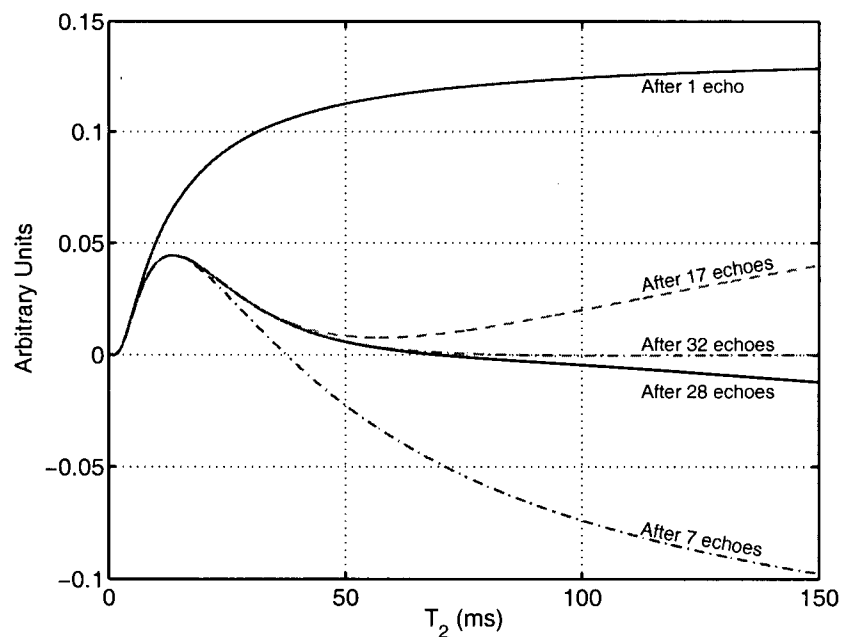


Figure 3.20: The short T_2 filter as a function of a consecutive subset of echoes based on the thirty-two coefficients. Each consecutive set of echoes constrains later parts of the filter.

3.8.5 Four Echo Non-equidistant Sampling

Fewer echo times require less power deposition and could be interleaved so multiple slices could be acquired in such a way the MT effect could be minimal. A set of four coefficients was calculated and are shown in Table 3.5. The echo times, along with the coefficients, were calculated as part

TE (ms)	c^s	c^a
10	3.1872	2.5642
30	-4.7952	-2.5133
120	2.3515	1.8698
270	-0.7539	-1.1654

Table 3.5: Coefficients for short and all T_2 filter based on four unevenly spaced echoes.

of the minimization procedure and are approximately logarithmically spaced. Each of the echo times are near an important region of the short T_2 filter. The first echo time, $TE = 10$ ms, defines the rapid increase in the portion of the curve for $0 \leq T_2 \leq 18$ ms. The second and third echoes, at $TE = 30$ ms and $TE = 120$ ms, bracket a portion of the T_2 filter where the filter changes from decreasing to flat. The fourth echo, at $TE = 270$ ms forces the tail of the filter to be near zero at long T_2 .

The short T_2 filter (Figure 3.21) calculated from the four echoes followed the T_2 filter calculated from 32 echoes. The ascending portion of the filter ($0 \lesssim T_2 \lesssim 15$ ms) was exactly the same in each as that portion of the curve is determined by the $TE = 10$ ms contribution only. The descending portion of the filter ($15 \lesssim T_2 \lesssim 100$ ms) was higher for the filter based on the four echoes as there were fewer degrees of freedom to be modified to force the filter lower. The short T_2 filter, from 4 echoes, was not as close to zero as the short T_2 filter from 32 echoes for $T_2 > 200$ ms. This was due to the lack of the number of data points at long echo times, which contribute to making the filter as flat as possible.

Myelin water maps were calculated from the four unevenly spaced echoes and is shown in Figure 3.21 along with a myelin water map from 32 echoes. There was little difference in the myelin water maps. The original multi-echo data were filtered with five iterations of the anisotropic diffusion filter.

The short T_2 filter had a very similar response with as few as four unevenly spaced echoes. Therefore, the primary information required to create such a selective filter was required to have

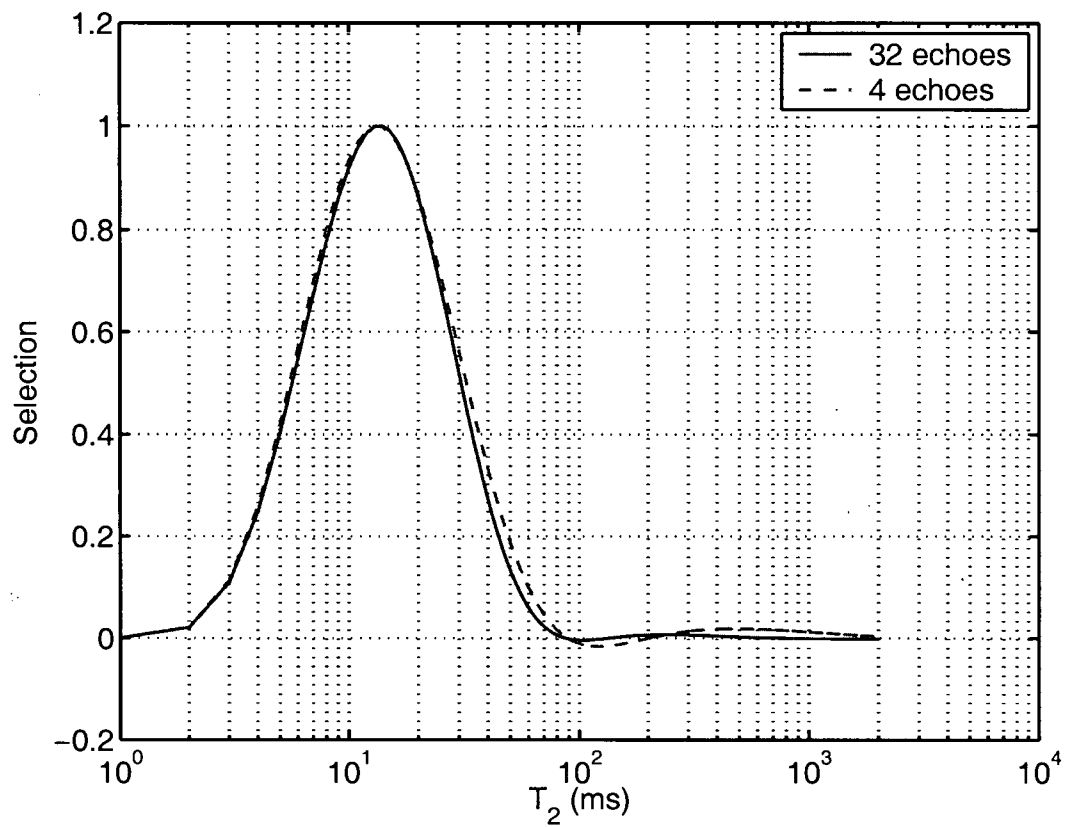


Figure 3.21: Short T_2 filter calculated from four echoes (red dashed line) and from 32 echoes (blue solid line). The height of the curve was normalized to one to allow a visual comparison of two curves. The filter is plotted on a log axis to visualize over a large range of T_2 .

several echoes at small TE, one echo near the T_2 where the filter dropped to zero and one echo at long TE.

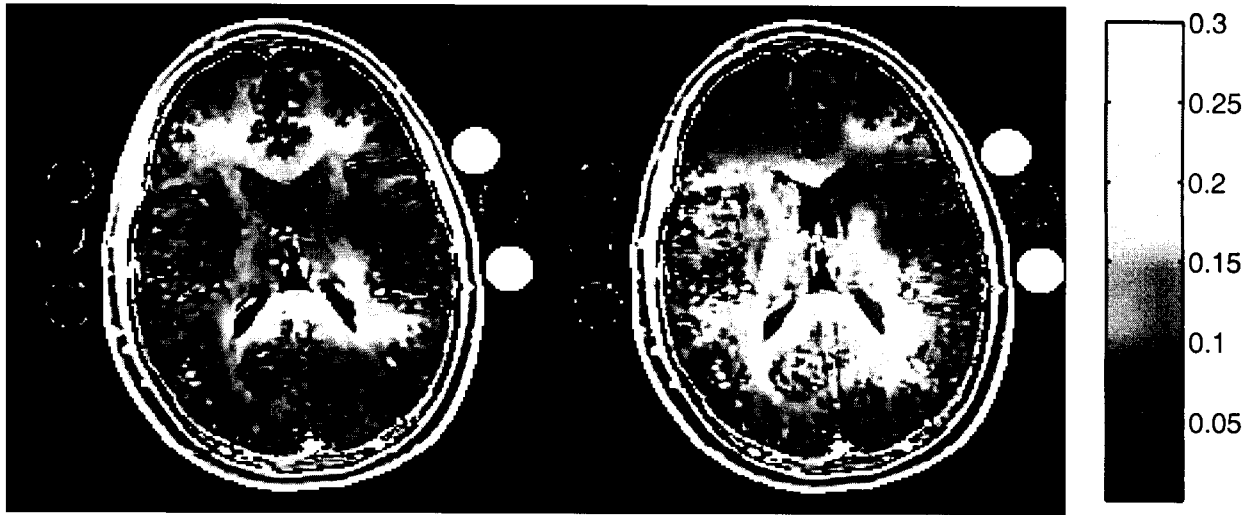


Figure 3.22: Myelin water map calculated by the linear combination method from four echoes of the 32 echo sequence (left) and the linear combination method from all 32 echoes (right). The two bright phantoms on the right side of each head are the nickel/agarose phantoms with a $T_2 \approx 20$ ms.

3.9 Conclusions

Fast accurate estimation of myelin water is important for assessing diseases such as multiple sclerosis. The current method to quantify the myelin water fraction *in vivo* is to acquire multi-echo images and compute the distribution of T_2 voxel-by-voxel. The myelin water fraction is calculated as the ratio of the signal of water with $10 \leq T_2 \leq 50$ ms to the total signal in the distribution. The calculation of the T_2 distribution for each voxel in an image is a slow process. Another method to estimate the signal of water within a range of T_2 is to linearly combine the multi-echo images with optimized coefficients.

I designed a non-linear algorithm to calculate two sets of optimized coefficients, one set to select water with a $10 \leq T_2 \leq 50$ ms (short T_2) and a second set to select water with $T_2 \geq 10$ ms (all T_2). The coefficients to select for short T_2 were applied to multi-echo images of a set of phantoms. The resulting short T_2 image had very good selection of the phantoms with T_2 near 20 ms and good suppression of phantoms with $T_2 > 70$ ms. The NNLS algorithm and linear combination method were applied to a set simulated, noisy bi-exponential decay curves, of white matter model. The mean myelin water fraction estimated from each of the algorithms was within 10% of the true myelin water fraction and the noise standard deviations were similar. Maps of

the *in vivo* myelin water fraction, from five volunteer MRI scans, were calculated by the two algorithms and had very similar detail.

The linear combination of multi-echo data was an efficient algorithm to calculate the myelin water fraction based on the short T_2 . It was 20,000 times faster than the regularized NNLS algorithm and the myelin water fraction was as accurate and precise. The strength of the linear combination method lies in the speed and that it does not depend on a construction method. Initial work showed fewer echoes may be required to estimate the myelin water fraction with the same accuracy and precision as the current technique.

Chapter 4

Non-180 Refocusing Pulses

4.1 Introduction

4.1.1 Motivation

Accurate T_2 estimation traditionally depends on accurate refocusing pulses. Many studies [31, 35, 71, 72] showed large deviations in the measured T_2 when the refocusing pulse flip angle deviates from 180° . For example, Majumdar [71] measured biases in R_2 ($R_2 = 1/T_2$) of greater than 10% for 20% deviations from an ideal pulse and biases of over 100% for deviations of greater than 35%. The biases result from a change in shape of the decay curve due to stimulated echoes superimposed on the primary echo and as the refocusing pulse flip angle α decreases from 180° .

There are many methods to reduce the stimulated echo “artifacts” during acquisition of T_2 decay curves. Levitt [30] proposed using composite refocusing pulses ($90_x-180_y-90_x$) to correctly rephase spins in the presence of moderate B_1 inhomogeneity. Zur and Stokar [73] analyzed artifacts due to inhomogeneous B_1 and developed a phase cycling scheme to dephase spurious echoes. Several other groups [31, 35, 74] proposed crusher patterns to dephase spurious echoes. Each method reduces artifacts well but increases power deposition or increases the minimum echo spacing.

Majumdar [71] modeled the magnetization at the i^{th} echo, measured from a train of N refocusing pulses, to be attenuated by the i^{th} power of a function $f(\alpha)$ for a pulse sequence that crushes stimulated echoes. The function $f(\alpha)$ was derived analytically for the first 3 echoes of pulse sequences consisting of simple RF pulses and of composite RF pulses. In 2000, Sled and Pike [75] described a method to correct inaccurate mono-exponential T_2 measurements due to imperfect refocusing pulses. A multi-echo pulse sequence was used to calculate the T_2 and a separate acquisition was required to calculate the B_1 map. The calculated T_2 was divided by $f(\alpha)$ to obtain a “corrected” mono-exponential T_2 . Another approach by Lepage [76] corrected

the experimentally determined T_2 of a gel phantom based on a B_1 map calculated from a different homogeneous gel phantom. The techniques by Sled and Lepage each required a separate acquisition to calculate the B_1 map.

4.1.2 Previous Work

The evolution of primary, stimulated and indirect echoes acquired from a train of refocusing pulses of flip angle α is usually calculated by the application of rotation matrices to magnetization vectors [37, 71, 77, 78, 79]. Woessner [37] derived a set of equations, based on the Bloch equations, that define magnetization immediately after a hard refocusing pulse given the magnetization immediately before:

$$\begin{aligned} F(t + t_w) &= F(t) \cos^2(\alpha/2) + F^*(t) \sin^2(\alpha/2) - iM_z(t) \sin(\alpha) \\ M_z(t + t_w) &= M_z(t) \cos(\alpha) - \frac{1}{2}i[F(t) - F^*(t)] \sin(\alpha) \end{aligned} \quad (4.1)$$

where $F(t)$ is the dephasing transverse magnetization, $F^*(t)$ is the rephasing transverse magnetization, $M_z(t)$ is the longitudinal magnetization, t_w is the pulse duration, and α is the flip angle of the pulse. These equations describe three echo pathways: a primary echo due to the phase reversal of the magnetization; a stimulated echo due to longitudinal magnetization rotated back into the transverse plane; and the “virtual” stimulated echo due to magnetization unaffected by the first pulse, inverted by the second and later rephased to form an echo.

Hennig [78] extended Woessner’s work to track groups of spins with the same phase coherence through a multi-pulse experiment. Magnetization after a non-180° refocusing pulse is distributed into the Z axis or remains in the transverse plane either defocusing or refocusing. To account for this, Hennig introduced magnetization sub-states defined by a net magnetization, phase accumulation, and direction of spins (refocusing or defocusing). Constant time between refocusing pulses greatly reduced the number of possible sub-states and allowed the phase accumulation to be grouped in an integral number of phase intervals over which phase is accumulated. Therefore, a multi-pulse experiment corresponds to an application of a rotation matrix, based on Equation 4.1, applied to each set of magnetization sub-states followed by an inter-pulse relaxation of $\exp(-2\tau/T_2)$ for $F(t)$ and $F^*(t)$, $\exp(-2\tau/T_1)$ for $M_z(t)$, and a generating term $M_0(1 - \exp(-2\tau/T_1))$ (where 2τ is the echo spacing). For accurate T_2 quantification, Hennig

suggested all magnetization from stimulated and indirect echoes must be removed by spoilers. On the contrary, accurate and precise T_2 quantification is possible from decay curves collected with stimulated and indirect echoes superimposed on the primary echoes.

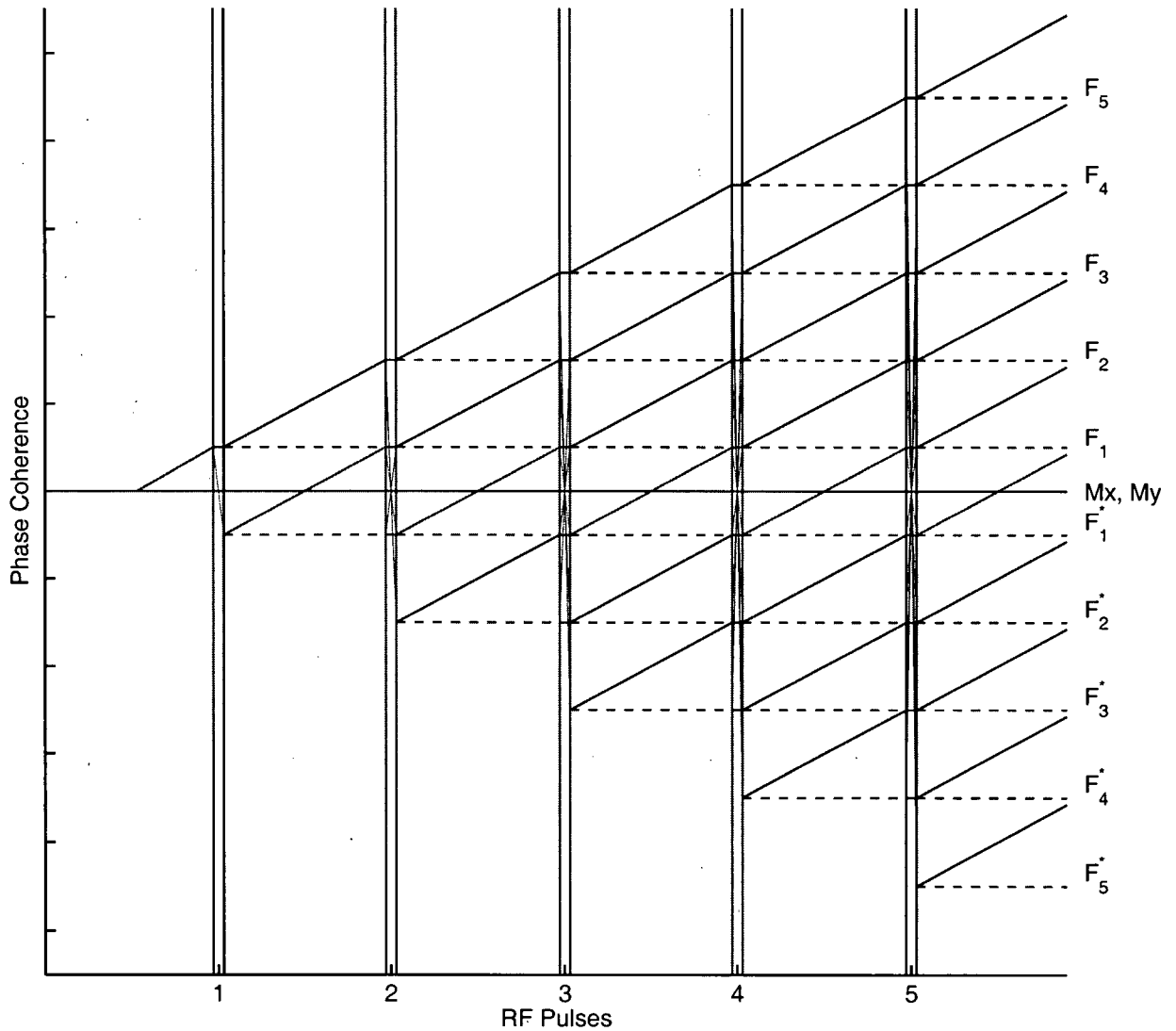


Figure 4.1: Phase coherence diagram based on a train of five refocusing pulses. The phase of the magnetization would follow the lines between F_1 and F_1^* around M_x, M_y if the refocusing pulses were 180° .

4.1.2.1 Mathematical Description of Woessner's Paper

Woessner [37] defines the Bloch equations in terms of U (in phase component), V (out-of-phase component) and M_z (longitudinal component) as:

$$\begin{aligned}\frac{d}{dt}U(t) &= -(\omega_0 - \omega)V - U(t)/T_2 \\ \frac{d}{dt}V(t) &= (\omega_0 - \omega)U - V(t)/T_2 - \omega_1 M_z(t) \\ \frac{d}{dt}M_z(t) &= -\frac{M_0 - M_z(t)}{T_1} + \omega_1 V(t)\end{aligned}\tag{4.2}$$

where ω_0 is the nuclear precessional frequency, ω is the frequency of the rotating coordinate system, and $\omega_1 = \gamma B_1$ is the frequency of the excitation pulse. The variable $F(t) = U(t) + iV(t)$ is the rotating component of the magnetization.

After a rotation of $\theta = \omega_1 t_w$ (where t_w is the width of the RF pulse):

$$\begin{aligned}U(t + t_w) &= U(t) \\ V(t + t_w) &= V(t) \cos(\theta) - M_z \sin(\theta) \\ M_z(t + t_w) &= V(t) \sin(\theta) + M_z \cos(\theta)\end{aligned}\tag{4.3}$$

and

$$\begin{aligned}F(t + t_w) &= U(t + t_w) + iV(t + t_w) \\ &= U(t) + iV(t) \cos(\theta) - iM_z \sin(\theta)\end{aligned}\tag{4.4}$$

Equation 4.4 is then written as a function of $F(t)$, $F^*(t)$, $M(t)$, and $M^*(t)$:

$$F(t + t_w) = U(t) + iV(t) \cos(\theta) - iM_z(t) \sin(\theta) \quad (4.5)$$

$$= U(t) [\cos^2(\theta/2) + \sin^2(\theta/2)] + iV(t) [\cos^2(\theta/2) - \sin^2(\theta/2)] - iM_z(t) \sin(\theta) \quad (4.6)$$

$$= U(t) \cos^2(\theta/2) + U(t) \sin^2(\theta/2) + iV(t) \cos^2(\theta/2) - iV(t) \sin^2(\theta/2) - iM_z(t) \sin(\theta) \quad (4.7)$$

$$= U(t) \cos^2(\theta/2) + iV(t) \cos^2(\theta/2) + U(t) \sin^2(\theta/2) - iV(t) \sin^2(\theta/2) - iM_z(t) \sin(\theta) \quad (4.8)$$

$$= [U(t) + iV(t)] \cos^2(\theta/2) + [U(t) - iV(t)] \sin^2(\theta/2) - iM_z(t) \sin(\theta) \quad (4.9)$$

$$= F(t) \cos^2(\theta/2) + F^*(t) \sin^2(\theta/2) - iM_z(t) \sin(\theta) \quad (4.10)$$

by using the cosine double angle formula:

$$\cos(\theta) = \cos^2(\theta/2) - \sin^2(\theta/2). \quad (4.11)$$

and the identity:

$$\cos^2(\theta/2) + \sin^2(\theta/2) = 1. \quad (4.12)$$

Then, $F(t + t_w)$ and $M_z(t + t_w)$, written as functions of $F(t)$ and $M_z(t)$, will be:

$$F(t + t_w) = F(t) \cos^2(\theta/2) + F^*(t) \sin^2(\theta/2) - iM_z(t) \sin(\theta) \quad (4.13)$$

$$F^*(t + t_w) = F(t) \sin^2(\theta/2) + F^*(t) \cos^2(\theta/2) + iM_z^*(t) \sin(\theta) \quad (4.14)$$

$$M_z(t + t_w) = M_z(t) \cos(\theta) - \frac{i}{2} [F(t) - F^*(t)] \sin(\theta) \quad (4.15)$$

$$M_z^*(t + t_w) = M_z^*(t) \cos(\theta) - \frac{i}{2} [F(t) - F^*(t)] \sin(\theta) \quad (4.16)$$

4.1.3 Implementation of Algorithm

The algorithm to calculate the signal of each echo from a train of RF pulses is shown in Algorithm 4.1. The first section creates the rotation matrix for the magnetization sub-states. The sub-state vector, B , is preallocated and set to $-i$, dephasing magnetization. Then, the algo-

rithm loops over each echo, applies the rotation matrix to each magnetization sub-state, saves the echo signal intensity, applies the relaxation and then applies the phase evolution. The T_1 (Algorithm 4.2) and T_2 (Algorithm 4.3) relaxation are applied to the longitudinal and transverse magnetization, respectively. The phase evolution (Algorithm 4.4) updates the magnetization sub-state vector B . Each defocusing sub-state is defocused by one time unit, each refocusing sub-state is defocused one time unit, and the magnetization sub-state that forms an echo becomes a defocusing sub-state. The phase evolution bookkeeping was simplified greatly due to the assumption the refocusing pulses were evenly spaced.

The primary signal attenuation is due to the dephasing of the spins and is accounted for by the T_2 decay, but there is also a weak signal dependence on the T_1 relaxation time. For the primary work in this chapter, involving the brain, the $T_1 \approx 650$ ms [80]. The T_1 relaxation is applied to magnetization stored in the longitudinal axis by the equation $\exp(-\tau/T_1)$. The important aspect, for this work, is $\exp(-\tau/T_1) \approx \exp(-5/650) = 0.9923$. Therefore, the decay curve will have a very small modulation because τ/T_1 is not zero. The decay curve dependence on T_1 could possibly be exploited as a means of calculating the T_1 along with T_2 , α , and ρ .

The signal intensity, y , was calculated (Algorithm 4.1) given T_2 , T_1 , α , τ , and the number of refocusing pulses. The algorithm calculated the 32-echo decay curve in approximately 25 ms on a P4 1.5 GHz computer with 1 Gigabyte of RAM.

Algorithm 4.1 Signal calculation from a train of refocusing pulses

```

function [decay] = stimulate(alpha, num_echoes, T1, T2, tau)
%   alpha = rotation vector in x'y'z frame of reference.
%   num_echoes = number of echoes.
%   T1 = T1 of tissue (ms)
%   T2 = T2 of tissue (ms)
%   tau = time between 90-180 (ms)

jay = sqrt(-1);

% Preallocate the signal intensity vector
decay = zeros(1, num_echoes);

% Preallocate the array of num_echoes substates [F F* Z Z*] and initialize
B = zeros(num_echoes*4, 1);
B(1) = 0 + jay*1;

% Precalculate rotation matrix Tone for one substate block
Tone = [[ (cos(alpha/2))^2, (sin(alpha/2))^2, -jay*sin(alpha), 0]; ...
         [ (sin(alpha/2))^2, (cos(alpha/2))^2, 0, jay*sin(alpha)]; ...
         [ (-jay)*1/2*sin(alpha), (jay)*1/2*sin(alpha), cos(alpha), 0]; ...
         [ (-jay)*1/2*sin(alpha), (jay)*1/2*sin(alpha), 0, cos(alpha)]];

% Calculate the sparse rotation matrix of "num_echoes" blocks
Tp = kron(sparse(diag(ones(1,num_echoes))), create_Tp(alpha));

% Apply initial T2 decay and T1 regrowth (between 90-180 pulses).
B = t2relax(B, tau, T2);
B = t1relax(B, tau, T1);

for echo = 1:num_echoes

    % Apply rotation matrix.
    % Each block of the rotation matrix acts on [F(k), F*(k), Z(k), Z*(k)]
    B = (Tp * B);

    % Save echo intensity, this is F1*
    decay(echo) = abs(B(2)) * exp(-tau/T2);

    % Apply transverse decay for time 2*tau.
    B = t2relax(B, 2*tau, T2);

    % Apply longitudinal regrowth for time 2*tau.
    B = t1relax(B, 2*tau, T1);

    % Let the spins dephase for time 2*tau
    B = evolution(B);
end

```

Algorithm 4.2 T_1 relaxation

```
function [B] = t1relax(B, tau, T1)

% The Z and Z* substates will be modified
indicies = [ 3:4:length(B) 4:4:length(B) ];

% Apply the T1 relaxation to the Z and Z* substates
B(indicies) = B(indicies) * exp(-tau/T1);
```

Algorithm 4.3 T_2 relaxation

```
function [B] = t2relax(B, tau, T2)

% The F and F* substates will be modified
indicies = [ 1:4:length(B) 2:4:length(B) ];

% Apply the T2 relaxation to the Z and Z* substates
B(indicies) = B(indicies) * exp(-tau/T2);
```

Algorithm 4.4 Phase evolution of magnetization

```
function [Bnew] = evolution(B)
% This function is a book-keeping method to track the phases of the spins
% as they are flipped and as they progress through the inter-pulse time.

Bnew = B;

% Number of elements in B
L = length(B);

% All F(n) go to F(n+1).
Bnew([ 5:4:L ]) = B([ 1:4:L-4 ]);

% F*(1) goes to F(1).
Bnew(1) = B(2);

% All F*(n) go to F*(n-1).
Bnew([ 2:4:L-4 ]) = B([ 6:4:L ]);
```

4.1.4 Overview of Work

I created a method to fit decay curves acquired from a multi-echo pulse sequence with non-180° refocusing pulses. This method was implemented in two algorithms: first, a non-linear curve fitting algorithm to estimate mono-exponential decay curve parameters (Section 4.2) and second, a non-negative least squares algorithm to estimate multi-exponential decay curve parameters (Section 4.3). A set of simulations were used to determine the accuracy and precision of the parameter estimation using each fitting algorithm. Scans of phantoms, from the MESE_c sequence with a train of α pulses, were used to verify the parameter estimation. A set of *in vivo* scans were acquired from volunteers and myelin water maps calculated from the MESE_c sequence were compared to myelin water maps calculated from the MESE_o. Several extensions to the work will be shown, including: slab selected, multi-slice acquisition (Section 4.4), the effect of the non-90° excitation pulse (Section 4.5), and trains of non-constant refocusing pulses (Section 4.6).

4.2 Mono-Exponential T₂ Decay Curve Fit

An algorithm to fit mono-exponential decay curves is described. Noise simulations were used to assess the accuracy and precision of the fit algorithm. Finally, a set of nickel/agarose phantoms, of known T₂ values, were scanned with different sets of refocusing pulses. The estimated T₂ was compared to the T₂ estimated from the MESE_o sequence and the refocusing pulse were compared to the prescribed.

4.2.1 Mono-Exponential Fit Algorithm

Each decay curve was fit to a function of proton density ρ , spin-spin relaxation time T₂, baseline offset d , and refocusing pulse flip angle α . A non-linear least squares algorithm (`lsqcurvefit` in Matlab [The Mathworks, Natick, MA]) minimized the misfit $\chi^2 = \sum_{i=1}^N (y_i - \hat{y}_i)^2 / \sigma_i^2$ where \mathbf{y} and σ were the mean and standard deviation of the measured data and $\hat{\mathbf{y}}$ was the decay curve estimated by the algorithm. Initial conditions for the curve fitting were: $\rho = 1200$, T₂ = 100 ms, $\alpha = 160^\circ$, $d = 5$. The reconstructed decay curve was calculated at each step of the least squares algorithm by calculating the primary, stimulated, and indirect echoes as defined in Hennig [78]. TR was considered infinite for all fitting.

4.2.2 Monoexponential Fit – Noise Simulation

A set of noise simulations was used to assess the decay curve parameter accuracy and precision from mono-exponential decay curves based on non-180° refocusing pulses. The mean and standard deviation were calculated for each parameter over the noise realizations.

Methods

A noiseless decay curve was created based on the model:

$$y = \rho \exp(-t/T_2) \quad (4.17)$$

where $\rho = 1000$ and $T_2 = 20, 80, 140$ ms. The decay curve was created based on flip angles of $\alpha = 90^\circ, 100^\circ, \dots, 180^\circ$ and echo times $t = 10, 20, \dots, 320$ ms. One thousand realizations of quadrature noise (SNR = 200) were added. TR was set to infinity. The T_2 decay curve parameters used in the simulation are similar to values for brain tissue.

The mean and standard deviation of the estimated parameters were calculated and compared to the true values.

Results and Discussion

Each parameter estimated from the decay curve, for $T_2 = 20, 80, 140$ ms was within 5% of the true parameter. Table 4.1 shows the results for $T_2 = 80$ ms. The parameters estimated from the decay curve were within 2% of the true parameter for $T_2 = 80, 140$ ms. The increased accuracy, as a function of T_2 , was expected as more echoes were able to contribute information to the solution as T_2 increased.

The variability in the estimated parameters was higher for the lower flip angles (for example, variability in T_2 in Table 4.1). To determine if the increased variability is related to the decrease in the flip angle, I re-ran the simulations and scaled the 1,000 realizations of noise by, $\sin^2(\alpha/2)$, on the relative attenuation due to the flip angle. For example, I multiplied the random noise by $\sin^2(\alpha/2) = 1.0$ for $\alpha = 180^\circ$ and by $\sin^2(\alpha/2) = 0.5$ for $\alpha = 90^\circ$. In this way the noise decay curves estimated with $\alpha = 90^\circ$ had the same SNR as the curves simulated with $\alpha = 180^\circ$. Then any discrepancies in the standard deviations of the parameters, were not be due to SNR issues.

$\alpha_{\text{true}} (^{\circ})$	$\hat{\alpha} (^{\circ})$	ρ	T_2 (ms)	χ^2
090	89.836 (0.964)	1001.220 (12.455)	79.296 (1.266)	28.413 (8.050)
100	99.848 (1.015)	1000.919 (11.116)	79.407 (1.139)	28.391 (8.017)
110	109.849 (1.117)	1000.774 (10.058)	79.492 (1.035)	28.285 (8.025)
120	119.851 (1.148)	1000.622 (8.817)	79.557 (0.939)	28.333 (8.070)
130	129.839 (1.269)	1000.551 (8.040)	79.594 (0.867)	28.270 (8.035)
140	139.848 (1.450)	1000.370 (7.292)	79.630 (0.799)	28.185 (8.058)
150	149.841 (1.669)	1000.269 (6.490)	79.650 (0.735)	28.137 (7.992)
160	159.851 (1.984)	1000.144 (5.717)	79.669 (0.686)	28.141 (8.011)
170	169.992 (2.726)	1000.027 (4.823)	79.681 (0.638)	28.177 (8.049)
180	177.474 (2.925)	1000.391 (4.179)	79.636 (0.605)	28.642 (8.030)

Table 4.1: The estimated ρ and T_2 (standard deviation in brackets) given the true $\rho = 1000$ and true $T_2 = 80$ ms.

$\alpha_{\text{true}} (^{\circ})$	$\hat{\alpha} (^{\circ})$	ρ	T_2 (ms)	χ^2
090	89.900 (0.464)	1000.469 (5.860)	79.532 (0.658)	7.132 (1.753)
100	99.902 (0.587)	1000.287 (6.211)	79.588 (0.709)	9.794 (2.384)
110	109.912 (0.670)	1000.094 (6.026)	79.638 (0.711)	12.822 (3.137)
120	119.932 (0.887)	999.904 (6.408)	79.678 (0.755)	15.928 (3.916)
130	129.982 (1.026)	999.612 (6.367)	79.707 (0.756)	19.117 (4.719)
140	139.988 (1.245)	999.597 (6.037)	79.704 (0.728)	22.015 (5.450)
150	149.964 (1.592)	999.713 (5.996)	79.689 (0.719)	24.446 (6.032)
160	160.159 (1.969)	999.381 (5.327)	79.711 (0.696)	26.423 (6.618)
170	170.412 (2.770)	999.490 (4.645)	79.693 (0.672)	27.776 (6.919)
180	177.861 (2.579)	1000.032 (4.348)	79.634 (0.661)	28.757 (6.986)

Table 4.2: The estimated ρ and T_2 from a simulation with SNR scaled as a factor of $\sin^2(\alpha/2)$ to determine whether the increased variability in the estimated parameters was due to the decrease in α .

The estimated parameters, derived from the variable noise decay curves, are shown in Table 4.2. The standard deviation of ρ and T_2 remain relatively constant as α decreased to 90° . The constant variability was true for $T_2 = 140$ ms as well. When $T_2 = 20$ ms, the variability was still a function of α , though decreased by approximately half when the SNR was scaled by the effect of the refocusing pulse.

Conclusions

Mono-exponential T_2 parameters were accurately and precisely estimated from decay curves simulated from non- 180° refocusing pulses. The accuracy and precision were found to depend on α , and the short T_2 was affected more by the decreased flip angle than the longer T_2 components.

4.2.3 Phantom Verification

A set of mono-exponential phantoms were used to confirm the accuracy of T_2 from a set of scans. A set of six nickel/agarose phantoms of known T_2 were scanned (Section 1.8) with a 16 echo pulse sequence with prescribed refocusing pulse flip angles.

Methods

The data was acquired with the single slice, 16 echo MESE_c pulse sequence with parameters: echo spacing = 11.1 ms, TR = 3000 ms and slice selective refocusing pulses.

Regions were drawn on the TE = 11.1 ms image for each of the phantoms. The signal was averaged, within the region, for each echo to create one decay curve for each phantom. The decay curves were fit using the mono-exponential algorithm (Section 4.2.1) in three ways: flip angle set to the prescribed flip angle α_p , flip angle set to $\alpha_{180} = 180^\circ$, and flip angle estimated to minimize misfit (α_{best}).

Results and Discussion

The measured data and curve fits are shown in Figures 4.2, 4.3, 4.4, and 4.5, for one phantom ($T_2 = 90.8$ ms). Curves fit with α as a parameter in the fitting algorithm were better representative of the subtle changes in the curve as seen in the decreased residuals (small panels of Figures 4.2, 4.3, 4.4, and 4.5). In comparison, the curves fit with α fixed to 180° had large residuals that

alternated positive and negative for successive echoes. The curve fitting algorithm worked well over a range of refocusing pulse flip angles and T_2 (not shown).

The estimated parameters of the mono-exponential fits to phantoms are shown in Table 4.3. The estimated flip angle α was always lower than the prescribed flip angle and was significantly lower when $\alpha_p = 180^\circ$. The T_2 was typically within $\pm 10\%$ of the T_2 estimated from the 48 echo MESE_o data.

α_p	α_{best}	ρ_{180}	ρ_p	ρ_{best}	$T_{2,180}$	$T_{2,p}$	$T_{2,\text{best}}$	χ_{180}^2	χ_p^2	χ_{best}^2
90	85	498.2	792.7	842.7	136.4	88.5	83.4	141.1	4.0	1.9
110	103	596.8	777.2	816.5	123.7	96.4	87.8	81.8	3.3	0.6
130	123	687.3	783.1	813.0	110.4	97.4	92.4	49.9	3.4	0.9
150	137	750.3	786.2	826.2	101.7	97.2	92.5	23.7	6.5	0.8
170	151	784.3	788.5	819.2	98.3	97.7	94.0	7.5	5.7	1.3
180	156	800.2	800.2	819.9	97.0	97.0	92.0	5.4	5.4	1.0

Table 4.3: Phantom decay curve parameters estimated from mono-exponential fits to decay curves collected using a train of 16 α_p refocusing pulses. Parameters with a subscript of p were estimated with α fixed to α_p . Parameters with a subscript of best were estimated allowing α to vary. Results are from one phantom ($T_2 = 90.8$ ms). Flip angles are in degrees and T_2 in milliseconds.

The measured refocusing pulse flip angles were always lower than expected. This is likely due to the shape of the refocusing pulse slice profile. A good slice selection profile requires a high power refocusing pulse, but the power of the refocusing pulse is limited as the pulse sequences used to acquire multi-echo data requires a train of RF pulses. Therefore, the slice profile will have a transition from no refocus to $\alpha = 180^\circ$. This transition zone will affect the integrated flip angle.

The mono-exponential curve fit was accurate at reproducing T_2 and α . To assess the effect of initial conditions on the final solution, a set of six other initial conditions were used one with each initial parameter above and then below the original initial condition. For every initial condition, the T_2 , ρ and α from each phantom decay curve were estimated to be the same as the result from the original initial condition. Therefore, the curve fits were reliable and not dependent on initial conditions.

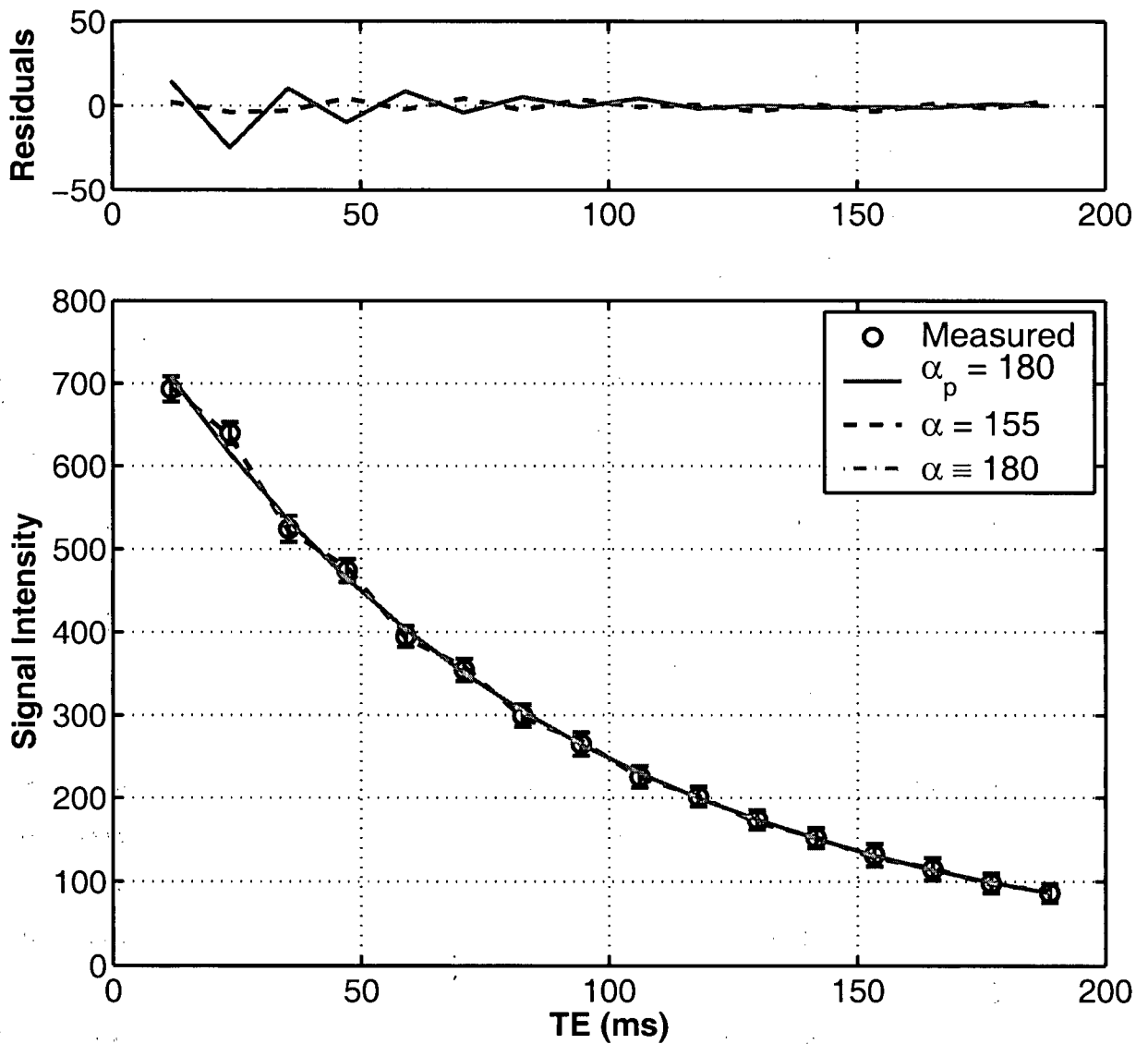


Figure 4.2: Decay curves calculated as the mean signal intensity over a region of one of the phantoms (error bar is one standard deviation). The large panel shows the measured data (circles), the mono-exponential least squares fit based on the prescribed refocusing pulse flip angle $\alpha_p = 180^\circ$ (solid line), the curve where the flip angle was estimated as a parameter of the fitting method (dashed line) and the fit in which the flip angle was assumed to be 180° (dash-dotted line). The small panel shows the residuals of the corresponding fit. $T_2 = 90.8$ ms for the phantom.

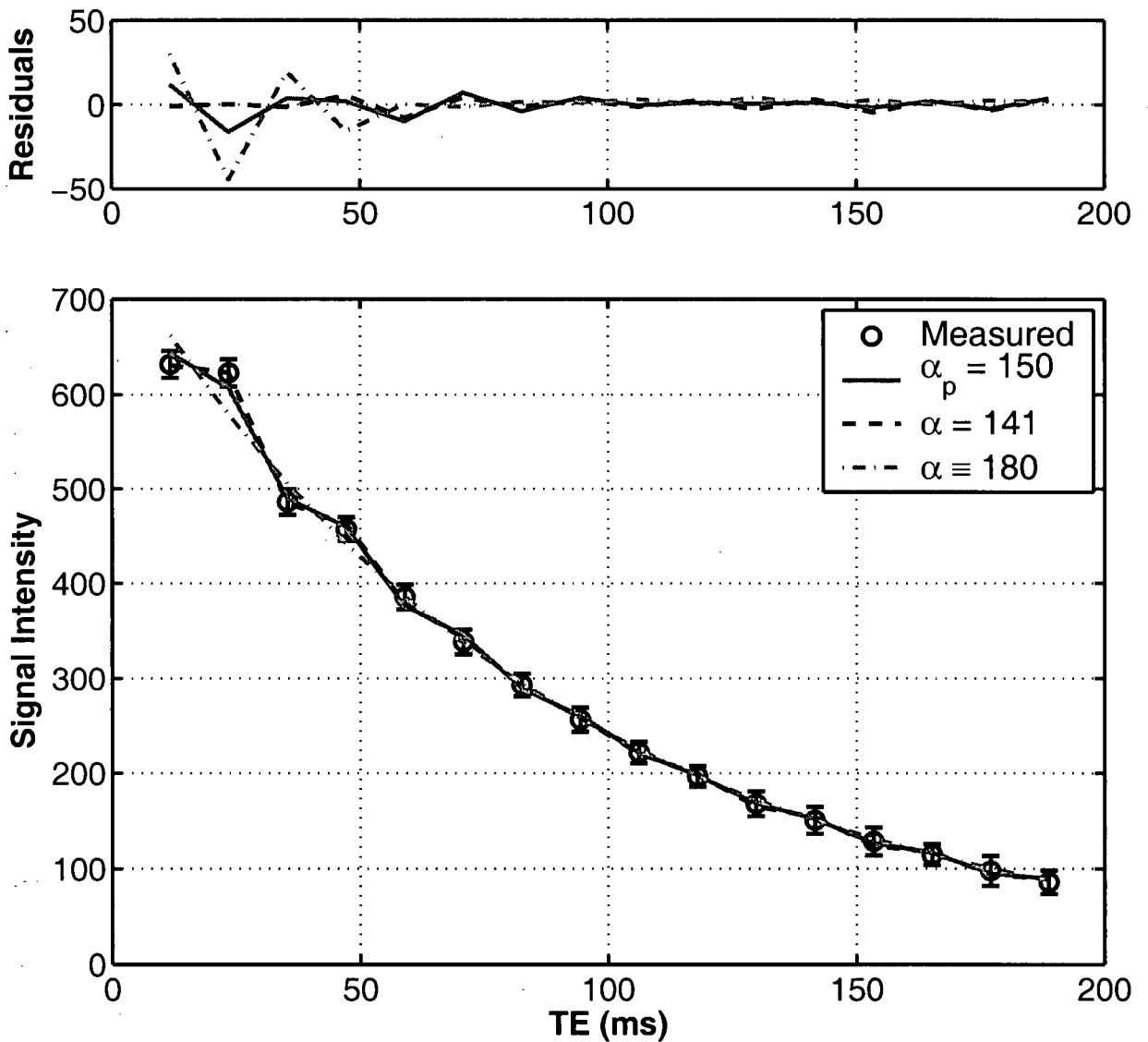


Figure 4.3: Decay curves calculated as the mean signal intensity over a region of one of the phantoms (error bar is one standard deviation). The large panel shows the measured data (circles), the mono-exponential least squares fit based on the prescribed refocusing pulse flip angle $\alpha_p = 150^\circ$ (solid line), the curve where the flip angle was estimated as a parameter of the fitting method (dashed line) and the fit in which the flip angle was assumed to be 180° (dash-dotted line). The small panel shows the residuals of the corresponding fit. $T_2 = 90.8$ ms for the phantom.

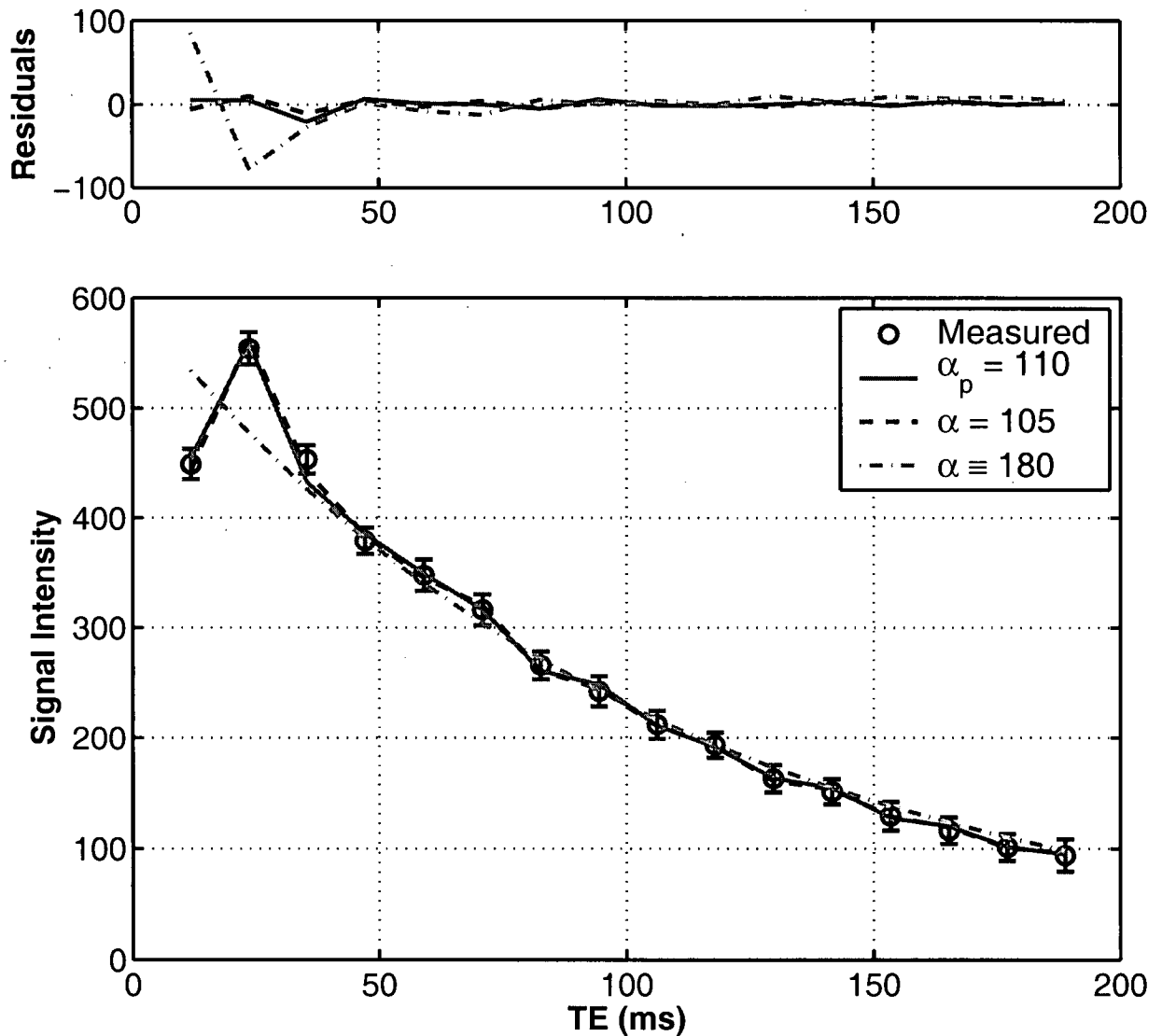


Figure 4.4: Decay curves calculated as the mean signal intensity over a region of one of the phantoms (error bar is one standard deviation). The large panel shows the measured data (circles), the mono-exponential least squares fit based on the prescribed refocusing pulse flip angle $\alpha_p = 110^\circ$ (solid line), the curve where the flip angle was estimated as a parameter of the fitting method (dashed line) and the fit in which the flip angle was assumed to be 180° (dash-dotted line). The small panel shows the residuals of the corresponding fit. $T_2 = 90.8$ ms for the phantom.

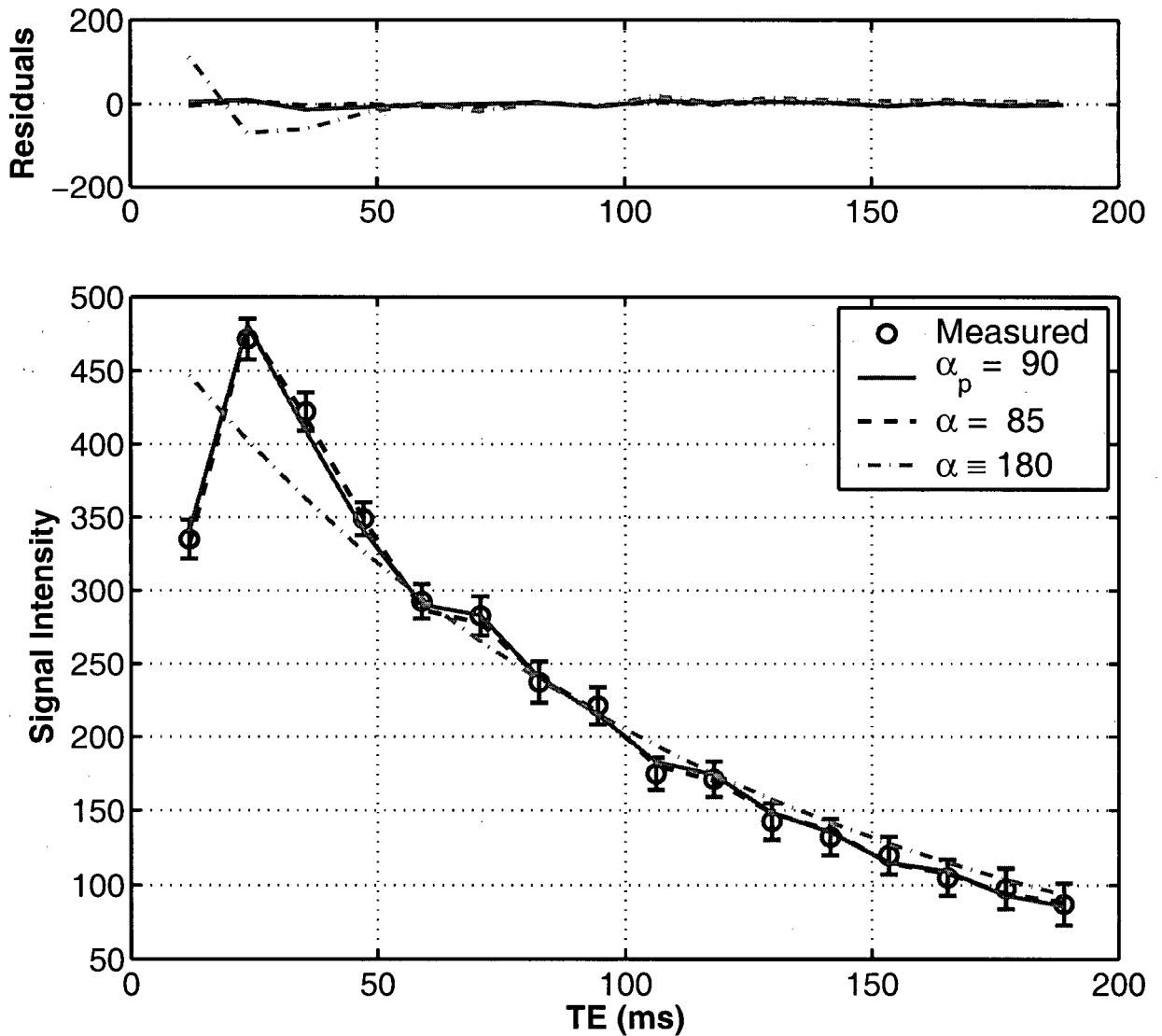


Figure 4.5: Decay curves calculated as the mean signal intensity over a region of one of the phantoms (error bar is one standard deviation). The large panel shows the measured data (circles), the mono-exponential least squares fit based on the prescribed refocusing pulse flip angle $\alpha_p = 90^\circ$ (solid line), the curve where the flip angle was estimated as a parameter of the fitting method (dashed line) and the fit in which the flip angle was assumed to be 180° (dash-dotted line). The small panel shows the residuals of the corresponding fit. $T_2 = 90.8$ ms for the phantom.

Conclusions

The decay curves from the mono-exponential phantoms were reliably fit using a mono-exponential curve fit algorithm designed to calculate the refocusing pulse flip angle during the fit. The decay curve fits that estimated the refocusing pulse flip angle were better representative of the acquired decay curve as seen by the decrease in the χ^2 misfit.

4.3 Multi-Exponential T_2 Decay Curve Fit

Similar to the previous section, an algorithm is defined for fitting multi-exponential decay curves collected from a pulse sequence with a train of α° refocusing pulses. The algorithm will be validated based on a set of simulated and *in vivo* multi-exponential decay curves.

4.3.1 Multi-Exponential Fit Algorithm

4.3.1.1 T_2 Decay Curve Fit Using NNLS

Multi-exponential fits of the *in vivo* data were done with the non-negative least squares (NNLS) algorithm [18, 39, 40]. NNLS solves $As = \mathbf{y}$ where $A_{ij} = \exp(-TE_i/T_{2,j})$, \mathbf{y} is the measured decay curve and s_j are the unknown amplitudes that correspond to $T_{2,j}$. The solution minimizes the χ^2 misfit. In the standard NNLS algorithm, each column A_j , of the matrix A , is a mono-exponential decay curve with $T_2 = T_{2,j}$. To account for α , I created a matrix A^α where each column was a decay curve, calculated using Hennig's method (Section 4.1.2), with $T_2 = T_{2,j}$ and flip angle α . Therefore, the objective was to find the minimum $\chi^2(\alpha)$ misfit of $A^\alpha \mathbf{s} = \mathbf{y}$ over the range of α . To do this, I created a new algorithm, NNLS $^\alpha$, to find the minimum $\chi^2(\alpha)$ by solving $A^\alpha \mathbf{s} = \mathbf{y}$ for α between 40° and 180° .

The multi-exponential fit algorithm I introduced, NNLS $^\alpha$, minimized χ^2 as a function of α . Figure 4.6 shows three example curves of χ^2 as a function of α for $\alpha_p = 90^\circ$ (solid line), $\alpha_p = 150^\circ$ (dashed line) and $\alpha_p = 180^\circ$ (dash-dotted line). Each of the curves has a distinct minimum at the true α .

Therefore, the goal is to find a fast, robust method to find the refocusing pulse flip angle that minimizes the χ^2 misfit.

The χ^2 misfit increases quickly as the α° refocusing pulse flip angle deviates from the true

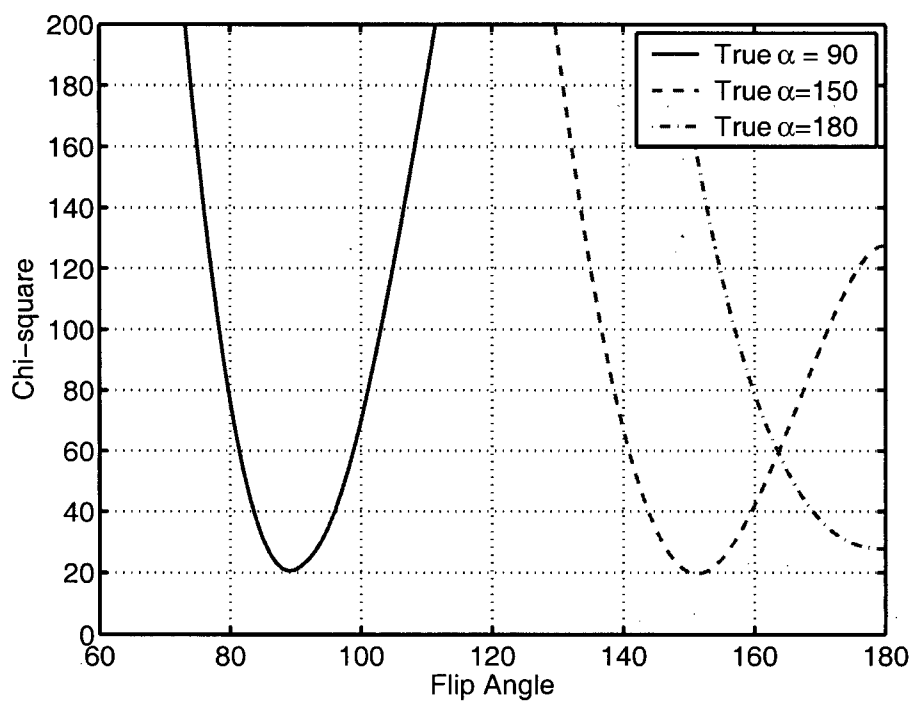


Figure 4.6: The χ^2 misfit plotted as a function of refocusing pulse flip angle α for a true flip angle of $\alpha = 90^\circ$ (solid line), $\alpha = 150^\circ$ (dashed line), and $\alpha = 180^\circ$ (dash-dotted line). The goal of the outer loop of the NNLS $^\alpha$ algorithm is to find the minimum χ^2 over α .

refocusing pulse flip angle (as seen in Figure 4.6). The goal is to create a fast and reliable algorithm to determine the refocusing pulse flip angle α with the minimum χ^2 . Two types of algorithms were assessed for speed and robustness. The first type of algorithm samples several points along the χ^2/α curve then fits the points and determines the minimum χ^2 from the curve fit. Two curve fit algorithms were tried, a quadratic fit and a spline fit. The second type of algorithm is the standard minimization technique where the minimum χ^2 is found by minimizing the function $\chi^2(\alpha)$ over α . The second technique was inherently slower, but more robust.

4.3.1.2 Analysis of the A^α Matrix

Introduction

The decay curves collected with $\alpha < 180^\circ$ have more structure than decay curves with $\alpha = 180^\circ$. Therefore, it may be the accuracy of quantitative T_2 measurements is higher when $\alpha < 180^\circ$ than when $\alpha = 180^\circ$. Decay curves near 150° tend to have more structure and therefore the columns of A may be more linearly independent.

Based on that theory, I defined an A^α matrix which was calculated for $\alpha = 1^\circ, 2^\circ, \dots, 270^\circ$. Two measures were calculated for each matrix 1) the rank and 2) the inverse of the condition number. The measures were calculated in `Matlab` (The Mathworks, Natick Mass) by the built-in functions `rank` and `svd`, respectively. The rank provides an estimate of the number of linearly independent rows or columns. The condition number is defined as the ratio of the largest singular value to the smallest, but for this work I used the ratio of the smallest singular value to the largest.

Two sets of A^α matrices were calculated. The first set was based on 32 echoes, $TE = 10$ ms, $T_1 = 800$ ms. The second set was based on 200 echoes, $TE = 5$ ms, $T_1 = 800$ ms. The T_1 was chosen to be 800 ms as that is approximately the T_1 of white and gray mater.

Results

32 Echoes

The rank (Figure 4.7) was found to be a maximum (rank of 31) between $136^\circ \leq \alpha \leq 158^\circ$ and was near the lowest (rank of 18) at $\alpha = 180^\circ$.

Similar results were found for the inverse of the condition number (Figure 4.7). The largest

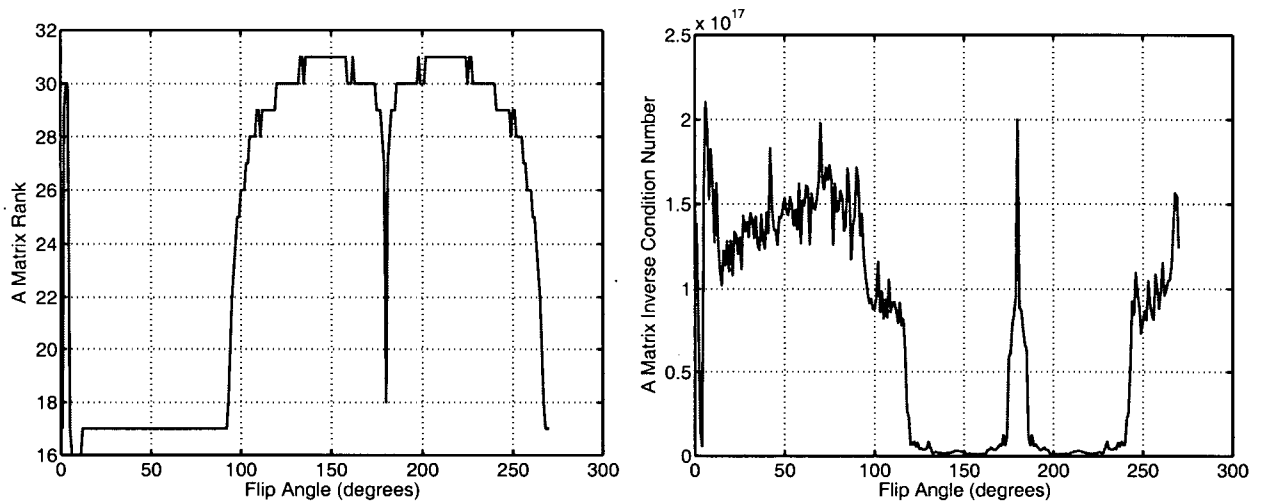


Figure 4.7: The rank (left) and inverse of the condition number (right) of A^α based on a 32 echo decay with $TE = 10$ ms and $TR = 800$ ms.

ratio (smallest to largest singular values) was 105.2686×10^{-17} at $\alpha = 158^\circ$ and the lowest was 0.4996×10^{-17} at $\alpha = 180^\circ$.

200 Echoes

Similar results were found with 200 echoes. The rank (Figure 4.8) was found to be a maximum (rank of 50) at $\alpha = 156^\circ$ and was the lowest (rank of 24) at $\alpha = 180^\circ$.

Similar results were found for the inverse of the condition number (Figure 4.8). The largest ratio (smallest to largest singular values) was 0.8023×10^{-17} at $\alpha = 150^\circ$ and the lowest was 0.0021×10^{-17} at $\alpha = 180^\circ$.

The small differences in the inverse of the condition number on opposite sides of $\alpha = 180^\circ$ was found to be due to very small differences in the A^α matrices. For example, the matrix with the largest inverse condition number was A^{208} , but the difference between The mono-exponential decay curves in A^{208} and A^{152} was less than 10^{-13} .

Conclusions

The matrix A^{180} has the lowest rank and the highest condition number and therefore is about the worst matrix with which to calculate T_2 distribution. By measuring the decay curve with a refocusing pulse flip angle of $\alpha = 159^\circ$ a higher rank (almost double) and a lower condition

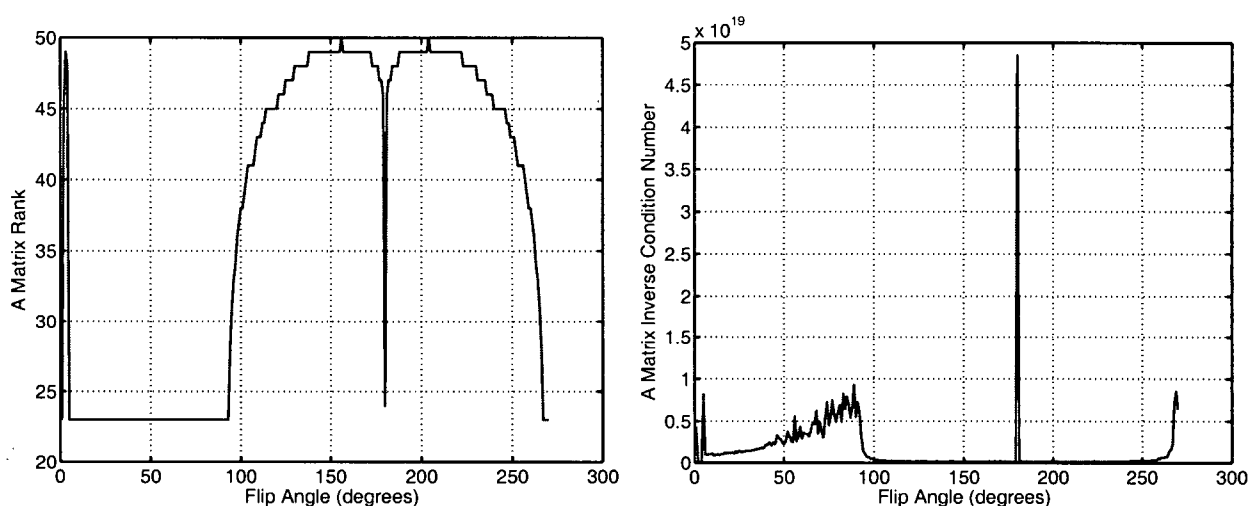


Figure 4.8: The rank (left) and inverse of the condition number (right) of A^α based on a 200 echo decay with $TE = 5$ ms and $TR = 800$ ms.

number (two orders of magnitude) should allow for better T_2 quantification. Another benefit of a multi-echo pulse sequence using 159° non-composite pulses is that the SAR would be lower than that of a sequence using 180° pulses by a factor of $(180/159)^2 = 1.28$. Even though there is a large relative change in the inverse of the condition number from $\alpha = 159^\circ$ to $\alpha = 180^\circ$, the magnitude of the inverse of the condition number for both flip angles is very large. Therefore, the theoretical gain in the matrix based on $\alpha = 159^\circ$ would likely not be realized given the SNR of the data from typical *in vivo* MRI data.

4.3.2 Bi-Exponential Parameters From Incorrect α

To determine the miscalculation of the bi-exponential parameters that result when an incorrect flip angle is assumed.

A bi-exponential model was used with a short T_2 compartment of $\rho^s = 200$ and $T_2^s = 20$ ms and $\rho^m = 800$ and $T_2^m = 80$ ms. A true decay curve was created using the bi-exponential model parameters and refocusing pulse flip angles of $\alpha_{\text{true}} = 90^\circ, 100^\circ, \dots, 180^\circ$. For each true decay curve one thousand realizations of $SNR = 200$ quadrature noise (Gaussian on two channels) were added.

The non-negative least squares algorithm was applied to each decay curve, assuming the refocusing pulse was $\alpha = 180^\circ$, and the decay curve parameters were calculated.

The myelin water fraction, proton densities and T_2 s had less than 10% error for $\alpha \geq 170^\circ$ (Table 4.4). All parameters were incorrectly determined when $\alpha < 170^\circ$. Therefore, accurate and precise quantification of T_2 parameters requires the flip angle be calculated as well.

α_{true}	f^s	T_2^s	f^m	T_2^m	χ^2
90	0.000 (0.000)	0.000 (0.000)	1.000 (0.000)	107.707 (0.956)	1123.617
100	0.000 (0.000)	0.000 (0.000)	1.000 (0.000)	98.013 (1.204)	955.397
110	0.000 (0.000)	0.000 (0.000)	1.000 (0.002)	89.886 (1.212)	767.491
120	0.000 (0.000)	0.000 (0.000)	0.984 (0.029)	82.727 (1.783)	579.248
130	0.003 (0.029)	0.716 (5.805)	0.919 (0.083)	75.387 (4.323)	405.741
140	0.150 (0.147)	25.070 (22.278)	0.838 (0.142)	82.402 (9.003)	256.958
150	0.255 (0.076)	34.956 (7.518)	0.744 (0.074)	86.947 (4.419)	142.229
160	0.219 (0.048)	26.921 (5.214)	0.779 (0.047)	82.931 (3.244)	66.923
170	0.209 (0.048)	21.753 (5.071)	0.790 (0.047)	80.270 (3.217)	32.087
180	0.204 (0.044)	19.804 (4.620)	0.794 (0.044)	79.259 (2.962)	26.948

Table 4.4: Measured parameters of a bi-exponential T_2 decay curve when the nominal flip angle is assumed to be $\alpha = 180^\circ$, but isn't. The true parameters are: $f^s = 0.20$, $dn^s = 200$, $T_2^s = 20$, $f^m = 0.80$, $dn^m = 800$, $T_2^m = 80$.

4.3.3 NNLS $^\alpha$ Multi-Exponential Simulations

A set of noise simulations were used to assess the accuracy and precision of the parameters of the T_2 distribution and refocusing pulse flip angle. A bi-exponential T_2 distribution as in Section 4.3.2 was used. The true parameters were $f^s = 0.20$, $T_2^s = 20$ ms, $f^m = 0.80$, and $T_2^m = 80$ ms.

The mean and standard deviation of the estimated parameters are shown in Table 4.5. As in the mono-exponential results, the accuracy of the parameters was within 10% for $\alpha > 100^\circ$. The standard deviation increased as the refocusing pulse decreased. As in the mono-exponential case, the simulations were repeated with the noise scaled by $1/\sin^2(\alpha/2)$. When the noise was scaled, the standard deviations of the parameters were similar as a function of α .

Noise simulations assessed the variability of the decay curve parameters for a bi-exponential distribution simulated with refocusing pulses from 90° to 180° . Table 4.5 shows the means and standard deviations of the parameters estimated by the NNLS $^\alpha$ algorithm. All estimated means were within 10% of truth for $\alpha > 100^\circ$.

In the multi-exponential noise simulations, the mean α was 2.5° lower than the true α and the variability was higher compared to the variability of the other true α . This was likely due

to noise in the decay curve causing noise in the α - χ^2 curve near 180° and the minimization of the outer loop settling at slightly less than $\alpha = 180^\circ$. The NNLS $^\alpha$ algorithm was robust in the presence of noise and was able to find the best refocusing pulse flip angle.

α_{true}	α	f_s	$T_{2,s}$	f_m	$T_{2,m}$
90	89.87 (1.44)	0.20 (0.13)	15.90 (10.63)	0.79 (0.17)	73.33 (15.66)
100	99.81 (1.47)	0.20 (0.12)	16.65 (9.67)	0.79 (0.15)	74.50 (13.89)
110	109.83 (1.57)	0.21 (0.11)	17.75 (9.17)	0.78 (0.12)	76.12 (12.15)
120	119.81 (1.63)	0.20 (0.10)	18.06 (8.20)	0.79 (0.10)	76.55 (9.98)
130	129.80 (1.68)	0.21 (0.09)	18.32 (7.70)	0.78 (0.10)	76.77 (9.78)
140	139.72 (1.72)	0.20 (0.08)	18.33 (6.43)	0.79 (0.08)	77.06 (7.98)
150	149.88 (1.96)	0.20 (0.07)	18.61 (6.11)	0.79 (0.07)	77.12 (7.44)
160	159.80 (2.10)	0.20 (0.07)	18.29 (6.29)	0.79 (0.07)	77.16 (7.03)
170	170.01 (2.98)	0.20 (0.07)	17.81 (6.87)	0.79 (0.07)	77.04 (7.21)
180	176.76 (2.97)	0.21 (0.07)	17.97 (6.62)	0.79 (0.07)	77.61 (6.78)

Table 4.5: Noise simulation where the decay curve parameters and refocusing pulse flip angle were estimated from 1,000 realizations of noise for $\alpha = 90^\circ, 100^\circ, \dots, 180^\circ$. The true bi-exponential distribution was $f_s = 0.2$, $T_{2,s} = 20$ ms, $f_m = 0.8$ and $T_{2,m} = 80$ ms. Flip angles are in degrees and T_2 in milliseconds.

4.3.4 Phantoms

The multi-exponential algorithm, NNLS $^\alpha$, to calculate the multi-component T_2 was validated based on a set of MRI scans of the nickel/agarose phantoms. The phantoms were scanned with the MESE $_c$ sequence, from which, the T_2 were compared to T_2 calculated from the MESE $_o$ sequence. The refocusing pulse flip angles were calculated from the MESE $_c$ sequence, as well, and compared to flip angles calculated from a technique by Stollberger [81]. The T_1 relaxation times were estimated from a pulse-saturation experiment for reference.

4.3.4.1 Methods

Data Acquisition

The T_2 measurements were done with a 32 echo MESE $_o$ pulse sequence with $TE = 10, 20, \dots, 320$ ms. Other parameters were $TR = 3000$ ms, 2 averages. The T_2 measurements were done with a 32 echo MESE $_c$ pulse sequence with an echo spacing of 12.1 ms. Other parameters were $TR = 3000$ ms, 2 averages. The B_1 measurements were calculated from a pair of spin echo images [81], the

first image was a standard spin-echo image, the second had an excitation pulse of 180° . Other parameters included $TE = 11.1$ ms, $TR = 3000$ ms, and no signal averaging.

Data Analysis

For each multi-echo data acquisition the decay curve was calculated as the mean signal intensity over the phantom and was fit using NNLS. The B_1 , from the pair of spin-echo images, was calculated as [81]:

$$\alpha_S = \cos^{-1} \left(\frac{I_{2\alpha}}{2 I_\alpha} \right) \quad (4.18)$$

where I_α was the standard spin-echo image with a prescribed excitation pulse of $\alpha = 90^\circ$, $I_{2\alpha}$ was the spin-echo image with a prescribed excitation pulse of 180° , and α_S was the spatially varying flip angle calculated by the Stollberger method. The excitation pulses will vary spatially and therefore, the prescribed $\alpha = 90^\circ$ will not be 90° throughout the slice.

For each phantom, the mean signal intensity over the phantom was fit to the equation $SI(TR_i) = \rho [1 - \exp(-TR/T_1)]$.

4.3.4.2 Results

T_2 Calculation

The T_2 relaxation times, shown in Table 4.6, were calculated from the $MESE_o$ sequence (for reference) and from the $MESE_c$ sequence. The T_2 relaxation times calculated from the decay curve collected by the $MESE_c$ sequence were within 8% of the relaxation times calculated from the decay curve collected by the optimized $MESE_o$ sequence.

The T_1 relaxation times, calculated from the pulse-saturation sequence, are shown in Table 4.8, for reference.

Phantom	MESE _o T ₂ (ms)	MESE _c T ₂ (ms)
bottom_left	24.3	22.9
bottom_middle	86.4	80.7
bottom_right	26.1	24.2
top_left	316.6	304.6
top_middle	99.3	91.7
top_right	110.6	102.8

Table 4.6: T₂ time calculated from the MESE_o sequence and the MESE_c (with the flip angle calculated).

The refocusing pulse flip angle was calculated by the Stollberger method (α_S) and from the decay curves acquired with the MESE_c sequence (α) and are shown in Table 4.7. The refocusing pulses calculated from the decay curve were within 6% of the refocusing pulses calculated by the Stollberger method.

Phantom	α (°)	α_S (°)
bottom_left	163.0	165.7
bottom_middle	159.0	166.3
bottom_right	163.0	167.7
top_left	156.0	164.8
top_middle	158.0	165.1
top_right	160.0	166.9

Table 4.7: The refocusing pulse flip angle was calculated by the Stollberger method (α_S) and from the decay curves acquired with the MESE_c sequence (α).

Phantom	T ₁ (ms)
bottom_left	343.4
bottom_middle	352.9
bottom_right	690.7
top_left	730.7
top_middle	712.0
top_right	1843.9

Table 4.8: Estimated T₁ from curve fits of five points (TR = 100, 300, 800, 2000, 3000 ms) from a pulse saturation experiment.

4.3.4.3 Conclusions

The nickel/agarose phantoms were scanned using the MESE_c sequence from which the T_2 and refocusing pulse flip angle α were estimated. The T_2 estimated from each phantom was within 10% of the estimated T_2 from the MESE_o sequence. The estimated refocusing pulse flip angle was also within 10% of the flip angle estimated by the Stollberger method.

4.3.5 *In Vivo* Multi-Exponential Fits

Two sets of *in vivo* scans were acquired, of a volunteer, with different setting of the refocusing pulse flip angle. For one scan, the flip angle was set to $\alpha_{\text{nom}} = 180^\circ$ and for the second scan, the flip angle was set to $\alpha_{\text{nom}} = 150^\circ$. From these two scans, the myelin water map was calculated, as was a map of the refocusing pulse flip angle and the mean T_2 .

4.3.5.1 Methods

Two sets of scans were done on a normal volunteer using the 16-echo MESE_c with $\text{TR} = 3$ s, $\text{TE} = 11.096$ ms, 256×128 freq \times phase, 24 cm FOV and 4 averages. The first scan was acquired as per normal with $\alpha_{\text{nom}} = 180^\circ$. The second scan was acquired with $\alpha_{\text{nom}} = 150^\circ$, by scaling the amplitude of the refocusing pulses by a factor of 150/180. Due to the long scan time of the two sequences, a MESE_o scan was not acquired.

The T_2 distribution was estimated voxel-by-voxel in each scan as well as the refocusing pulse flip angle using the algorithm described in Section 4.3.1. Maps of the myelin water fraction, refocusing pulse flip angle and mean T_2 calculated from each scan were compared visually. For the first analysis, the T_2 information was calculated along with the flip angle at every voxel (“Variable Flip Angle”) in the image and for the second analysis the flip angle was assumed $\alpha = 180^\circ$ at every voxel (“Fixed Flip Angle”).

4.3.5.2 Results

Variable Flip Angle

Maps of the myelin water were estimated from the multi-echo data with $\alpha_{\text{nom}} = 180^\circ$ and with $\alpha_{\text{nom}} = 150^\circ$ and are shown in Figure 4.9. The map of the myelin water was qualitatively very similar to other myelin water maps acquired with the optimized MESE_o . The map from the

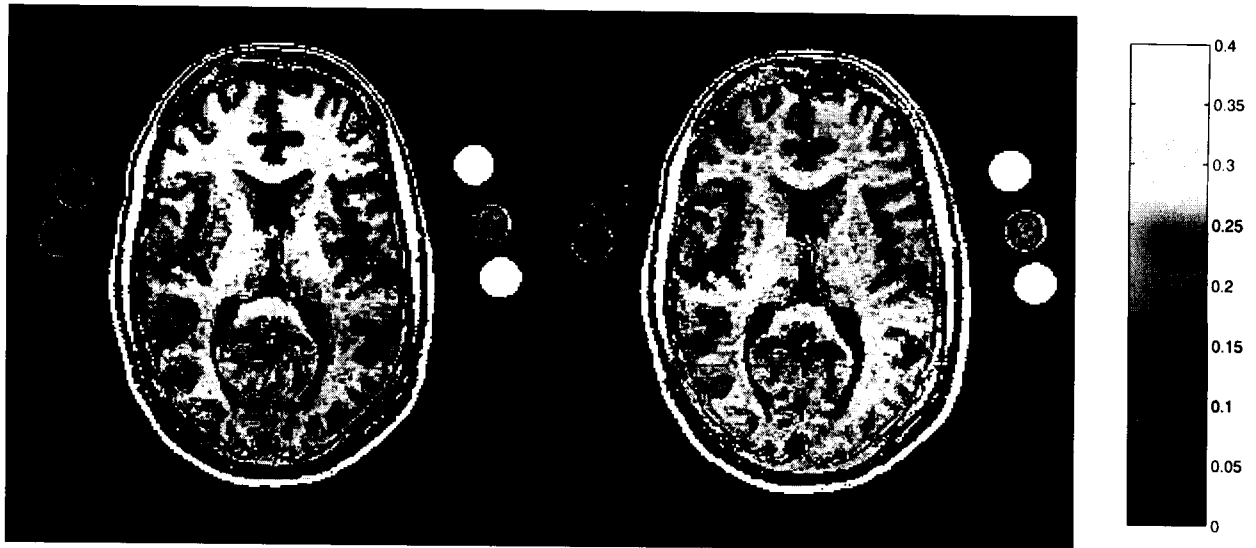


Figure 4.9: The myelin water maps calculated from the pulse sequence with a refocusing pulse flip angle prescribed as 180° (left) and 150° (right).

$\alpha_{\text{nom}} = 180^\circ$ (Figure 4.9, left) was brighter in the top part of the image compared to the bottom part of the image. This shading was not seen on the myelin water map from $\alpha_{\text{nom}} = 150^\circ$ (Figure 4.9, right). The histogram of the myelin water fraction, within the brain, was narrower for $\alpha_{\text{nom}} = 150^\circ$ than for $\alpha_{\text{nom}} = 180^\circ$. As well, there was more myelin water structure visible in the middle portion of the myelin water map acquired with $\alpha_{\text{nom}} = 150^\circ$. The bright phantoms on the right side of each myelin water map are the short T_2 nickel/agarose phantoms.

Region	MWF ($\alpha_{\text{nom}} = 150^\circ$)	MWF ($\alpha_{\text{nom}} = 180^\circ$)
caudate (left)	3.6 (1.7)	0.8 (1.5)
caudate (right)	2.4 (2.2)	0.1 (0.2)
putamen (left)	3.2 (2.7)	1.6 (1.7)
putamen (right)	3.9 (2.3)	0.1 (0.0)
frontal (left)	16.4 (2.3)	20.9 (2.0)
frontal (right)	15.3 (1.9)	17.8 (4.1)
genu	18.1 (5.9)	24.6 (4.4)
ic (left)	20.8 (1.5)	24.4 (4.5)
ic (right)	16.9 (2.5)	22.4 (1.7)
post (left)	13.0 (3.6)	13.3 (2.6)
post (right)	10.8 (4.3)	8.3 (2.0)

Table 4.9: Percent myelin water estimated from scans with $\alpha_{\text{nom}} = 150^\circ$ and $\alpha_{\text{nom}} = 180^\circ$.

The maps of the refocusing pulse flip angles were calculated voxel-by-voxel from the two scans, one with $\alpha_{\text{nom}} = 180^\circ$ and the other with $\alpha_{\text{nom}} = 150^\circ$, and are the top pair of images in Figure 4.10. The mean refocusing pulse flip angle from MESE_c with $\alpha_{\text{nom}} = 150^\circ$ was 138.2° and the mean refocusing pulse flip angle with $\alpha_{\text{nom}} = 180^\circ$ was 156.3° . The bottom pair of images in Figure 4.10 are the refocusing pulse flip angle maps normalized by the mean refocusing pulse flip angle.

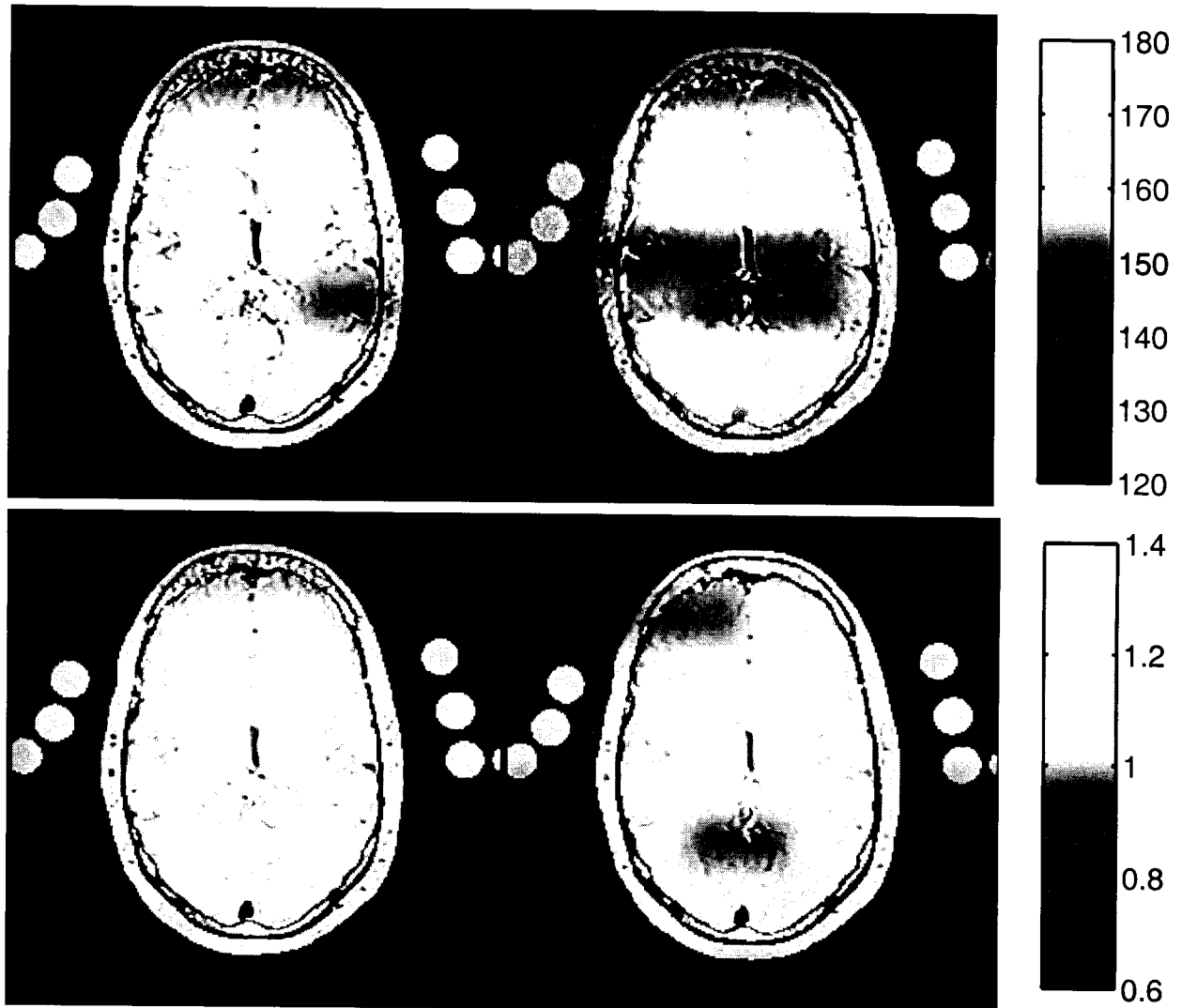


Figure 4.10: The refocusing pulse flip angle maps calculated from the pulse sequence with a refocusing pulse flip angle prescribed as 180° (left) and 150° (right). The top plot is in degrees and the bottom plot was normalized by the mean flip angle over the whole map.

Region	α ($\alpha_{\text{nom}} = 150^\circ$)	α ($\alpha_{\text{nom}} = 180^\circ$)
caudate (left)	140.0 (1.9)	157.5 (1.6)
caudate (right)	142.3 (0.9)	158.6 (1.1)
putamen (left)	139.9 (1.3)	157.2 (1.0)
putamen (right)	140.8 (1.1)	156.6 (2.4)
frontal (left)	139.8 (1.2)	159.3 (1.5)
frontal (right)	141.5 (1.1)	161.4 (1.5)
genu	142.2 (4.4)	163.6 (3.9)
ic (left)	143.4 (1.4)	161.1 (1.3)
ic (right)	143.4 (2.1)	158.1 (2.7)
post (left)	139.1 (2.0)	159.1 (2.0)
post (right)	138.4 (1.8)	158.7 (1.7)

Table 4.10: Refocusing pulse flip angle calculated over the regions from the scans with $\alpha_{\text{nom}} = 150^\circ$ and $\alpha_{\text{nom}} = 180^\circ$.



Figure 4.11: The arithmetic mean T_2 maps calculated from the pulse sequence with a refocusing pulse flip angle prescribed as 180° (left) and 150° (right).

The geometric mean T_2 of the medium T_2 component estimated from $MESE_c$ with $\alpha_{nom} = 180^\circ$ and $\alpha_{nom} = 150^\circ$ are the left and right images, respectively, in Figure 4.11. The mean T_2 of the medium component was calculated from several regions within the brain and is shown in Table 4.11. The $\overline{T_2^m}$ from the two scans were within 4%.

Region	$\overline{T_2^m}$ (ms)	$\overline{T_2^m}$ (ms)
caudate (left)	81.1 (2.1)	79.0 (1.6)
caudate (right)	80.5 (1.5)	79.4 (1.1)
putamen (left)	71.6 (1.6)	70.3 (0.6)
putamen (right)	71.6 (1.7)	70.5 (1.4)
frontal (left)	76.9 (1.3)	77.5 (2.4)
frontal (right)	76.8 (1.1)	75.4 (1.7)
genu	74.6 (5.4)	74.1 (2.0)
ic (left)	77.3 (0.8)	79.3 (5.2)
ic (right)	76.9 (1.0)	78.4 (4.2)
post (left)	78.4 (1.9)	81.3 (4.1)
post (right)	76.9 (1.2)	77.7 (1.2)

Table 4.11: Geometric mean T_2 of the medium component from select regions throughout the image.

The χ^2 , calculated during the estimation of the T_2 distribution, is shown in Figure 4.12. The regions of high χ^2 , and therefore, poor curve fit, are primarily in the cerebrospinal fluid (CSF). There are two possible reasons. First, the CSF is flowing and therefore may cause artifacts on the decay curves that can not be accounted for by echo formation. Second, the T_2 of CSF is very long, but for this data only 16 echoes were collected with an echo spacing of 11.1 ms, therefore, the decay curve may not be sufficiently sampled to accurately determine T_2 distribution of CSF.



Figure 4.12: The χ^2 maps calculated from the pulse sequence with a refocusing pulse flip angle prescribed as 180° (left) and 150° (right).

Fixed Flip Angle

For comparison, the T_2 distribution was calculated voxel-by-voxel from the two scans assuming $\alpha_{\text{nom}} = 180^\circ$. Based on the results in Section 4.3.2, I expect the myelin water fraction to decrease in regions where $\alpha < 180^\circ$. Figure 4.13 shows the myelin water fraction calculated from the two scans assuming $\alpha_{\text{nom}} = 180^\circ$. As expected, the regions of the image with $\alpha < 180^\circ$, for example, the lower part of the image, show a greatly reduced myelin water fraction.

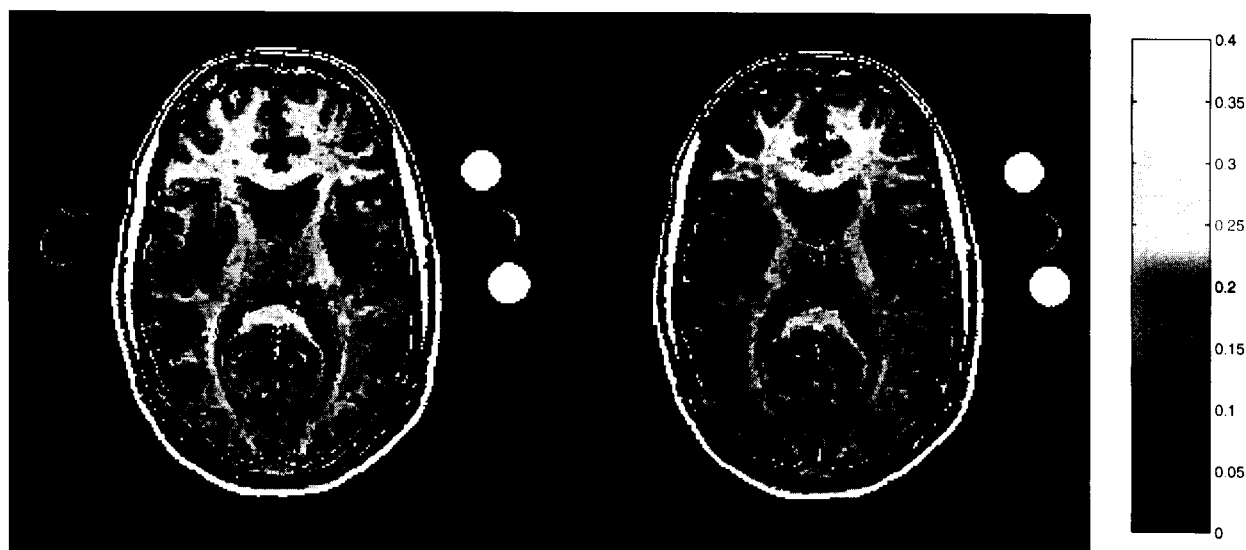


Figure 4.13: The myelin water maps calculated from the pulse sequence with a refocusing pulse flip angle prescribed as 180° (left) and 150° (right). The NNLS algorithm was applied assuming, incorrectly, the refocusing pulse flip angle was 180° .

4.3.5.3 Conclusions

The myelin water map estimated from both scans was similar to myelin water maps estimated from an optimized MESE_o sequence. Quantitatively the estimated percent myelin water, refocusing pulse flip angle, and geometric mean T_2 from the two scans corresponded very well. The voxels in the brain with CSF tended to be poorly fit (high χ^2 misfit) which could be due to flow effects or an under-sampled T_2 decay curve.

4.4 Multi-Slice, Multi-Echo

4.4.1 Introduction

The current multi-echo acquisition method, MESE_o , is able to collect only a single slice within the given scan time, due to the hard, composite pulses. The MESE_c pulse sequence can be used to acquire multiple slices within one slab with the same SNR as the MESE_o sequence. This is important when viewing pathology, for example multiple sclerosis lesions, as they extend across several slices. Acquiring more slices will enable better interpretation of the MS lesions. The ability to collect multiple slices in a clinically feasible scan time will be an important step in the

use of the myelin water imaging.

I scanned a volunteer using the 3D MESE_c sequence. Six slices were acquired, within the brain, as well as a slice acquired with the MESE_o for comparison. Myelin water maps were calculated for each slice of the MESE_c sequence and the single slice of the MESE_o. The myelin water maps were compared as well as the myelin water fraction from select regions.

4.4.2 Methods

Two sets of data were collected: first, a standard 32 echo MESE_o with 4 averages and TE = 10 ms; and second, a 6 slice slab, 42 echo 3D-MESE_c sequence with 1 average and TE = 10.1 ms. Other parameters for both sequences were: FOV = 24 cm, TR = 3000 ms, and 5 mm thick slices. Phantoms were placed on either side of the head (top and bottom phantoms on right side of image were the short T₂ phantoms).

Both sets of multi-echo data were filtered with the anisotropic diffusion filter algorithm (3 iterations) and the myelin water maps were calculated, per voxel, with the small norm NNLS model described in Section 1.7.1.2.

A regional T₂ analysis compared decay curve parameters estimated by a mono-exponential and NNLS from the MESE_o dataset and the corresponding slice of the 6 slice slab MESE_c data set. Finally, the myelin water map was calculated such that the refocusing pulse flip angle was calculated per voxel. The resulting myelin water map was compared to that calculated assuming $\alpha = 180^\circ$ throughout the image.

4.4.3 Results and Discussion

4.4.3.1 Images

Figure 4.14 shows the TE = 10 ms image (top) and the TE = 10.1 ms images (second and third rows) of the brain. The outer slices of the six slice slab (first image of row 2 and last image of row 3) have aliasing artifact due to the slab selective excitation pulse. The aliasing artifact occurs in the slice phase encode direction as the head extends beyond the FOV and spins are not mapped to the correct location. The images are normally not reconstructed during a clinical scan, but were in this work for completeness.

The myelin water maps estimated from the MESE_o sequence and each slice of the MESE_c

sequence are shown in Figure 4.15.

As can be seen in Figure 4.16 there is a small increase in the myelin water fraction in the top right portion of the image.

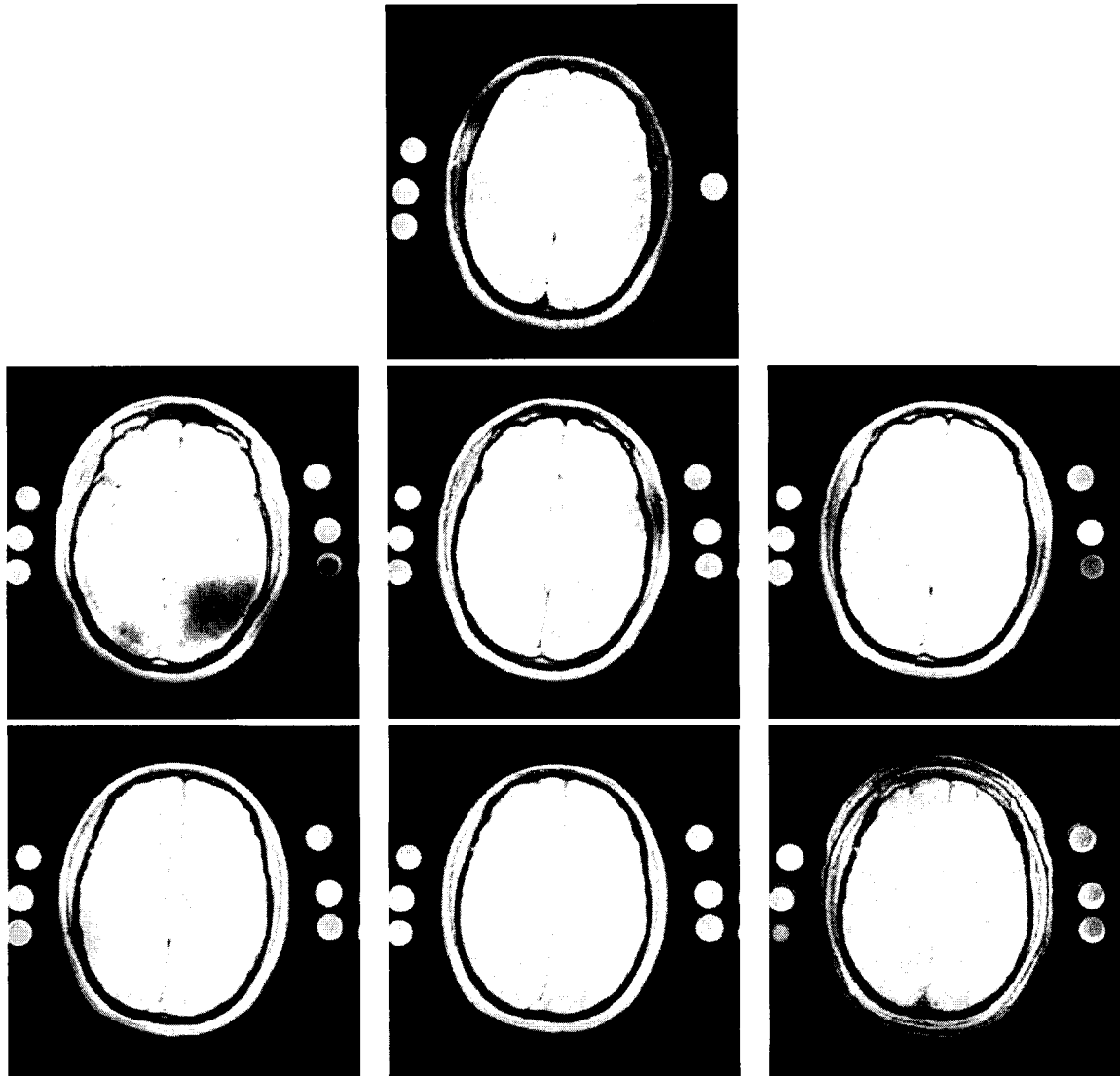


Figure 4.14: The $TE = 10$ ms image from the four average, 32 echo $MESE_o$ sequence (top row). The six slices of the six slice slab $MESE_c$ acquisition (bottom two rows). The outside two slices of the slab selective sequence (second row, left image and third row, right image) have an aliasing artifact which results in a ghost-like overlay of another slice.

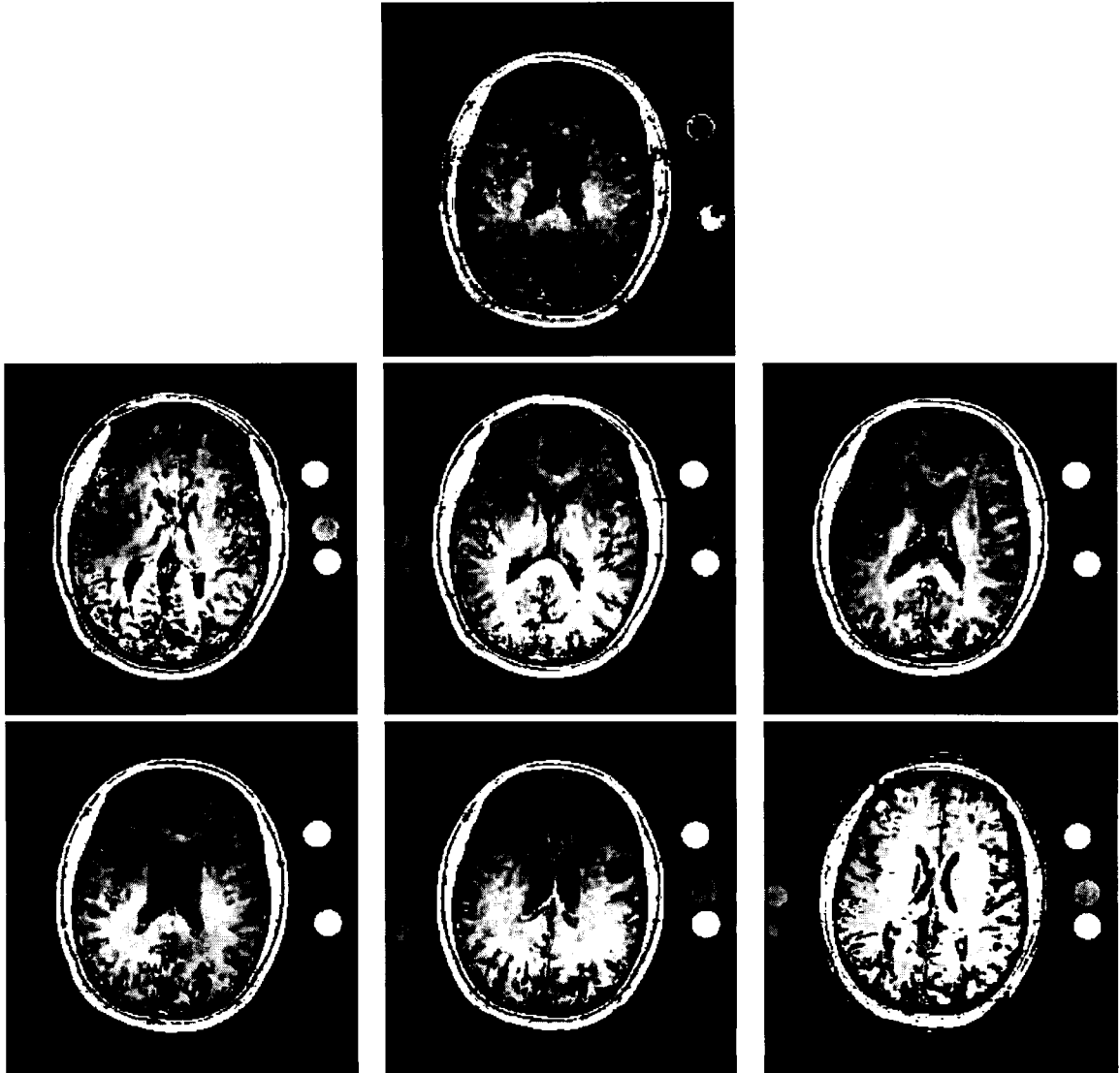


Figure 4.15: Myelin water maps calculated using the small norm NNLS solution based on data from the 6 slice, 42 echo pulse sequence $MESE_c$. The two outside slices (top left and bottom right) were not expected to be reasonable as they had significant (as expected) aliasing artifacts. The images were thresholded based on other parameters calculated (global variance, χ^2 and global density) which is why the two phantoms on the right side were thresholded.

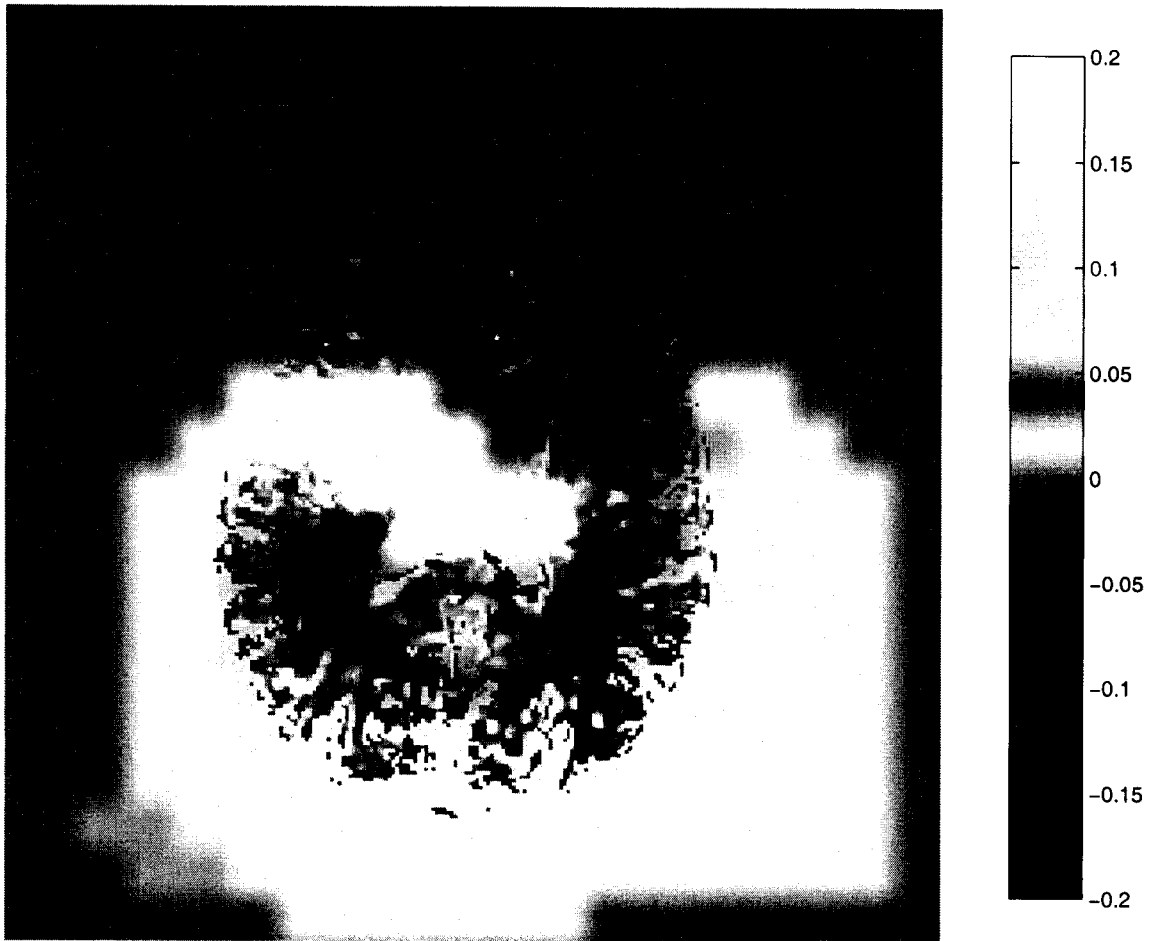


Figure 4.16: Difference between the myelin water map calculated from the MESE_o sequence and the myelin water map calculated from the MESE_c sequence.

4.4.3.2 Regional Analysis

Regions were selected in white matter and gray matter areas of the earliest echo image. The signal intensity of each region was averaged, for each echo, to calculate a T_2 decay curve. The NNLS ^{α} algorithm was applied to the decay curve. The short T_2 and medium T_2 parameters were calculated for various regions of interest (left and right): frontal white matter (frontal_wm), genu of the corpus callosum (genu_wm), posterior white matter (post_wm), mid-brain white matter (mid_wm), peri-ventricular gray matter (perivent_gm), and posterior gray matter (post_gm). The myelin water fraction calculated from data acquired with the MESE_c sequence, was always higher than the myelin water fraction calculated from the data acquired with the MESE_o sequence (Table 4.12). The decay curves were further assessed by comparing curves acquired from the two pulse sequences. One example T_2 decay curve is shown in Figure 4.17. In general, the T_2 decay curve acquired with the slab selected, multi-slice MESE_c sequence decayed faster than the T_2 decay curve acquired with the MESE_o sequence. The MESE_c sequence may have subtle differences in the acquisition method to accommodate the acquisition of multiple slices within the slab.

Structure	Sequence	NNLS			
		Short ρ	Short T_2	Med ρ	Med T_2
frontal_wm_l	MESE _o (180)	47.258 (4.6%)	15.000	931.387 (91.5%)	79.337
frontal_wm_l	MESE _c (180)	78.021 (8.0%)	36.109	863.296 (88.1%)	80.566
frontal_wm_l	MESE _c (174)	83.473 (8.5%)	34.430	873.974 (88.8%)	81.122
frontal_wm_r	MESE _o (180)	36.290 (3.5%)	15.000	977.200 (93.7%)	79.755
frontal_wm_r	MESE _c (180)	138.347 (13.5%)	24.656	885.655 (86.5%)	83.284
frontal_wm_r	MESE _c (180)	138.347 (13.5%)	24.656	885.655 (86.5%)	83.284
genu_wm_l	MESE _o (180)	94.612 (9.2%)	22.819	908.342 (88.0%)	77.340
genu_wm_l	MESE _c (180)	150.983 (15.2%)	37.115	837.326 (84.4%)	78.994
genu_wm_l	MESE _c (180)	150.983 (15.2%)	37.115	837.326 (84.4%)	78.994
genu_wm_r	MESE _o (180)	99.003 (9.3%)	15.127	947.429 (89.4%)	78.345
genu_wm_r	MESE _c (180)	179.500 (17.8%)	35.845	798.541 (79.3%)	81.258
genu_wm_r	MESE _c (173)	179.886 (17.8%)	35.065	799.187 (78.9%)	80.791
post_wm_l	MESE _o (180)	88.007 (8.5%)	17.971	942.529 (91.5%)	92.041
post_wm_l	MESE _c (180)	244.997 (24.4%)	35.921	686.287 (68.4%)	96.742
post_wm_l	MESE _c (180)	244.997 (24.4%)	35.921	686.287 (68.4%)	96.742
post_wm_r	MESE _o (180)	70.068 (6.7%)	15.291	808.996 (77.5%)	87.281
post_wm_r	MESE _c (180)	224.328 (22.3%)	40.148	589.941 (58.5%)	86.406
post_wm_r	MESE _c (180)	224.328 (22.3%)	40.148	589.941 (58.5%)	86.406
mid_wm_l	MESE _o (180)	177.964 (17.2%)	29.219	607.018 (58.8%)	82.458
mid_wm_l	MESE _c (180)	215.597 (22.4%)	39.133	500.218 (52.0%)	79.342
mid_wm_l	MESE _c (180)	215.597 (22.4%)	39.133	500.218 (52.0%)	79.342
mid_wm_r	MESE _o (180)	168.491 (16.7%)	29.417	606.233 (60.0%)	85.955
mid_wm_r	MESE _c (180)	228.307 (23.1%)	30.727	567.696 (57.3%)	86.775
mid_wm_r	MESE _c (178)	229.005 (23.1%)	30.709	567.653 (57.3%)	86.831
perivent_gm_l	MESE _o (180)	0.000 (0.0%)	—	1161.671 (100.0%)	76.568
perivent_gm_l	MESE _c (180)	0.000 (0.0%)	—	1196.713 (100.0%)	68.768
perivent_gm_l	MESE _c (172)	0.000 (0.0%)	—	1200.621 (100.0%)	68.533
perivent_gm_r	MESE _o (180)	17.381 (1.5%)	15.000	1173.212 (98.5%)	81.559
perivent_gm_r	MESE _c (180)	0.000 (0.0%)	—	1163.000 (100.0%)	73.643
perivent_gm_r	MESE _c (180)	0.000 (0.0%)	—	1163.000 (100.0%)	73.643
post_gm_l	MESE _o (180)	0.000 (0.0%)	—	1018.847 (100.0%)	86.499
post_gm_l	MESE _c (180)	197.091 (19.1%)	42.066	745.337 (72.2%)	79.251
post_gm_l	MESE _c (159)	139.822 (13.1%)	22.560	926.926 (86.9%)	79.282
post_gm_r	MESE _o (180)	0.000 (0.0%)	—	873.843 (83.6%)	84.274
post_gm_r	MESE _c (180)	199.367 (19.3%)	42.229	607.816 (59.0%)	79.542
post_gm_r	MESE _c (172)	209.809 (20.3%)	41.925	599.110 (58.0%)	80.114

Table 4.12: Decay curve parameters estimated for white matter regions throughout the brain. The small norm NNLS solution was calculated from the MESE_o and MESE_c data. For each triple of lines, the parameters were estimated based on the assumption that the refocusing pulse flip angle was $\alpha = 180^\circ$, the parameters on the bottom line were estimated based a best estimate of the flip angle (shown in brackets). The NNLS short and medium parameters were estimated from bins $10 \leq T_2 \leq 50$ ms and $50 < T_2 < 120$ ms, respectively.

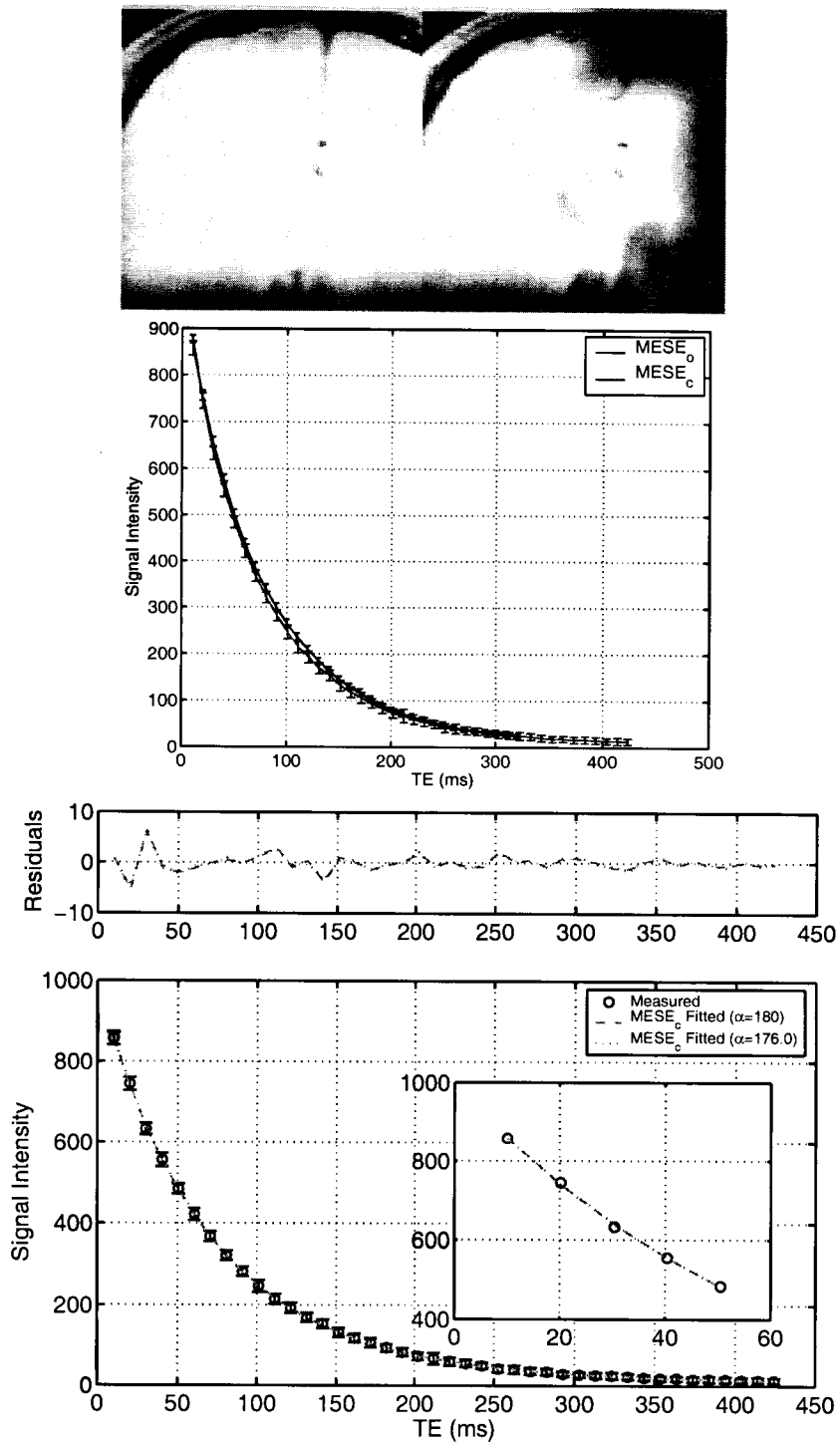


Figure 4.17: Region (genu_wm_l) shown on the top figure, T_2 decay curves acquired by the $MESE_o$ and $MESE_c$ (middle figure). NNLS fits to the $MESE_c$ data, one assuming the refocusing pulse flip angle was 180° and the other where the optimal flip angle was calculated (bottom figure).

4.4.3.3 Flip Angle Estimation

The slice from the slab MESE_c that corresponded to the slice from the single-slice MESE_o was further analyzed. The myelin water map was calculated per voxel in two ways: 1) assuming that the refocusing pulse flip angle was $\alpha = 180^\circ$ everywhere (mwm^{180}) and 2) estimating the refocusing pulse flip angle per voxel (mwm^e).

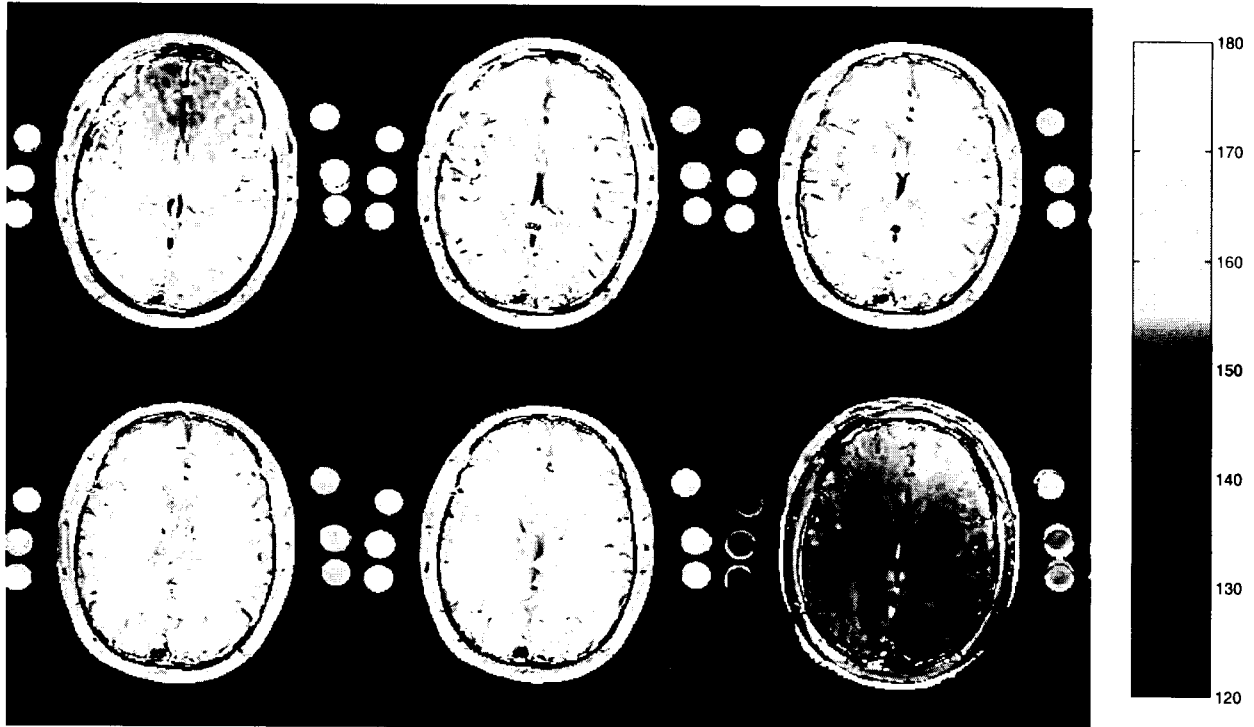


Figure 4.18: Maps of the refocusing pulse flip angle calculated from the 6 slice, 42 echo pulse sequence MESE_c . The two outside slices (top left and bottom right) were not expected to be reasonable as they had significant (as expected) aliasing artifacts.

4.4.4 Conclusions

Moving from single-slice to multiple slices (slab selection) per acquisition will greatly improve the utility of the myelin water mapping. To acquire multiple slices per acquisition slice-selective refocusing pulses are necessary. The flip angle of slice-selective refocusing pulses is inaccurate and must be accounted for during T_2 estimation from a multi-echo decay data. A set of six slices, each with 42 echoes, was acquired. Myelin water maps and flip angle maps were calculated from each of the six slices. Myelin water maps of the inner four slices were similar to myelin water

maps calculated from MESE_o. The T₂ estimated from the decay curves of regions within the six slices had a faster decay than expected, but is believed to be a problem with the pulse sequence and not the theory.

4.5 Non 90° Excitation Pulse

The standard MRI pulse sequence contains two types of RF pulses, an excitation pulse, used to rotate the magnetization away from the longitudinal axis, and a set of refocusing pulses, used to refocus the magnetization in the transverse plane. Both sets of pulses are affected by imperfections in the hardware. The signal intensity along a decay curve is a function of the excitation pulse (α_e), the refocusing pulse (α_r) and the tissue parameters, ρ , T₂, T₁. The goal of this work is to determine the effect of an “imperfect” excitation pulse on quantification of the tissue parameters and flip angles.

4.5.1 Decay Curve Calculation

Given the tissue parameters T₂, T₁, ρ and the pulse sequence parameters TE, α_e and α_r , the decay curves were calculated by using a modified version of Hennig’s work [78]. The magnetization vector $\mathbf{M} = [F \ F^* \ Z \ Z^*]^T$ where F and F^* are transverse magnetization components, Z and Z^* are longitudinal components. The components without a superscript * are dephasing magnetization and components with a superscript * are rephasing magnetization. The initial magnetization is defined to be $\mathbf{M} = [0 \ 0 \ 1 \ 0]^T$ and was then rotated by an angle α based on the rotation matrix:

$$R(\alpha) = \begin{bmatrix} \cos^2(\alpha/2) & \sin^2(\alpha/2) & \sin(\alpha) & 0 \\ \sin^2(\alpha/2) & \cos^2(\alpha/2) & 0 & \sin(\alpha) \\ -1/2 \sin(\alpha) & 1/2 \sin(\alpha) & \cos(\alpha) & 0 \\ 1/2 \sin(\alpha) & -1/2 \sin(\alpha) & 0 & \cos(\alpha) \end{bmatrix}. \quad (4.19)$$

4.5.2 Simulation Methods

Three sets of simulations were done to determine the effect of knowing or not knowing the excitation pulse flip angle α_e . The first simulation (Section 4.5.3) had an excitation pulse that varied and the decay curve parameters were calculated assuming the excitation pulse was $\alpha_e = 90^\circ$ and

the refocusing pulse was calculated. The second simulation (Section 4.5.4) set $\alpha_e = \alpha_r/2$ but assumed the excitation pulse $\alpha_e = 90^\circ$. The third simulation (Section 4.5.5) had the excitation and refocusing pulses varied (but still $\alpha_e = \alpha_r/2$) and calculate both α_e and α_r .

4.5.3 Simulation 1: Inaccurate Excitation and Accurate Refocusing, Assume both Accurate

This simulation will assess the effect of having an inaccurate excitation pulse but a perfect refocusing pulse $\alpha_r = 180^\circ$.

Methods

A set of true decay curves were calculated with the excitation pulse flip angle set to $\alpha_e = 90^\circ, 85^\circ, \dots, 50^\circ$. Other parameters were: $\alpha_r = 180$, 32 echoes, $T_1 = 1000$ ms, $T_2 = 80$ ms, $TR = \infty$, echo spacing = 10 ms and $\rho = 1000$. For each setting of the excitation pulse, 500 realizations of quadrature noise (Gaussian on two channels) with $SNR = 200$ were added to the true decay curve. For each decay curve with noise, α_r was calculated, as well as, ρ , T_2 and χ^2 (the misfit).

Results and Discussion

This simulation assessed the parameter estimation when **only** the excitation pulse was varied and the curve fitting was done assuming only the refocusing pulse was variable. The primary result is that all parameters were estimated as accurately when $\alpha_e \neq 90^\circ$ as when $\alpha_e = 90^\circ$, except for ρ . The average ρ decreased as a function of $\sin(\alpha_e)$. The χ^2 misfit remained constant at approximately 27, therefore the decrease in ρ corresponds very well to a decrease in α_e . This would imply that if the only α_e or ρ changed, they could not be distinguished.

The acquisition of data with an imperfect excitation pulse and perfect refocusing pulse would be unlikely. This simulation was done for completeness and for comparison with Simulation 2 and Simulation 3.

True α_e (°)	α_r (°)	ρ	T_2 (ms)	χ^2
90	176 (4.3)	1011.2 (17.2)	79.2 (2.3)	27.9 (7.5)
85	176 (4.5)	1008.9 (18.8)	79.2 (2.0)	27.6 (7.5)
80	176 (4.5)	996.4 (16.8)	79.1 (2.0)	27.9 (7.5)
75	176 (4.5)	978.3 (18.2)	79.0 (1.7)	27.4 (7.0)
70	176 (4.5)	951.4 (16.7)	79.0 (1.9)	27.7 (7.7)
65	176 (5.0)	917.4 (17.5)	79.1 (2.6)	27.8 (7.7)
60	176 (4.8)	877.6 (18.3)	79.0 (2.7)	26.8 (6.9)
55	176 (4.6)	830.4 (17.7)	79.0 (2.6)	27.3 (7.2)
50	175 (5.2)	777.8 (17.4)	78.9 (3.5)	26.8 (7.0)

Table 4.13: The excitation pulse was varied from 90° to 50° and the parameters were calculated assuming only the refocusing pulse was incorrect. The primary effect of an imperfect excitation pulse is an overall decrease in the decay curve.

4.5.4 Simulation 2: Inaccurate Excitation and Inaccurate Refocusing, Assume Accurate Excitation

This simulation will assess the effect of having $\alpha_e = \alpha_r/2$ but assuming $\alpha_e = 90^\circ$ for the curve fitting. This simulation closer to reality when acquiring multi-exponential data, as spatial nonuniformities in the transmit power will affect both the excitation and refocusing pulses.

Methods

The parameters for the simulation are: 32 echoes, $T_1 = 1000$ ms, $T_2 = 80$ ms, $TR = \infty$, echo spacing = 10 ms and $\rho = 1000$. The excitation pulse was varied: $\alpha_e = 90^\circ, 85^\circ, \dots, 50^\circ$ (and $\alpha_r = 2\alpha_e$ in every case). For each setting of α_e - α_r , 500 realizations of quadrature noise (Gaussian on two channels) with $SNR = 200$ were added to the true decay curve. For each decay curve with noise, α_r was calculated as well as ρ , T_2 and χ^2 (the misfit). The excitation pulse flip angle was assumed to be $\alpha_e = 90^\circ$.

Results and Discussion

The estimated parameters are shown in Table 4.14. The refocusing pulse flip angle α_r was estimated reasonably accurately, but all other parameters had problems. As in the first simulation, ρ decreased almost as a function of $\sin(\alpha_e)$. As well, T_2 decreased as α_e decreased. The χ^2 misfit increased as α_e decreased, therefore the curve fits got progressively worse as the excitation and

refocusing pulses decreased.

True α_e/α_r (°)	α_r (°)	ρ	T_2 (ms)	χ^2
90/180	176 (4.3)	1011.2 (17.2)	79.2 (2.3)	27.9 (7.5)
85/170	173 (6.0)	1004.4 (17.3)	79.6 (2.4)	27.9 (7.6)
80/160	167 (9.6)	983.5 (16.5)	80.1 (2.4)	38.2 (9.2)
75/150	151 (6.3)	974.5 (20.7)	79.4 (2.0)	57.9 (11.7)
70/140	138 (2.3)	955.0 (15.2)	78.9 (2.7)	77.0 (16.0)
65/130	127 (1.9)	925.7 (9.2)	78.6 (2.0)	92.1 (17.4)
60/120	117 (1.7)	902.2 (8.5)	77.2 (1.3)	103.1 (18.7)
55/110	107 (1.4)	871.6 (9.0)	76.3 (1.7)	113.6 (18.7)
50/100	97 (1.3)	852.8 (10.2)	74.0 (0.9)	123.1 (20.4)

Table 4.14: The excitation and refocusing pulses were varied with $\alpha_e = 90^\circ, 85^\circ, \dots, 50^\circ$ and $\alpha_r = 2\alpha_e$. The curve fitting calculated α_r , T_2 , ρ and χ^2 assuming $\alpha_e = 90^\circ$. The true $T_2 = 80$ ms and $\rho = 1000$.

4.5.5 Simulation 3: Inaccurate Excitation and Inaccurate Refocusing

The realistic scenario is the excitation pulse and refocusing pulse are both inaccurate and need to be calculated during T_2 estimation. This simulation will assess the effect of having $\alpha_e = \alpha_r/2$ and calculating both α_e and α_r along with the other parameters.

Methods

The parameters for the simulation were: 32 echoes, $T_1 = 1000$ ms, $T_2 = 80$ ms, $TR = \infty$, echo spacing = 10 ms and $\rho = 1000$. The excitation pulse was varied: $\alpha_e = 90^\circ, 85^\circ, \dots, 50^\circ$ (and $\alpha_r = 2\alpha_e$ in every case). For each setting of α_e , 500 realizations of quadrature noise (Gaussian on two channels) with $SNR = 200$ were added to the true decay curve. For each decay curve with noise, the α_r , α_e , ρ , T_2 and χ^2 (the misfit) were calculated. The decay curve was fit assuming the ratio $\alpha_e/\alpha_r = 1/2$.

Results and Discussion

All parameters (shown in Table 4.15) were estimated accurately, including α_e and α_r . The standard deviation of the estimated T_2 and ρ increased by a factor of two as $\alpha_e = 90^\circ$ to $\alpha_e = 50^\circ$. The standard deviation of the estimated parameters doubled as the excitation/refocusing pulse flip angle halved.

True α_e/α_r (°)	α_e (°)	α_r (°)	ρ	T_2 (ms)	χ^2
90/180	88 (2.4)	176 (4.8)	1013.1 (17.8)	79.2 (1.8)	28.0 (7.6)
85/170	86 (2.3)	172 (4.5)	1007.2 (18.0)	79.3 (2.1)	27.7 (7.6)
80/160	80 (1.7)	161 (3.3)	1004.9 (17.4)	79.5 (1.8)	27.8 (7.5)
75/150	76 (0.8)	152 (1.6)	998.1 (14.7)	79.7 (1.7)	28.1 (7.6)
70/140	70 (1.0)	140 (2.0)	1013.9 (24.8)	78.8 (1.7)	27.9 (7.4)
65/130	65 (0.6)	130 (1.1)	1008.3 (18.2)	79.3 (2.7)	27.6 (7.3)
60/120	60 (0.7)	120 (1.5)	1011.5 (23.5)	79.1 (2.4)	27.5 (7.6)
55/110	55 (0.5)	110 (1.0)	1005.4 (20.2)	79.5 (3.0)	28.0 (7.5)
50/100	50 (0.6)	100 (1.3)	1011.3 (28.3)	79.3 (3.6)	26.9 (6.8)

Table 4.15: The excitation and refocusing pulses were varied with $\alpha_e = 90^\circ, 85^\circ, \dots, 50^\circ$ and $\alpha_r = 2\alpha_e$. The curve fitting calculated α_e , α_r , T_2 , ρ and χ^2 assuming $\alpha_e/\alpha_r = 1/2$.

4.5.6 Discussion

The accuracy of the excitation and refocusing pulse each affect the estimation of the decay curve parameters. The accuracy of the refocusing pulse flip angle is more important and more difficult to attain than the accuracy of the excitation pulse flip angle.

The primary reason the refocusing pulse flip angle is more important is there is an accumulation of errors in the magnetization along a train of refocusing pulses. It is exactly this accumulation of errors which I have exploited to estimate the refocusing pulse flip angle. The excitation pulse is applied once at the beginning of the train and therefore there is not an accumulation effect. The estimated T_2 , when the excitation pulse flip angle was assumed to be $\alpha_e = 90^\circ$, was as accurate and precise (Table 4.14) as the T_2 estimated when the excitation pulse flip angle was estimated along with the refocusing pulse flip angle (Table 4.15).

A second reason the excitation pulse is less important than the refocusing pulse is related to the linearity of the Bloch Equations. The magnetization profile deviates from the Fourier transform of the pulse profile when the flip angle exceeds 30° [82]. The linearity of the Bloch Equations is reasonable up to 90° , but larger errors in the shape of the slice profile occur as α increases to 180° . Therefore, excitation pulses near 90° produce a slice profile closer to the desired than refocusing pulses near 180° .

4.5.7 Conclusions

The excitation pulse flip angle, as well as the refocusing pulse flip angle, is affected by the inhomogeneity and imperfections in the hardware. The inhomogeneities and imperfections lead to spatially varying flip angles. The simulations in this section were used to assess the accuracy and precision of the decay curve parameter estimation in the presence of inaccurate pulses. As was seen, the accuracy and precision of the decay curve parameter estimations, if the flip angles were fit, were similar to the accuracy and precision from a sequence with $\alpha_e = 90^\circ$ and $\alpha_r = 180^\circ$.

4.6 Non-Constant Train of Flip Angles

The work previously showed that T_2 decay curve parameters are accurately and precisely determined when the train of refocusing pulses is less than 180° . As well, as the refocusing pulse flip angle decreased, the signal to noise in the data decreased. This decrease in SNR will lead to increased variability of the measured decay curve parameters.

The short T_2 is of primary interest and is determined from the signal in the decay curve with $TE \leq 50$ ms. Therefore, the refocusing pulses with $TE \leq 50$ ms should be near 180° to retain the signal to noise, but the refocusing pulses where $TE > 50$ ms can be decreased. One method to do this is to decrease the amplitude of latter pulses and have the earlier pulses remain at 180° . This would provide a reasonable trade-off between decreased power deposition and high SNR in the early echoes. The decrease in amplitude was accomplished by defining a scaling vector, \mathbf{s}_α , in which each element can vary between 0 and 1. Each element in the scaling vector \mathbf{s}_α is then multiplied by 180° to create the vector of refocusing pulse flip angles.

There are an infinite number of combinations to scale the flip angle of the refocusing pulses within a pulse train. For the simulations and scanner results of a 16 echo pulse train, I analyzed four possibilities:

- $\mathbf{s}_\alpha^{(1)} = \overbrace{1.0, \dots, 1.0}^{16}$
- $\mathbf{s}_\alpha^{(2)} = \overbrace{0.5, \dots, 0.5}^{16}$
- $\mathbf{s}_\alpha^{(3)} = 1.0, 1.0, 1.0, \overbrace{0.5, 0.5, \dots, 0.5}^{13}$

- $\mathbf{s}_\alpha^{(4)} = 1.0000, 0.9048, 0.8187, 0.7408, 0.6703, 0.6065, 0.5488, 0.4966, 0.4493, 0.4066, 0.3679, 0.3329, 0.3012, 0.2725, 0.2466, 0.2231.$

The first set of scalings, $\mathbf{s}_\alpha^{(1)}$, is a standard pulse train of 180° refocusing pulses. The second set of scalings, $\mathbf{s}_\alpha^{(2)}$, is a pulse train of 90° refocusing pulses. Both of these were used for reference when testing $\mathbf{s}_\alpha^{(3)}$ and $\mathbf{s}_\alpha^{(4)}$. The third set of scalings (Figure 4.19), $\mathbf{s}_\alpha^{(3)}$, is an amalgamation of the first two, it retains 180° refocusing pulses for the first part of the train to retain the higher SNR and the last part of the train is 90° to decrease the power deposition. The fourth set of scalings (Figure 4.20), $\mathbf{s}_\alpha^{(4)}$, was defined as $\mathbf{s}_\alpha^{(4)}(i) = \exp(-i/10)$ for $i = 0, 1, \dots, 15$. The denominator within the exponential was chosen so the decay in the scalings was not too fast. This last one resulted in a smooth decrease in the amplitude of the refocusing pulses throughout the train.

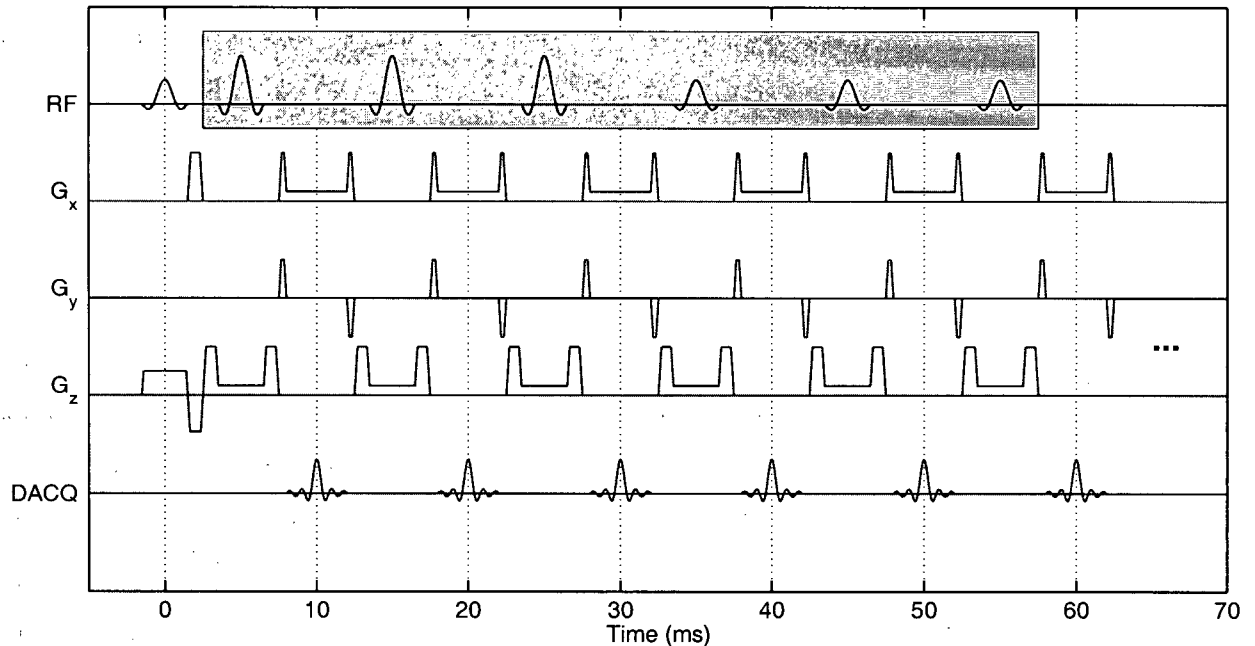


Figure 4.19: A multi-echo, spin echo pulse sequence in which the first three refocusing pulses have a flip angle of 180° and the remaining thirteen have a flip angle of 90° (only six of the 16 shown).

A set of simulations were used to assess the accuracy and precision of decay curve parameter estimation from decay curves collected with non-constant refocusing pulse trains. A pulse sequence was modified to allow arbitrary scaling of the refocusing pulses through the train and was used to assess the effect on the phantoms (Section 1.8).

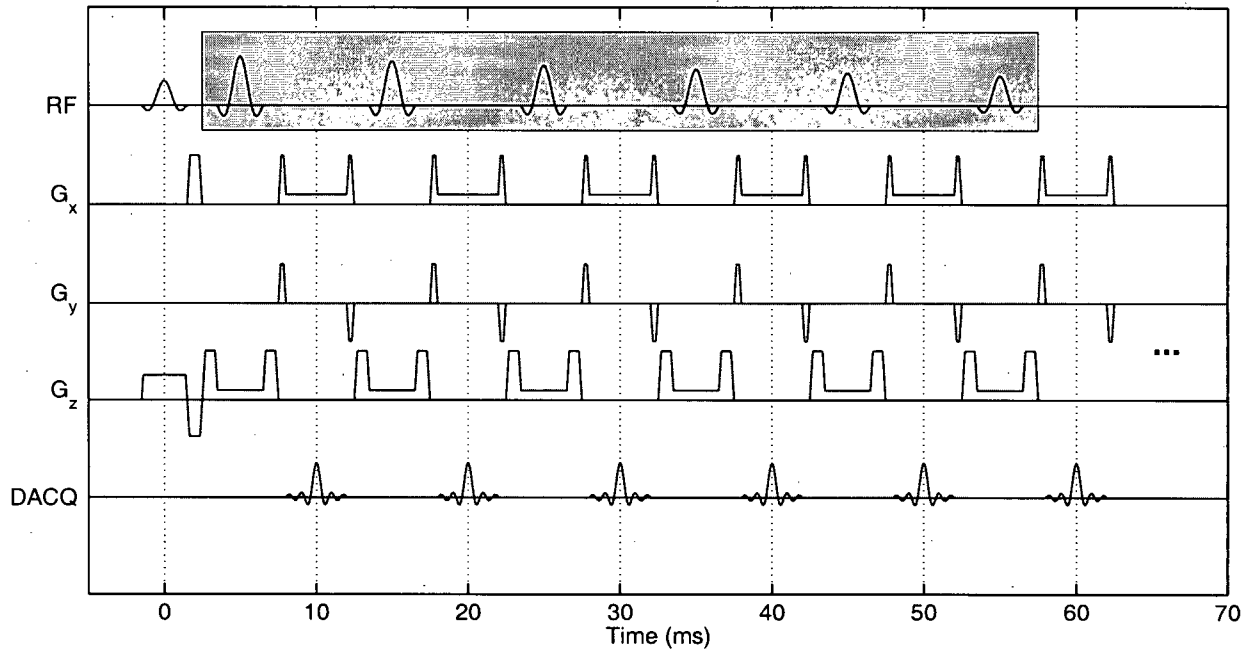


Figure 4.20: A multi-echo, spin echo pulse sequence in which the refocusing pulse amplitudes are decaying exponentially.

4.6.1 Simulations

Determine the accuracy and precision of calculating the proton density, T_2 and flip angle from a decay curve that was “collected” with non-constant refocusing pulses through the train.

4.6.1.1 Methods

I created a set of simulations with $\rho = 1000$, $T_2 = 80$ ms, $\alpha_e = 90^\circ$. The four sets of refocusing pulse trains, defined above, were used. For each decay curve with noise, the decay curve parameters were calculated and compared to truth.

For the decay curves with non-constant refocusing pulses, the relative scale between each pulse was assumed to be known. For example, the relative scale between pulses in the third refocusing pulse train was assumed to be 1.0, 1.0, 1.0, 0.5, \dots , 0.5.

4.6.1.2 Results

The parameters α , ρ , and T_2 were estimated from the simulated data for each of the scalings and are shown in Table 4.16. There was negligible difference between refocusing pulse train $\mathbf{s}_\alpha^{(3)}$ and

$s_{\alpha}^{(4)}$ compared to the constant refocusing pulse train of $\alpha_r = 180^\circ$. As expected, ρ and T_2 had a higher standard deviation in simulation $s_{\alpha}^{(2)}$.

Simulation	α_r	ρ	T_2 (ms)	χ^2
$s_{\alpha}^{(1)}$	176 (4.5)	1010.6 (19.6)	78.7 (2.6)	13.0 (5.4)
$s_{\alpha}^{(2)}$	90 (1.4)	1005.2 (27.3)	78.4 (5.5)	12.8 (4.9)
$s_{\alpha}^{(3)}$	176 (4.5)	1010.6 (19.8)	78.8 (2.8)	12.6 (4.8)
$s_{\alpha}^{(4)}$	176 (4.4)	1010.0 (20.1)	78.8 (2.9)	12.8 (5.1)

Table 4.16: Decay curve parameters calculated for each of the four refocusing pulse trains. For simulation $s_{\alpha}^{(3)}$ and $s_{\alpha}^{(4)}$, the refocusing pulse flip angle, α_r in the second column is to be multiplied by the assumed relative scale to obtain the train of refocusing pulse flip angles. The true T_2 was 80 ms and $\rho = 1000$.

4.6.2 Scanning

The four sets of scalings were implemented in a single slice, 16 echo MESE_c pulse sequence. The nickel/agarose phantoms were scanned with the pulse sequence and the estimated T_2 were compared to the T_2 estimated from the MESE_o sequence.

4.6.2.1 Methods

Scans of the nickel/agarose phantoms were acquired with each of the set of scalings of the refocusing pulse flip angles. Other scan parameters were: FOV = 16 cm, TE = 12.12 ms, TR = 3000 ms, and 16 echoes. The scalings were defined in a file on the scanner computer. At the beginning of the scan() routine, the amplitude of the i^{th} RF pulse (ia_rf2) was scaled by s_{α}^i defined in the file.

4.6.2.2 Results and Discussion

The decay curves for each phantom were fit using NNLS and the results for two phantoms are shown in Figures 4.21 and 4.22. The fitted decay curve was very close to the measured decay curve for both $s^{(3)}$ and $s^{(4)}$. There was a small discrepancy between the measured and fitted decay curves, in particular with $s^{(4)}$, at the fourth echo, which is the first echo after the large change in refocusing pulse flip angle within the train.

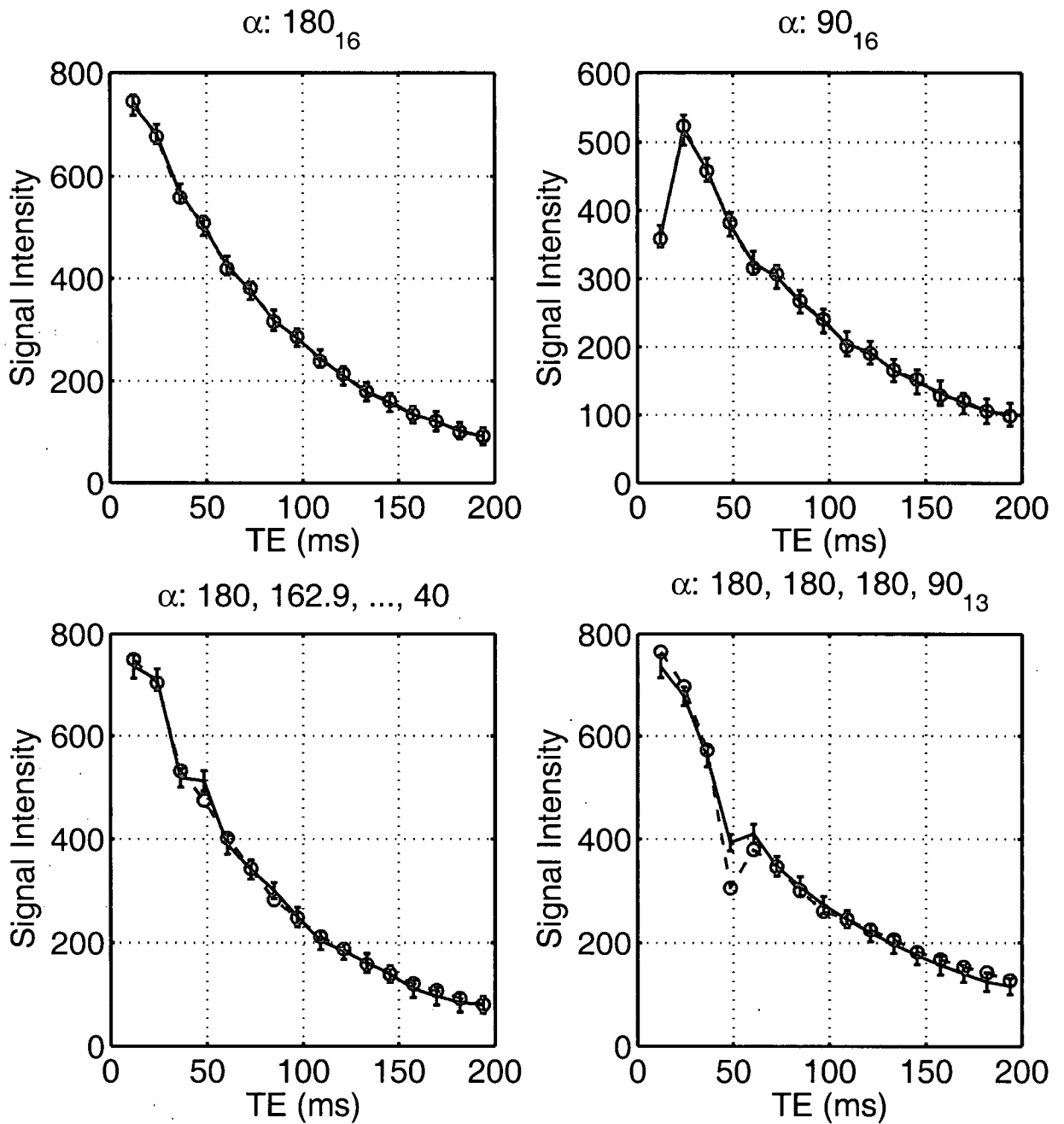


Figure 4.21: Decay curve fit of the bottom, middle phantom, for refocusing pulse trains of 180_N° (top, left), 90_N° (top, right), exponential decay of refocusing pulse flip angles (bottom, left), and $180^\circ, 180^\circ, 180^\circ, 90^\circ, \dots, 90^\circ$ (bottom, right). Measured data shown with whiskers and fitted data shown as circles.

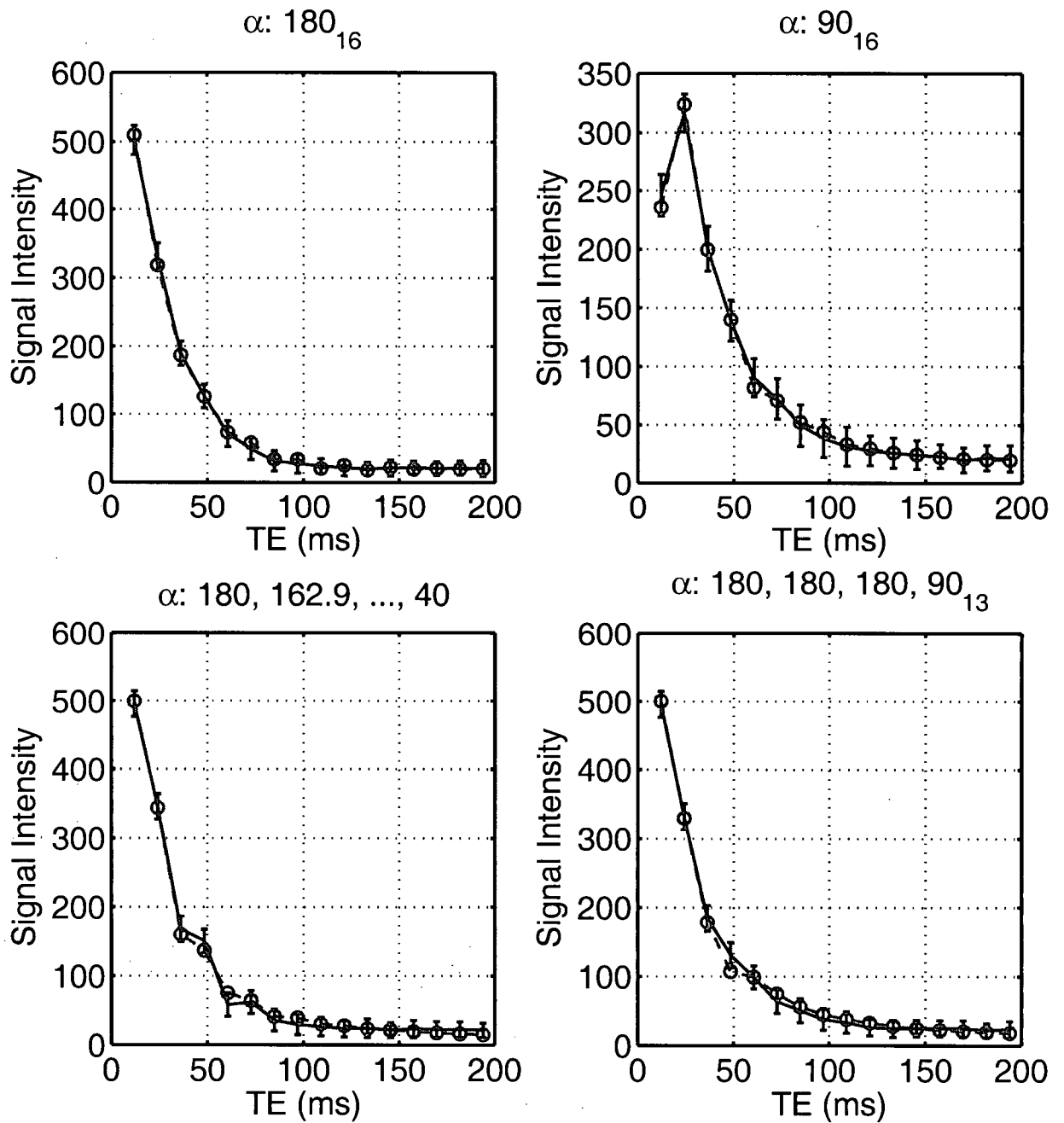


Figure 4.22: Decay curve fit of the bottom, right phantom, for refocusing pulse trains of 180_N° (top, left), 90_N° (top, right), exponential decay of refocusing pulse flip angles (bottom, left), and $180^\circ, 180^\circ, 180^\circ, 90^\circ, \dots, 90^\circ$ (bottom, right). Measured data shown with whiskers and fitted data shown as circles.

The T_2 of each phantom was calculated from each pulse sequence and is shown in Table 4.17. The exponentially decaying refocusing pulse train typically underestimated the T_2 by approximately 10%.

Phantom	Sequence	T_2 (ms)	α ($^\circ$)	χ^2
bottom_left	$s^{(1)}$	24.6	162.0	2.0
bottom_left	$s^{(2)}$	20.9	81.0	1.0
bottom_left	$s^{(3)}$	24.6	154.0	7.0
bottom_left	$s^{(4)}$	21.2	142.0	2.8
bottom_middle	$s^{(1)}$	83.2	157.0	1.0
bottom_middle	$s^{(2)}$	70.0	85.0	0.6
bottom_middle	$s^{(3)}$	82.8	156.0	38.9
bottom_middle	$s^{(4)}$	75.0	145.0	7.7
bottom_right	$s^{(1)}$	23.0	166.0	1.5
bottom_right	$s^{(2)}$	17.3	80.0	1.1
bottom_right	$s^{(3)}$	22.5	156.0	3.4
bottom_right	$s^{(4)}$	20.3	148.0	3.6
top_left	$s^{(1)}$	299.2	156.0	0.4
top_left	$s^{(2)}$	109.9	83.0	1.4
top_left	$s^{(3)}$	374.9	155.0	58.1
top_left	$s^{(4)}$	280.4	146.0	16.0

Table 4.17: The T_2 and refocusing pulse flip angle (for the first echo) calculated from each train of refocusing pulses. The T_2 , from the MESE_o sequence were: 25 ms (bottom, left), 85 ms (bottom, middle), 24 ms (bottom, right), and 280 ms (top, left).

One thing that was a little odd was the curves for $s^{(4)}$ did not follow as well as I would have expected. I noticed from previous work that the calculated refocusing pulse flip angle given $\alpha_0 = 180^\circ$ is approximately $\alpha_{\text{calc}} = 157^\circ$ and given $\alpha_0 = 90^\circ$ is approximately $\alpha_{\text{calc}} = 83^\circ$. The ratio $157^\circ/180^\circ = 0.8722$ does not coincide with $83^\circ/90^\circ = 0.9222$. This would imply that even though I scale the amplitude of the RF pulses by 1.0 and 0.5 when I have two different scalings in the same pulse train, I don't know if I can expect to calculate the same relative scalings. Another way to put it, I don't believe the amplitude scaling of the RF pulses results is linearly correlated with the actual applied RF pulse flip angle.

s_{90}	χ^2	T_2 (ms)
0.50	3.434	22.47
0.53	2.551	22.39
0.55	1.851	22.38
0.57	1.387	22.48
0.60	0.987	22.50
0.62	0.735	22.54
0.65	0.603	22.74
0.68	0.596	22.81
0.70	0.647	23.00
0.72	0.780	23.21
0.75	0.969	23.53

Table 4.18: The resulting χ^2 misfit given the scaling of the RF pulses was 1.0, 1.0, 1.0, s_{90} from $s^{(4)}$. The small misfit was when the scaling of the last 13 echoes was set to 0.68 rather than 0.5, as expected. Row with the minimum χ^2 is in bold.

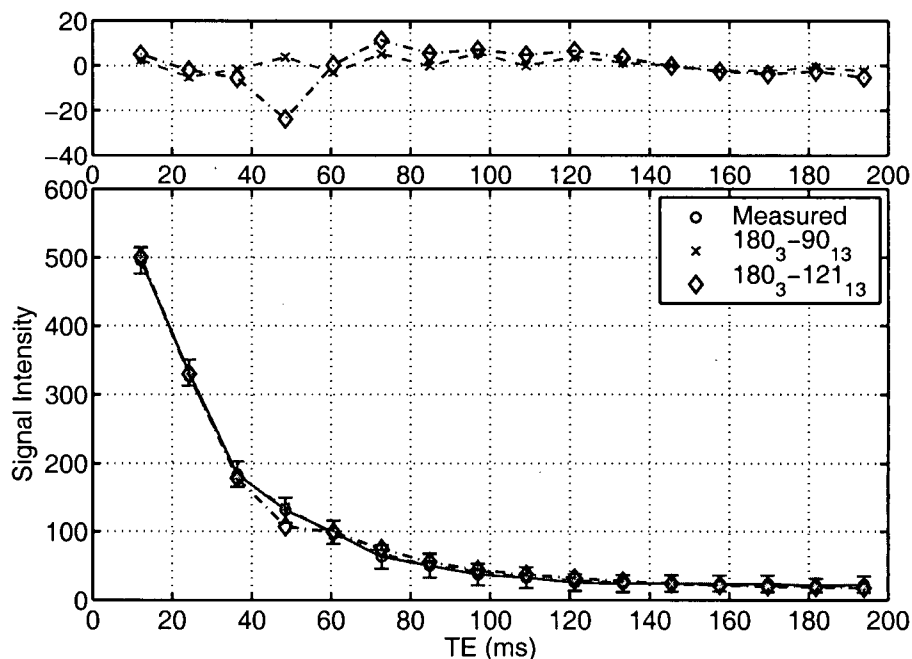


Figure 4.23: The measured data (blue circles), fitted data assuming the scaling of the last 13 echoes was 0.5 (red dashed line) and fitted data assuming scaling was 0.68 (black dot-dashed line). Residuals of fit to measured data shown in top panel.

4.6.3 Conclusion

The amplitude of the RF pulses in the train can be scaled to have any amplitude and the T_2 tends to be reasonably accurate. There does seem to be a non-linear correlation between the input scale parameter and the calculated scaling which may cause some problems. Possibly, this could be included as another step in the fitting process or could be calibrated.

4.7 Conclusions

Methods for T_2 correction due to B_1 inhomogeneities have relied on the acquisition of a B_1 map or based on uniform phantoms. Other methods required two acquisitions to calculate the corrected mono-exponential T_2 , one acquisition to calculate the multi-echo decay curve and the second acquisition to estimate the B_1 field. The method I propose requires only one acquisition, the multi-echo decay curve is sufficient to calculate T_2 and α . Therefore, the T_2 and B_1 are inherently registered and the B_1 accounts for coil loading. As well, the method can be incorporated into any curve fitting technique and, as shown above, is able to accurately quantify multi-exponential decay curves.

High field systems ($\geq 3T$) have inhomogeneous B_1 fields, due to the dielectric effect [83], and require high power deposition for 180° refocusing pulses [84]. Gareau *et al.* [85] compared T_2 distributions of guinea pig brain at 1.5T and 4T and found both the short and medium T_2 peaks had a faster decay at the higher field strength. The decrease in T_2 at higher field would require shorter echo times. I have shown that decay curve parameters can be calculated in the presence of refocusing pulses with $\alpha \leq 180^\circ$. Another equally important observation is that quantitative T_2 measurements can be estimated from a train of α refocusing pulses having $\alpha \ll 180^\circ$. There has been a restriction on the length of the train of 180° refocusing pulses due to the power deposition *in vivo*. The methodology described enables quantitative T_2 measurements to be done on high field systems and will account for the echo artifacts.

Chapter 5

Conclusions

5.1 Filtering

Image processing, noise reduction filters are a simple and fast method to decrease the variability in local areas of an image. The goal of the work was to decrease the variability in local areas of the myelin water map by filtering the multi-echo data acquired by an MRI machine. Variability in the myelin water fraction over a region was a logical and simple measure to analyze the filters. Simulated multi-echo data was an important step in assessing the filters as there were no artifacts due to imaging, for example flow, head motion, and Fourier transform reconstruction. The *in vivo* myelin water maps looked much better if the multi-echo data was processed using a noise reduction filter. For myelin water maps calculated from the non-linear curve fitting algorithms, it is important to apply the noise reduction filter to the original multi-echo data.

The image processing filters, presented in this work, are the more popular noise reduction filters used in MRI today. Image processing is an evolving field and there will likely be other filters which could prove to be better. The primary goals for a noise reduction filter, applied to myelin water quantification, should include: ability to smooth over homogeneous areas and retain the boundaries between the tissues, produce little or no bias in the mean myelin water fraction over a region, and reduce the variability of the myelin water fraction within a local region.

5.2 Linear Combination

The linear combination method to calculate the myelin water fraction was shown to be robust and very fast, in addition to its extreme ease of implementation after the coefficients are determined. The short T_2 filter was to select for T_2 near 20 ms only, and suppressed all T_2 above 70 ms. The myelin water maps were comparable to myelin water maps calculated by the NNLS algorithm. The linear combination method to analyze T_2 from a multi-echo MRI dataset is restricted primarily to

the short T_2 range. The restriction is due to the broad selection if longer T_2 are of interest. The broad selection would negate the use of linear combination for T_2 longer than 50 ms. Therefore, the curve fitting algorithms which provide information about the T_2 distribution are still required if the T_2 of interest is greater than 50 ms.

The coefficients calculated using the non-linear algorithm, applied to the calculation of the myelin water fraction, were shown to provide robust myelin water fraction measures. Though, other sets of coefficients could provide more robust myelin water fraction measures. Other types of algorithms could be used to create another set of coefficients. One method is to fit the filter to a pre-defined filter and minimize the misfit between the two. Another method is to change the constraints, used in the algorithm presented, to create a more appropriate filter. One must remember that the underlying data is a set of exponentials, and exponentials are very non-orthogonal as a function of T_2 . Therefore, it may not be possible to create a better filter than what is presented.

The short T_2 filter associated with the coefficients calculated in this chapter is slightly asymmetric in that the filter for $20 \leq T_2 \leq 70$ ms is less sharp than the filter for $10 \leq T_2 \leq 20$ ms. This provides a difficulty that a myelin water compartment which has an increase in the T_2 is indistinguishable from a myelin water compartment that has only a decrease in the amplitude of the T_2 peak. But, this has provided some interesting insight into one region of the brain. The internal capsules (at the level of the genu and splenium of the corpus callosum) typically appear brighter on a myelin water map, which implies a higher myelin water fraction. Myelin water maps, from the linear combination method, appear to have a decreased myelin water fraction in the same region. This would seem to imply there is a shift in the myelin water T_2 toward higher T_2 and is corroborated by results based on the NNLS algorithm. The shift toward higher T_2 would be accounted for by a greater distance between the lipid bilayers compared to the distance between the lipid bilayers in other white matter.

The linear combination for myelin water quantification provides a fast and reliable method to assess myelin water. The technique applied to 32 echoes proved to be robust relative to the NNLS technique, though, using fewer echoes may prove to be an important step. Shorter trains of RF pulses are more desirable than longer trains as there is less power deposition, but also, the "dead time" may be used in creative ways. A four-echo, interleaved in time and space may allow myelin water quantification from a volume of the brain.

5.3 B_1/T_2

The T_2 distribution is calculated from a multi-echo decay curve. The decay curve is a combination of the primary echo as well as stimulated and indirect echoes. The stimulated and indirect echoes are a function of the refocusing pulse flip angle (α). Therefore, a modified T_2 curve fitting algorithm should be able to estimate the T_2 distribution, as well as the refocusing pulse flip angle, from a multi-echo decay curve.

I presented an algorithm to estimate T_2 and α from a mono-exponential decay curve and a modified NNLS algorithm, NNLS $^\alpha$, to estimate the T_2 distribution and α from a multi-exponential decay curve. Noise simulations showed that the accuracy and precision were similar to the standard method to estimate T_2 . A decrease in the precision of the estimation was shown to be a function of the decreased α .

Several extensions to the method were discussed: slab selected multi-slice, train of non-constant refocusing pulses and the effect of a non-90° excitation pulse. The method enables the use of slice-selective refocusing pulses, as the accuracy of the refocusing pulse is less important as it is calculated during the curve fit. Therefore, multiple slices, within a slab, can be excited and acquired. This is an important extension to the current single-slice method. Multiple sclerosis lesions, for example, may span several slices, and therefore, to track lesions over time, it is important to obtain a view of normal and diseased tissue above and below a lesion. A second strength of the method is the curve fit algorithm is able to estimate the T_2 from a train of non-180° refocusing pulses. A pulse sequence, with a train of non-180° refocusing pulses deposits less power into a patient. Therefore, T_2 estimation on a high field system (e.g., 3T) would be possible with a train of refocusing pulses less than 180°, though a trade-off may happen due to the decrease in T_2 of the short and medium components.

The amplitude of a refocusing pulse is not the only property that can be changed, another option is to change the phase of the pulse. Many groups have worked on phase schemes for more robust T_2 decay curves, which have resulted in the Meiboom-Gill [86] extension to the original Carr-Purcell [87] pulses, and MLEV phase cycling [30]. The effectiveness of adjusting the phase of the RF pulse, rather than the amplitude, is that adjusting the phase can be done more precisely. The relationship between the amplitude of an RF pulse and the flip angle is based on a small tip angle assumption, which is weakly valid for $\alpha > 30^\circ$ and less-so for $\alpha > 90^\circ$ (this is likely

the cause of some discrepancies seen in Section 4.6, tailored RF pulses, such as those from the Shinnar-Le Roux algorithm, seek to work around these assumptions).

Three weaknesses exist in the standard method to estimate the myelin water fraction: 1) low SNR, 2) single slice, and 3) long scan time. The first and third weaknesses are tightly coupled. The primary method to obtain a higher SNR is to do multiple averages. Decreasing the scan time, without a large decrease in the SNR, would increase the clinical feasibility of myelin water imaging. The standard assumption in quantitative T_2 is the pulse sequence must have a long TR to allow magnetization relax back to thermal equilibrium along the longitudinal axis. Currently, the time between the final echo and the following excitation is at least one second. More efficient use of the dead time is required. One possibility is to decrease the dead-time between the final echo and the next excitation pulse. If possible, it would be best to find a method to force all magnetization back to the longitudinal axis. A second possibility, would be to apply the phase coherence information in Section 4.1.2 and to track the magnetization not only through a single pulse train, but through successive pulse trains.

5.4 Preferred T_2 Quantification Protocol

The quantification of myelin water is important for continued basic science research. The current protocol, using MRI, to quantify the myelin water fraction is to use an optimized 32-echo spin-echo pulse sequence to collect the multi-echo data, then quantify the short T_2 using the NNLS algorithm. The multi-echo sequence and NNLS algorithm were shown, previously, to be a good combination to quantify the myelin water fraction. There are three motivations to change the current protocol: first, higher SNR data is required for more robust quantification of the myelin water fraction; second, averaging of single slice data is an inefficient use of time; third, more slices are necessary to assess Multiple Sclerosis lesions and their change over time. Therefore, given the motivations to change the current protocol, the following protocol is suggested.

The preferred method to calculate the myelin water fraction is to collect a multi-slice, multi-echo MRI dataset with a long TR. The dataset would be processed with the 3D anisotropic diffusion filter which averages the signal based on edge information derived over the channels (channel filtering). The non-negative least squares algorithm, modified to calculate the B_1 at each voxel, would be applied voxel-by-voxel to the noise-reduced, 3D dataset.

Bibliography

- [1] F. Bloch. Nuclear induction. *Phys. Rev.*, 70(7,8):460–474, 1946.
- [2] N. Bloembergen, E. M. Purcell, and R. V. Pound. Relaxation effects in NMR absorption. *Phys. Rev.*, 73:679–712, 1948.
- [3] P. Morell and W.T. Norton. Myelin. *Scientific American*, 242(5):88–117, 1980.
- [4] R.B. Dietrich and C. Hoffmann. Myelination and dysmyelination. In D.D. Stark and Jr. W.G. Bradley, editors, *Magnetic Resonance Imaging*, chapter 23, pages 1057–1080. Mosby Year Book, Inc., St. Louis, Missouri, second edition, 1992.
- [5] E.R. Kandel, J.H. Schwartz, and Jessel T.M., editors. *The Principles of Neural Science*. Prentice Hall, 3rd edition, 1985.
- [6] A.J. Barkovich. Concepts of myelin and myelination in neuroradiology. *Am J Neuroradiol*, 21:1099–1109, 2000.
- [7] P. Morell, editor. *Myelin*. 2nd edition, 1985.
- [8] T.J. Copeland. <http://www.albany.net/~tjc/gloss1-m.html#M>.
- [9] G. R. Cherryman and F. W. Smith. Nuclear magnetic resonance in adrenoleukodystrophy: report of a case. *Clin Radiol*, 36(5):539–40, Sep 1985.
- [10] J. C. Masdeu, J. Moreira, S. Trasi, P. Visintainer, R. Cavaliere, and M. Grundman. The open ring. a new imaging sign in demyelinating disease. *J Neuroimaging*, 6(2):104–7, Apr 1996.
- [11] M. H. Teicher, C. M. Anderson, A. Polcari, C. A. Glod, L. C. Maas, and P. F. Renshaw. Functional deficits in basal ganglia of children with attention-deficit/hyperactivity disorder

- shown with functional magnetic resonance imaging relaxometry. *Nat Med*, 6(4):470–3, April 2000.
- [12] V. Vasilescu, V. Simplaceanu E. Katona and, and D. Demco. Water compartments in the myelinated nerve. III. Pulsed NMR results. *Experientia*, 34:1443–1444, 1978.
- [13] RM Kroeker and Henkelman RM. Analysis of biological NMR relaxation data with continuous distributions of relaxation times. *J. Magn. Reson.*, 69:218–235, 1986.
- [14] R. S. Menon and P. S. Allen. Application of continuous relaxation time distributions to the fitting of data from model systems and excised tissue. *Magn Reson Med*, 20:214–227, 1991.
- [15] A. L. MacKay, K. P. Whittall, K. S. Cover, D. K. B. Li, and D. W. Paty. In vivo visualization of myelin water in brain from mr spin-spin relaxation measurement. In *Proceedings of the RSNA*, page 142. RSNA, 1991.
- [16] A. L. MacKay, K. P. Whittall, K. S. Cover, D. K. B. Li, and D. W. Paty. In vivo T_2 relaxation measurements of brain may provide myelin concentration. In *Proceedings of the SMRM*, page 917. SMRM, 1991.
- [17] W. A. Stewart, A. L. MacKay, K. P. Whittall, G. R. W. Moore, and D. W. Paty. Spin-spin relaxation in experimental allergic encephalomyelitis. analysis of CPMG data using a non-linear least squares method and linear inverse theory. *Magn. Reson. Med.*, 29:767–775, 1993.
- [18] A. MacKay, K. Whittall, J. Adler, D. Li, D. Paty, and D. Graeb. In vivo visualization of myelin water in brain by magnetic resonance. *Magn Reson Med*, 31(6):673–7, Jun 1994.
- [19] K. P. Whittall, A. L. MacKay, D. Graeb, R. Nugent, D. K. B. Li, and D. W. Paty. In vivo measurement of T_2 distributions and water contents in normal human brain. *Magn. Reson. Med.*, 37:34–43, 1997.
- [20] C Beaulieu, FR Fenrich, and PS Allen. Multicomponent water proton transverse relaxation and T_2 -discriminated water diffusion in myelinated and nonmyelinated nerve. *Magn Reson Imaging*, 16(10):1201–1210, 1998.

- [21] IM Vavasour, KP Whittall, AL MacKay, DK Li, G Vorobeychik, and DW Paty. A comparison between magnetization transfer ratios and myelin water percentages in normals and multiple sclerosis patients. *Magn Reson Med*, 40(5):763–768, 1998.
- [22] GJ Stanisz, A Kecojevic, MJ Bronskill, and RM Henkelman. Characterizing white matter with magnetization transfer and T2. *Magn Reson Med*, 42(6):1128–1136, 1999.
- [23] P.J. Gareau, B.K. Rutt, S.J. Karlik, and J.R. Mitchell. Magnetization transfer and multi-component T2 relaxation measurements with histopathologic correlation in an experimental model of MS. *J. Magn. Reson. Imag.*, 11(6):585–595, 2000.
- [24] G.J. Stanisz and R.M. Henkelman. Diffusional anisotropy of T2 components in bovine optic nerve. *Magn. Reson. Med.*, 40:405–410, 1998.
- [25] R. S. Menon and P. S. Allen. Application of continuous relaxation time distributions to the fitting of data from model systems and excised tissue. *Magn. Reson. Med.*, 20:214–227, 1991.
- [26] D. L. Phillips. A technique for the numerical solution of certain integral equations of the first kind. *Journal of the ACM*, 9:84–97, 1962.
- [27] P. C. Hansen. Numerical tools for analysis and solution of Fredholm integral equations of the first kind. *Inverse Problems*, 8:849–872, 1992.
- [28] C. L. Lawson and R. J. Hanson. *Solving least square problems*. Prentice Hall, Englewood Cliffs NJ, 1974.
- [29] DB Twieg. The k-trajectory formulation of the NMR imaging process with applications in analysis and synthesis of imaging methods. *Med. Phys.*, 10:610–621, 1983.
- [30] M.H. Levitt and R. Freeman. Compensation for pulse imperfections in NMR spin-echo experiments. *J. Magn. Reson.*, 43:65–80, 1981.
- [31] C.S. Poon and R.M. Henkelman. Practical T₂ quantitation for clinical applications. *J. Magn. Reson. Imag.*, 2:541–553, 1992.
- [32] R. M. Henkelman. Measurement of signal intensities in the presence of noise in MRI images. *Med. Phys.*, 12(2):232–233, 1985.

- [33] E. W. Weisstein. Rice distribution. *Eric Weisstein's World of Mathematics*, 2000. <http://mathworld.wolfram.com/RiceDistribution.html>.
- [34] James A. Roberts. http://people.eecs.ku.edu/~jroberts/private/Appendix_A.pdf.
- [35] A.P. Crawley and R.M. Henkelman. Errors in T_2 estimation using multislice multiple-echo imaging. *Magn. Reson. Med.*, 4:34–47, 1987.
- [36] I. M. Vavasour, K. P. Whittall, D. K. Li, and A. L. MacKay. Different magnetization transfer effects exhibited by the short and long T_2 components in human brain. *Magn Reson Med*, 44(6):860–6, December 2000.
- [37] D.E. Woessner. Effects of diffusion in nuclear magnetic resonance spin-echo experiments. *J. Chem. Phys.*, 34(6):2057–61, 1961.
- [38] J.H. Jensen, R. Chandra, and H. Yu. Quantitative model for the interecho time dependence of the CPMG relaxation rate in iron-rich gray matter. *Magn. Reson. Med.*, 46:159–165, 2001.
- [39] C.L. Lawson and R.J. Hanson. *Solving least square problems*. Prentice Hall, Englewood Cliffs NJ, 1974.
- [40] K.P. Whittall and A.L. MacKay. Quantitative interpretation of NMR relaxation data. *J. Magn. Reson.*, 84:134–152, 1989.
- [41] K. P. Whittall, M. J. Bronskill, and R. M. Henkelman. Investigation of analysis techniques for complicated NMR relaxation data. *J. Magn. Reson.*, 95:221–234, 1991.
- [42] R. M. Kroeker and R. M. Henkelman. Analysis of biological NMR relaxation data with continuous distributions of relaxation times. *J. Magn. Reson.*, 69:218–235, 1986.
- [43] K. P. Whittall and A. L. MacKay. Quantitative analysis of NMR relaxation data. *J. Magn. Reson.*, 84:134–152, 1989.
- [44] S. J. Graham, P. L. Sanchez, and M. J. Bronskill. Criteria for analysis of multicomponent tissue T_2 relaxation data. *Magn. Reson. Med.*, 35(3):370–378, 1996.

- [45] K. P. Whittall, A. L. MacKay, and D. K. B. Li. Are mono-exponential fits to a few echoes sufficient to determine T_2 relaxation for in vivo human brain? *Magn. Reson. Med.*, 41(6):1255–1257, 1999.
- [46] K. A. Kraft, P. P. Fatouros, G. D. Clarke, and P. R. S. Kishore. An MRI phantom material for quantitative relaxometry. *Magn. Reson. Med.*, 5:555–562, 1987.
- [47] J. O. Christoffersson, L. E. Olsson, and S. Sjöberg. Nickel-doped agarose gel phantoms in mr imaging. *Acta Rad.*, 32:426–431, 1991.
- [48] M. D. Mitchell, H. L. Kundel, L. Axel, and P. M. Joseph. Agarose as a tissue equivalent phantom material for NMR imaging. *Magn. Reson. Imag.*, 4:263–266, 1986.
- [49] A.L. MacKay, K.P. Whittall, J. Adler, D.K.B. Li, D.W. Paty, and D. Graeb. *In vivo* visualization of myelin water in brain by magnetic resonance. *Magn. Reson. Med.*, 31:673–677, 1994.
- [50] P. Perona and J. Malik. Scale space and edge detection using anisotropic diffusion. *Proc. IEEE Computer Society Workshop on Computer Vision*, 1987.
- [51] G. Gerig, O. Kubler, R. Kikinis, and F. Jolesz. Nonlinear anisotropic filtering of MRI data. *IEEE Transactions on Medical Imaging*, 11(2):221–231, 1992.
- [52] J. R. Mitchell, S. J. Karlik, D. H. Lee, M. Eliasziw, G. P. Rice, and A. Fenster. Quantification of multiple sclerosis lesion volumes in 1.5 and 0.5 T anisotropically filtered and unfiltered MR exams. *Med Phys*, 23(1):115–26, 1996.
- [53] B. Mackiewicz. Intracranial boundary detection and radio frequency correction in magnetic resonance images. Master’s thesis, Simon Fraser University, 1995.
- [54] M. M. Orkisz, C. Bresson, I. E. Magnin, O. Champin, and P. C. Douek. Improved vessel visualization in MR angiography by nonlinear anisotropic filtering. *Magn Reson Med*, 37(6):914–9, 1997.
- [55] R. Zingale and A. Zingale. Detection of MRI brain contour using isotropic and anisotropic diffusion filter. A comparative study. *J Neurosurg Sci*, 42(2):111–4, 1998.

- [56] S.M. Smith and J.M. Brady. SUSAN - a new approach to low level image processing. *Int. J. Comput. Vis.*, 23:34ff, 1997.
- [57] L. Woog. *Adaptive waveform algorithms for denoising*. PhD thesis, Yale University, 1996.
- [58] R.R. Coifman, M.V. Wickerhauser, and L. Woog. *Adaptive design toolkit software*. Fast Mathematical Algorithms and Software Corporation, 1997.
- [59] J.C. Wood and K.M. Johnson. Wavelet packet denoising of magnetic resonance images: Importance of rician noise at low SNR. *Magn Reson Med*, 41:631–635, 1999.
- [60] Ingrid Daubechies. *Ten lectures on wavelets*. Society for Industrial and Applied Mathematics, 1992.
- [61] H. Gudbjartsson and S. Patz. The Rician distribution of noisy MRI data. *Magn. Reson. Med.*, 34:910–914, 1995.
- [62] B. Efron and R. Tibshirani. Bootstrap methods for standard errors, confidence intervals, and other measures of statistical accuracy. *Statistical Science*, 1(1):54–77, 1986.
- [63] A. Macovski. Selective projection imaging: Applications to radiography and NMR. *IEEE Trans. on Med. Imag.*, 1(1):42–47, July 1982.
- [64] T. Brosnan, G. Wright, D. Nishimura, Q. Cao, A. Macovski, and F.G. Sommer. Noise reduction in magnetic resonance imaging. *Mag Reson Med*, 8:394–409, 1988.
- [65] K.P. Whittall, M.J. Bronskill, and R.M. Henkelman. Investigation of analysis techniques for complicated NMR relaxation data. *J Magn Reson*, 95:221–234, 1991.
- [66] G.E. Backus and J.F. Gilbert. The resolving power of growth earth data. *Geophys. J. Roy. Astron. Soc.*, 16:169–205, 1968.
- [67] G.E. Backus and J.F. Gilbert. Uniqueness in the inversion of inaccurate gross earth data. *Phil. Trans. Roy. Soc. London Ser. A*, 266(123-192), 1970.
- [68] David Heeger. Linear Systems. <http://white.stanford.edu/~heeger/linear-systems/linear-systems.html>.

- [69] J.M. Bland and D.G. Altman. Statistical method for assessing agreement between two methods of clinical measurement. *The Lancet*, i:307–310, 1986.
- [70] J.M. Bland and D.G. Altman. Measuring agreement in method comparison studies. *Statistical Methods in Medical Research*, 8:135–160, 1999.
- [71] S. Majumdar, S.C. Orphanoudakis, A. Gmitro, M. O'Donnell, and J.C. Gore. Errors in the measurements of T_2 using multiple-echo MRI techniques I. Effects of radiofrequency pulse imperfections. *Magn. Reson. Med.*, 3:397–417, 1986.
- [72] G.P. Liney, A.J. Knowles, D.J. Manton, and A. Horsman. T_2 mapping with the fast spin-echo and conventional spin-echo sequences in the presence of B_1 inhomogeneities. In *Proceedings of the ISMRM*, page 2071, 1997.
- [73] Zur Y. and Stokar S. A phase-cycling technique for cancelling spurious echoes in NMR imaging. *J. Magn. Reson.*, 71:212–228, 1987.
- [74] J.H. Duijun, J.H.N Creyghton, and J. Smidt. Suppression of artifacts due to imperfect π pulses in multiple echo Fourier imaging. In *Proceedings of the Third Annual Society for Magnetic Resonance*, number 197-198, 1984.
- [75] J.G. Sled and G.B. Pike. Correction for B_1 and B_0 variations in quantitative T_2 measurements using MRI. *Magn. Reson. Med.*, 43:589–593, 2000.
- [76] M. Lepage, P.S. Tofts, S.Å.J. Bäck, P.M. Jayasekera, and C. Baldock. Simple methods for the correction of T_2 maps of phantoms. *Magn. Reson. Med.*, 46:1123–9, 2001.
- [77] R. Kaiser, E. Bartholdi, and R.R. Ernst. Diffusion and field-gradient effects in NMR fourier spectroscopy. *J. Chem. Phys.*, 60(8):2966–2979, 15 April 1974.
- [78] J. Hennig. Multiecho imaging sequences with low refocusing flip angles. *J. Magn. Reson.*, 78:397–407, 1988.
- [79] J Simbrunner. Generalization of the partition method for calculating echo magnitudes. *J. Magn. Reson. A*, 109:117–120, July 1994.

- [80] C. Seong, D. Jones, W.E. Reddick, R.J. Ogg, and R.G. Steen. Establishing norms for age-related changes in proton T1 of human brain tissue in vivo. *Magn Reson Imag*, 15(10):1133–1143, 1997.
- [81] R Stollberger and P Wach. Imaging of the active B1 field in vivo. *Magn Reson Med*, 35(2):246–51, 1996.
- [82] E. T. Lebsack and S. M. Wright. Iterative RF pulse refinement for magnetic resonance imaging. *IEEE Trans Med Biol Eng*, 49(1):41–48, 2002.
- [83] M. Alecci, C. M. Collins, M. B. Smith, and P. Jezzard. Radio frequency magnetic field mapping of a 3 Tesla birdcage coil: Experimental and theoretical dependence on sample properties. *Magn Reson Med*, 46(2):379–385, 2001.
- [84] D.I. Hoult. Signal and Power in High Field Engineering. In *ISMRM Workshop on High Field Engineering*, pages 2–3, 14 October 1999.
- [85] P.J. Gareau, B.K. Rutt, C.V. Bowen, S.J. Karlik, and J.R. Mitchell. In vivo measurements of multi-component T2 relaxation behaviour in guinea pig brain. *Magn. Reson. Imag.*, 17(9):1319–1325, 1999.
- [86] S. Meiboom and D. Gill. Modified spin-echo method for measuring nuclear relaxation times. *Phys. Rev.*, 29:688–691, 1958.
- [87] H.Y. Carr and E.M. Purcell. Effects of diffusion on free precession in nuclear magnetic resonance experiments. *Phys. Rev.*, 94:630–639, 1954.

Appendix A

Related Publications

- **Chapter 2: Myelin Water Fraction Noise Reduction**

- Paper: **Jones, C.K.**, Whittall, K.P., Mackay, A.L., "Robust Myelin Water Quantification: Averaging vs Spatial Filtering", *Magn Reson Med* (in press), 2003.
- Presentation: **Jones, C.K.**, Whittall, K.P., MacKay, A.L., "Validation of Anisotropic Filtering for Myelin Water Maps". Proceedings of the International Society of Magnetic Resonance in Medicine. Glasgow, Scotland, April 21-27, (2001). Page 820.

- **Chapter 3: Myelin Water Fraction from Linear Combination**

- Paper: **Jones, C.K.**, Xiang, Q.S., Whittall, K.P., Mackay, A.L., "Short T_2 Selection From Linear Combination of Images", *Magn Reson Med* (accepted), 2003.
- Presentation: **Jones, C.K.**, Xiang, Q.S., Whittall, K.P., Mackay, A.L., "Multi-Echo Linear Combination for Myelin Water Imaging". Proceedings of the International Society of Magnetic Resonance in Medicine. Honolulu, HI, May 18-24, (2002). Page 2289

- **Chapter 4: Non-180 Refocusing Pulses**

- Paper: **Jones, C.K.**, Xiang, Q.S., Whittall, K.P., Mackay, A.L., "Calculating T_2 and B_1 from Decay Curves Collected with non-180° Refocusing Pulses", *Magn Reson Med* (submitted), 2003.
- Presentation: **Jones, C.K.**, Xiang, Q.S., Whittall, K.P., Mackay, A.L., "Calculating T_2 and B_1 from Decay Curves Collected with non-180° Refocusing Pulses", Proceedings of the International Society of Magnetic Resonance in Medicine. Toronto, ON, July 10-16, (2003).